L. deBarbaro

R-1237
CU-403
Nevis-297

Columbia University
Department of Physics
New York, New York 10027

MEASUREMENTS OF R_{long} AND $|V_{cs}|$ FROM THE CCFR EXPERIMENT

Cynthia Kay McNulty

Submitted in partial fulfillment of the
requirements for the degree
of Doctor of Philosophy
in the Gradauate School of Arts and Sciences
COLUMBIA UNIVERSITY

National Science Foundation
NSF PHY 95-12810

1997

MEASUREMENTS OF R_{long} AND $|V_{cs}|$ FROM THE CCFR EXPERIMENT

Cynthia Kay McNulty
Columbia University, New York, NY

* Research supported by the National Science Foundation.
† Submitted in partial fulfillment of the requirement for the degree of Doctor of Philosophy in the Graduate School of Arts and Sciences, Columbia University.

Abstract

The four structure functions F_2, R_{long}, xF_3^{ν}, and $xF_3^{\bar{\nu}}$ are extracted from measurements of inclusive charged-current ν-Fe interactions in the CCFR detector at the Fermilab Tevatron. The analysis produces measurements of the CKM matrix element $|V_{cs}| = 1.05 \pm 0.10\ ^{+0.07}_{-0.11}$ and measurements of R_{long} made at $0.0 \geq x \geq 0.425$ and $1 \geq Q^2 \geq 100\ GeV^2$. The new R_{long} measurements probe a low-x kinematic region ($x = 0.01$) which is important for constraining the gluon distribution.

Table of Contents

List of Figures

List of Tables

1 Introduction

Physics is concerned with understanding what our world is made of and how it evolves. Physicists study many different types of systems ranging from enormous, complicated ones like the galaxies to tiny, simple ones like the fundamental building blocks that make up all matter, the so-called elementary particles. This study zooms down to the present inward frontier going deep inside the proton to look at one family of elementary particles, the quarks. We know of six types of quarks: the up, down, strange, charmed, top and bottom quarks. They communicate with one another by exchanging a particle called a gluon. A continuous exchange of gluons holds the quarks together to form objects like the proton. This thesis concentrates on measuring two quantities, R_{long} and κ (*kappa*). As will be explained, R_{long} illuminates the actions of the gluons. κ determines how many strange quarks exist inside the proton relative to the other quark varieties.

There are no instruments capable of seeing inside a proton. However, we can "hit" it with some energy. The energy will be absorbed by one of the quarks that make up the proton. This quark will begin to break away from the others, triggering a cascade of quark interactions. They will break their existing bonds and make new ones by exchanging gluons. If we hit the proton hard enough the new combinations will "fly out" and we can record and study them. Quarks have the interesting property that they do not exist by themselves in nature. Hence we will not see individual quarks flying out, but combinations of quarks. These combinations are generically labeled "hadrons". You could say we are smashing the proton apart and studying the hadronic remnants. The process is formally called "*neutrino-nucleon deep-inelastic scattering*" (ν-N DIS).

Consider the name of this process one word at a time. Like the quarks, the *neutrino* (ν) is also an elementary particle but it belongs to a different family, the leptons. The study of leptons is also interesting, but we are only going to use the neutrino as a tool to smash the proton. "*Nucleon*" (N) refers to either a proton or its sibling the neutron which is also made of quarks. Logistically, using both the neutron and the proton as a source for quarks will be preferable because the ν travels through a lot of material before interacting and it is easier to amass several hundred tons of steel (which is made of protons and neutrons) than an equivalent amount of hydrogen molecules. In general an interaction is said to be *elastic* if the participants remain intact. Our process is "*inelastic*" because the neutrino will hit the nucleon "*deeply*" enough to break it up. The neutrino "hits" the quark by passing energy to it, consequently conservation of momentum causes the neutrino to recoil. A physicist describes this interaction by saying the neutrino "*scatters*" off the nucleon. The following equation is a short-hand description:

$$\nu_\mu + N \rightarrow \mu + X \tag{1.1}$$

This equation represents an event in which a muon neutrino (ν_μ) scatters off of a Nucleon (N) producing a muon (μ) and a shower of hadrons (X). Thus we have "*neutrino-nucleon deep-inelastic scattering*".

This chapter sketches out a formalism for measuring R_{long} and κ using ν-N DIS. To begin with, the Standard Model of particle physics introduces the elementary particles and the forces by which they interact. A motivation for using ν-N DIS to study the quarks follows. The kinematic variables that are used to describe a DIS interaction are defined. Using these variables, a mathematical representation of the interaction is derived in terms of structure functions (SF), including R_{long}. As their

name suggests, the structure functions represent an internal blueprint of the nucleon. Ultimately the chapter will focus on two quantities which come directly from these structure functions, ΔxF_3 and R_{long}. Models will be introduced that link these mathematical expressions to the underlying physics: ΔxF_3 holds information on the strange quark and R_{long} provides information on the gluons.

1.1 The Standard Model

People have long wondered what makes up our physical world. In the 5th century B.C. the Greek philosophers Leukippos and Demokritos proposed a theory which described all matter as being composed of finite, indivisible particles. Many centuries of accomplishments have gone into the theories which today are lumped into the category of "classical" physics. In the early part of the 20th century physicists began to radically change the way they thought of matter. My first quantum mechanics teacher introduced the subject by saying "if you aren't confused by quantum mechanics then you don't understand it." (good luck)

Classical physics focuses on describing the interactions of matter as the result of four forces: the electro-magnetic force, the strong nuclear force, the weak nuclear force, and the gravitational force. Classical physics describes the consequences of a force acting on matter but not the mechanism employed by that force. It was quite successful at cataloging a set of conservation laws which are largely still accepted, but it cannot explain what motivates them.

Over the last three decades, particle physics has filled in many details. Its so-called *Standard Model* attempts to create a self contained description of the quantum world of matter and quantum interactions in a relatively simple formalism. A complete

introduction to this model can be found in textbooks [Per82, Hal84]. Included here is a brief description of the properties that are related to the topics of this thesis. Although attempts have been made to include gravity in the model, they have never been completely successful. For the most part, I will ignore gravity in this discussion.

A fundamental tenet of quantum mechanics is based on the statement that sometimes particles have the properties of waves, and sometimes waves have the properties of particles. Therefore a physical object cannot always be thought of simply as a wave or a particle but must be considered one or the other depending on the application. The standard model describes everything in terms of particles, in the high-energy regions we are considering this is a valid assumption. However you must keep in mind this simple particle description has a wave-nature counterpart.

In order to get down to the most basic building blocks we begin by defining certain things as "fundamental" or "elementary". These words imply that fundamental objects can combine to form more complicated ones, but they themselves are not made of anything more basic. As a consequence they have no internal structure, and can be thought of (in the particle picture) as only existing at one point in space.

All matter is made up of these fundamental "particles." The standard model explains the classical notion of "force" as the exchange of energy and information from one fundamental particle to another. Mechanically they do this by exchanging a "mediator". Mediators are also fundamental but they are distinct from the particles that make up matter, the quarks and the leptons. As far as we know, mediators do not bind together to form long-lived composite objects (with one exotic exception). They simply transport information and energy from one particle to another. A particle is

said to "couple" to a mediator at a "vertex". Figure 1.1 is a typical interaction: one particle (in this case a ν) emits a mediator (the W^+) at one vertex, another particle (the quark) absorbs the mediator at a second vertex.

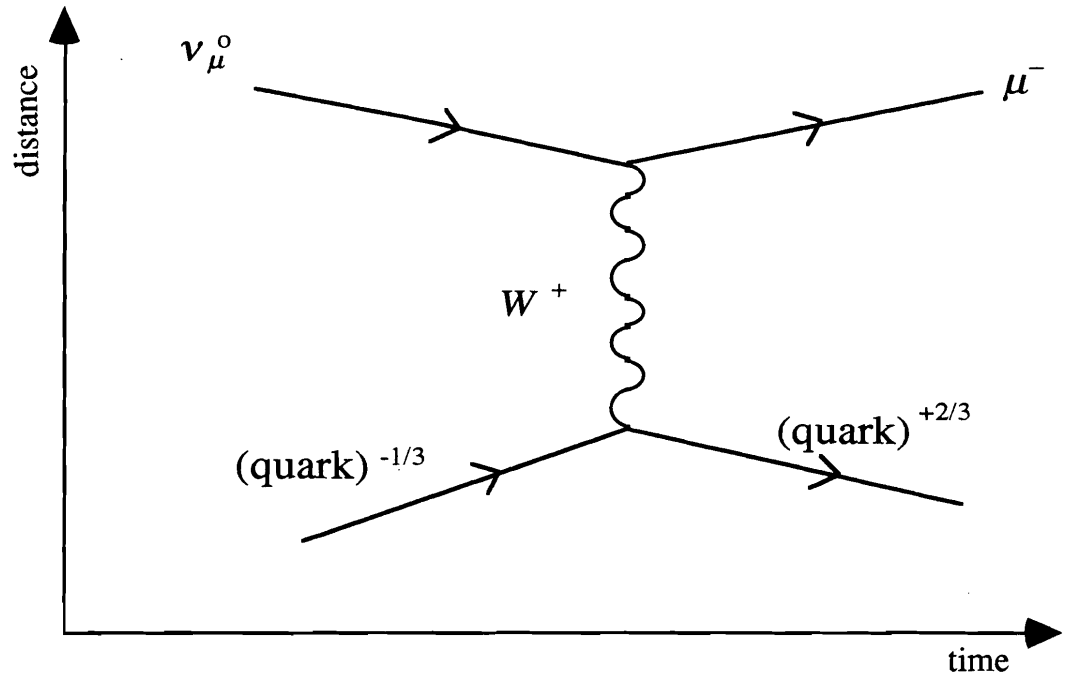

Figure 1.1: A typical interaction between 2 elementary particles, in this case a lepton (ν_μ) and a quark.

There are specific mediators associated with each force, but only certain particles couple to any given mediator. This is analogous to saying that a given force only has influence on certain fundamental particles. We say a particle "carries" the "charges" associated with the mediators it couples to. There is one charge associated with each force. You may be familiar with the classical notion of the charge associated with the electromagnetic force, the electric charge (e). Particles that carry electric charge may have different values of e. For example: the electron has $e=-1$, the positron has $e=+1$, the neutrino is neutral so it doesn't carry electric charge at all. This means the

electromagnetic mediator (the photon) cannot couple to the neutrino. The Standard Model extends this notion of charge to the other two forces. So there is an analogous weak charge and strong charge. The strong force has a charge that comes in 3 different varieties; they are called "colors" and the varieties are red, green and blue. The charge associated with the weak force is simply referred to as the weak charge. It only comes in one variety and all quarks and leptons carry it.

The charges that a particle carries along with its mass define the identity of that particle. The quarks and the leptons are the two families of particles. The quarks carry all possible charges, but the leptons only carry certain ones. Table 1.1 fills in the details.

Table 1.1: Interactions in the Standard Model. The relative strengths of the forces are roughly indicated, for scales of a few *GeV*.

Force	Experimentally measured Relative strength	Mediator	Mediator Mass (GeV)	Participating particles
strong	1	gluon (g)	0	quarks
electromagnetic	10^{-2}	photon (γ)	0	quarks and charged leptons
weak	10^{-5}	Z^0 and $W^{\pm}$	91 and 80	quarks and all leptons

Table 1.2 illustrates a further division within each family into three generations. Roughly speaking, mass is what distinguishes one generation from the next. This is one quality the standard model has not been able to explain. It simply describes particles with different masses as having different "flavors". Within each generation there are two different particles distinguished by their electric charges.

Table 1.2: The quarks and leptons, constituents of matter.

	Electric charge	First Generation	Second Generation	Third Generation
Quarks	+2/3	up (u)	charm (c)	top (t)
	−1/3	down (d)	strange (s)	bottom (b)
Leptons	−1	electron (e)	muon (μ)	tau (τ)
	0	e-neutrino (ν_e)	μ-neutrino (ν_μ)	τ-neutrino (ν_τ)

There is one last complication. For each particle there exists an "anti"-particle. Particles and anti-particles have the same mass and carry the same types of charges, this is what identifies them as particle/anti-particle partners. However even though the size of their charges are the same, the signs are opposite. In the case of electric charge if a particle (like the electron) has e=-1, then its anti particle has charge e=+1 (the positron). In the case of the strong force if the particle has color charge red then its anti-particle is said to have color charge anti-red.

The ultimate validity of any model rests in confirmation by experiment. The Standard Model has stood up to tests with surprising success. However, some big questions are still unanswered. For example, why do the particles have different masses and what mechanism motivates the values of these masses? The term "parameter" applies to aspects of a theory that cannot be explained within that theory. They can only be measured by experiments like this one, or predicted by a more inclusive theory. I have not explained all of them, but examples of parameters within the Standard Model are listed in Table 1.3. Physicists expect eventually to find an elegant theory beyond the Standard Model which would not require such a

Table 1.3: Some parameters in the Standard Model. (The neutrinos, photons, and gluons are assumed massless.)

Type of parameter	Number of parameters
quark masses	6
charged lepton masses	3
Higgs particle mass	1
Z^0 and $W^{\pm}$ masses	2
CKM mixings	4
α_{em} electromagnetic coupling	1
G_F weak coupling	1
fractional charges	2
α_S strong coupling	1

large number of unexplained features. Twenty five centuries later the questions raised by Leukippos and Demokritos are yet to be fully answered.

1.2 Neutrino-Nucleon Scattering

The particle properties described by the Standard Model can be used to design an experiment to probe nucleon structure. The first question we might consider is, which probe should be used to study the quark system?

Why would we choose a neutral lepton (the neutrino)? As an elementary particle, the neutrino does not have any internal structure. As a lepton it does not carry strong charge. Being neutral, it does not carry electromagnetic charge. The only force that affects the neutrino is the weak force. The theory of Quantum Electrodynamics (QED) has been shown to describe the weak force with precision. Relatively

speaking then, it will be easy to model the vertex of this structure-less, neutral, weakly interacting particle with the well understood theory of QED.

The weak force is aptly named. It is not strong enough to induce the neutrinos to interact very often. Neutrinos generally pass through quark matter undetected, but every once in a while they will interact. This quality makes it easy for us to isolate each interaction between the ν and the quark system. We end up with a probe that is theoretically easy to model and produces events that are easy to capture and isolate.

What about mediators? The neutrino can exchange a W (an electrically charged weak mediator) or a Z (an electrically neutral weak mediator). These interactions are referred to as "charged-current" (CC) or "neutral-current" (NC) respectively for obvious reasons. There are two big advantages to analyzing charged-current events.

First, one of the remnants of a charged-current ν_μ event is a muon. Muons are easy to detect because like the neutrino (but unlike quark matter), they travel through sizable amounts of material before stopping. Muons leave a long track in the detector making CC events quite distinctive. By contrast, there are several types of events that are easily mistaken for neutral-current events.

Secondly, conservation of electric charge requires a flavor change for the quark which absorbs a W. If the W carries electric charge of e = +1 (labeled a W^+), then only the quarks with e = -1/3 can absorb it. Upon absorption of the W^+, they will become a quark with e = +2/3. The quarks with e = +2/3 are incapable of receiving a W^+ because there is no quark variety for them to transform into which has e = +5/3. Thus when a W^+ (or W^-) is involved, only about half of the available quarks can interact. In this way, the charged current interactions provide flavor information that

the neutral current interactions cannot. The analysis for this thesis only looks at the charged current events in our data sample.

In order to make use of this information, we must be able to determine which W-boson was exchanged, the W^+ or the W^-. Charge must also be conserved at the neutrino vertex. When the neutrino releases a mediator with $e = +1$, it must turn into the charged lepton associated with its generation (which has $e = -1$). The muon version of this interaction is shown in figure 1.1. As far as we know, neutrinos only couple to their associated charged leptons; i.e. the electron-neutrino always turns into an electron, likewise for the muon and the tau. This is expressed as a rule called conservation of lepton number which is analogous to conservation of electric charge. Then we can determine the type of neutrino and the charge of the boson exchanged by determining the charge of the muon that exits the interaction. This is easily done in a magnetic field.

We will only use one type of neutrino as a probe, the muon neutrino. It is not only the easiest neutrino to create, but the muon is also the easiest lepton to identify in our detector. These details will be discussed in Chapter 2.

1.3 Kinematics of a Charged-Current ν Event

Three kinematic variables provide a full description of one deep-inelastic scattering event. The measured quantities will be the muon momentum (p_μ), the angle of the outgoing muon (θ_μ), and the observed energy of the outgoing hadrons (E_{HAD}). In a fixed target experiment, the proton is assumed at rest because any momentum associated with it is small compared to the high momentum of the incoming

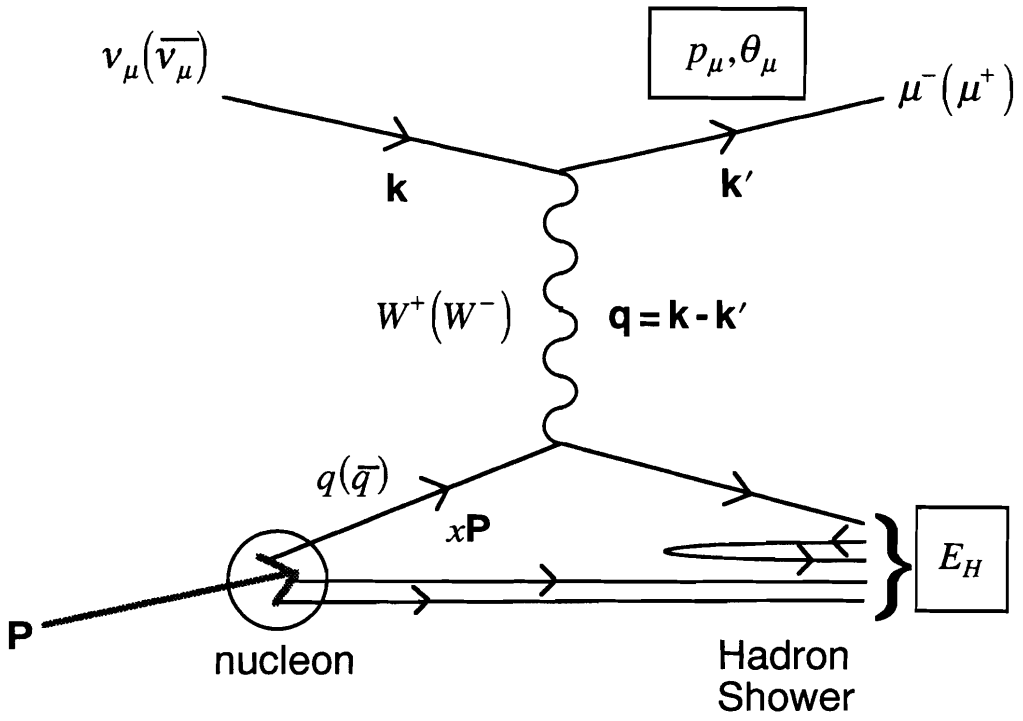

Figure 1.2: Kinematic variables of deep-inelastic scattering. A point-like constituent of the nucleon, a parton, carries a fraction x of the nucleon's momentum p. The measured experimental quantities are enclosed in rectangles.

neutrino. It follows from the measured parameters that the neutrino energy is $E_\nu = E_{HAD} + E_\mu - M$, where M is the rest mass of the nucleon.

The most commonly used kinematic variables for deep-inelastic scattering are shown in Figure 1.2. The lepton is designated by four-momentum k, the hadron system by momentum p, and after scattering their four-momenta are designated by k' and p', respectively. The W-boson has its own four-momentum q. In terms of the experimental quantities each of these four-momenta in the lab system are:

$$k = \left(E_\nu, 0, 0, E_\nu\right) \tag{1.2}$$

$$k' = \left(E_\mu, p_\mu \sin\theta_\mu \cos\phi_\mu, p_\mu \sin\theta_\mu \sin\phi_\mu, p_\mu \cos\theta_\mu\right) \tag{1.3}$$

$$p=(M,0,0,0) \tag{1.4}$$

$$p'=p+q=p+(k-k'). \tag{1.5}$$

Lorentz-invariant variables commonly used to describe deep-inelastic scattering are derived as follows.

The square of the center of mass energy:

$$s=(p+k)^2=M^2+2ME_\nu. \tag{1.6}$$

The energy transferred to the hadronic system (the mass of the unobserved baryon is neglected):

$$\nu=\frac{p\cdot q}{M}=E_\nu-E_\mu=E_{HAD}. \tag{1.7}$$

The negative square of the four-momentum transfer:

$$Q^2=-q^2=-(k-k')^2=m_\mu^2+2E_\nu\left(E_\mu-p_\mu\cos\theta_\mu\right). \tag{1.8}$$

The invariant mass of the hadronic system:

$$W^2=(p')^2=(p+q)^2=M^2+2M\nu-Q^2. \tag{1.9}$$

The Bjorken scaling variable, which represents the fractional momentum of the struck parton within the nucleon:

$$x=\frac{-q^2}{2p\cdot q}=\frac{Q^2}{2M\nu}. \tag{1.10}$$

The inelasticity:

$$y = \frac{p \cdot q}{p \cdot k} = \frac{E_{HAD}}{E_\nu}. \tag{1.11}$$

The inelasticity y is related to the lepton scattering angle θ^* in the center-of-mass frame:

$$y \approx 1 - \frac{1}{2}\left(1 + \cos\theta^*\right). \tag{1.12}$$

1.4 The Formalism of Deep-Inelastic Scattering

Now that a probe has been chosen and the variables have been defined, a mathematical description of the interaction can be built. The number of expected events will be proportional to the number of neutrinos coming in (as expressed per unit time by the flux Φ) multiplied by the probability that the ν will interact with the nucleon (as expressed by the cross section σ): $N = \Phi\sigma$. Consider the number of events in one infinitesimally small area of our kinematic range: $dN = \Phi(E_\nu)d\sigma$. This counting equation is the basis for Fermi's Golden Rule:

$$dN = \Phi(E_\nu)d\sigma = |M|^2 d\Gamma. \tag{1.13}$$

The small increment $d\Gamma$ is the area of phase space available to our interaction given the kinematic values of the two incoming objects, the ν and the nucleon. The mathematical form of this element is obtained by applying classical conservation laws. The matrix element M contains all of the information on the structure found in the two vertices joined by the charged current (Figure 1.2).

The matrix element is broken down into contributions from the lepton vertex and the hadron vertex as [Rob90]:

$$\mathcal{M} = \frac{G_F}{\sqrt{2}} \frac{1}{\left(1+Q^2/M_W^2\right)} \underbrace{\bar{u}_\mu(k',s')\gamma_\alpha\left(1-\gamma_5\right)u_\nu(k,s)}_{\text{lepton}} \underbrace{\left\langle X\left|J_{CC}\right|N;p,s\right\rangle}_{\text{hadron}},$$

where G_F is the weak coupling constant, M_W is the mass of the W-boson, (k,s) is the four-momentum and helicity of the incoming neutrino, (k',s') is the four-momentum and helicity of the outgoing muon, (p,s) is the four-momentum and helicity of the target nucleon, and $\bar{u}_\mu$ and u_ν are the lepton spinors. Squaring the matrix element and putting it into Fermi's Golden Rule, the inclusive, spin-averaged cross-section proportional to $|\mathcal{M}|^2$ takes the form:

$$\frac{d^2\sigma^{\nu N}}{d\Omega_\mu dE_\mu} = \frac{1}{\left(1+Q^2/M_W^2\right)^2} \frac{G_F^2}{2} \frac{m_\nu}{E_\nu} \frac{m_\mu}{E_\mu} \frac{E_\mu^2}{(2\pi)^2} L_{\alpha\beta} W^{\alpha\beta}, \tag{1.14}$$

where E_ν and E_μ are the energies of the incident neutrino and final-state muon in the lab frame (nucleon at rest), and Ω is the solid angle into which the scattered muon lies. The leptonic tensor $L_{\alpha\beta}$ is given by

$$\begin{aligned} L_{\alpha\beta} &= \sum_{s,s'} \bar{u}_\mu(k',s')\gamma_\alpha(1-\gamma_5)u_\nu(k,s)\bar{u}_\nu(k,s)\gamma_\beta(1-\gamma_5)u_\mu(k',s') \\ &= \frac{2}{m_\nu m_\mu}\left[k'_\alpha k_\beta + k'_\beta k_\alpha - k\cdot k' g_{\alpha\beta} \mp i k^\gamma k'^\delta \varepsilon_{\gamma\delta\alpha\beta}\right] \end{aligned}, \tag{1.15}$$

where the –(+) term applies to incident neutrinos (anti-neutrinos). The leptonic vertex is relatively simple, it consists of one elementary point-like particle (the ν) exchanging a point-like mediator. The hadronic vertex is not as simple as the leptonic one, for it consists of a composite hadronic particle (the proton or neutron) absorbing a mediator. The composite nature of the nucleon complicates certain questions, for instance even though theory can describe the absorption of a boson by a particular quark, the theory cannot determine which one of the quarks inside the

proton will do the absorbing. Also, given the proton's momentum it is not clear how much of the total momentum is carried by each individual quark. Thus, the hadronic tensor $W^{\alpha\beta}$ cannot be entirely written down from first principles. It is necessary to parameterize the nucleon structure, and hence this vertex.

There are only two independent vectors upon which $W^{\alpha\beta}$ can depend, p and q. The most general rank-2 tensor that can be constructed out of these two vectors is

$$\begin{aligned} W^{\alpha\beta} = & -g^{\alpha\beta}W_1 + \frac{p^\alpha p^\beta}{M^2}W_2 - \frac{i\varepsilon^{\alpha\beta\gamma\delta}p_\gamma q_\delta}{2M^2}W_3 \\ & + \frac{q^\alpha q^\beta}{M^2}W_4 + \frac{\left(p^\alpha q^\beta + p^\beta q^\alpha\right)}{M^2}W_5 \\ & + \frac{i\left(p^\alpha q^\beta - p^\beta q^\alpha\right)}{2M^2}W_6 \end{aligned} \tag{1.16}$$

Each of these terms represents an orthogonal 4x4 matrix. The W_i are real functions that depend only on q^2 and $p\cdot q$. They are called the *structure functions*.

The quark mass is negligible in comparison to the energies of our typical interactions so we can use order of magnitude arguments to effectively ignore the terms which depend on the quark masses. In the limit of zero quark mass:

$$q^\alpha L_{\alpha\beta} = q^\beta L_{\alpha\beta} = 0. \tag{1.17}$$

These are the coefficients of W_4, W_5, and W_6. After contracting the lepton and hadron tensors, Equation 1.14 becomes (neglecting Q^2/M_W^2 terms and lepton masses):

$$\frac{d^2\sigma^{\nu(\bar{\nu})N}}{d\Omega dE_\mu} = \frac{G_F^2}{2\pi^2} E_\mu^2 \left[\begin{array}{l} \cos^2\frac{\theta}{2} W_2^{\nu(\bar{\nu})N} + 2\sin^2\frac{\theta}{2} W_1^{\nu(\bar{\nu})N} \\ \pm \frac{E_\nu + E_\mu}{M} \sin^2\frac{\theta}{2} W_3^{\nu(\bar{\nu})N} \end{array} \right], \tag{1.18}$$

where the +(–) term corresponds to neutrino (anti-neutrino) scattering. In general, the structure functions, $W_i\left(q^2, p\cdot q\right)$, depend on the target and may depend as well on the neutrino helicity.

In terms of the absorption cross-sections for left-handed, right-handed, and scalar W bosons (σ_L, σ_R, σ_S), the structure functions can be written as:

$$W_1 = \frac{K}{\pi G_F \sqrt{2}}\left(\sigma_R + \sigma_L\right), \tag{1.19}$$

$$W_2 = \frac{K}{\pi G_F \sqrt{2}} \frac{Q^2}{Q^2 + \nu^2}\left(\sigma_R + \sigma_L + 2\sigma_S\right), \tag{1.20}$$

$$W_3 = \frac{K}{\pi G_F \sqrt{2}} \frac{2M}{\sqrt{Q^2 + \nu^2}}\left(\sigma_R - \sigma_L\right), \tag{1.21}$$

where K represents the flux of virtual Ws. As will become apparent, the variables x, y and Q^2 are particularly illustrative when it comes to exploring nucleon structure. Making a change of variables from (E_μ, E_ν and θ) to (x, y and Q^2), Equation 1.18 becomes

$$\frac{d^2\sigma^{\nu(\bar{\nu})}}{dx\,dQ^2} = \frac{G_F^2}{2\pi x}\left[\left(1 - y - \frac{Mxy}{2E}\right) \nu W_2^{\nu(\bar{\nu})} + y^2 xM W_1^{\nu(\bar{\nu})} \pm y\left(1 - \frac{y^2}{2}\right) x\nu W_3^{\nu(\bar{\nu})}\right] \tag{1.23}$$

In the modern structure-function notation,

$$2xMW_1(\nu,Q^2) = 2xF_1(x,Q^2), \tag{1.24}$$

$$\nu W_2(\nu,Q^2) = F_2(x,Q^2), \tag{1.25}$$

$$x\nu W_3(\nu,Q^2) = xF_3(x,Q^2). \tag{1.26}$$

In this notation, the differential cross-section takes the form

$$\frac{d^2\sigma^{\nu(\bar{\nu})}}{dx\,dy} = \frac{G_F^2 ME}{\pi}\left[\left(1-y-\frac{Mxy}{2E}\right)F_2^{\nu(\bar{\nu})} + \frac{y^2}{2}2xF_1^{\nu(\bar{\nu})} \pm y\left(1-\frac{y^2}{2}\right)xF_3^{\nu(\bar{\nu})}\right] \tag{1.27}$$

Equation 1.27 is the master equation of deep-inelastic neutrino scattering. It represents the point where theory meets experiment. To go beyond equation 1.27 these quantities must be measured phenomenologically. The structure functions contain all that can be known about the structure of the nucleon from deep-inelastic scattering.

1.5 The Parton Model

Once the structure functions are measured experimentally a theoretical model must be used to interpret the numbers in terms of the physically significant quarks and gluons inside the nucleon. To begin with, consider a relatively simple model called the Parton Model.

In the Parton Model, the nucleon is assumed to be made of point-like constituent objects generically labeled partons. As the "deep" part of the term implies, deep-inelastic scattering involves high energy particles which can be pictured in a highly relativistic frame, the "infinite momentum frame." Interactions of such particles take place over a very short period of time, $\Delta E\Delta t \sim 1$. By contrast, the partons inside a

nucleon interact among themselves on a time scale much longer than that of the collision, so inter-parton communication can largely be ignored. Hence inelastic neutrino-nucleon scattering can be simplified to elastic scattering between the neutrino and one free, individual parton inside the nucleon. This scattering must be elastic because the partons are assumed to be structure-less fundamental particles, unable to break up.

For the following arguments, assume the partons travel collinearly with the nucleon, and thus carry a fraction x of its momentum. In the energy range typical of DIS we can assume the partons to be massless.

Elastic scattering of two point particles is easy to represent mathematically. It only depends on two variables: the energy in the system ($s^2 \approx 2M_{proton}E_\nu$) and its net angular momentum. Neutrinos are left-handed and anti-neutrinos are right-handed. Consider a state of two massless fermions where the angular momentum is $j^i = s_1 + s_2 = 1/2 + 1/2 = 1$ and $m_j^i = \pm 1, 0$. One can represent the initial and final states $\phi_{init}(\theta)$ and $\phi_{final}(\theta)$ in terms of $2j+1$ spin states: (j, m_i^j). The $d_{mm'}^j$ coefficients (commonly referred to as rotation matrices) are used as expansion coefficients,

$$\phi(\theta) = \sum_{m'} d_{m,m'}^j(\theta) \left| j, m' \right\rangle. \tag{1.28}$$

The initial angular momentum state, $\phi_{init}(\theta)$, is transformed into a new state, $\phi_{final}(\theta)$, under a rotation through an angle θ^*. Consider the possible final states. The V–A structure of the weak interaction causes parity to be maximally violated, so the mediator can only couple to left-handed particles or right-handed anti-particles (unless the particle is massive). The mediator cannot change particles to anti-particles, or vice versa because of charge conservation. So the final states will not

Figure 1.3: Possible helicity configurations for high-energy neutrinos and anti-neutrinos scattering from quarks and anti-quarks.

allow any spin flips at the hadron vertex. The resulting four possible helicity configurations for high-energy neutrino-quark scattering are shown in Figure 1.3.

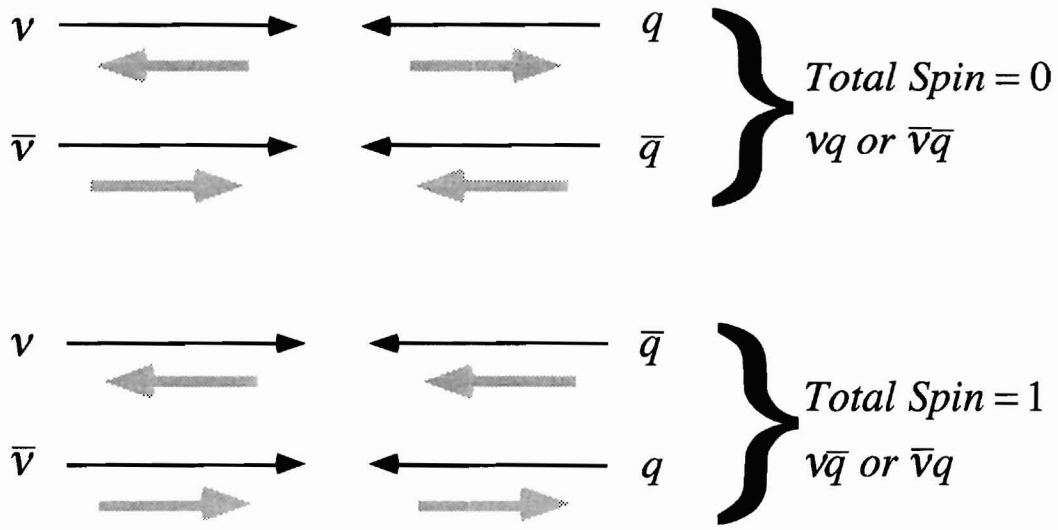

Considering only these possible final states ($d^{j}_{m,m'}(\theta)|j,m'\rangle$) in the expansion of $\phi_{final}(\theta)$, and making an overlap with the possible initial states in the expansion of $\phi_{init}(\theta)$, one ends up with cross sections whose angle terms come from the appropriate $d^{j}_{mm'}$ coefficients:

$$\text{total spin } 0: \frac{d\sigma^{\nu q}}{d\cos\theta^{*}} = \frac{d\sigma^{\bar{\nu}\bar{q}}}{d\cos\theta^{*}} = \frac{G^{2} ME_{\nu}}{\pi\left(1+Q^{2}/M_{W}^{2}\right)^{2}}, \tag{1.29}$$

$$\text{total spin } 1: \frac{d\sigma^{\nu\bar{q}}}{d\cos\theta^{*}} = \frac{d\sigma^{\bar{\nu}q}}{d\cos\theta^{*}} = \frac{G^{2} ME_{\nu}}{\pi\left(1+Q^{2}/M_{W}^{2}\right)^{2}}\left(\frac{1+\cos\theta^{*}}{2}\right)^{2}, \tag{1.30}$$

$$\text{total spin } \frac{1}{2}: \frac{d\sigma^{\nu k}}{d\cos\theta^*} = \frac{d\sigma^{\bar{\nu} k}}{d\cos\theta^*} = \frac{2G^2 ME_\nu}{\pi\left(1+Q^2/M_W^2\right)^2}\left(\frac{\cos\theta^*}{2}\right)^2, \tag{1.31}$$

where θ^* is the muon's center-of-mass scattering angle. The superscripts identify the *spin*-1/2 partons with the quarks and anti-quarks. In principle, a *spin*-0 constituent may also be present, which is identified by the superscript k. As shall be seen, while the neutrino does not directly interact with a *spin*-0 component, the $p_\perp$ of the quark gives rise to an effective *spin*-0 component in the cross section formalism.

The probability of scattering from a particular type of parton is introduced as a parton distribution function $p(x)$. The quantity $p(x)dx$ is interpreted as the probability of finding a parton of type p that carries a fraction x to $x + dx$ of the hadron's momentum. Using the parton momentum distribution function $xp(x)$, the differential cross-section for scattering off one parton is

$$\frac{d^2\sigma}{dx\,dy} \propto \frac{G^2\,2ME}{\pi\left(1+Q^2/M_W^2\right)^2} xp(x). \tag{1.32}$$

Gathering all contributions from the constituents of a target T (T being a proton or neutron), the cross-sections for neutrino and anti-neutrino scattering are

$$\frac{d^2\sigma^{\nu T}}{dx\,dy} = \frac{G^2 xs}{\pi\left(1+Q^2/M_W^2\right)^2}\left[q^{\nu T}(x) + (1-y)^2\,\bar{q}^{\nu T}(x) + 2(1-y)k^{\nu T}(x)\right], \tag{1.33}$$

$$\frac{d^2\sigma^{\bar{\nu} T}}{dx\,dy} = \frac{G^2 xs}{\pi\left(1+Q^2/M_W^2\right)^2}\left[\bar{q}^{\bar{\nu} T}(x) + (1-y)^2\,q^{\bar{\nu} T}(x) + 2(1-y)k^{\bar{\nu} T}(x)\right]. \tag{1.34}$$

The parton distributions are associated with the structure functions by comparing the y dependencies of the above formulas with Equation 1.27, yielding

$$2xF_1^{\nu(\bar{\nu})T} = 2\left[xq^{\nu(\bar{\nu})T}(x) + x\bar{q}^{\nu(\bar{\nu})T}(x)\right], \tag{1.35}$$

$$F_2^{\nu(\bar{\nu})T} = 2\left[xq^{\nu(\bar{\nu})T}(x) + x\bar{q}^{\nu(\bar{\nu})T}(x) + 2xk^{\nu(\bar{\nu})T}\right], \tag{1.36}$$

$$xF_3^{\nu(\bar{\nu})T} = 2\left[xq^{\nu(\bar{\nu})T}(x) - x\bar{q}^{\nu(\bar{\nu})T}(x)\right], \tag{1.37}$$

where the Q^2/M_W^2 and $Mxy/2E$ terms have been neglected. Thus using the parton model, the deep-inelastic structure functions can be linearly related to the momentum fractions of the partons in a target nucleon.

If the scattering were to take place exclusively from free *spin*-1/2 constituents with no transverse momentum, the Callan-Gross relation,

$$2xF_1 = F_2, \tag{1.38}$$

would be satisfied. However, at available energies, partons have non-negligible transverse momenta, which gives them apparent *spin*-0 behavior in the infinite-momentum-frame formalism. This leads to a difference between F_2 and $2xF_1$.

As previously mentioned, neutrino scattering has the ability to resolve the flavor of the nucleon's constituents. The charge-current interaction changes the flavor of the struck quark. Conservation of charge at the quark vertex limits neutrinos to scatter from d, s, $\bar{u}$, and $\bar{c}$ quarks, and anti-neutrinos to scatter from $\bar{d}$, $\bar{s}$, u, and c quarks. Considering a parton target, the quark densities that contribute to the structure functions are

$$q^{\nu p}(x) = d^{p}(x) + s^{p}(x), \tag{1.39}$$

$$\bar{q}^{\nu p}(x) = \bar{u}^{p}(x) + \bar{c}^{p}(x), \tag{1.40}$$

$$q^{\bar{\nu}p}(x) = u^{p}(x) + c^{p}(x), \tag{1.41}$$

$$\bar{q}^{\bar{\nu}p}(x) = \bar{d}^{p}(x) + s^{p}(x). \tag{1.42}$$

Strong isospin invariance demands a symmetry between the proton and the neutron light quark densities:

$$d(x) \equiv d^{p}(x) = u^{n}(x), \tag{1.43}$$

$$\bar{d}(x) \equiv \bar{d}^{p}(x) = \bar{u}^{n}(x), \tag{1.44}$$

$$u(x) \equiv u^{p}(x) = d^{n}(x), \tag{1.45}$$

$$\bar{u}(x) \equiv \bar{u}^{p}(x) = \bar{d}^{n}(x). \tag{1.46}$$

Nucleons exhibit no net strangeness or charm, and these heavier flavors have isospin of zero. For this analysis, the following symmetries are assumed:

$$s(x) \equiv s^{p}(x) = s^{n}(x), \tag{1.47}$$

$$\bar{s}(x) \equiv \bar{s}^{p}(x) = \bar{s}^{n}(x), \tag{1.48}$$

$$c(x) \equiv c^{p}(x) = c^{n}(x), \tag{1.49}$$

$$\bar{c}(x) \equiv \bar{c}^{p}(x) = \bar{c}^{n}(x), \tag{1.50}$$

$$s(x) \equiv \bar{s}(x), \tag{1.51}$$

$$c(x) \equiv \bar{c}(x). \tag{1.52}$$

Using these symmetries, the quark distributions of the neutron and the proton are described in terms of the proton quark distributions. All the parton distributions that follow are those for the proton.

$$q^{\nu n}(x) = u(x) + s(x), \tag{1.53}$$

$$\bar{q}^{\nu n}(x) = \bar{d}(x) + \bar{c}(x), \tag{1.54}$$

$$q^{\bar{\nu} n}(x) = d(x) + c(x), \tag{1.55}$$

$$\bar{q}^{\bar{\nu} n}(x) = \bar{u}(x) + \bar{s}(x). \tag{1.56}$$

Finally, the parton densities for an isoscalar nucleon, N = 1/2 × (proton + neutron), are

$$q^{\nu N}(x) = \frac{1}{2}[u(x) + d(x) + 2s(x)], \tag{1.57}$$

$$q^{\bar{\nu} N}(x) = \frac{1}{2}[u(x) + d(x) + 2c(x)], \tag{1.58}$$

$$\bar{q}^{\nu N}(x) = \frac{1}{2}[\bar{u}(x) + \bar{d}(x) + 2\bar{c}(x)], \tag{1.59}$$

$$\bar{q}^{\bar{\nu} N}(x) = \frac{1}{2}[\bar{u}(x) + \bar{d}(x) + 2\bar{s}(x)]. \tag{1.60}$$

The quark content of the isoscalar structure function $2xF_1$ for neutrino scattering is obtained by substituting these densities into Equation 1.35:

$$2xF_1^{\nu N}(x) = 2xF_1^{\bar{\nu} N}(x) \tag{1.61}$$

$$= xu(x) + x\bar{u}(x) + xd(x) + x\bar{d}(x) + xs(x) + x\bar{s}(x) + xc(x) + x\bar{c}(x).$$

The structure function F_2 is identical to $2xF_1$ with the addition of the spin zero component k.

$$F_2^{\nu N}(x) = F_2^{\bar{\nu} N}(x)$$

$$= xu(x) + x\bar{u}(x) + xd(x) + x\bar{d}(x) + xs(x) + x\bar{s}(x) + xc(x) + x\bar{c}(x) + 4xk.$$

The structure function xF_3, associated with the parity-violating weak interaction, represents the momentum density of valence quarks. Substituting the parton densities into Equation 1.37 yields

$$xF_3^{\nu N} = xu_V(x) + xd_V(x) + 2xs(x) - 2xc(x), \tag{1.62}$$

$$xF_3^{\bar{\nu} N} = xu_V(x) + xd_V(x) - 2xs(x) + 2xc(x), \tag{1.63}$$

where $u_V \equiv u - \bar{u}$ and $d_V \equiv d - \bar{d}$ are the proton's valence densities.

1.6 The Strange Sea

Examination of Equations 1.62 and 1.63 shows that $xF_3^{\nu N} \neq xF_3^{\bar{\nu} N}$ where

$$xF_3^{\nu} - xF_3^{\bar{\nu}} = 4x[s(x) - c(x)] \approx 4xs(x). \tag{1.64}$$

The last approximation is made by assuming c/s is small [Mis89]. Thus by measuring xF_3 with neutrinos and anti-neutrinos separately, one can use the difference $\Delta xF_3 = xF_3^{\nu} - xF_3^{\bar{\nu}}$ to measure the size of the strange sea. This analysis assumes a shape for the strange sea which comes from a previous measurement [Baz95], but we shall allow the magnitude of the strange sea relative to the other

quark varieties to vary. Conventionally this magnitude is called kappa (κ) and is formally given by:

$$\kappa = \frac{xs(x)}{x\bar{u}(x) + x\bar{d}(x)}. \tag{1.65}$$

1.7 QCD

The parton model explains the structure functions in terms of point-like constituents, but offers no explanation for the dynamics between these constituents. There are a few glaring questions that the simple parton model cannot answer. It cannot explain why the quarks are never observed in isolation, yet when they participate in high Q^2 scattering they behave like free particles. The model predicts how the SFs should vary with x, but detailed studies show that the SFs also have a Q^2 dependence which the model cannot explain.

A more complete theory called Quantum Chromodynamics (QCD) provides a detailed phenomenology of deep inelastic scattering that resolves these conflicts. The parton model augmented with a higher order QCD formalism is used to study nucleon structure in this thesis.

A QCD calculation is carried out as a perturbative expansion in the coupling constant α_s. The simple parton model only considers terms that are of leading order (LO) in α_s, that is it only considers interactions that do not have a strong vertex and hence the mathematical expressions do not contain the strong coupling constant. Higher order terms in the expansion are referred to as "next-to leading order" (NLO) which represent terms that go like α_s and likewise "next-to-next-to leading order" (NNLO) refers to terms that go like α_s^2. In a physical sense the higher order terms represent

interactions that have a given number of strong vertices, each coupling vertex contributing one strong coupling constant (α_s) to the mathematical expression. Figure 1.5 gives diagrammatic examples of the ordered interactions.

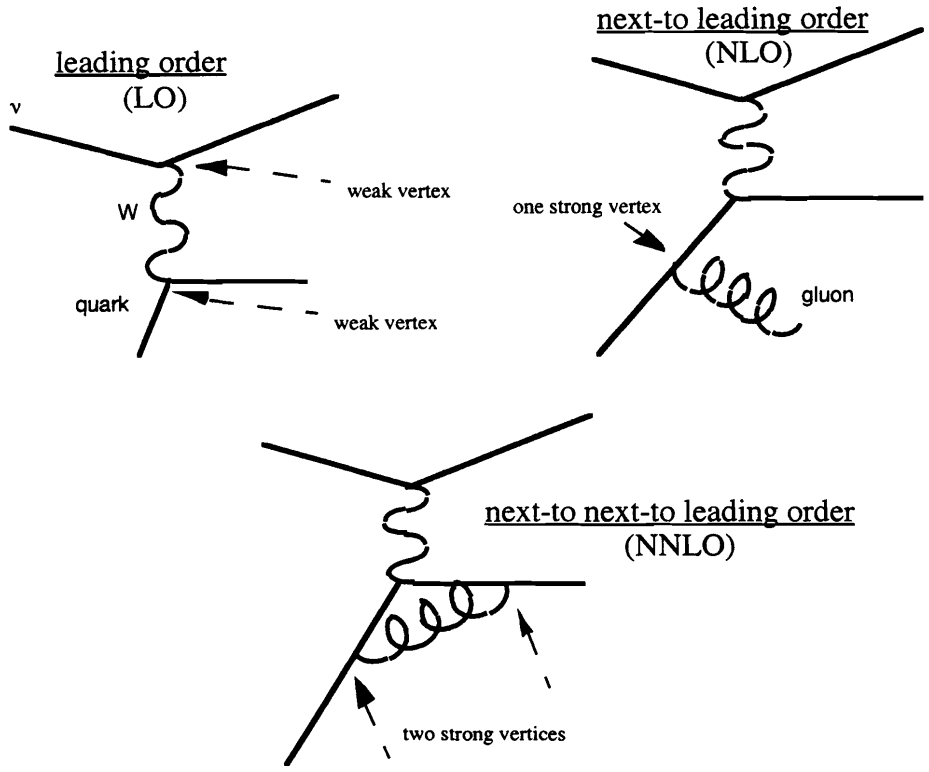

Figure 1.5: Typical LO, NLO and NNLO QCD diagrams.

The behavior of quarks as quasi-free particles in high Q^2 processes is explained in QCD by a property called asymptotic freedom. In QCD the mediators of the strong force (the gluons) can interact with each other because like the quarks, the gluons themselves carry color charge. The self-interactions of the gluons tend to anti-screen a color charge, so that the strong force between two quarks increases as the distance between the two quarks gets larger prohibiting quarks from splitting away from their quark partners. However, at shorter distances (equivalently larger momentum transfers), the strong coupling α_s decreases, so that finally α_s goes to zero as Q^2

becomes infinitely large and quarks appear to be free of their quark partners. This behavior also explains the Q^2 dependence of the SFs.

1.8 The Structure Function R_{long}

Equation 1.27 represents the nucleon cross section in terms of the standard structure functions $2xF_1, F_2$ and xF_3. As shown, these SF can be represented in the Quark-Parton model in terms of *spin-1/2* partons which are interpreted as the quarks. An effective *spin-0* component of the cross-section is represented by the *k*-term of F_2 in Eqn 1.36. This *spin-0* component is one of the primary subjects of this thesis. This section will isolate the component, and ultimately link it to the gluon distribution.

The so-called "longitudinal" structure function R_{long} isolates the *k-term* of Eqn 1.36 by taking the difference between $2xF_1$ and F_2:

$$R_{long}(\nu,Q^2)=\frac{F_2\left(1+\frac{4m^2x^2}{Q^2}\right)-2xF_1}{2xF_1}\approx\frac{W_2}{W_1}\left(1-\frac{\nu^2}{Q^2}\right)-1=\frac{\sigma_{long}}{\sigma_{trans}}. \qquad (1.66)$$

Working with Equations 1.19 through 1.27, one can alternatively express R_{long} in terms of the longitudinal and transverse cross sections, σ_{long} and σ_{trans} where the approximation in Eqn 1.66 assumes $(mx/Q)^2$ is small. These cross sections represent the probability for the absorption of a *spin-1* boson (the W) by a point-like particle inside the nucleon (the parton). With *spin=1*, the W can be longitudinally polarized ($m_S=0$) or transversely polarized ($m_S=\pm 1$, where $\pm$ refers to right and left polarizations).

For the following arguments, assume the parton has no angular momentum aside from its spin, and no mass. To be general we should imagine that the parton could be fermionic (with half-integral spin) or bosonic (with integral spin).

In the appropriate frame (the "brick wall" frame), the incoming parton flips its linear momentum in the absorption of the W boson. The parton must also flip its spin in order to conserve helicity. If all partons were *spin-1/2* they could not absorb a longitudinally polarized boson (which has m_s=*0)* because the longitudinal boson could not provide the necessary spin flip to conserve helicity. The resulting R_{long} would be zero:

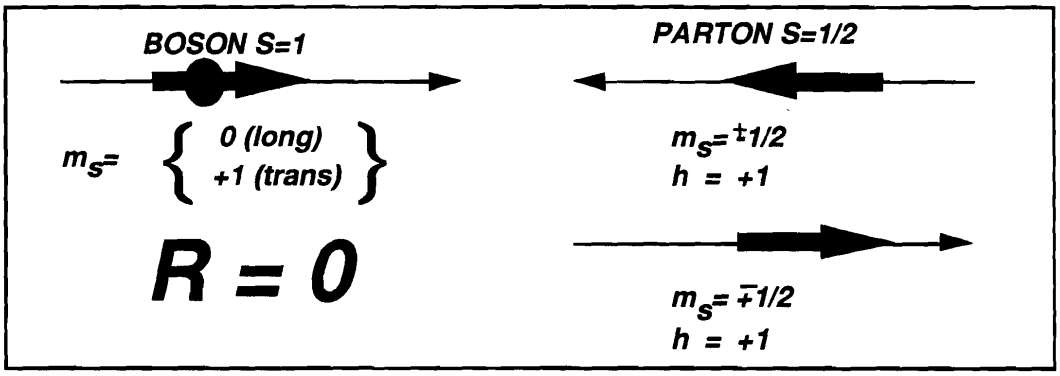

Figure 1.6: The helicity configuration for the absorption of a spin 1 mediator by a spin 1/2 parton implies a very small R_{long}.

If the partons were all *spin-0* , then by conservation of angular momentum they would be unable to absorb an $m_s = \pm 1$ boson (transversely polarized) and R_{long} would be infinite:

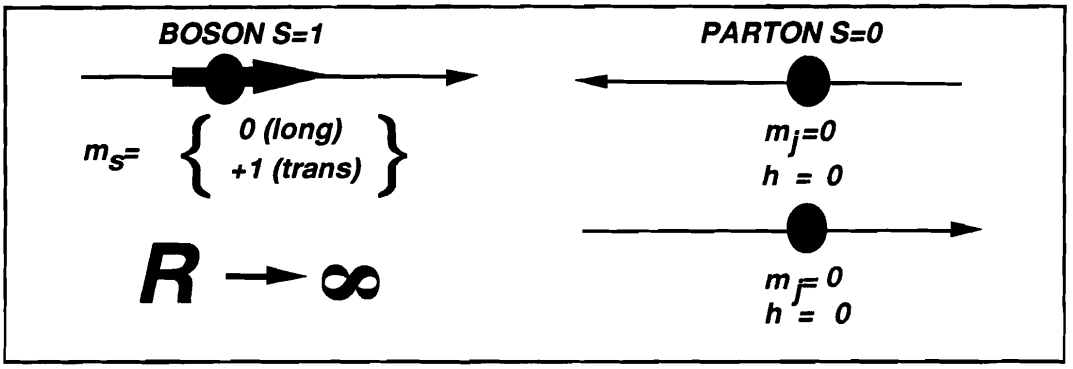

Figure 1.7: Helicity configuration for the absorption of a spin 1 mediator by a spin 0 parton implies a large R_{long}.

Early electron scattering experiments confirmed that R was close to zero. Hence the measurement of R_{long} led to the previously mentioned simple parton model which modeled the picture of nucleons which consisted of free *spin-1/2* partons. In this scheme, there is no spin 0 component and the partons have no transverse momentum, hence $F_2=2xF_1$. This is known as the Callan-Gross relationship.

Later more precise measurements showed that R_{long} did not equal 0 in the small x and small Q^2 region. This led physicists to wonder what else was going on. One explanation was that the spin 1/2 partons had a component of angular momentum aside from their intrinsic spin. With additional angular momentum ($j=1/2+l$) an m_j=0 state is possible for a *spin-1/2* particle. A fermion could absorb a longitudinally polarized boson. How can partons obtain additional angular momentum?

It turns out that quarks (with *spin-1/2*) and gluons (with *spin-0*) are both inside the nucleon. However, the weak mediator (the W-boson) only couples to the quarks because the gluon has no weak charge. With this in mind, R_{long} can be thought of as a measurement of the quark's transverse momentum. Quarks obtain transverse momentum by interacting with one another, exchanging gluons. The Quark-Parton model cannot model such a phenomena, a higher-order QCD picture is necessary to

explain the non-zero R_{long}. In NLO terms, quarks obtain angular momentum by emitting gluons, or quarks can be pair produced with transverse momentum by gluons.

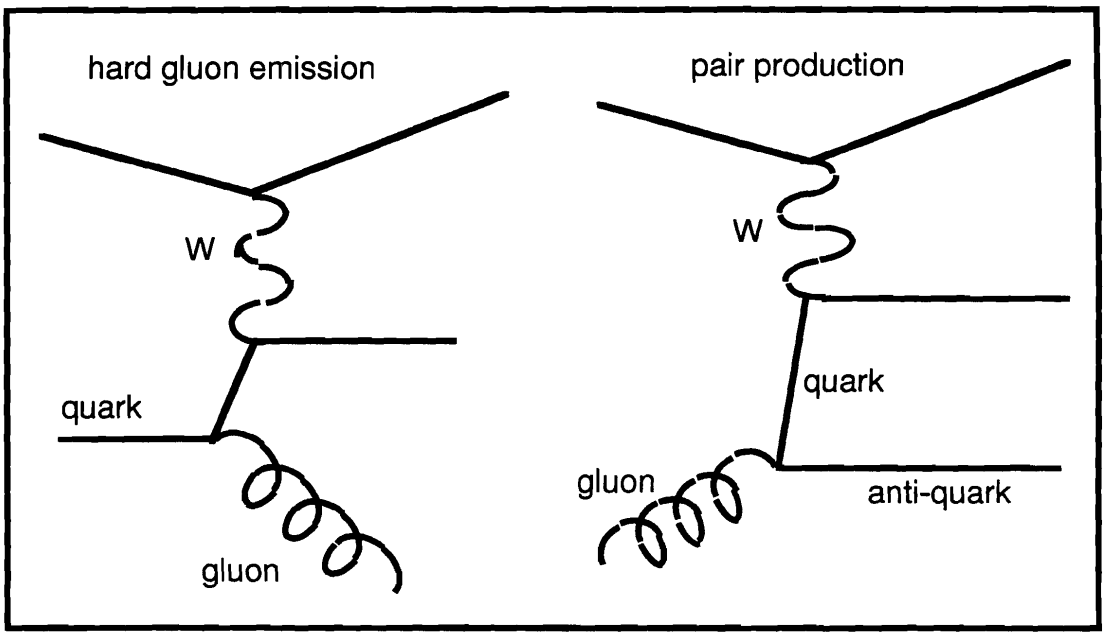

Figure 1.8: NLO QCD diagrams.The hard gluon emission diagram and the pair production diagram demonstrate the simplest processes by which quarks obtain transverse momentum.

NLO QCD expresses R_{long} as an integral in terms of these processes [Alt78]. The hard gluon emission term is proportional to the gluon momentum distribution $G(x,Q^2)$, and the pair production term is proportional to the sum of all quarks represented by $F_2(x,Q^2)$:

$$R_{QCD}(x,Q^2) = \frac{\alpha_s(Q^2)x^2}{2\pi 2xF_1(x,Q^2)} \int_x^1 \frac{8dz}{3z^3} \left[F_2(x,Q^2) + 4f(1-\frac{x}{z})zG(x,Q^2) \right]. \qquad (1.67)$$

f is the number of quark flavors available at the given x, and α_s is the strong coupling constant.

Making a change of variables from $2xF_1$ to R, the cross section of Equation 1.27 can be expressed as:

$$\frac{d^2\sigma^{\nu(\bar{\nu})}}{dx\,dy} = \frac{G_F^2 ME}{\pi}\left[\begin{array}{l}\left(1-y-\frac{Mxy}{2E}+\frac{y^2}{2}\frac{1+4M^2x^2/Q^2}{1+R(x,Q^2)}\right)F_2^{\nu(\bar{\nu})} \\ \pm y\left(1-\frac{y^2}{2}\right)\nu F_3^{\nu(\bar{\nu})}\end{array}\right]. \qquad (1.68)$$

This is the form of the differential cross-section used to extract the SFs F_2, R_{long}, and xF_3 in this thesis.

1.9 Analysis Overview

The CCFR collaboration performed many neutrino DIS experiments at the Fermilab Tevatron. In 1985 and 1987 they performed two experiments, E744 and E770, whose data will be analyzed in this thesis. In these two experiments collisions of 800 GeV protons on a BeO target produced pion and kaon secondaries. These mesons were allowed to decay in flight resulting in a beam of high-energy muon-type neutrinos and anti-neutrinos. Most of the charged-particle remnants of these decays are stopped by an aluminum beam dump. The muons which are capable of penetrating the dump will be stopped by a kilometer of earth and steel that separate the neutrino source from the CCFR detector. This detector consists of a target-calorimeter followed by a toroid-spectrometer. The unmagnetized target provides a source of matter for interactions between the neutrinos and nucleons. Both the calorimeter and the spectrometer are segmented with scintillation counters and drift chambers so that the angle of the muon, the total hadronic energy, and the muon momentum can be measured.

Approximately 3.7 million charged-current event triggers were analyzed yielding approximately 1.3×10^6 charged-current events for this SF analysis. Since the flux of the neutrino beam cannot be directly measured, it is derived from an independent sample of approximately 5×10^5 charged-current, low-hadronic-energy events.

From the flux and the number of observed events, the structure functions (F_2, R_{long}, xF_3) are simultaneously determined by combining equations 1.13 and 1.68. The determination is made by comparing the y-distributions of the data to the theoretical expectations determined by a Monte Carlo (MC) simulation. The Monte Carlo models the dependence of the physics parameters as well as the experimental effects of detector acceptance and resolution smearing. The SF values are determined at 50 points in x-Q^2 space.

Through equation 1.64, the difference between xF_3^{ν} and $xF_3^{\bar{\nu}}$ provides the means to measure the size of the strange sea relative to the non-strange sea:

$$\kappa = \frac{2s}{\bar{u}+\bar{d}} = 0.453 \pm 0.106 \pm \begin{matrix} 0.028 \\ 0.074 \end{matrix}. \qquad (1.69)$$

This measurement of κ can be combined with a result from an independent study of ν–*charm* production ($\frac{\kappa}{\kappa+2}|V_{cs}|^2 B_c = (2.00 \pm .15) \times 10^{-2}$) [Baz95] and a value for the charmed branching ratio ($B_c = 0.099 \pm 0.012$ determined by combining charmed particle semileptonic branching ratios measured at e^+e^- colliders [Phy96] with the neutrino production fractions measured by the Fermilab E531 neutrino-emulsion experiment [Ush88]) to produce a measurement of the CKM matrix element $|V_{cs}|^2$:

$$|V_{cs}|^2 = 1.05 \pm 0.13 \begin{matrix} +0.08 \\ -0.10 \end{matrix}. \qquad (1.70)$$

The CKM matrix describes the mixing of the mass eigenstates into weak eigenstates allowing the weak force to mediate "cross generational" transitions. The element $|V_{cs}|$ describes the coupling of charm quarks to strange quarks.

The chapters of the thesis are organized as follows: The experimental apparatus, including the accelerator facilities at Fermilab, the neutrino beam and the CCFR detector are described in Chapter 2. Chapter 3 describes the data preparation including the calibration of the detector, the principles involved in the data analysis and the event reconstruction. Chapter 4 describes the Monte Carlo event generator and the detector simulation which are used to model the data and experimental effects. Chapter 5 details the flux determination and the associated iterative procedure involved in the SF measurement. Chapter 6 goes into further detail on the SF measurement, focusing on the fitting techniques used in comparing the data to the MC y-distributions. Chapter 7 presents the resulting SF measurements along with the κ and $|V_{cs}|^2$ measurements. It compares these results to existing measurements.

2 The Neutrino Beam and Detector

The hardware involved in a high-energy accelerator-based neutrino experiment can be broken down into two main categories, the beam and the detector. The nature of neutrinos makes the tasks of producing a beam and detecting the subsequent interactions a challenge.

• *The neutrino's long mean free path* leads to detectors that are generally large and massive. The detector provides both the target quarks and the detection devices for the interaction.

• Because *neutrinos do not interact electromagnetically*, it is not possible to use the standard techniques of accelerating or steering beam particles using electric and magnetic fields.

• *Neutrino beams must be intense*. This increases the probability for at least one neutrino to interact, and decreases the ratio of neutrino events to the primary background, cosmic rays.

The beam has three stages. First, high energy protons hit a BeO target producing mesons (primarily pions and kaons). Secondly, these mesons are allowed to decay in flight producing neutrinos and their accompanying leptons. Lastly, all charged particles are stopped by a 6m block of aluminum followed by approximately 241m of steel shielding and 582m of earth berm. Only the neutrinos penetrate this material and continue traveling ahead towards the detector.

The experiment presented in this thesis was performed at the Fermi National Accelerator Laboratory. Fermilab's 800 *GeV* proton beam was used to produce a wide-band beam of neutrinos and anti-neutrinos. This is the highest-energy neutrino beam yet produced. The experiment was done with the CCFR detector located in Lab E, one of several experimental areas in the Fermilab neutrino beam line. The detector consists of a 690-ton sampling calorimeter and a muon spectrometer. The data were gathered in two runs: E744 ran from February to August 1985 and E770 started in June 1987 and concluded in February 1988.

This chapter describes the experimental apparatus in further detail. The final sections elaborate on the triggering criteria and discuss the raw data preparation.

2.1 Neutrinos at the Fermilab Tevatron

The experiment took place at the Fermilab Tevatron, which is presently the highest-energy accelerator in the world. Fermilab's 800-*GeV* protons produced a beam of neutrinos and anti-neutrinos with an average energy of about 140 *GeV*, with maximum neutrino energies going as high as 600 *GeV*. A schematic diagram of the Fermilab accelerator complex is shown in Figure 2.1. Below is a description of the various stages used to accelerate the proton beam:

- ION SOURCE: H^- ions are produced by a cesium cathode immersed in hydrogen gas.

- COCKROFT-WALTON ACCELERATOR: The Cockroft-Walton is an electrostatic machine which begins the proton acceleration process. By

employing multiple electrostatically-induced potential drops, the ions are collected from the source and accelerated to 750 *keV*.

- LINAC: A linear accelerator, consisting of a chain of radio-frequency cavities, increased the energy of the H^- ions to 200 *MeV*. As the ions exit the LINAC they pass through a carbon foil, which strips them of their two electrons.

- BOOSTER: The Booster is a 140 *m* diameter synchrotron. A synchrotron is a ring-shaped machine in which an applied magnetic field maintains the protons in the proper orbit while an accelerating rf electric field is provided at gaps along the ring. As the particles gain energy, the magnetic field is increased to preserve the orbit while the frequency of the accelerating electric field also increases. The Booster accelerates the protons to 8 *GeV* and injects them into the main ring.

- MAIN RING: The main ring is a 2 *km* diameter synchrotron that accelerates the protons to 150 *GeV*. It contains 1000 conventional, copper-coiled magnets to bend and focus the protons. Prior to construction of the Tevatron ring, the main ring served as Fermilab's primary accelerator.

- TEVATRON RING: The Tevatron is a super-conducting proton synchrotron. It shares the tunnel with the main ring and is positioned immediately below it. The Tevatron's super-conducting magnets operate in the temperature range of liquid helium and provide a 40 *kG* field. The accelerator was designed to accelerate particles to 1 *TeV*. During this experiment, the protons were accelerated to 800 *GeV*, a choice of energy that optimized the machine performance.

When operating in fixed-target mode (as opposed to collider mode) the Tevatron operates on a 60-second cycle. During each cycle the Tevatron is filled with approximately 10^{13} protons. The protons are held at their maximum energy for about a third of the cycle and extracted in fast and slow spills. The fast spills are called pings and are of millisecond duration while the slow spills last two seconds. Protons from slow spill are directed to other experiments, while the pings are used exclusively to create the neutrino beam.

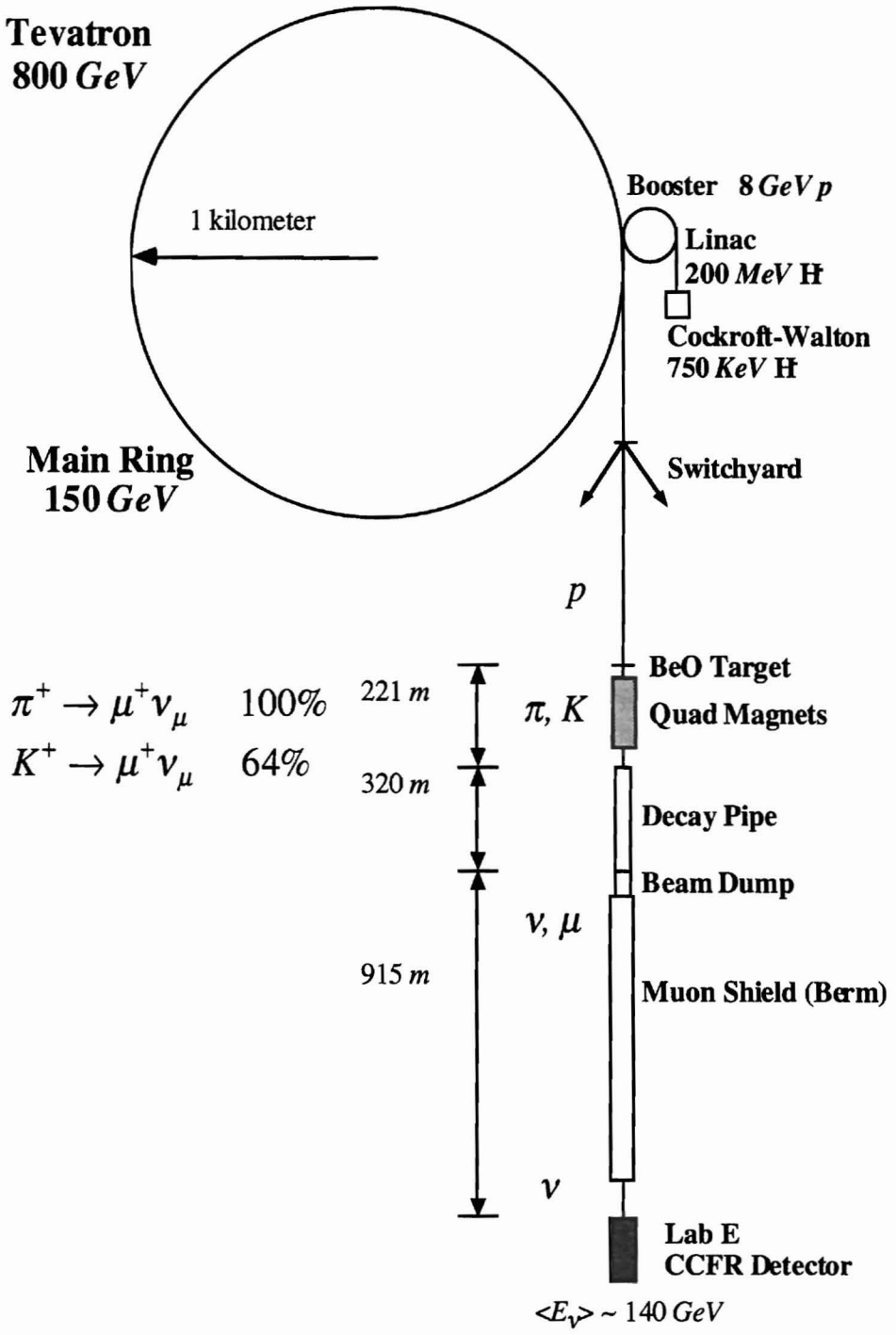

Figure 2.1: Fermilab neutrino beamline layout.

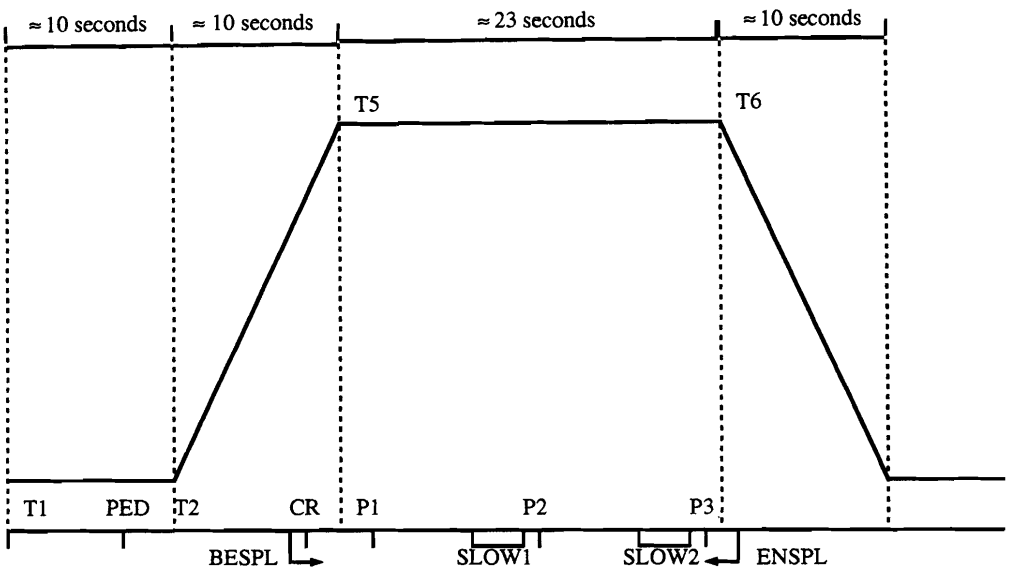

Figure 2.2: Tevatron magnet current versus time during fixed-target operation. The magnet cycle is described in the text.

The timing structure of the Tevatron magnets is shown in Figure 2.2. The cycle begins at time T1. The Tevatron is filled with protons that have been stored in the main ring and after ten seconds, at time T2, the current in the Tevatron magnets begins to ramp up, and the protons are accelerated. The increase in the magnetic field is synchronous with the increasing rf frequency. After 10 seconds and approximately 10^{13} revolutions, the protons reach 800 *GeV*. The beam is stored at this energy for 23 seconds, between T5 and T6, while the protons are extracted. This neutrino experiment uses relatively short beam extractions during the flat top period. However, we share the beam with other experiments, hence the relatively long flat-top (23 seconds) is produced for the experiments that prefer a nice steady flow of beam. P1, P2, and P3 indicate the fast spills, while two slow spills are extracted between them. At T6 the magnets being to ramp down and the cycle repeats.

2.2 Neutrino Beam

For neutrino production, the proton beam was directed onto a 33 cm long (1 interaction length) beryllium-oxide target in the Neutrino Center beamline. The length is chosen to optimize the maximum number of interactions producing the highest energy mesons. The number of interactions increases with a wider target but the energy of the resultant mesons decreases with the width of the target. This decrease comes from the secondary particles themselves interacting in a wider target.

A secondary beam of mesons emerges from the target and is focused by a triplet of quadrupole magnets. The secondaries enter a 320 m decay region 221 meters beyond the target. Pions and kaons decay in flight, with dominant decay modes:

$$\pi^+ \rightarrow \mu^+ \nu_\mu,\ \pi^- \rightarrow \mu^- \overline{\nu}_\mu \qquad \text{BR} = 99.99\% \tag{2.1}$$

$$K^+ \rightarrow \mu^+ \nu_\mu, K^- \rightarrow \mu^- \overline{\nu}_\mu \qquad \text{BR} = 63.5\%. \tag{2.2}$$

The maximum neutrino energy is governed by the mass ratio of the muon and the decaying particle:

$$E_\nu^{\max} = E_{\pi,K}\left(\frac{m_{\pi,K}^2 - m_\mu^2}{m_{\pi,K}^2 + m_\mu^2}\right) \approx E_{\pi,K}\left(1 - \frac{m_\mu^2}{m_{\pi,K}^2}\right), \tag{2.3}$$

so that the neutrino beam exhibits a dichromatic spectrum, with the more energetic neutrinos coming from the kaon decays:

$$\left(E_\nu^{\max}\right)_K = 0.95 E_K \tag{2.4}$$

$$\left(E_{\nu}^{\max}\right)_{\pi} = 0.43 E_{\pi}. \tag{2.5}$$

The original protons preferentially create positively charged secondaries so the neutrinos outnumber anti-neutrinos two to one in the final flux.

A schematic drawing of the Fermilab Neutrino beamline is shown in Figure 2.3. Event timing is initiated by a signal pulse as the proton bunch passes through a toroid (NC1TOR) upstream of the target. After the BeO target, the focusing of pions, kaons, and other charged particles is done by a triplet of quadrupole magnets, NC1Q4 through NC1Q6. The triplet gathers the mesons off the target and collimates them into a parallel beam in the decay region. To gain maximum acceptance, no sign or momentum selection is done, and the beamline is configured as a *wide-band beam* with large momentum acceptance.

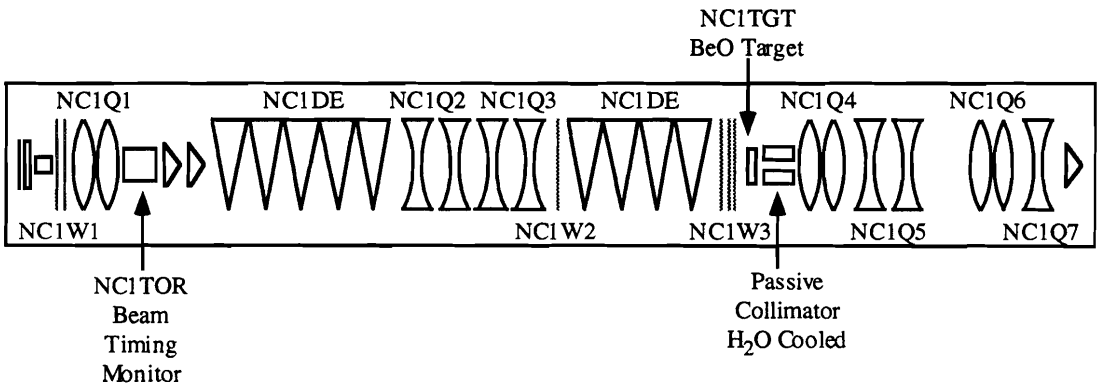

Figure 2.3: Neutrino Center beamline. Dipole magnet are indicated by prisms (triangles), and quadrupole magnets are indicated by concave and convex lenses.

Once through the decay region, the remainder of the beam is dumped into a 6 *m* block of aluminum followed by steel shielding. The CCFR detector is positioned 915 *m* beyond the dump. The muons and neutrinos that penetrate the aluminum beam

dump encounter approximately 241 *m* of steel shielding and 582 *m* of earth berm before reaching the detector. This material in front of the detector is sufficient for the muons from the meson decays to range out, so that of all the particles entering the berm, only the neutrinos penetrate into the experimental area.

However, neutrinos may interact inside the berm, and a small number of berm muons do enter the experimental hall. Events due to muons are identified and discarded by their interaction in the veto wall, a set of scintillation counters positioned upstream of the target calorimeter. The front face of the CCFR detector is 915 *m* from the end of the decay region, and neutrinos strike the detector within about a one meter radius around the beam axis. Therefore, the neutrinos have an incident angle no larger than about 1 *mrad.* In the Monte Carlo, the neutrino's stike the target at normal incidence. A small correction is applied for making this approximation. The procedure used to determine the neutrino flux is described in Chapter 5 and the relative neutrino and anti-neutrino flux is shown in Figure 5.7.

2.3 Detector

The following sub-sections describe the CCFR detector and trigger system. Figure 2.4 sketches the detector. The event display in Figure 2.5 indicates the response of the detector elements to a typical charged-current event.

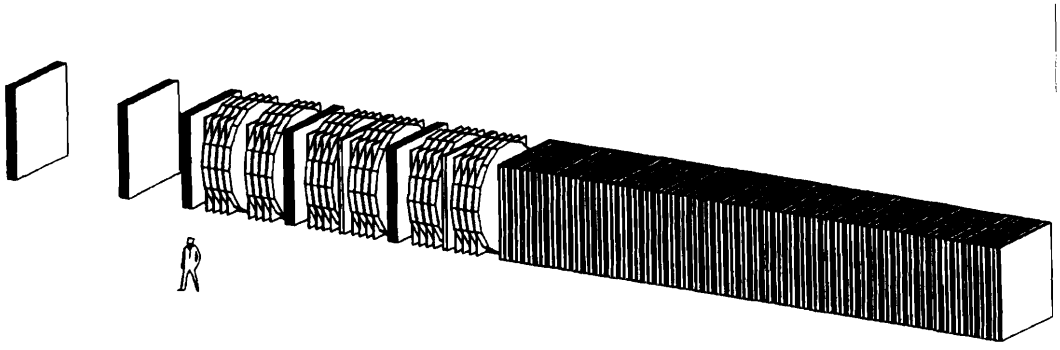

Figure 2.4: Schematic representation of the CCFR detector. The neutrino beam enters from the right. The target calorimeter is to the right of the muon spectrometer. The two leftmost banks of drift chambers are known as the blue cart.

2.3.1 Target Calorimeter

The large-area target calorimeter consists of steel plates, liquid scintillation counters and drift chambers. It has a mass of 690 tons, is 17.7 *m* long and measures 10 feet by 10 feet transversely. It is made up of six identical modules called carts. Each cart contains twenty eight steel plates, seven drift chamber stations, and fourteen scintillation counters. Each steel plate is 5.15 *cm* thick. A liquid scintillation counter is positioned between every two plates and a drift chamber is placed between every four plates. Each scintillation counter occupies 6.48 *cm* along the beam axis, and each drift chamber station occupies 8.87 *cm*. A schematic view of one cart is shown in Figure 2.6. The carts are numbered so that cart 6 is the most upstream and cart 1 is the most downstream. The counters are numbered so that counter 84 is the most upstream and counter 1 is near the toroid.

2.3.1.1 Scintillator Counters

The active energy sampling fraction of the scintillation counters in the calorimeter is approximately 11%. The measurement is made by scintillation counters. The active area of the counter setup is an acrylic tank measuring 10 × 10 feet by 1 inch filled with mineral oil doped with scintillating fluors. Plastic bags filled with water occupy the space between the acrylic tank and the steel plates to balance the pressure on the acrylic walls (see figure 2.7). Each of the acrylic tanks is enveloped in opaque material (Marvel Guard) to prevent external light from reaching the scintillator. A photomultiplier tube (PMT) at each corner of the square counter is used for readout.

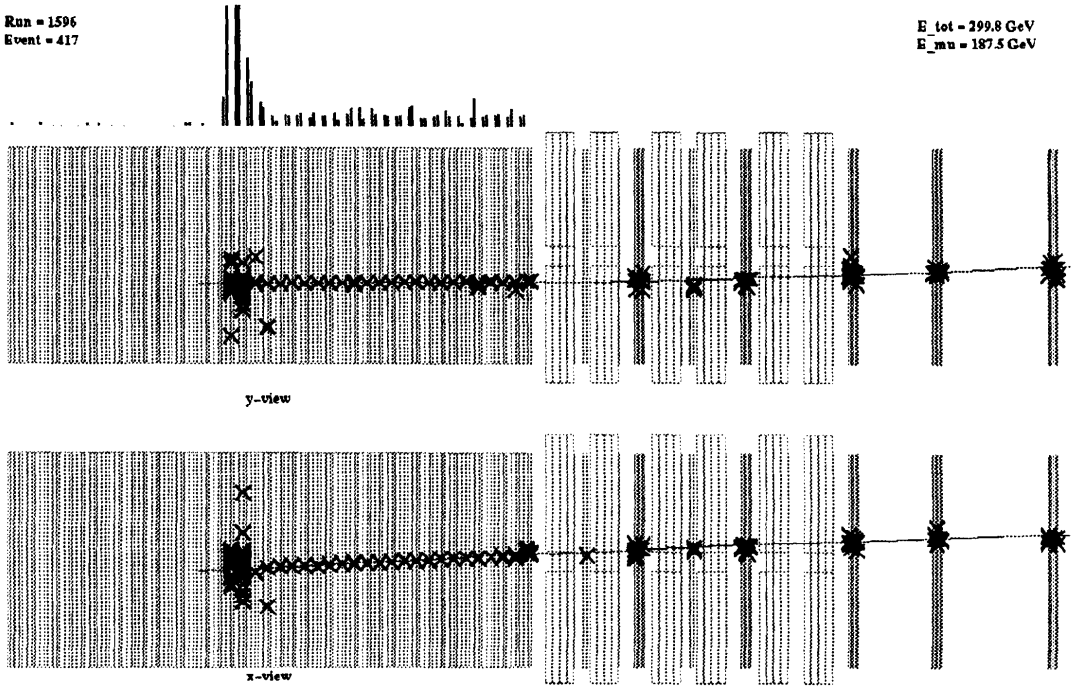

Figure 2.5: A typical charged-current event as seen by the elements of the CCFR detector. Both overhead and lateral views are shown. Hits in the drift chambers are shown as "X"s. Pulse heights in the scintillators are shown in a logarithmic scale above the target. The line linking the hits in the target and the toroid is derived by the tracking software as described in Chapter 3.

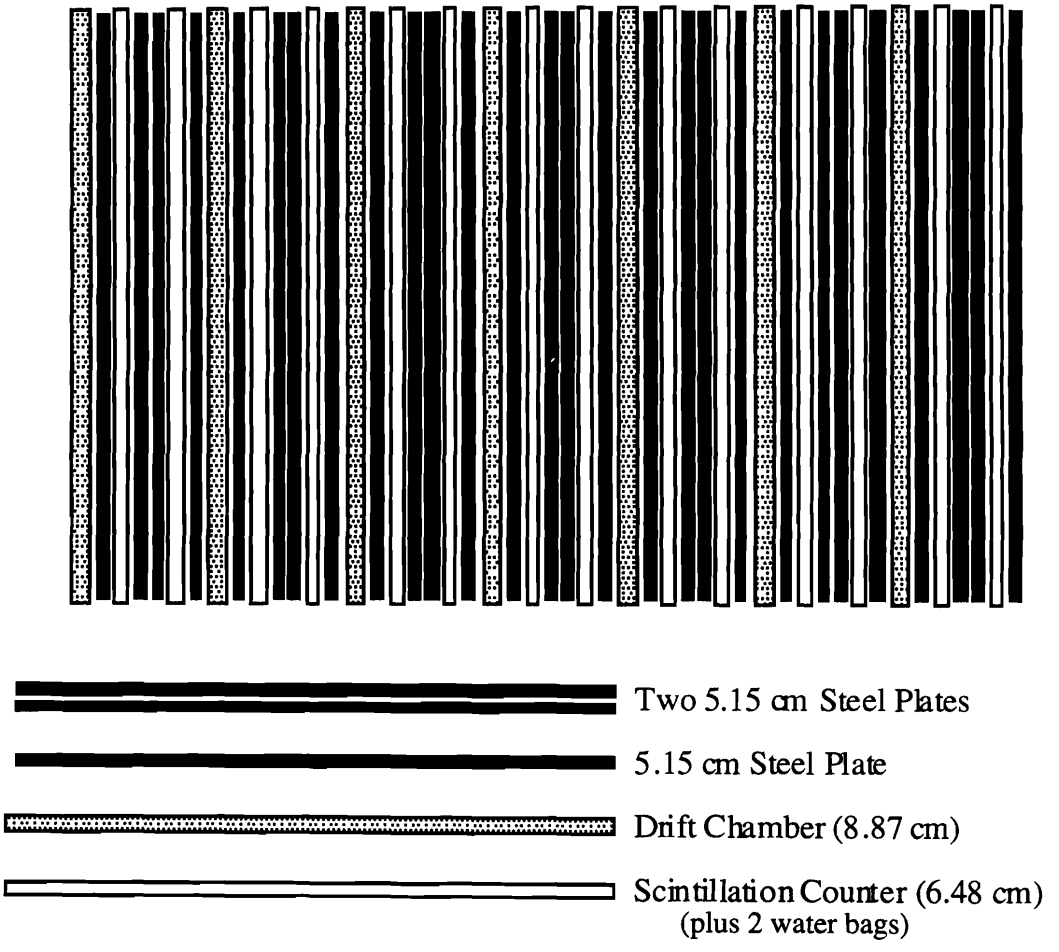

Figure 2.6: Stack layout of a CCFR target cart. A drift chamber is positioned after every two steel plates and a scintillation counter is found after every four.

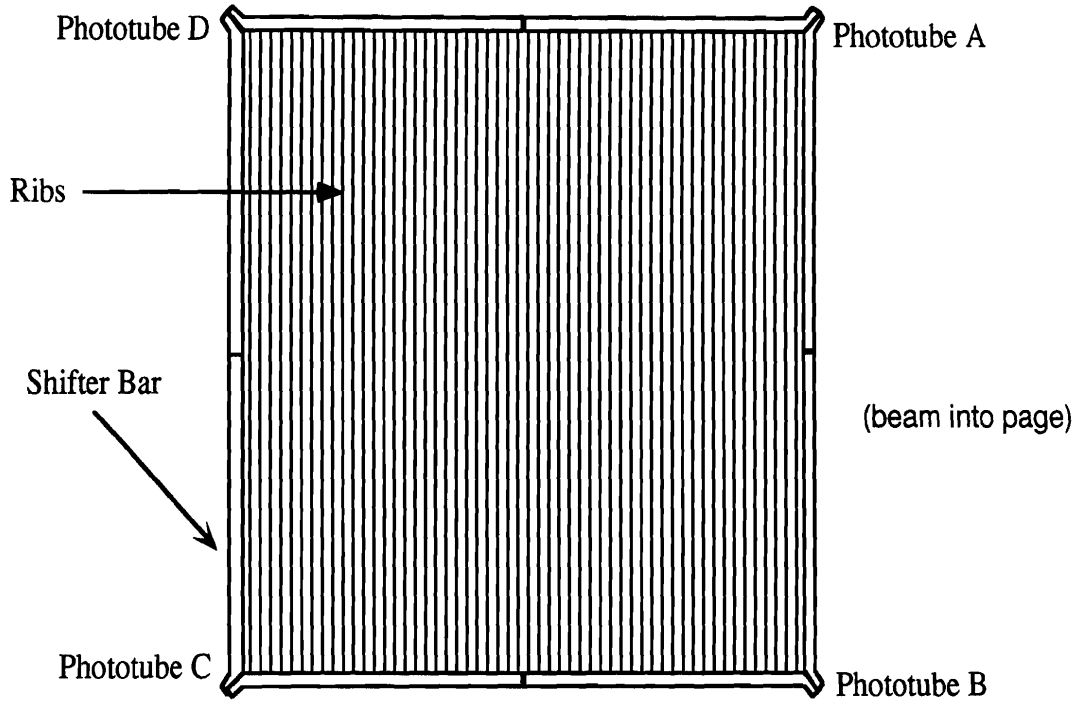

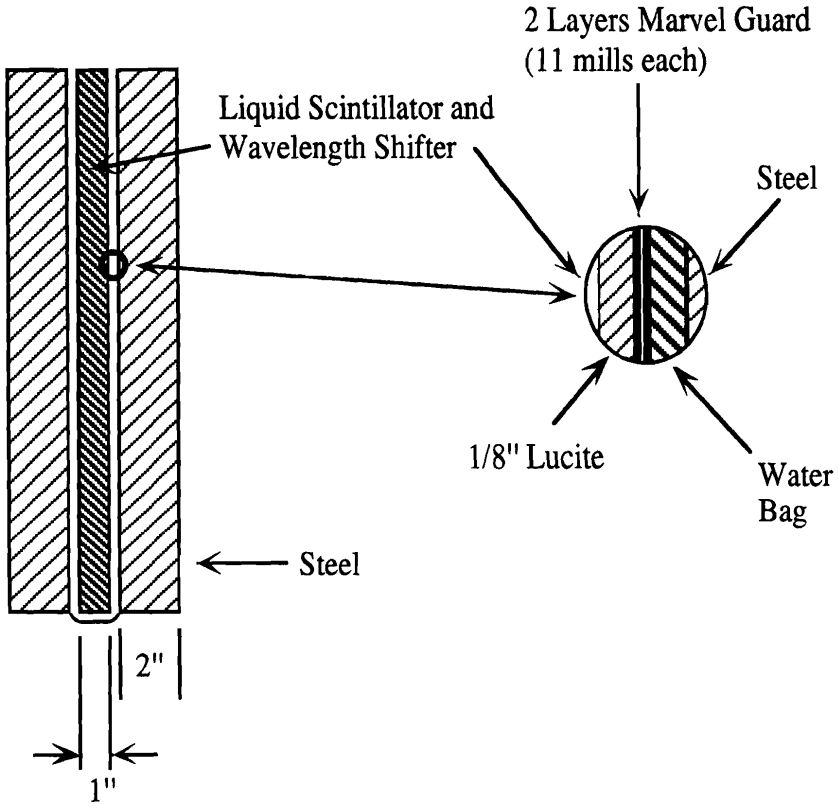

Figure 2.7: CCFR scintillation counter.

A charged particle passing through the counter excites primary fluors in the oil, which radiate ultraviolet light. The ultraviolet light is absorbed by secondary fluors in the oil, which emit visible blue light. The blue light has a longer attenuation length in the oil, about 40 inches, and light emerging below the critical angle is transmitted to the edges of the counter through total internal reflection. At the edges there are BBQ-doped plastic bars that absorb the blue light and re-emit green light. Finally, the green light is guided to the ends of the bars where the phototubes are positioned.

Each counter has four RCA 6342A phototubes, which were operated with a potential drop of 1400 volts across the cathode to anode. A photon striking the cathode has about a 20% probability of liberating an electron. The tube multiplies this signal with a series of ten dynodes, each dynode emitting an average of four electrons for each one absorbed. A single initial photoelectron produces a signal of about 0.25 picoCoulombs. The sensitivity to a muon traversing through the center of a counter is about 2.5 photoelectrons per phototube.

The phototube signal is digitized by a LeCroy 4300 FERA, a fast and buffered readout system of analog-to-digital converters with 11 bits of dynamic range. The gate width of the ADCs is 244 *nsec*, on average this gate begins 30 *nsec* before the leading edge of the phototube signal arrives at the ADC. The average integration time is then 214 *nsec*. The charge collected is stored on a capacitor and then digitized by measuring the time required to discharge the capacitor through a resistor. Digitizing the signal requires 8.5 μsec and another 3.2 μsec is needed to buffer the data, leading to a dead time of 11.7 μsec. A pedestal voltage of approximately 50 counts is applied to each ADC. This pedestal is recorded before the first ping of

every accelerator cycle. By taking twenty such "fake" events a typical pedestal can be subtracted from each data reading.

At the Tevatron, the accelerator rf buckets arrive in intervals of 18.6 *ns*. Event timing is measured at each counter using the same time-to-digital converters (TDCs) that are used for the drift chambers (see the next Section). The TDCs provide a time resolution of 4 *nsec*. When information from all active counters is combined, the overall event time resolution has an rms of 2.4 *nsec*.

2.3.1.2 Drift Chambers

Muons emerging from the neutrino interaction are tracked inside the calorimeter target by drift chamber stations. A drift chamber records the passage of a charged particle by detecting ionized electrons. These electrons are liberated from atoms of the argon gas which fills the inside of each chamber. Each drift chamber station has an active area of 10ft x 10ft and is comprised of 24 horizontal and 24 vertical cells. Each cell is 5 inches across and 0.75 inches thick and contains three wires. Figure 2.8 shows a sketch of a drift chamber cell.

Each chamber is constructed of Hexcel-covered aluminum walls. Parallel aluminum I-beams spaced every five inches support G-10 cover plates and define the drift chamber cells. Within each cell, a 127 μm diameter copper-beryllium central field wire is held at +350 volts. Two 30 μm diameter gold-plated tungsten wires run on either side of the field wire and are held at +1750 volts. Nylon spacers placed every 12 inches maintain 2 *mm* spacing between each sense wire and the field wire. The I-beams are maintained at –4500 volts. Finally, the inside of the G-10 cover within

each cell is clad with 19 copper cathode strips, each of which is held at a particular voltage so that a uniform electric field of 690 volts/*cm* is created.

The chambers are filled with an equal mix of argon and ethane. A noble gas, argon does not form molecules and so lacks vibrational or rotational modes of excitation. Therefore, argon readily ionizes when excited by a passing energetic charged particle. After the primary ionization, the electrons and ions separate due to the applied electric field. The electrons drift toward the anode sense wires and accelerate, producing secondary ionizations. Ethane, an organic compound, is included to render the chamber self-quenching. That is, the ethane absorbs the ultraviolet photons liberated in the argon as the electrons drift towards the sense wires. This limits the avalanche of charge that would otherwise smear the signal pulse along the sense wire.

The drift velocity of electrons in the drift chamber is 50 $\mu m/nsec$, so that the total drift time to cross 2.5 *in* inside a cell is 1.3 μsec. The arrival time of the drift chamber pulse on one wire relative to the event time allows the determination of the particle's position in one dimension, up to the ambiguity of knowing on which side of the wire the particle passed. Having two sense wires per cell resolves this ambiguity, as the wire closer to the particle received the ionization first. Combining the hit information from two adjacent orthogonal cells provides the determination of the particles' position in the x-y plane.

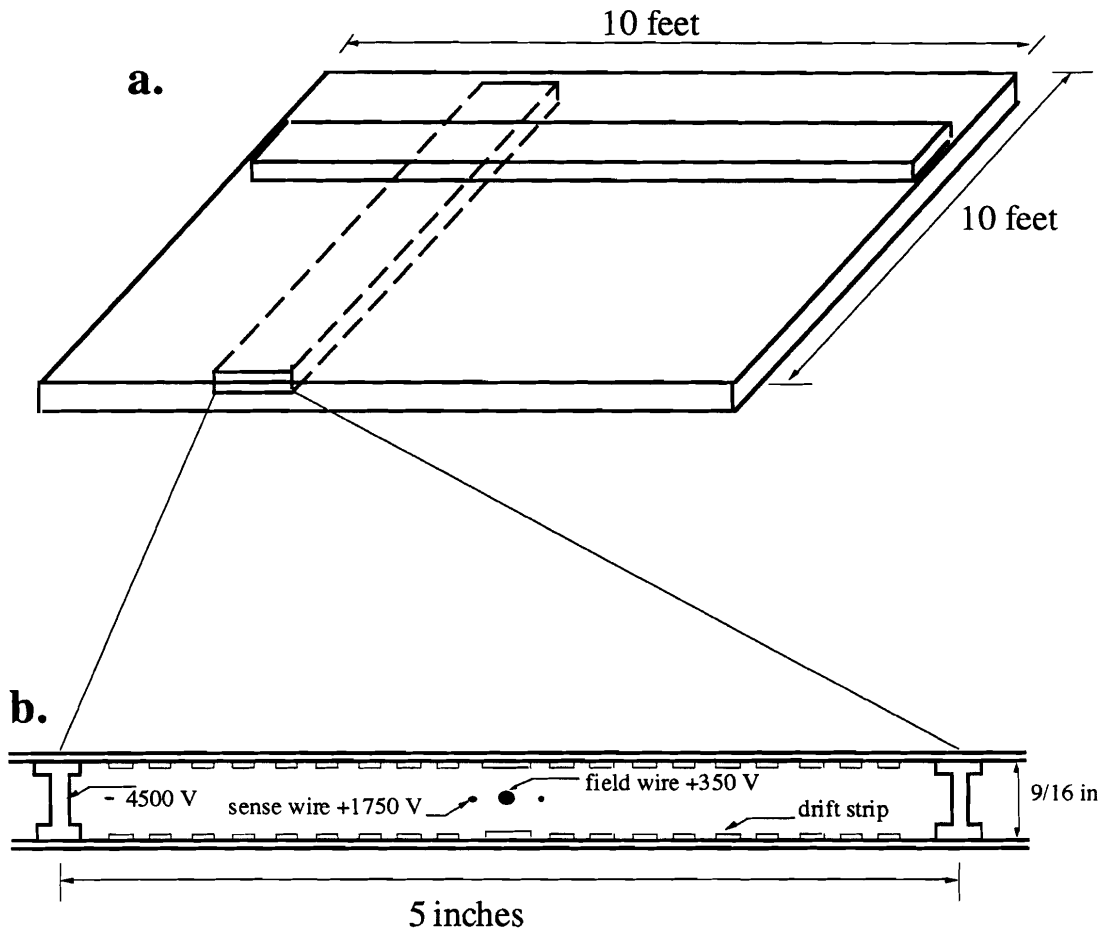

Figure 2.8: Sketch of CCFR target drift chamber section. **a.** Diagram of one chamber. There are two orthogonally-oriented planes per station, consisting of three-wire cells. **b.** A three-wire drift-chamber cell.

The signal from the sense wires is amplified and sent to two coupled TDCs, which have their 8 *nsec* time bins staggered by 4 *nsec*. Thus the coupled TDC digitizes the time of the pulse in 4 *nsec* bins. The TDC is capable of buffering hits in 512 bins, so its live time is slightly in excess of 2 μ*sec* allowing it to buffer the full drift range of the cell. The TDC then takes 8 *nsec* to transfer its information into a first-in-first-out (FIFO) buffer. The FIFO buffer can store 32 events per spill.

The overall position resolution of the drift chambers depends on the time resolution of the TDCs, variations in the electric field, and misalignment of the chambers. All elements of the detector were aligned with an optical survey, and precise alignment of the chambers was accomplished by using high-energy straight-through muons with $p_\mu > 125\ GeV$. The alignment procedure iteratively varied the chamber coordinates to provide the best fit to the sample of straight-through muons. In the target, such an alignment procedure was straightforward because the target is unmagnetized, and the effects of multiple Coulomb scattering (described in the next Chapter) diminish with energy. The intrinsic position resolution of the target drift chambers is 225 μm.

2.3.2 Muon Spectrometer

Downstream of the target calorimeter lies a muon spectrometer consisting of three large toroidal iron magnets instrumented with acrylic counters and with arrays of 10-square-foot- drift chambers. Each of the three instrumented magnets is referred to as a toroid cart. A sketch of a typical toroid cart is shown in Figure 2.9. Each toroid cart is segmented into eight 8-inch-thick cylinders, called washers, each with a 70-inch outer radius and a 5-inch inner radius. Each washer is divided horizontally into semicircles. The bottom of each washer includes two iron legs that support the magnets on movable platforms.

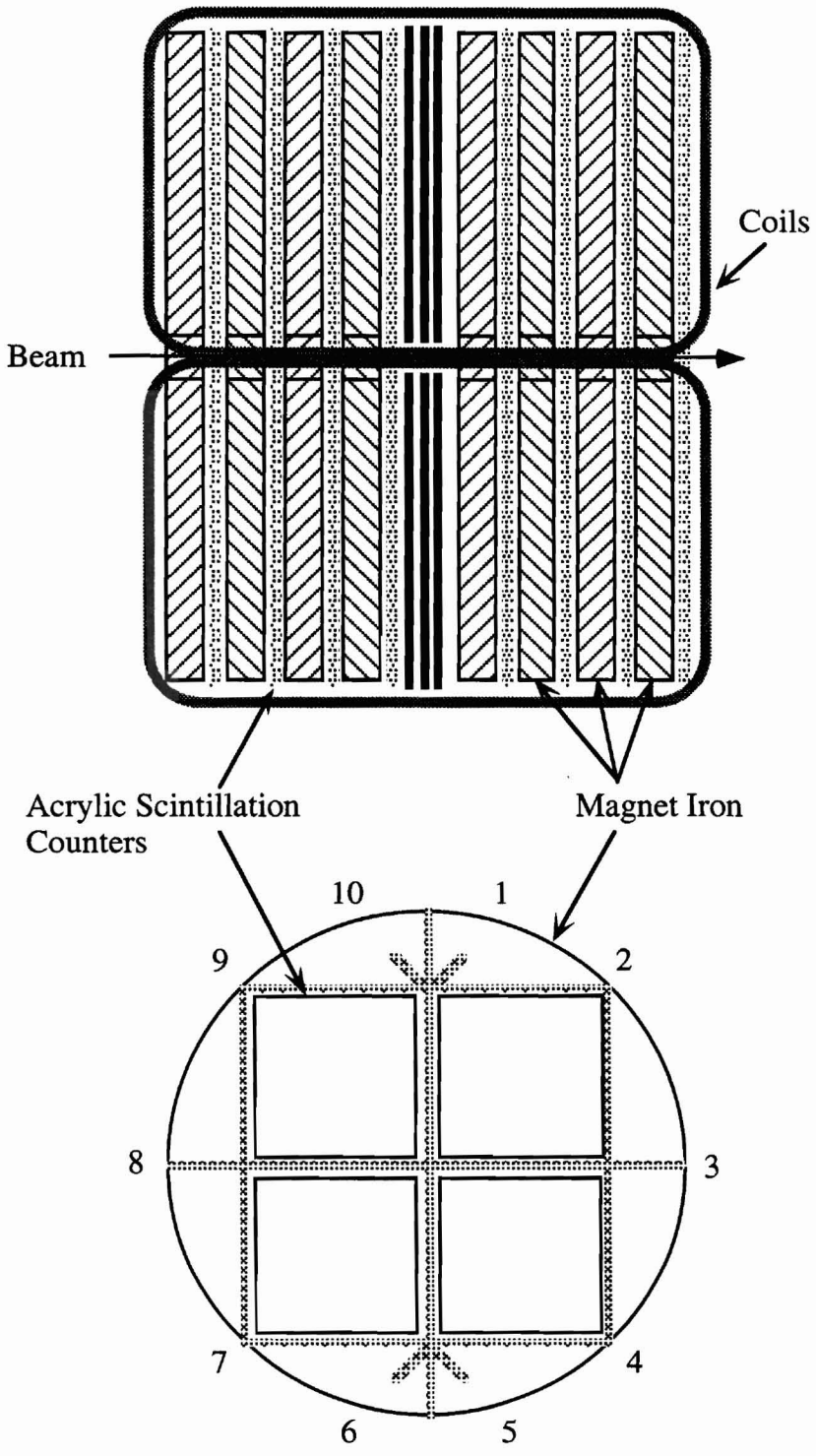

Figure 2.9: Schematic drawing of a CCFR toroid cart, showing overhead and transverse views. In the transverse view, the shaded liens indicate the wave shifter bars along the outer edges of the

scintillators, and the numerals indicate the positions of phototubes.

Four copper coils of 12 turns each encircle the magnets at 90° intervals. A current of 1200 *A* produces a magnetic field ranging from 1.9 *T* near the center of the toroid to 1.55 *T* near the outer edge. The field was found to be azimuthal throughout the magnets except for a small radial component at the iron legs [Kin91]. A muon traveling the length of the spectrometer receives a 2.4 *GeV* transverse momentum component from the magnetic field.

Tracking muons through the spectrometer is accomplished by five sets of drift chambers, positioned immediately downstream of each toroid cart and 3 *m* and 7 *m* behind the last toroid. The two most downstream sets of drift chambers are referred to as the blue cart. The drift chambers in the muon system contain one-wire cells. To resolve the left-right ambiguity, the chambers are staggered by 1/4 of a cell width. This staggering method is possible in the muon spectrometer because successive drift chambers are not separated by steel, as they are in the target, making the effects of multiple Coulomb scattering between chamber planes negligible. Muons are tracked cleanly through the set of five drift chambers, allowing the five to be treated as a unit.

Alignment of the drift chambers in the toroid spectrometer using straight-through muons was more complicated than in the case of the target calorimeter because of the bending of tracks in the spectrometer's magnetic field. A description of the alignment procedure can be found in [Rab92]. The alignment of the toroid drift chambers was accomplished to within 380 μm, and the overall position resolution of these drift chambers is 0.5 *mm*.

There is an acrylic counter plane positioned after every washer. Each of these planes is divided into four separate counters, so that the quadrant through which the muon traveled is determined (see figure 2.9). The four planes in one half-cart are grouped together. These counters, forming 24 planes in all, are used to define the PTOR trigger condition, which is described in the next section.

The muon spectrometer is additionally instrumented with some extra sets of scintillation counters for fast detection of muons for triggering. These counters are equipped with 56AVP phototubes. They are located in the gaps between the three main sections of the toroid (see figure 2.10). The planes are composed of narrow counters, referred to as hodoscopes, and a few larger counters (see trigger section 2.4.1 for details and figures). The term "hodoscope" refers to a scintillation counter system composed of transversely segmented counters. Usually such a setup is used to determine the particle's position. In this case, no measurement of position is made, the counters are used for fast charge current triggering. The trigger condition for the gap is satisfied if any counter in that gap records a particle traversal.

2.4 Data Acquisition

The target calorimeter and muon spectrometer produce the raw data of a neutrino event. The "raw" signals come in two forms: (1) pulse heights from the phototubes of the scintillation counters and (2) timing pulses from the drift chambers . These signals must be converted to physical quantities like muon energy, muon angle, and hadronic energy. In the analysis, the data is reduced to select the events of interest, while discarding events due to background or noise. This selection process is begun by the trigger system.

2.4.1 The Trigger System

When a set of signals comes off of the detector the pulse heights are initially tested to see if the information is worth writing to tape. "Worthy" data must appear to have been generated by a neutrino event as opposed to a cosmic ray event or the result of electronic noise. Several sets of criteria are put together to test a set of pulse heights. Each one models a different type of neutrino event as seen by the detector, the group of criteria should cover all of the neutrino's potential electronic signatures. Once one of these criteria have been satisfied, the data acquisition system is triggered to record the full detector response and save it as an "event". For this reason each set of criteria (or electronic signature) is called an "event trigger".

The "trigger system" is a set of electronic devices put together for this purpose. Its response must be swift. The evaluation of a set of signals needs to be completed before another set arrives. The CCFR trigger system was designed to respond in approximately 200 nanoseconds. The challenge in designing such a system is to have enough requirements to get rid of the unwanted events but not so many that you miss some of the more eccentric events you do want. The complexity of the criteria is also limited by the time demand.

Some of the unwanted events are beam-related backgrounds caused by charged particles emanating from neutrino interactions in the earthen berm. Two $17.5 \times 4.5\ m$ scintillation counter arrays are positioned immediately upstream of the first calorimeter cart to form a veto wall (see figure 2.10) to exclude these events. During beam running, secondary particles from the berm interact with the air above the detector and illuminate the detector with low-energy photons. For this reason, the veto wall counters are shielded by a one-meter-thick concrete wall, and lead sheets

are mounted between the two scintillator planes of the veto wall. A layer of lead bricks is stacked above the toroid gaps to shield the trigger counters.

The remainder of this section details the counter signals on which the trigger is based, and the 6 sets of criteria (the event triggers).

2.4.1.1 The Phototube Signals

The logic of the trigger system uses the phototube signals coming from the scintillation counters. It does not use timing or position information from the drift chambers because those signals take too long to process.

The various scintillation counters are shown in figure 2.10. There are 84 scintillation counters that regularly segment the target, 25 counters that regularly segment the toroid, the counters that constitute the veto wall and the additional counters that are located in the gaps between the three main sections of the toroid. The gap counters are labeled T2, T3, H1, H2 and H3.

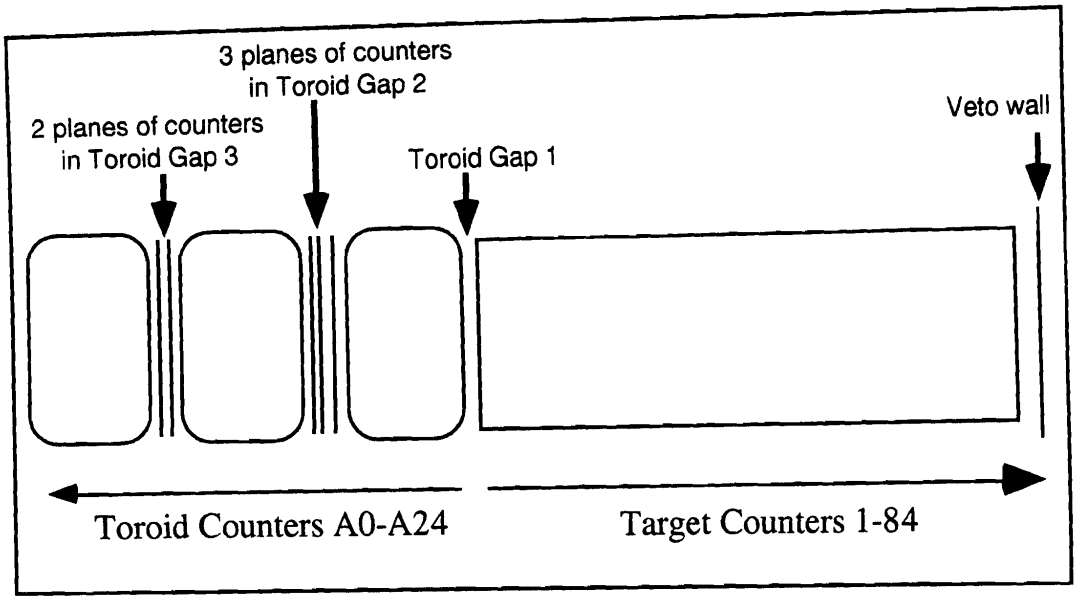

Figure 2.10: Map of counters. There are 84 regularly spaced target counters, 25 regularly spaced toroid counts, veto wall counters, and the toroid gap counters

The different types of counters have their own distinct phototube configurations. All configurations are described from a downstream perspective.

- The target counters have four phototubes labeled a-d (clockwise) located on each corner (see figure 2.7).

- One toroid counter is made of 4 individual sections of plastic scintillator. These quadrants are labeled A-D. Each toroid counter has 10 phototubes labeled 1-10 also labeled clockwise (see figure 2.9).

- The additional counters located in the toroid gaps are particularly important for the charged current triggers. Their phototube configurations are pictured below in figures 2.11 and 2.12.

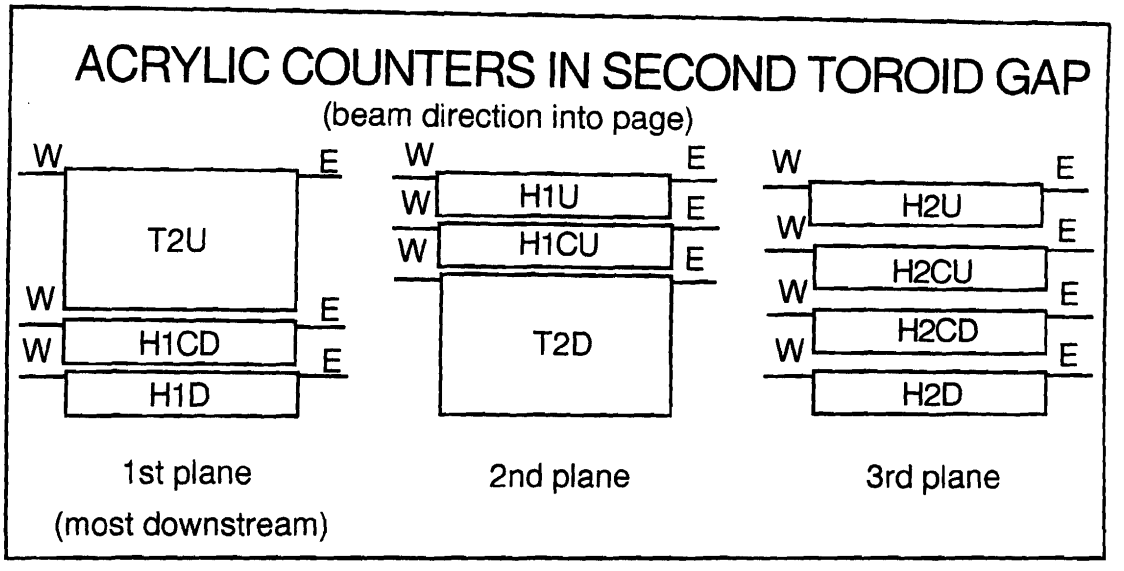

Figure 2.11: Tube and counter configurations in the 2nd toroid gap.

The counter commonly referred to as T2 is really two separate sections of plastic scintillator called T2U (for T2 up) and T2D (for T2 down). The two are located in sequential planes combined with the four H1 counters. When the logic documentation refers to T2 it more precisely refers to a logical "or":

$$T2 = T2U + T2D. \tag{2.6}$$

The tubes on these gap counters are labeled by their counter segment and their eastern or western position on that segment. For example the western tube on the T2U counter would be labeled T2UW (see figure 2.11). T2U itself as referred to in eqn 2.7 is a logical "or" of the two tubes on T2U:

$$T2U = T2UW + T2UE. \tag{2.7}$$

Likewise the counter commonly referred to as H1 (named as the most upstream set of hodoscope counters in the toroid gaps) is really a set of 4 counters: H1U (H1 up),

H1CU (H1 center up), H1CD (H1 center down) and H1D (H1 down) each with 2 tubes:

H1 = H1UE + H1UW + H1CUE + H1CUW + H1CDE + H1CDW + H1DE + H1DW

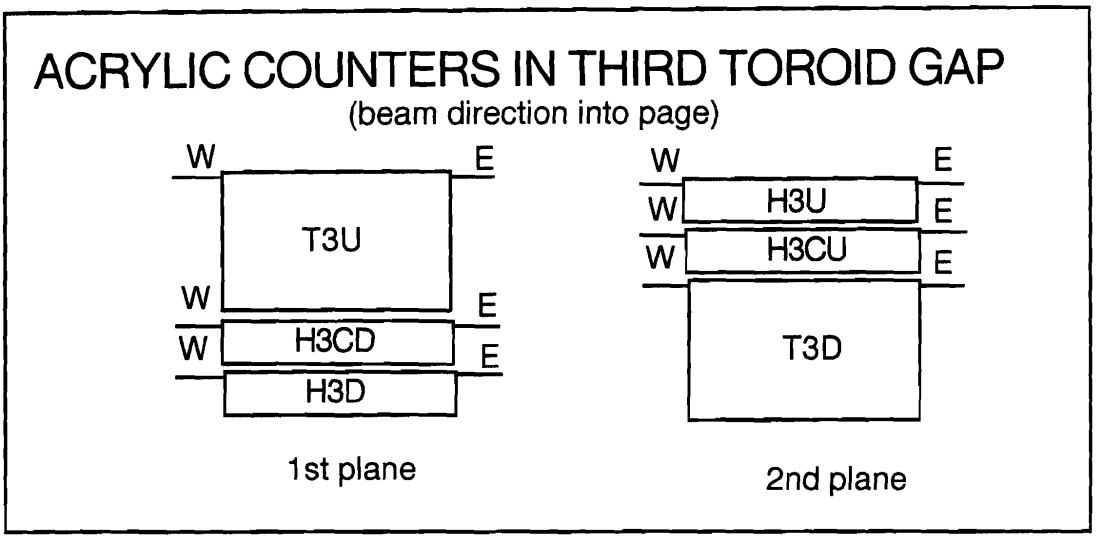

Figure 2.12: Counter and tube configuration in the 3rd toroid gap.

The phototube signals from each target counter (and some of the toroid counters) are stored in seven different ADC channels with differing sensitivities (see figure 2.13):

- THE LOWS: ("LO") Each individual phototube signal is fanned out and one channel of each fan out goes directly to the ADCs. Typically a muon passing through the center of a target counter will produce 2 ADC counts in this LO channel.

- THE COMBINATION LOWS ("COMBLO") All of the phototube signals from one counter are added together. This combined signal is fanned out and one channel goes to the ADCs. Typically a muon passing through a target counter yields 8 ADC counts in this channel.

• THE HIGHS: ("HI") One of the channels from the COMBLO is amplified by ten and sent to the ADCs. A typical muon target signal in this channel is 80 counts.

• THE SUPER LOWS: ("SUPERLO") One of the channels from the LO fan out is attenuated by a factor of six. Combinations of these smaller signals are added together in sets of ten. The ten signals are from counters as far from each other in the detector as possible (typically ten counters). This minimizes the number of high signals in each bunch for a given event in order to avoid saturating the measurement device. A typical muon signal in the target in this channel is 0.2 counts.

The signals are digitized in these different configurations to maximize the dynamic range of the total event picture. A hadron shower will typically produce 1000 to 2000 counts in one counter. This signal will saturate the HIs but can be measured directly by the LOs. A strong shower could saturate the LOs (greater than $2^{11} - 1 = 2047$ counts) but the SUPERLO is then available to measure the energy deposit. The HI channel is used to measure the passage of a muon, whose signal (about 2 mV) is too small to be measured by the LOs. The COMBLOs are primarily used to form triggers and for calibrations of the HI to LO response.

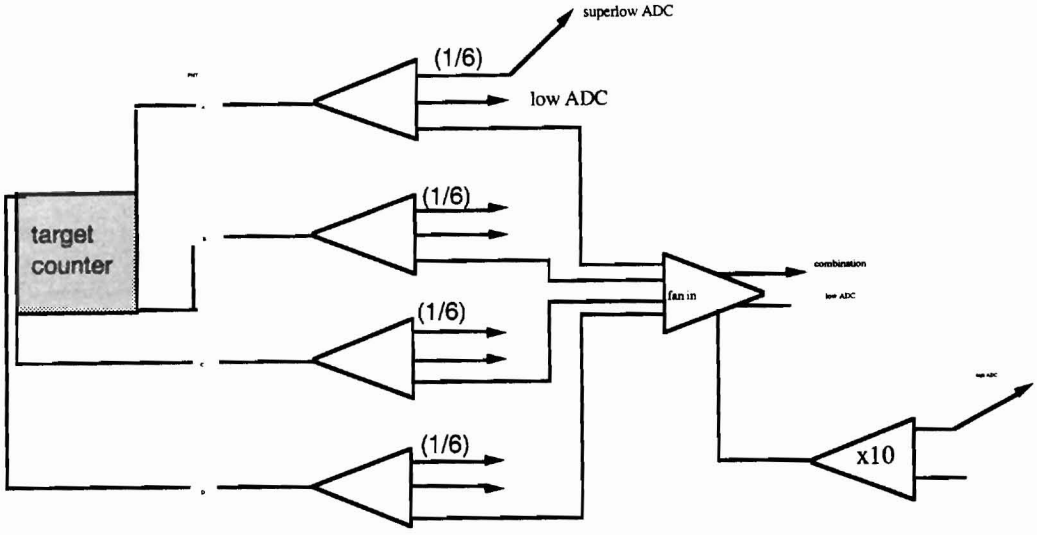

Figure 2.13: Readout electronics for a single scintillation counter. Each counter's signal is digitized in several different ADC channels, as described in the text.

In general, the signals are duplicated by a device called a fan-out. One channel of the fan-out is sent to the ADCs. The other fan-out channel is discriminated, testing the signal for a given minimum energy level. If the requirement is met the discriminator fires and this information goes on to form triggers (its timing is also recorded in the TDCs). The different "bits" (as the discriminated signals are called) are constructed as follows:

SBIT: (thresh = 150mV, input = COMBLO x 100)

The sbits are designed to identify at least one charged particle (single muons) passing through a counter. This discriminator tests the combined signal (COMBLO) after it has been through two x10 amplifiers. This amplified signal is discriminated at 150 mV. This bit should fire for a typical muon which has a signal of 2 mV (after amplification 200 mV).

TBIT: (thresh = 450mV, input = COMBLO x 100)

The tbits are designed to distinguish between showers and single muons. This discriminator tests the combined signal (COMBLO) after it has been through two x10 amplifiers. This amplified signal must be at least 450 mV. This bit should NOT fire for a typical single muon but it should fire if more than one charged particle passes through the counter.

NBIT: (thresh = 88mV, input = sum of 8 COMBLO)

This bit was constructed to test the amount of energy deposited by a shower. This information is useful in distinguishing between cosmic ray events and NC neutrino events. This discriminator tests the combined signals (COMBLO) of a sum of eight consecutive counters with no amplification. The tested level is set at eight GeV (88mV). A typical cosmic ray event will not deposit this much energy but a typical CCFR neutrino shower is well above this level.

HBIT: (thresh = 44mV, input = sum of 8 COMBLO)

The HBIT is just like an NBIT but its energy requirement is lower. This discriminator tests the combined signals (COMBLO) of a sum of eight consecutive counters with no amplification. The tested level is set at 4 GeV (44mV).

NCBIT:

This "bit" is really a logical "and" designed to identify showers. It takes the output of an NBIT and makes an additional length requirement by looking at the 4 most upstream TBITS of the counters in the NBIT sum and asking that two of them fire (see the trigger 2 diagram in Appendix H).

2.4.1.2 The Six Main Event Triggers

Six sets of criteria are formed. Each one is designed to test for a particular electronic signature in our detector. Put together, these six signatures should cover every type of event CCFR is interested in recording. As soon as any one of the sets of criteria are satisfied, the data acquisition system is triggered to store the buffered information in the ADCs and TDCs as an event.

There are only a few (fast) ways to distinguish neutrino events from the unwanted events.

- HORIZONTAL PENETRATION: The most typical cosmic rays enter the detector at a steep angle. We can remove many of these by requiring several consecutive counters to fire.

- ENERGY: Each neutrino event has a hadronic shower which deposits more energy than the typical cosmic ray.

- VETO: All neutrino triggers require no activity in the veto wall. This removes interactions from the berm, and low angle cosmic rays.

The six triggers are combinations of these requirements. The trigger system is efficient at filtering out typical cosmic rays and uncorrelated noise. However both large bursts of correlated noise and low-angle cosmic rays still get past the trigger criteria. These events must be "removed" from the data off-line. This is done in part by collecting events when there is no neutrino beam in order to determine how many unwanted events satisfy the trigger system criteria.

The six main triggers are detailed in Appendix H which contains design and logic diagrams.

2.4.2 Data Collection

The raw data collected in both runs of the experiment fill about 1000 open-reel tapes, comprising approximately 300 gigabytes of information. The number of events recorded according to trigger type is listed in Table 2.1.

Once written on tape, the data passed through several stages of off-line processing, which ultimately reduced it to data summary tape (DST) format. The raw data's first pass was through a process called stripping, which unpacked ADC pulse heights and subtracted their pedestal values, and otherwise rewrote the data in a modified format. The second-pass put the stripped data through a program called the cruncher, which did the bulk of the processing to extract the events' characteristics: pulse heights were converted to hadron energies, TDC times to hit positions. A pattern-recognition algorithm fit muon tracks to the hit positions, leading to a determination of the muon angle and energy. The final event observables—the hadron energy, the muon angles and energies, and secondary variables like x and y—were written to a DST. The DST file contains the basic set of data used for physics analysis.

Event reconstruction, writing DSTs, and the final physics results are all predicated on the ability to measure the absolute hadron shower and muon angles and energies, the parameters that define a charged-current deep inelastic scattering event. The next chapter describes the detector calibration: the process that determines the precise number of ADC counts that correspond to a given hadronic energy, and the precise bend of a muon's trajectory that corresponds to a given muon momentum.

Table 2.1: Triggers written to tape in E744 and E770. An event can satisfy more than one trigger.

Trigger Type	E744	E770
1	1740427	1981136
2	2267724	2915707
3	1611230	2001988
4	696664	806985
5	16447	64627
6	166682	1406410
Total	3235717	5095487

Differences in the rates from the two experiments can be accounted for by various small improvements or changes. For instance, E744 pre-scaled the trigger 6 rate. Analysis proved these events to be useful enough to gather without pre-scaling in the subsequent E770 run. Another example is the change in the vertex position between the two experiments. The E744 vertex was skewed due a beam related misalignment which was corrected in E770.

3 Calibration and Data Analysis

Neutrino and antineutrino deep inelastic scattering events are specified by three parameters: the energy of the outgoing muon E_μ, the angle of the muon θ_μ, and the total energy of the hadronic shower E_{HAD}. This Chapter describes how each of these three quantities are measured and calibrated.

3.1 Hadron Energy Measurement

When a neutrino scatters inelastically with a nucleon, the nucleon is broken apart and its constituents emerge in the form of hadrons, primarily pions, kaons, protons, and neutrons. In the detector, these hadrons interact producing a hadron shower that propagates until its energy is totally absorbed by the calorimeter. The shower propagates through active detector elements (the scintillation counters and drift chambers) and passive elements (primarily the steel plates). The fraction of shower energy deposited in the counters provides a sample of the total shower energy.

The energy deposited in any material by a high-energy particle is largely independent of particle type and energy, and is referred to as the minimum-ionizing energy. As each secondary particle passes through a scintillator, it deposits the same minimum-ionizing energy, and so by dividing the amount of energy measured in a single scintillator by the amount of minimum-ionizing energy, one measures the number of "minimum-ionizing particles," or MIPs. This is why the layers of scintillator in the detector are called scintillation "counters," they effectively count the number of particles passing through them.

Although the counters are of identical design, slight variations in their construction, the phototube gain, and the counter electronics cause their responses to vary. Therefore, each counter is calibrated separately. In practice the response of each counter is determined by a set of calibration coefficients and phototube gains, which provide the conversion between ADC counts and MIPs for each counter.

To turn the number of MIPs into hadron energy a test beam was run. The response of the detector to hadrons, electrons and muons of a given energy where recorded (each type recorded separately). From these data an overall energy calibration of 0.211 MIPs per *GeV* was determined.

3.1.1 Counter Gain Calibration

The muon energy loss distribution as measured for one of the counters is plotted in Figure 3.1. A muon's energy deposit provides the standard measure of minimum-ionizing energy. Muon energy loss is well-understood. It is described by a Landau distribution, with a pronounced peak due to ionization and a long high energy tail. The tail is due to stochastic energy losses from bremsstrahlung, pair production, and delta-ray production. Each counter's response is calibrated to the standard muon signal by analysis of the sample of Trigger 1 and Trigger 6 data. The muons in this sample are momentum-analyzed by the toroid spectrometer, and small muon-energy dependent corrections are also included in determining the counters' response.

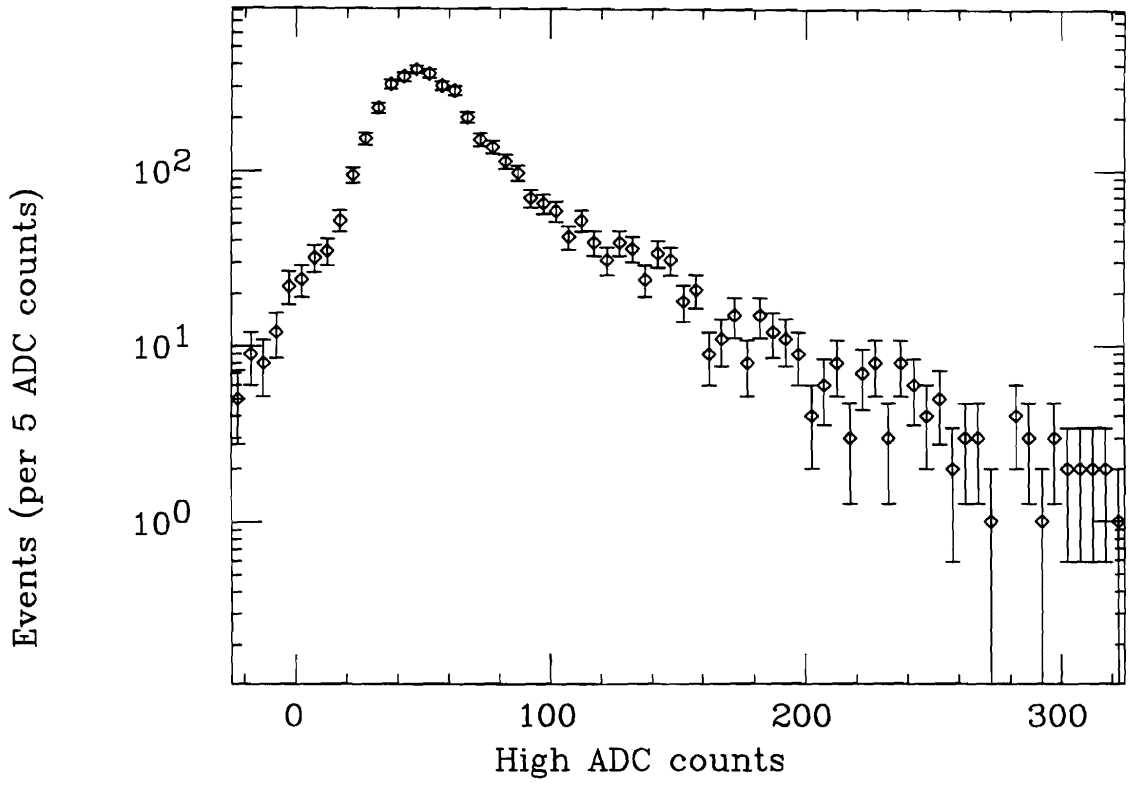

Figure 3.1: Muon energy loss distribution in a scintillation counter.

In order to find each counter's response to a minimum-ionizing particle, an iterative procedure called the "truncated mean" is used. First, the mean energy deposited by muons in a scintillation counter is measured in units of ADC counts. The distribution is truncated from 0.2 to 2.0 times this mean and a new mean is found. This process is repeated, each time returning to the original ADC count distribution, truncating from 0.2 to 2.0 around the new mean, until the mean converges. This procedure minimizes the effects of events in the tails that change the average behavior as a function of energy. The truncated mean of the distribution is taken to be one MIP in that counter and is denoted by $\Delta E_i\left(V_x, V_y, t\right)$, indicating that this mean depends on the counter i, the vertex position $\left(V_x, V_y\right)$, and the time t as measured by the SBITS (see section 2.4.1.1).

Muon energy loss is measured with the HI ADC channels, but the hadron energy measurement is made with the LO channels or the SUPERLO channels (if the LO channels are saturated). To convert the muon energy loss measured by the HIs to that measured by the LOs and the COMBLOs, a set of inter-channel calibration coefficients is used. The relationships between the channels for each counter in terms of the counter's calibration coefficients:

$$A_i^{COMBLO} = \sum_{j=1}^{4} a_{ij} A_{ij}^{LO} \,, \tag{3.1}$$

$$A_i^{HI} = \beta_i A_i^{COMBLO}, \tag{3.2}$$

where A_i refers to the response of counter i in a particular channel, β_i is each counter's HI-to-LO calibration coefficient, and a_{ij} are calibration coefficients for

each phototube j in counter i. The calibration coefficients are determined by minimizing the quantities

$$\sum_{events} \sum_{i=counters} \left(A_i^{COMBLO} - \sum_{j=1}^{4} a_{ij} A_{ij}^{LO} \right)^2 \tag{3.3}$$

and

$$\sum_{events} \sum_{i=counters} \left(A_i^{HI} - \beta_i A_i^{COMBLO} \right)^2 \tag{3.4}$$

and are determined to better than 1% because of good overlap in the dynamic range of the channels (small nonlinearities in the electronics were also measured and included). Typical values are $a \sim 0.8$ and $\beta \sim 12$.

Assuming no variation in response over time or position within a counter, the LO energy in MIPs for each counter is given by

$$\Delta E_i = \beta_i \sum_{j=1}^{4} a_{ij} A_{ij}^{LO} \, . \tag{3.5}$$

3.1.2 Map and Time Variation Corrections

A counter's energy response is not uniform over the active area nor does it stay constant with time. The counter response differs according to the position in the counter where the particle passed, due to the attenuation of light within the scintillator oil and wave-shifter bars and differences in phototube response. Counter response is also time-dependent, primarily because phototube gains tend to drift, and because of a slight degradation of the scintillator oil. Frequent measurements of

phototube gains were made to account for detector changes over time. Differences in detector response due to position are handled with map corrections. All counter measurements are corrected so that they can be interpreted as having occurred at t = 0 and $\left(V_x, V_y\right) = (0,0)$.

The map corrections are determined by dividing the active area of each counter into nine-by-nine inch squares, and measuring the counter's response to muons in each of these position bins separately. The value of the energy distribution for each square bin is determined using the truncated mean algorithm, and a bin-center correction is made because the event distribution and energy response varies within each bin. The final map correction is given by

$$R_i^{map}\left(V_x, V_y, 0\right) = \frac{\Delta E_i\left(V_x, V_y, t=0\right)}{\Delta E_i\left(0,0,t=0\right)}. \tag{3.6}$$

Figure 3.2 shows a counter map, which displays contours of the muon response relative to the center of the counter.

The time variations in counter response are measured at the center of a counter, where the event population is highest. To account for drift in phototube gains or changes within the counter themselves, the gain for each tube relative to the four in the counter is determined by the quantity

$$G_{ij}(0,0,t) = \frac{4a_{ij}(t)A_{ij}^{LO}(0,0,t)}{\sum_{k=1}^{4} a_{ik}(t)A_{ik}^{LO}(0,0,t)}. \tag{3.7}$$

Measurements of the relative phototube gains were made frequently (monthly). At the start of E744 and again at the start of E770, the phototube base voltages were adjusted to equalize the relative gains of a counter's four tubes. In this procedure, known as balancing, a 1 *mCi* ^{137}Cs source was positioned at the center of a counter and the voltage at each phototube base was set to make the tubes' anode currents equal to within ±25%. The muon data were used to better determine the relative gain throughout the running. From time to time during the run, counters that fell severely out of balance were readjusted with the source.

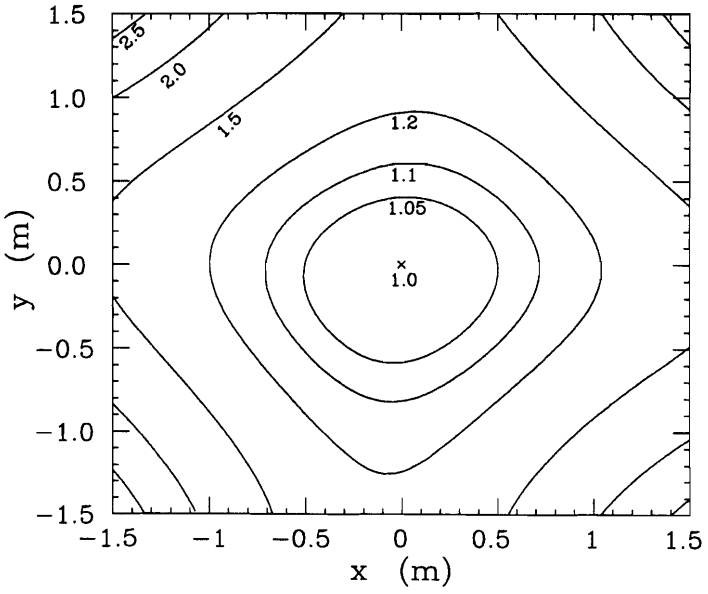

Figure 3.2: Contours of the relative muon response for counter 37.

Combining the map and time variations together, the energy loss in MIPs measured by a scintillation counter is given by

$$\Delta E_i = \frac{\beta_i(t)\sum_{j=1}^{4} A_{ij}^{LO}(t) G_j(0)/G_j(t)}{\Delta E_i(0,0,t) R_i\left(V_x, V_y, 0\right)}, \tag{3.8}$$

with all position and time-dependent corrections included. A small adjustment is made to assure that the counter response is the same for all counters.

3.1.3 Calorimeter Energy Calibration

The target calorimeter was calibrated with hadron test beams [Sak90]. These calibration runs took place before E744 in 1984, and in the middle and end of E770, at the end of 1987 and early 1988. The neutrino test west (NTW) beamline at Fermilab transported beams into the CCFR experimental hall (Lab E) and various target carts were moved into the test beam for calibration. The NTW beam contained secondary particles produced by the primary Tevatron proton beam, which were selected by charge and momentum. Pions were the dominant component of the test beam. For positively-charged test beams, the proton fraction was about 20% at 100 *GeV*, increased to about 50% at 300 *GeV*. The electron component was about 10% at 50 *GeV* and increased at lower momenta; the kaon component was about 5%, and the muon component was about one percent.

The total energy response of the calorimeter is obtained from runs where the test beam is centered on the target. Figure 3.3 plots $\langle E/p \rangle$ versus $\langle p \rangle$, where $\langle\ \rangle$ indicates the mean of a distribution from various test beam runs, where p is the

momentum of the test beam and E the total energy measured by the calorimeter in units of MIPs. $\langle E/p \rangle$ is constant to within 1% [Sak90] at 4.74 MIPs/GeV, indicating that the response of the calorimeter is linear to better than 1%. Furthermore, there is no difference in the response of the identical target carts at the 1% level and the calibration between the E744 and E770 calibration runs is different by 0.3%.

The calorimeter's resolution function for hadrons is Poisson-like [Sak90] and is parameterized by the function

$$f(x,\bar{x}) = \frac{\bar{x}^{x} e^{-\bar{x}}}{\Gamma(x+1)}, \tag{3.9}$$

where $x = E/s$, s is a scaling parameter, and $\bar{x}$ is the mean. The energy distributions of 25 and 200 GeV hadrons from the E770 test beam are shown in Figure 3.4. By fitting for s and $\bar{x}$, the values of $\sigma = s\sqrt{\bar{x}}$ and $\langle E \rangle = s\bar{x}$ give the fractional sampling resolution $\sigma/\langle E \rangle$. This resolution is characterized by the statistical fluctuations of the N particles sampled in the shower, therefore the resolution is dominated by sampling fluctuations.

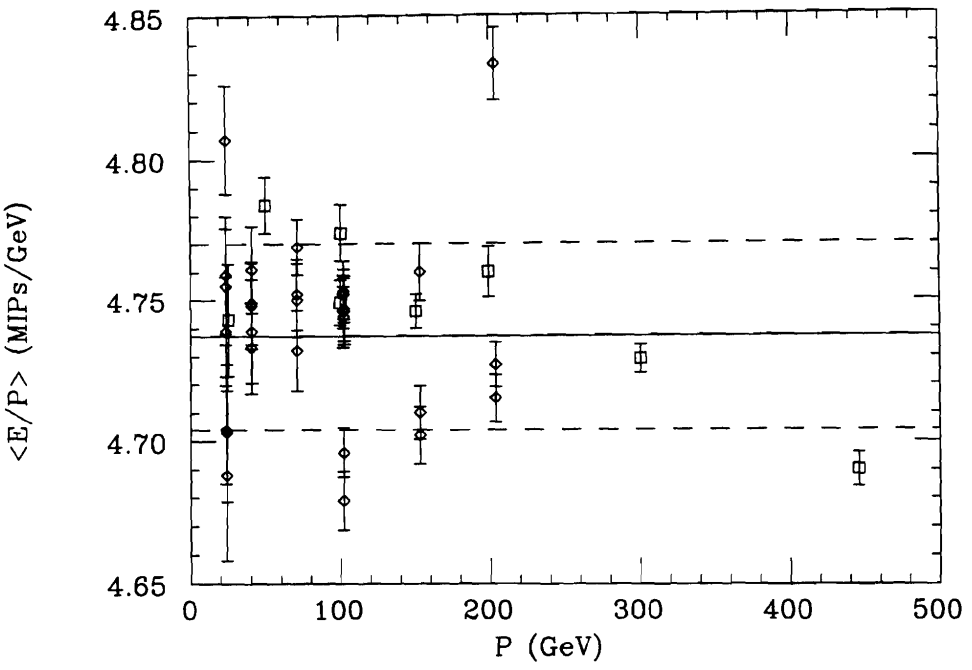

Figure 3.3: Energy response of the CCFR calorimeter, relating MIPs to *GeV*. Hadronic test beam data are for E744 (squares) and E770 (diamonds). The horizontal line is a weighted mean of the E770 points, 4.737 MIPs/*GeV*. The fractional rms dispersion about the mean for the E770 (E744) point is 0.7% (0.8%), and is shown for the E770 points by the dashed lines. The weighted mean of the E744 points is 4.724 MIPs/*GeV*.

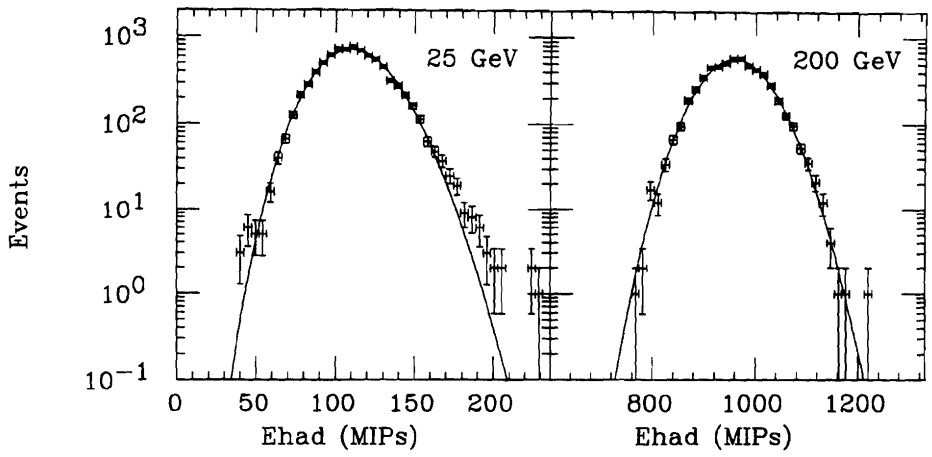

Figure 3.4: Energy distributions of 25 and 200 *GeV* hadrons from the 1987 calibration. The Poisson-like parameterizations of the resolution functions are shown by the solid curves.

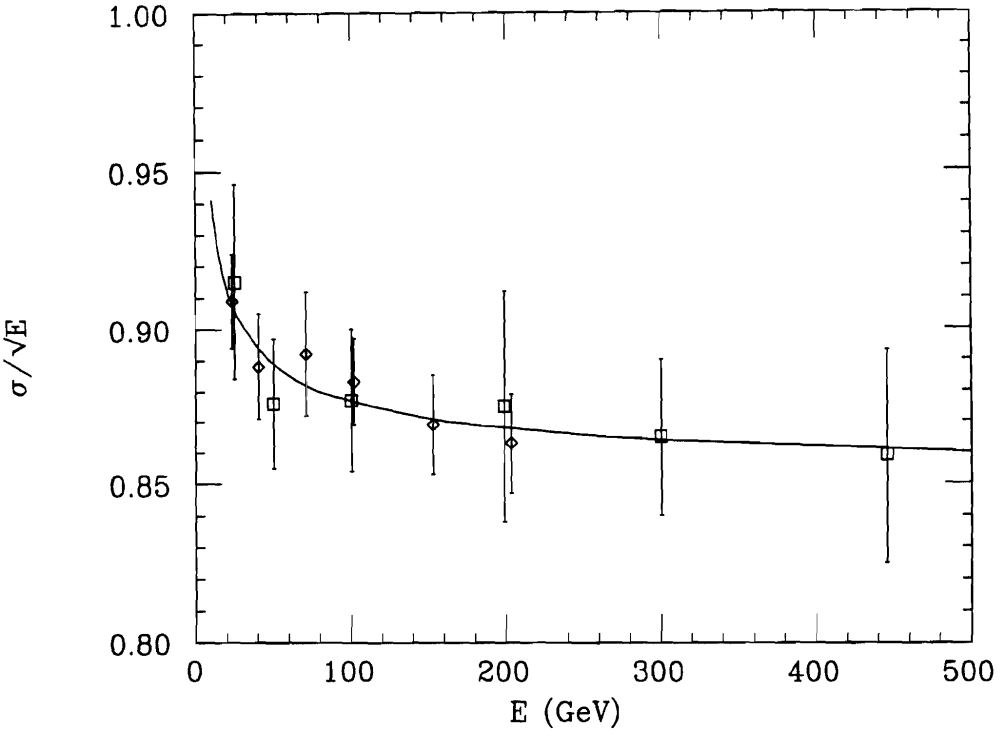

Figure 3.5: The hadron shower energy resolution of the CCFR calorimeter from 25 to 240 *GeV* test beam calibrations. The curve is the value of Equation 3.10.

From these data, the energy resolution is found to be

$$\frac{\sigma}{E} = \frac{0.847 \pm 0.015}{\sqrt{E}} + \frac{0.30 \pm 0.12}{E}, \tag{3.10}$$

where E is in GeV. The values of $\sigma/\sqrt{\langle E \rangle}$ are shown in Figure 3.5 for various test beam energies. The term proportional to $1/\sqrt{E}$ measures the sampling fluctuations, and the term proportional to $1/E$ is characteristic of detector-related noise.

The calorimeter response to electromagnetic showers was calibrated using the electron component of the 25 and 50 GeV test beams. The electromagnetic resolution was found to be $\sigma_e / E = 0.60/\sqrt{E}$.

As a final study of the calorimeter response, the *de/dx* calibration for range-out muons was determined using the E744 sample of neutrino-induced charged-current events in which the muons ranged out inside the calorimeter. Muons emerging far from the end of the hadron shower were selected in order to measure the response to muons alone. Using this sample, the muon energy in GeV, denoted by p, is determined by comparing the track length to entries in range-energy tables [Koi78]. The distribution of E/p for the range-out muons, where E is the total energy deposited by the muon in the counters, is shown in Figure 3.6. The resolution for these range-out muons is $\sigma_\mu / E = 0.17$.

The energy calibration of the CCFR calorimeter is summarized in Table 3.1, for hadronic showers (π), electromagnetic shower (e), and minimum-ionizing muons (μ). The errors given include both statistical and dominant systematic errors. As

shown in the Table, the calorimeter response to π's and e's is very close: the ratio of the electromagnetic to hadronic response of the calorimeter, denoted by e/π, is 1.1.

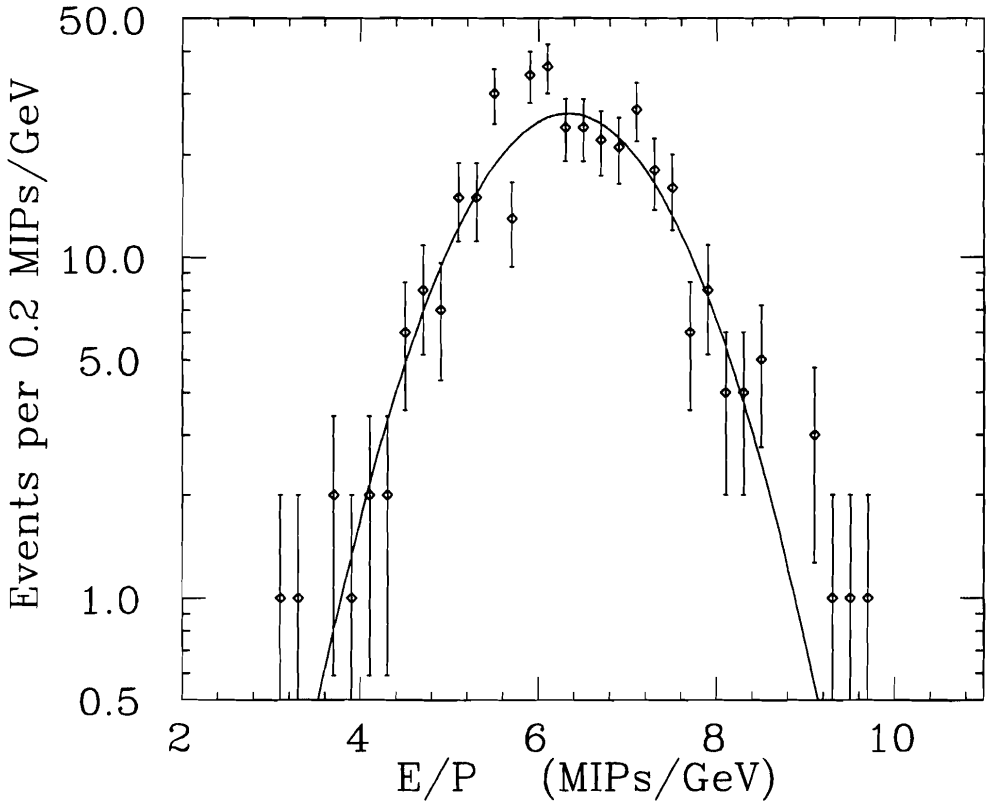

Figure 3.6: The E/p distribution for E744 range-out muons. E is the energy measured along the track length in the counters in *MIPs*; p is the muon energy in *GeV* obtained from the path length and the range-energy tables.

Table 3.1: CCFR calorimeter calibration constants.

Type of signal	calibration	σ/E
π	4.73 ± 0.02 MIPs/GeV	$0.847/\sqrt{E} + 0.30/E$
e	5.25 ± 0.10 MIPs/GeV	$0.60/\sqrt{E}$
μ	6.33 ± 0.17 MIPs/GeV	0.17

3.1.4 Hadron Energy Calculation

The detector region over which the counter response is summed in order to contain a hadronic shower (or electromagnetic shower) is rigorously defined. The origin of a shower, called *PLACE*, is the more upstream of the most upstream pair of counters than each containing more than 4 MIPs of energy. The shower end, called *SHEND*, is defined as the first counter downstream from *PLACE* that is followed by three consecutive counters with less than 4 MIPs. The total shower energy is defined as the sum of the energy measurement from all counters from *PLACE* to (*SHEND* – 5), so as to include the lowest energy particles at the end of a shower.

A determination of hadronic energy exclusive of muon energy deposition requires the subtraction of 1 MIP from each counter for each muon track in the event. This same muon energy loss (*RMIP)* in the shower region is added to the muon energy. Since the MIPs in the hadron shower region are interpreted as hadronic interactions in the calorimeter, the hadron energy calibration constant C_{HAD} =0.211 GeV/MIP is used in the calculation. Thus the hadron energy is given by:

$$EHAD = C_{HAD} \times \left(\frac{\beta_i(t) \sum_{j=1}^{4} A_{ij}^{LO}(t) G_j(0)/G_j(t)}{\Delta E_i(0,0,t) R_i\left(V_x, V_y, 0\right)} - RMIP \right), \qquad (3.11)$$

The MIPs are measured in the calorimeter, but *RMIP* is a function. Therefore, if a hadron shower stochastically deposits a small number of MIPs, the value of *EHAD* may be negative.

3.2 Muon Angle and Momentum Measurement

Muons can travel a long distance through matter. They are "penetrating" particles because they do not interact strongly and their large mass keeps them from quickly losing their energy through electromagnetic interactions. Hence their presence can be detected by a long trajectory in the target calorimeter and muon spectrometer. A tracking algorithm fits drift chamber hits and thus determines the muon's path. In the target, where there is no magnetic field, a muon approximately travels in a straight line. This allows the angle to be precisely measured. The bend of a muon's path in the toroid system provides a measurement of its momentum. Complicating both measurements, however, is the effect of multiple coulomb scattering (MCS)—a muon traversing a medium is deflected by many small angle scatters in the target and toroid steel. Due to MCS θ_μ and p_μ are correlated and must be determined together using an iterative procedure.

3.2.1 Muon Tracking Procedure

The z-position of the vertex V_z is assigned to be halfway between *PLACE* and the adjacent upstream counter. V_x and V_y are initially assigned by taking the centroid of the drift chamber hit positions within the hadron shower region. If a muon track is found, the x- and y- positions are revised by extrapolating the track to V_z.

At the start of the iterative track-fitting procedure, a line segment is chosen in the calorimeter to fit the hits in the eight most-downstream chambers. In the toroid spectrometer, line segments are fit to the hits in each set of five chambers following each toroid cart. A crude initial estimate of the muon momentum is made by using the track deflection $\Delta\theta_{bend}$ in the first toroid gap:

$$p_\mu = 0.3\langle B\rangle\rho, \tag{3.14}$$

where ρ is the track's radius of curvature and $\langle B\rangle$ is the mean magnetic field strength is kilogauss ($\langle B\rangle \approx 17\ kG$).

In the next iteration, the initial determination of p_μ is used to include MCS effects. A particle with momentum p_μ traversing a distance L_k in a material with radiation length X_0 will undergo MCS deflections with a distribution whose width is

$$\sigma_k = \frac{0.015}{p_\mu}\sqrt{L_k / X_0}\,. \tag{3.15}$$

The expected MCS width over each discrete track segment is used to form a χ^2 function, which is minimized to fit the track:

$$\chi^2 = \sum_i \sum_j \left(x_i - x_i^p\right) M_{ij}^{-1} \left(x_j - x_j^p\right), \tag{3.16}$$

where x_i are the measured chamber hit positions and x_i^p are the predicted track positions in the i-th plane. The full error matrix M_{ij} is defined by

$$M_{ij} = \left\langle \left(x_i - x_i^p\right)\left(x_j - x_j^p\right)\right\rangle = \sum_{k=1}^{i} \sigma_k^2 \left[\frac{L_k^2}{3} + \frac{L_k}{2}\left(z_{kj} + z_{ki}\right) + z_{kj} z_{ki}\right] + \sigma_0^2 \delta_{ij}, \tag{3.17}$$

where L_k is the distance in inches between the k-th and (k + 1)-st chamber planes and $z_{ki} = \sum_{m=k+1}^{i} L_m$ is the distance from the k-th to the i-th plane. The track fit through the toroid includes the full error matrix and the fit in the target omits the off-diagonal (z_{ki}) terms. The intrinsic drift chamber resolution is included with $\sigma_0 = 225\,\mu m$.

3.2.2 Muon Angle Measurement

The vertex angle is determined by fitting the track near the vertex at position V_z. However, the large number of hits near the vertex from particles in the hadron shower limits the tracking ability. As a result, the few chambers nearest the vertex are not used for tracking. The number of drift chambers nearest the vertex position that are omitted from tracking is known as the tracking vertex offset. A study of Trigger 1 (charged-current) events determined the magnitude of the offset as a function of hadron energy and track length [Rab92]. To include a chamber in the track fit, the probability for choosing a good hit had to be twice that of selecting a bad one. Using this criterion, the study found that events with $E_{HAD} < 25\ GeV$ require no offset, those with $25 < E_{HAD} < 50\ GeV$ should be offset by one chamber, and those with $E_{HAD} > 50\ GeV$ should be offset by two chambers. Including the E_{HAD} offset, hits in the six chambers closest to the vertex are fit to a line which determines the angle θ_μ with respect to the beam axis.

The resolution of the muon angle at the event vertex is limited by MCS effects and the hadron energy. MCS effects are most severe at low muon momenta, as seen from Equation 3.15, whereas large hadron energies lead to high hit multiplicities that make tracking near the vertex difficult. The angular resolution was determined by studying the Trigger 6 sample of stiff muon tracks ($75 < \theta_\mu < 200\ GeV$) in which the

track angle determined by upstream and downstream track segments was compared on either side of a simulated "vertex" chosen at the center of the track. The angular resolution was found to be [Rab92]:

$$\sigma_\theta = a + \frac{b}{P_\mu}(\text{mrad}), \tag{3.18}$$

with parameters a and b given in Table 3.2

Table 3.2: Muon Angular Resolution.

Track Length	$E_{HAD} < 25GeV$		$25GeV < E_{HAD} < 50GeV$		$E_{HAD} > 50GeV$	
(chambers)	a	b	a	b	a	b
4	0.535	35.4	0.547	46.0	0.407	75.0
5	0.366	49.5	0.393	57.3	0.343	77.8
6	0.294	56.6	0.361	59.4	0.260	84.9
7	0.235	61.5	0.337	62.2	0.235	87.0
8	0.235	61.5	0.337	65.8	0.235	87.7

Since the muon angle measurement depends on the magnitude of the muon momentum, the θ_μ measurement procedure is repeated, using the more precise measurement of p_μ from fitting the muon track through the toroidal spectrometer.

3.2.3 Muon Momentum Measurement

The muon momentum measurement required a detailed map of the muon spectrometer's toroidal magnetic field. Such a map was prepared from Hall probe measurements of the field strength at numerous points along the z-x plane of the magnets and from measurement of the current in the magnet windings, up to a single

overall normalization, N_{field}. The value of N_{field} was determined using momentum-analyzed muon test beams.

The muon momentum measurement is made via the above iterative procedure, using the same algorithm used to track the muon in the target. Using the initial determination of the muon angle and position at the front face of the spectrometer, the predicted muon trajectory is extrapolated through the steel of the magnets in 4 *in* steps, and the energy loss due to ionization is accounted for in each step. The predicted muon track is compared to the hits in the drift chambers located between the toroids, and a χ^2 function comparing the predicted and measured hit positions, Equation 3.16, is minimized by varying the momentum. After each new minimization the full error matrix, Equation 3.17, is recalculated. This procedure continues until the momentum differs by less than 0.5% from the previous iteration.

The resolution of the muon momentum measurement is limited by the effects of multiple Coulomb scattering in the solid-steel toroids. The resolution can therefore be simply estimated by considering a track that traverses the entire spectrometer, or 500 *cm* of steel. Having received a 2.4 *GeV* transverse momentum kick, the track is magnetically deflected by

$$\theta_{bend} = \frac{p_{\perp}}{p_{\mu}} = \frac{2.4}{p_{\mu}}. \tag{3.19}$$

The typical sigma for an angular deflection of this track due to MCS is

$$\sigma_{\theta_{mcs}} = \frac{0.015}{p_{\mu}}\sqrt{500/1.76} = \frac{0.25}{p_{\mu}}. \tag{3.20}$$

Therefore the spectrometer resolution is estimated by

$$\frac{\sigma}{p} = \frac{\sigma_{\theta_{mcs}}}{\theta_{bend}} \approx 10\%, \tag{3.21}$$

and should be independent of momentum.

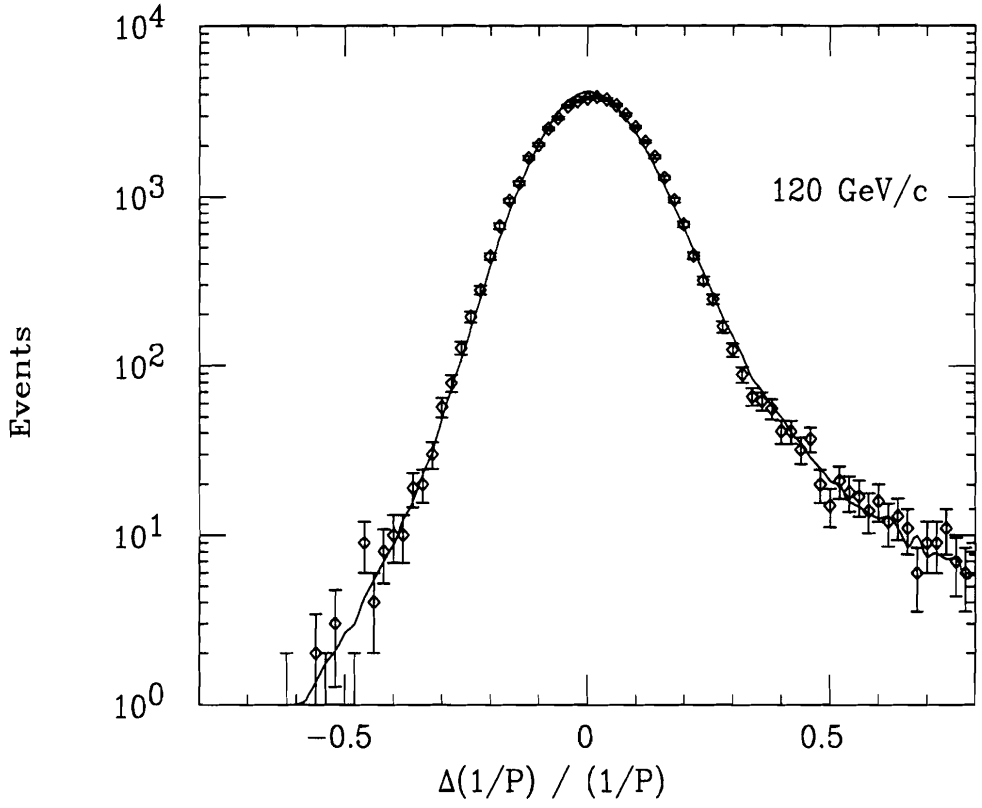

Figure 3.7: Muon momentum resolution function for 120 *GeV* muons. The points are measurements of test beam muons, the solid line is an independent Monte Carlo prediction. The tail of the negative side is due to hard single scatters and the tail of the positive side is due to catastrophic energy losses.

The spectrometer resolution was measured using a 120 *GeV* muon test beam. Figure 3.7 shows the experimental resolution function obtained. The central region is well approximated by a Gaussian distribution with an rms width of 10.1%, as expected.

3.2.4 Muon Energy Calculation

The toroid fit determines the muon momentum at the start of the spectrometer, *EMUFF* (meaning the muon energy at the front face of the toroid). The muon momentum at the event vertex is determined by adding the amount of energy the muon lost as it traversed the target calorimeter, E_{μ}^{loss}, to the toroid momentum measurement. As it traverses the target, a muon loses energy primarily through ionization, and typically deposits one MIP of energy in each counter. Occasionally, a high-energy muon may deposit a larger amount of energy, due to processes such as pair production and bremsstrahlung, which are known as catastrophic losses.

The energy lost by the muon outside the hadron shower region is determined by looking at the number of MIPs deposited in each counter from (*SHEND* – 6) to counter 1. If the amount of energy deposited in a counter is 3 MIPs or less, the entire amount is attributed to muon ionization losses and multiplied by the muon-ionization-loss calibration constant of C_{μ} = 0.158 *GeV*/MIP (see Table 3.1). If the amount of counter energy is more than 3 MIPs, the first 3 MIPs attributed to muon ionization and the excess over 3 MIPs is attributed to catastrophic loss, which is multiplied by the electromagnetic calibration constant of C_e = 0.190 *GeV*/MIP. Hence the energy loss of a muon outside the hadron shower is given by

$$ELOSS = \sum_{i=SHEND-6}^{1} \left[MIN(3, \mathrm{MIP}_i) \times C_{\mu} + MAX(0, \mathrm{MIP}_i - 3) \times C_e \right]. \qquad (3.22)$$

Comparisons with the muon energy loss seen by the data versus that predicted by a Monte Carlo simulation indicated that the calorimeter had a slightly different muon energy calibration constant during the E744 and E770 runs. The most likely explanation for this is an error in the ADC pedestal subtraction for the HI channels. The value of C_μ for E770 was increased by 0.5% to cause the energy-loss distributions for the two experiments and the Monte Carlo simulation to agree.

Inside the hadron shower region, the energy loss of the muon cannot be directly observed. Instead, an approximation to the average restricted loss is used:

$$RMIP = \sum_{i=PLACE}^{SHEND-5} \left(.9315 + .02418 \ln E_i^{EST}\right) \Big/ \cos\theta_\mu , \tag{3.23}$$

where E_i^{EST}, the estimated energy in *GeV* of the muon at counter *i*, is given by:

$$E_i^{EST} = EMUFF + 0.15952 \times SHEND, \tag{3.24}$$

and the energy loss of muon for each counter is given by 0.15952 *GeV*/counter. Note that while E_i^{EST} is measured in *GeV*, the units of *RMIP* are MIPs. Equation 3.23 parameterizes the characteristic "relativistic rise" of the ionization loss, making *RMIP* a weak function of the particle energy.

Hence the energy of the muon is taken to be the muon momentum measured at the front face of the toroid, plus the measured energy loss outside the hadron shower, plus the estimated restricted energy loss inside the hadron shower:

$$EMU = EMUFF + ELOSS + C_\mu \times RMIP. \tag{3.25}$$

Although finding the muon energy in the shower involves an approximation, the procedure is completely mimicked in the MC including all stochastic and non-stochastic processes.

3.3 Analysis Cuts

After reconstruction, the data events are cut according to criteria that ensure good efficiency and small acceptance corrections. The criteria are grouped together into sets defined in the following sub-sections.

3.3.1 Fiducial-Volume Cuts

The following cuts ensure that the event takes place within the active area of the detector. The one exception is the dimuon cut, which is not strictly a "fiducial-volume" cut, but is included in this set to correspond to the Monte Carlo procedure for eliminating the dimuon cross-section from the event sample.

- *RUN/IGATE/NSTIME:* This cut eliminates runs for which the quality of the neutrino beam was poor or the detector was not functioning properly. It also eliminates all events detected during the non-neutrino portions of the accelerator cycle (see Section 2.1).

- *NO DIMUONS:* This cut eliminates events with a second track that either enters the toroid spectrometer, or penetrates more than 19 counters. The latter condition implies that the second particle had an energy greater than 3 *GeV*. The reason for this cut is the neutrino species of a charged-current event is determined from the higher-energy muon. For low values of x, especially at high y, there is a

significant contamination of neutrino dimuon events in the anti-neutrino event sample, and this would affect the low-x value of xF_3. Also, if the non-leading muon enters the toroid but the primary muon does not, the kinematics of the event will not be properly reconstructed. Hence the potential dimuon events are removed from the data sample. These events are also removed from the Monte Carlo sample.

- $20 < PLACE < 80$: This cut assures good longitudinal containment of the hadron shower in the calorimeter.

- $-50 < V_x < 50$ *in*, $-50 < V_y < 50$ *in*: This cut assures good transverse containment of the hadron shower in the calorimeter.

3.3.2 Geometric Cuts

The following cuts assure good momentum resolution in the toroid spectrometer.

- *Trigger 1:* This cut assures that a muon entered the spectrometer.

- *Target Track:* Enough hits must be detected in the target drift chambers for a muon track to be identified in the calorimeter. This assures that the muon angle can be measured in the target.

- *Toroid Containment:* The muon track in the target is extrapolated from the event vertex through the toroid, without assuming any deflection due to multiple scattering or the magnetic field. The extrapolated track must have a radius < 64 *in.* at the front face of the toroid, and must have a radius at the T2 counter of less than 55 *in.*

- *Toroid Track:* Enough hits must be detected in the toroid drift chambers for a muon track to be identified in the toroid.

- *Good Fit:* The muon track must be fit in the toroid.

- *Fit Quality:* The χ^2/dof of the fit must be less than 10.

3.3.3 Cross-section Cuts

The following cuts were developed for use in the cross-section analysis.

- $\theta_\mu < 150 mr$ and $R_{FF} > 6$ *in.*— The muon angle cut assures good acceptance of the muon track as it passes through the muon spectrometer. R_{FF} is the radius of the muon track at the front face of toroid and this radial cut assures that the muon does not pass through the hole in the center of the spectrometer.

- $E_\mu > 15 GeV$ — 15 GeV is the lower limit of the acceptance of the muon spectrometer.

3.3.4 Structure-Function Cuts

The following additional cuts are applied for the structure-function analysis described in Chapter 6.

- $E_{HAD} > 10 GeV$ — This lower limit on E_{HAD} was picked to minimize the correlations between the flux and structure-function data sample (see Chapter 5).

- $Q^2 > 1 GeV^2$ — This eliminates the quasi-elastic events from the data sample, which are not modeled in our Monte Carlo.

- $30 GeV < E_\nu < 360 GeV$ — The lower limit of 30 GeV was chosen because below that energy a large acceptance correction is required. The upper limit of 360 GeV was chosen because above that energy the error on the Monte-Carlo smearing corrections becomes greater than 10%; also, the number of anti-neutrino events above 360 GeV is small and hence would not make a significant impact on the analysis.

	E744				E770			
Type / Focus	ν / μ^-	ν / μ^+	$\bar{\nu} / \mu^-$	$\bar{\nu} / \mu^+$	ν / μ^-	ν / μ^+	$\bar{\nu} / \mu^-$	$\bar{\nu} / \mu^+$
Raw Events	1105779	1245383	121077	161835	1924218	1874926	247233	291201
run/gate/time	1086466	1222146	117810	156712	1902484	1854792	243981	286897
PLACE	786975	896006	73760	156712	1121063	1050494	106411	122056
Vertex	644404	736608	63183	78964	911043	856865	93164	104937
Trigger 1	355863	400606	62418	77469	481959	470789	92630	103833
Target Track	355271	400076	62395	77430	481086	470789	92598	103714
Toroid Contain.	304136	352426	57778	69173	423590	402606	85632	92609
Toroid Track	302682	346125	57778	69173	416388	400463	85632	92609
Good Fit	302605	345982	57739	69062	416217	400330	85572	92483
Fit Quality	302204	345425	57616	68873	415382	399801	85400	92199
$\theta_\mu < 150 mr$	298585	342615	57468	68606	415382	399801	85400	92199
Toroid hole	298560	342599	56464	68600	412065	395036	85201	91863
$15 > E_\mu > 600$	292332	337052	56426	66946	405774	386986	83714	89689
$E_\mu^{FF} > 3 GeV$	292171	336975	56409	66907	405757	386861	83709	89633
Shower Contain	291899	336573	56387	66865	405339	386459	83673	89607
$E_{HAD} > 10$	240154	276449	38790	45996	334629	319652	56725	60982
$Q^2 > 1 GeV^2$	232072	267192	36329	43079	323641	309115	53072	57052
$30 > E_\nu > 600$	231649	266731	36269	42997	323083	308555	52977	56942
No Dimuons	228704	263228	35640	42235	318936	304593	52115	56053

Table 3.3: Effect of cuts on data counts.

4 The Monte Carlo

The Monte Carlo is a computer program that generates fake events by using the theoretical models we wish to test combined with a simulation of the detector characteristics. The underlying physics in the model is varied until the simulated event distributions fit the real data event distributions as well as possible.

The previous CCFR SF measurements presented by William Seligman [Sel97] were made with a MC called the "fast" charged-current Monte Carlo. A new MC called NUMONTE was used for this analysis. For charged-current analyses, the NUMONTE Monte Carlo has some improvements over the fast MC. Most notably, NUMONTE is more modular and easier to run. The following section lists a few of the other differences:

4.1 NUMONTE versus the Fast MC

- NUMONTE has full tracking of the muon through the toroid. The Fast MC did not. This makes it possible for NUMONTE to do the muon smearing strictly from the 120 GeV test beam, scaling the width of p_{smear}/p_{μ} according to how far the muon made it through the toroid. The old MC did muon energy smearing according to a set of histograms that were produced by an even earlier MC (the "full" MC). This method was developed as an improvement, but no substantive changes resulted as it was put into practice.

- The new MC breaks the cross section down into separate contributions which can be chosen according to the study being done.

The individual differential cross section contributions come from: a zeroeth-order calculation, a longitudinal contribution, a lepton mass correction, separate strange, charm & charm-sea contributions, a VDM calculation, elastic & resonant contributions, a target mass correction, an exclusive charm calculation, charm-VDM, isoscalar and propagator corrections. This flexibility makes the new MC more versatile. It can be used for NC studies, CC studies, dimuon studies or even cosmic ray studies. Certain contributions such as charm production can be calculated to NLO. The routine also has an interface to other standard structure function sets through the PDFLIB package for LO and NLO parton distributions. PDFLIB is a central repository of parton distribution functions maintained by CERN.

- The new MC has options to also generate fully reconstructed dimuon events.

4.2 Event Generation

To begin, the Monte Carlo generates "true" kinematic variables. They are either randomly assigned or determined from the cross section and flux. The MC then manipulates the "true" variables to reflect the effects of detector geometry, detector resolution, kinematic cuts, and various physical effects such as the cross section suppression due to a massive charm quark.

The MC event generation will depend on the beam kinematics and detector settings for the experiment. This analysis uses data from two different experiments, E770 and E744. The two experiments had different fluxes and slightly different detector

calibrations. Each experiment ran with a beam composed of neutrinos and anti-neutrinos which have different flux spectra. Each experiment was run with two different toroid field polarizations. The muon spectrometer was set to focus either positively-charged muons (optimized for anti-neutrino events) or negatively-charged muons (optimized for neutrino events). These settings have different acceptance corrections. Hence events are divided into sets with different flux and different spectrometer settings. Each of the eight different categories (two experiments × two neutrino species × two toroid polarities) has separate Monte-Carlo corrections. The details of each individual correction are described below.

First, the method of generating Monte Carlo events is discussed. The procedure for generating a charged-current event in the structure-function Monte Carlo is as follows:

- Randomly choose the neutrino type: neutrino vs. anti-neutrino, for toroid focusing vs. de-focusing negatively-charged muons. The ratio of different neutrino types generated by the Monte Carlo is approximately the same as that of the data. Since the ratio of $\bar{\nu}$-induced to ν-induced Monte Carlo events is renormalized to agree with the data, there is no need for this ratio to be accurate in the Monte Carlo.

- Pick *ENEUG*, the generated neutrino energy, from the input flux distribution Φ_{EST}. Throw *VERTX* and *VERTY*, the (x,y) vertex of the event, from the vertex flux distribution $\Phi(E_i, V_x, V_y)$.

- From estimated parton distributions q_{EST} and the physics model defined in Section 4.5 which uses the SF parameterization, we throw for *XG* (the generated

x) and *YG* (the generated y).† From *ENEUG, XG,* and *YG,* the variables *EHADG* (the generated hadron energy), *EMUG* (the generated muon energy), and *THETAG* (the generated muon angle) are calculated. *PHIG* (the azimuthal angle of the muon) is thrown uniformly between 0 and 2π.

- *PLACE* is chosen uniformly along the z-axis of the calorimeter. The hadron shower length *(PLACE–SHEND*+5) is thrown randomly from a set of *EHADG*-dependent shower-length distributions determined from a study of the data [Sel97].

- The muon track is propagated through the calorimeter using a full energy-loss algorithm. Simulated energy losses for muons with more than 5 *GeV* at the vertex include ionization, bremsstrahlung, pair production, and δ-ray production. Muons with less than 5 *GeV* have their ionization losses simulated according to range-energy tables. The multiple Coulomb scattering of the muon is modeled as well.

- For each drift chamber through which the muon passed, the Monte Carlo keeps track of the restricted energy loss (ionization), *RESLOS*, and the catastrophic energy loss (bremsstrahlung, pair production, and gamma rays), *CATLOS*.

---

† XG and YG are generated randomly using the rejection method [Pre92] from the $d^2\sigma(E,x,y)/dx\,dy$ distribution implied by the parton distribution q_{EST}. If *XG* and *YG* are rejected, the event-generation process begins again with the random throwing of *ENEUG* in the previous step.

- When the modeled track reaches the front face of the toroid spectrometer, the total *dE/dx* loss of the muon (*RESLOS* + *CATLOS*) is subtracted from *EMUG*, giving *EMUFFG*. The position of the muon at this point is given by *VXFF* and *VYFF*.

4.3 Resolution Smearing

As detailed in the previous section, the Monte Carlo generates the quantities *ENEUG, EHADG, EMUG, THETAG, PHIG, RESLOS, CATLOS, EMUFFG, VERTX, VERTY, VXFF,* and *VYFF*. The first eight variables in this list are smeared to simulate detector resolution effects as described below. The position resolution of the muon track is less than 0.1 *in* (see Chapter 2), small enough that the smearing of the last four variables is not significant for the charged-current analysis.

EHADG, the generated hadron energy, is smeared according to the resolution function given by Equation 3.10. *THETAG* and *PHIG*, the generated muon angle parameters, are projected onto the *x*- and *y*- axes and separately smeared according to the angular resolution given by Equation 3.18.

As described in Section 3.2.2, the muon momentum resolution function for the toroid spectrometer was measured with a test beam at E_μ = 120 *GeV*. This resolution function is extended to other energies by using a scaling algorithm that considers how far the muon traveled through the toroid.

The fractional muon momentum measurement error

$$\mathcal{F} \equiv \frac{1/p_{meas} - 1/p_{gen}}{1/p_{gen}} = \frac{p_{gen}}{p_{meas}} - 1 \qquad (4.1)$$

was histogrammed in bins of p_{gen} after cross-section cuts were applied. In the structure-function Monte Carlo, these resolution histograms were used to smear the generated muon momentum *EMUFFG* to give *EMUFF*.

4.4 Muon Energy Loss

As described above, the restricted energy loss (due to ionization) and the catastrophic energy loss (due to bremsstrahlung, pair production, and δ-ray production) is calculated for the muon as it passes from one drift chamber to the next in the calorimeter. This energy loss must be interpreted in the same way by both the data analysis and the Monte Carlo. The following transformations to *RESLOS* and *CATLOS* assure that this is the case.

• The sum (*RESLOS* + *CATLOS*) is smeared according to an electromagnetic energy resolution function determined in the test beam analysis [Sak90].

• Inside the region of the hadron shower (between *PLACE* and *SHEND*–5), the energy loss is multiplied by the ratio 0.211/0.158, the ratio of the hadronic to the muonic *MIPs/GeV* (see Section 3.1.3). This is done because, in the data analysis, all *MIPs* seen in the hadron shower region are interpreted as being hadronic. The sum of the smeared muonic energy loss in the hadron shower is thus given by:

$$ELOSSH = \frac{0.211}{0.158} \times \sum_{i=PLACE}^{SHEND-5} (RESLOS + CATLOS)_i^{smeared} . \qquad (4.2)$$

• Outside the region of the hadron shower (between *SHEND–6* and counter 1), the energy loss is interpreted in the same way as in the data: the portion of the energy loss less than 3 *MIPs* is multiplied by the muon calibration constant, while the

portion of the energy loss greater than 3 *MIPs* is multiplied by the electromagnetic calibration constant,

$$ELOSS = \sum_{i=SHEND-6}^{1} \left[\begin{array}{l} MIN(3,(RESLOS + CATLOS)_i / 0.158) \times 0.158 \\ + MAX(0,((RESLOS + CATLOS)_i / 0.158) - 3) \times 0.190 \end{array} \right]. \tag{4.3}$$

Therefore, the reconstructed muon energy from the Monte Carlo is given by

$$EMU^{MC}_{reconstructed} = EMUFF + ELOSS + RMIP, \tag{4.4}$$

and the reconstructed hadron energy is given by

$$EHAD^{MC}_{reconstructed} = EHADG_{smeared} + ELOSSH - \left(RMIP \times \frac{0.211}{0.158} \right), \tag{4.5}$$

where *RMIP* is defined by Equation 3.23. Note that *RMIP* in Equation 4.5 must be multiplied by the ratio of the hadronic to muonic calibration constants, because in the hadron shower region the *MIPs* are interpreted hadronically in the data.

Appendix H contains the Figures that compare the distributions of kinematic quantities observed in the data and simulated by the Monte Carlo after structure-function cuts.

4.5 The Physical Cross-section

The physical cross-section is based on the following equation which was derived in Chapter 1:

$$\frac{d^2\sigma^{(-)}_{\nu}}{dx\,dy} = \frac{G_F^2 ME}{\pi}\left[\left(1 - y - \frac{Mxy}{2E} + \frac{y^2}{2}\frac{1+\frac{4M^2x^2}{Q^2}}{1+R(x,Q^2)}\right)F_2^{(-)\nu} \pm y\left(1-\frac{y^2}{2}\right)\nu F_3^{(-)\nu}\right]. \tag{4.1}$$

The cross section is expressed in terms of the 3 SFs which are themselves functions of x and Q^2: $F_2(x,Q^2)$, $R(x,Q^2)$, and $xF_3(x,Q^2)$. This is called the "bare" cross section. Using it to generate the MC events requires values of the SF which we ultimately want to measure, so the SF measurement process is an iterative one. This iterative procedure is fully discussed in Chapter 5. The initial generation of MC events uses a parameterization that represents the SF measurements of the previous iteration. This parameterization is discussed in section 5.3.

Various physical effects must be applied to the bare cross-sections in order to accurately model the differential cross-sections for ν-N interactions in our iron-scintillator detector, as detailed in the following sections.

4.5.1 Isoscalar Correction

The calorimeter used in this experiment does not consist solely of isoscalar nuclei; it contains about 5.67% more neutrons than protons averaged over the entire fiducial volume [Kin94]. The effect of such an asymmetry on the differential cross-sections can be described by the parameter

$$v_f = \frac{N-Z}{A} = 0.0567, \tag{4.6}$$

where N, Z, and A are the number of neutrons, protons, and nucleons, respectively. The effective quark momentum density "seen" by neutrinos interacting in the calorimeter is then given by

$$\begin{aligned} xq^{\nu} &= 2\left\{\frac{Z}{A}\left(xd^{p}+xs^{p}\right)+\frac{A-Z}{A}\left(xd^{n}+xs^{n}\right)\right\} \\ &= 2\left\{\frac{Z}{A}(xd+xs)+\frac{A-Z}{A}(xu+xs)\right\} \\ &= \left(1-v_f\right)xd_v+\left(1+v_f\right)xu_v+xd_s+xs \\ &= \left(1-v_f\right)xd_v+\left(1+v_f\right)xu_v+\frac{1+\kappa}{2+\kappa}xS \end{aligned} \tag{4.7}$$

and the effective anti-quark density is

$$\begin{aligned} x\bar{q}^{\nu} &= 2\left\{\frac{Z}{A}x\bar{u}^{p}+\frac{A-Z}{A}x\bar{u}^{n}\right\} \\ &= 2\left\{\frac{Z}{A}x\bar{u}+\frac{A-Z}{A}x\bar{u}\right\} \\ &= \frac{1}{2+\kappa}xS \end{aligned} \tag{4.8}$$

To derive Equations 4.7 and 4.8, we have made use of isospin conservation for the strong interaction, which leads to the relations $u^{p}=d^{n}$ and $u^{n}=d^{p}$. We also assume that $\bar{u}^{p}=\bar{u}^{n}$ and $\bar{d}^{p}=\bar{d}^{n}$. The effective momentum densities seen by anti-neutrinos are similarly given by

$$xq^{\bar{\nu}} = \left(1+v_f\right)xd_v+\left(1-v_f\right)xu_v+\frac{1}{2+\kappa}xS, \tag{4.9}$$

$$x\bar{q}^{\bar{\nu}} = \frac{1+\kappa}{2+\kappa}xS. \tag{4.10}$$

The Monte Carlo has a cross section generating FORTRAN routine called SIGMCQ. A flag can be set when calling SIGMCQ which causes the routine to calculate the isoscalar version $\sigma(v_f = 0)$ or the iron version $\sigma(v_f = 5.67\%)$ of the cross section. Each theory event is adjusted for the non-isoscalarity of the CCFR target by multiplying the event weight by a ratio of these two cross sections (see section 6.1.1).

4.5.2 Radiative Correction

Radiative corrections to the total cross-section were calculated using the prescription of Bardin [Bar86]. The Bardin calculation includes the QED corrections involving the outgoing muon radiating a photon (see Figure 4.1) and also includes the quark leg of the diagram, including interaction between the outgoing muon and the quark (see Figure 4.2).

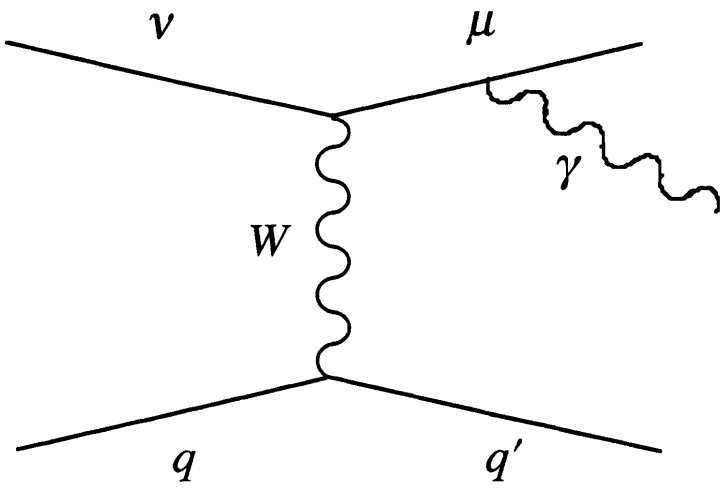

Figure 4.1: Radiative-correction diagram from the muon leg.

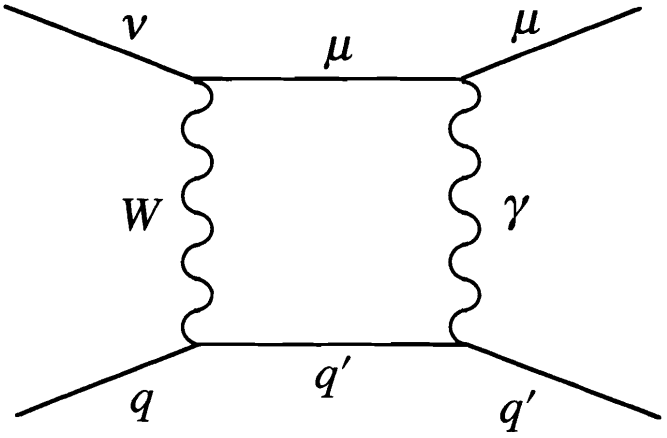

Figure 4.2: Radiative-correction diagram including the quark leg.

The Bardin calculation is too time-consuming to calculate on an event-by-event basis. Instead, tables of corrections were prepared for a range of values of E_ν, x, and y using an approximate differential cross section that was consistent with the data. The correction for a given bin was derived from the table by linear interpolation.

4.5.3 Charm Production Threshold

The slow-rescaling model [Bar76, Geo76] is used to account for the effects of charm production with a charm quark mass, m_c. In this model the normal scaling variable x

no longer represents the momentum fraction carried by the struck quark. Instead, the momentum fraction, ξ, is given by:

$$\xi = x\left(1 - \frac{m_c^2}{Q^2}\right). \tag{4.11}$$

The inclusive cross-sections are modeled as the sum of two semi-inclusive cross-sections: charm-producing (cp) and non-charm-producing (ncp) pieces. Correspondingly, the effective momentum densities were split into charm-producing and non-charm-producing pieces:

$$xq_{ncp}^{\nu} = \left(\left(1 - v_f\right)xd_v + \left(1 + v_f\right)xu_v + \frac{xS}{2+\kappa}\right)\cos^2\theta_c + \frac{\kappa}{2+\kappa}xS_S\sin^2\theta_c \tag{4.12}$$

$$xq_{cp}^{\nu} = \left(\left(1 - v_f\right)xd_v + \left(1 + v_f\right)xu_v + \frac{xS}{2+\kappa}\right)\sin^2\theta_c + \frac{\kappa}{2+\kappa}xS_S\cos^2\theta_c \tag{4.13}$$

$$x\bar{q}_{ncp}^{\nu} = \frac{1}{2+\kappa}xS \tag{4.14}$$

$$x\bar{q}_{cp}^{\nu} = 0 \tag{4.15}$$

$$xq_{ncp}^{\bar{\nu}} = \left(1 + v_f\right)xd_v + \left(1 - v_f\right)xu_v + \frac{xS}{2+\kappa} \tag{4.16}$$

$$xq_{cp}^{\bar{\nu}} = 0 \tag{4.17}$$

$$x\bar{q}_{ncp}^{\bar{\nu}} = \frac{1}{2+\kappa}xS\cos^2\theta_c + \frac{\kappa}{2+\kappa}xS_S\sin^2\theta_c \tag{4.18}$$

$$x\bar{q}_{cp}^{\bar{\nu}} = \frac{1}{2+\kappa}xS\sin^2\theta_c + \frac{\kappa}{2+\kappa}xS_S\cos^2\theta_c \tag{4.19}$$

where *cp* (*ncp*) indicates charm-producing (non-charm-producing) and θ_c = 13.2° is the Cabibbo angle and $m_c = 1.31\ GeV$ [Rab93].

Concentrating now on the charm-producing cross-sections, note that the transformation $x \rightarrow \xi$ preserves the differential area

$$\left|\frac{\partial(\xi,y)}{\partial(x,y)}\right| = 1. \tag{4.20}$$

Therefore, the charm-producing cross-section in the ξ-variable can be obtained by the following transformations:

$$2x\mathcal{F}_1^{\nu,\bar{\nu}cp}(x) \rightarrow \frac{x}{\xi} 2\xi\mathcal{F}_1^{\nu,\bar{\nu}cp}(\xi)\theta(1-\xi), \tag{4.21}$$

$$\mathcal{F}_2^{\nu,\bar{\nu}cp}(x) \rightarrow \mathcal{F}_2^{\nu,\bar{\nu}cp}(\xi)\theta(1-\xi), \tag{4.22}$$

$$x\mathcal{F}_3^{\nu,\bar{\nu}cp}(x) \rightarrow \frac{x}{\xi}\xi\mathcal{F}_3^{\nu,\bar{\nu}cp}(\xi)\theta(1-\xi). \tag{4.23}$$

The θ-function is used to insure sufficient energy transfer for charm production.

In order to preserve the identity of

$$\mathcal{F}_2(x,Q^2) \equiv \frac{1+R(x,Q^2)}{1+4M^2x^2/Q^2} 2x\mathcal{F}_1(x,Q^2) \tag{4.24}$$

under the transformation $x \rightarrow \xi$, it is necessary to perform the transformation $R \rightarrow R'$ where

$$R(x) \equiv \frac{\mathcal{F}_2^{cp}(x)}{2x\mathcal{F}_1^{cp}(x)}\left(1+\frac{4M^2x^2}{Q^2}\right)-1, \tag{4.25}$$

and

$$\begin{aligned} R'(x) &= \frac{\xi}{x}\frac{\mathcal{F}_2^{cp}(x)}{2\xi\mathcal{F}_1^{cp}(x)}\left(1+\frac{4M^2x^2}{Q^2}\right)-1 \\ &= \frac{\xi}{x}\frac{1+R(\xi)}{1+4M^2\xi^2/Q^2}\left(1+\frac{4M^2x^2}{Q^2}\right)-1 \end{aligned} \tag{4.26}$$

Note $R'(x) = R'\big([R(x)],\xi\big)$ and will, in general, be different for neutrinos and anti-neutrinos. Substituting for R' in Equation 4.26 yields

$$\mathcal{F}_2^{cp}(\xi) \to \frac{1+R(\xi)}{1+4M^2\xi^2/Q^2}2\xi\mathcal{F}_1^{cp}(\xi). \tag{4.27}$$

Combining the charm-producing and non-charm-producing contributions to the cross-sections results in the following leading-order physical structure functions:

$$2x\mathcal{F}_1^{\nu} = xq_{ncp}^{\nu}(x)+\bar{q}_{ncp}^{\nu}(x)+\frac{x}{\xi}q_{cp}^{\nu}(\xi), \tag{4.28}$$

$$2x\mathcal{F}_1^{\bar{\nu}} = xq_{ncp}^{\bar{\nu}}(x)+\bar{q}_{ncp}^{\bar{\nu}}(x)+\frac{x}{\xi}\bar{q}_{cp}^{\bar{\nu}}(\xi), \tag{4.29}$$

$$\mathcal{F}_2^{\nu} = \frac{1+R(x)}{1+4M^2x^2/Q^2}\left(q_{ncp}^{\nu}(x)+\bar{q}_{ncp}^{\nu}(x)\right)+\frac{1+R(x)}{1+4M^2\xi^2/Q^2}q_{cp}^{\nu}(\xi), \tag{4.30}$$

$$\mathcal{F}_2^{\bar{\nu}} = \frac{1+R(x)}{1+4M^2x^2/Q^2}\left(q_{ncp}^{\bar{\nu}}(x)+\bar{q}_{ncp}^{\bar{\nu}}(x)\right)+\frac{1+R(x)}{1+4M^2\xi^2/Q^2}\bar{q}_{cp}^{\bar{\nu}}(\xi), \tag{4.31}$$

$$x\mathcal{F}_3^{\nu} = xq_{ncp}^{\nu}(x)-\bar{q}_{ncp}^{\nu}(x)+\frac{x}{\xi}q_{cp}^{\nu}(\xi), \tag{4.32}$$

and

$$x\mathcal{F}_3^{\bar{\nu}} = xq_{ncp}^{\bar{\nu}}(x) - \bar{q}_{ncp}^{\bar{\nu}}(x) - \frac{x}{\xi}\bar{q}_{cp}^{\bar{\nu}}(\xi), \tag{4.33}$$

where the Q^2-dependence and the $\theta(1-\xi)$ terms multiplying the *cp* terms are suppressed.

Like the isoscalar correction, a charmed mass correction is applied to the differential cross section via a flag in the cross section generating routine SIGMCQ. Each theory event weight is multiplied by the ratio of a call to SIGMCQ with and without the charmed suppression turned on (see section 6.1.1).

$$corr^{charm-mass} = \frac{\sigma(m_c = 0)}{\sigma(m_c = 1.31GeV)}. \tag{4.34}$$

4.5.4 Propagator Correction

The neutrino cross-section is slightly reduced at high Q^2 due to the mass of the *W* propagator. The effect of the massive *W*-boson propagator is accounted for by a re-definition of the Fermi-coupling constant:

$$G_F^2 \rightarrow \frac{G_F^2}{\left(1+\left(Q^2/m_W^2\right)^2\right)}, \tag{4.35}$$

where the approximation $m_W = 80GeV/c^2$ [Aba96] is used for this analysis. Therefore, the effects of the propagator are applied to the theory events by multiplying the event weights by the proper ratio (see section 6.1.1):

$$corr^{propagator} = \frac{\sigma(m_W = 0)}{\sigma(m_W = 80GeV/c^2)}. \quad (4.36)$$

4.3 Dimuon Events

It is possible for a second muon to result from semi-leptonic and leptonic decays of hadrons in the shower of a charged current event. When considering dimuon events it is important to determine which muon came from the primary vertex and which one resulted from a hadronic decay in the shower. This analysis cuts data events that contain two muons. In part this was done in order to use a measurement of the strange sea which comes from an analysis of these CCFR dimuon events. Cutting dimuon events kept the two data sets independent and thus the measurements independent. As a secondary benefit, this analysis could ignore the tricky issue of identifying the primary muon. However we can only cut data events that unmistakably have a second muon track. If the muon track doesn't extend past the end of the hadron shower it will not be identified as a dimuon and thus will pass the data cuts for a single muon charged current event. So it is still necessary to generate dimuon events in the MC and keep the ones that range out inside the shower, or exit the detector before SHEND (the counter designated as the shower end). NUMONTE simulates charged-current dimuon events that result from charm, pion and kaon decays. The normalized sample of MC single-muon events is used to generate the sample of simulated dimuon events.

For charm decay, the first step is to demand that each of the single-muon events produces the proper hadron using the event's available hadronic energy. Next the hadron is assigned a fraction of its maximum available momentum, according to a fragmentation function that has been shown to fit the meson production data. Finally,

the event generator allows the hadron to decay semi-leptonically. The decay muon is tracked and its momentum and angle are measured. The event's new E_{had} and y are reconstructed, which differ from their original values because of the missing energy associated with the neutrino that is also a product of the hadron decay. A Collins-Spiller fragmentation function was used to determine the energy fraction of the D-meson. The Mark III decay spectrum in D. Coffman's thesis [Cof87] was used for the D-meson decay probability.

In the case of π/κ decay the production probability was determined from a study done by K. Bachmann of the CCFR collaboration [Bac88]. Bachmann parameterized the probability of getting a second muon from the CCFR hadron test beam.

5 Iteratively Determined Flux and SF

Structure function measurements are made by comparing the number of observed events to the number of expected events. The number of events observed in the detector depends on how many neutrinos come in (the flux) and the probability for a neutrino to interact with a nucleon (the cross section):

$$\frac{d^2N(E,x,y,V_x,V_y)}{dxdy} = \Phi(E,V_x,V_y)\frac{d^2\sigma(E,x,y)}{dxdy}. \tag{5.1}$$

N is the number of observed charged-current events in the detector at a given vertex position (V_x,V_y) in a given kinematic region (x,y,Q^2). $\Phi(E,V_x,V_y)$ is the incident neutrino flux. Given the flux and the number of events in a kinematic bin, the differential cross-section can be determined which leads to structure function measurements through Equation 1.68.

In principle, the neutrino flux could be determined from the secondary beam particles. However, the width of the energy spectrum of the CCFR beam is quite wide and the intensity is extremely high within a short beam spill time (called a "ping"). During a ping, 10^{13} protons hit the target in a matter of milliseconds. These factors make a direct measurement of the flux difficult. Therefore the flux is determined from a subset of the charged-current data set where the cross section is fairly independent of energy.

To determine the flux from the data through Eqn 5.1, a set of SF values must be assumed. The flux and the SFs cannot both be determined from the same data set, so the data is divided into two subsets. One set is used for the flux determination

assuming values for the SF. The other set is used for determining the SFs assuming values for the flux. Hence the tasks of measuring the flux and SF are intertwined and the combined process becomes iterative. The iterative cycle is detailed in the next section. Subsequent sections describe the flux extraction and the SF parameterization. Extracting the structure functions is described in the next Chapter.

5.1 Iteration Cycle

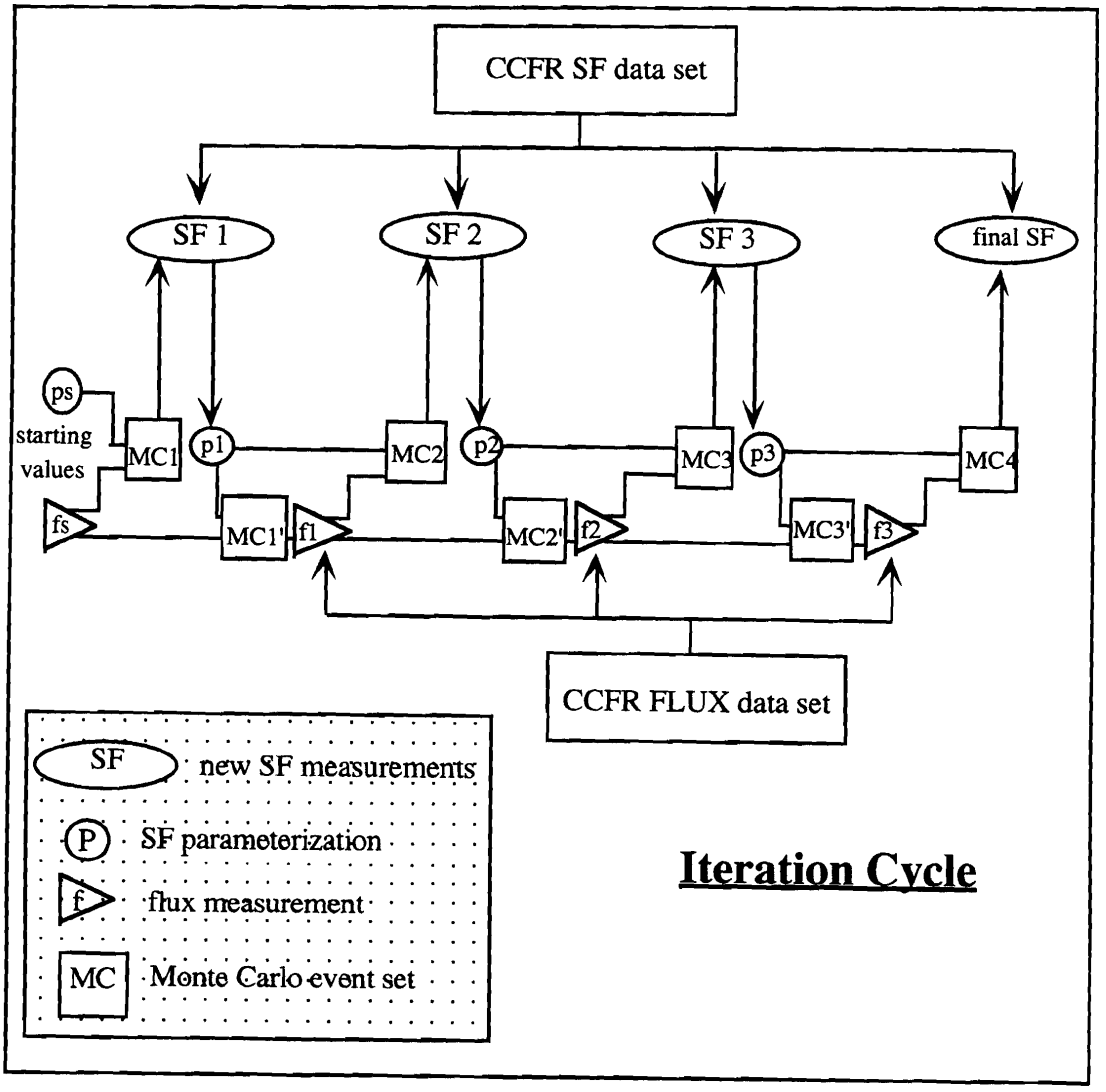

Figure 5.1: Iteration Cycle.

Figure 5.1 maps out the SF/flux measurement iteration cycle. Each box represents a Monte Carlo event set, the ovals represent a SF parameterization, and the triangles represent a flux measurement.

Consider the cycle one step at a time. The first Monte Carlo event set ($MC1$) was made with NUMONTE using the previous CCFR SF parameterization (ps) and flux file (fs) [Sel 97]. With $MC1$ and the CCFR SF data set a minimization is done resulting in new SF measurements ($SF1$). These new SF measurements are parameterized ($p1$). $MC1$ is reweighed with the new parameterization ($p1$) to create $MC1'$. The creation of $MC1'$ results in event number sums which are used to make a new flux measurement ($f1$). The new SF parameterization ($p1$) and the new flux measurement ($f1$) are used to create *MC2*. This cycle repeats to create *MC3* and then *MC4* from which the final SF values are extracted.

Convergence was achieved after 2 cycles, a third cycle was completed as a check.

5.1.1 Event Re-weighting

The new Monte Carlo event sets are made by reweighting the events in the original set MC1. Each event is re-weighed individually. The re-weight factor depends on the new and old SF parameterizations, the new and old flux values and the kinematic variables x,y,Q^2 and E_ν:

$$EventWeight = \left(\frac{new\ flux}{old\ flux}\right)_{E_\nu bin} \times \left(\frac{SIGMCQ(new\ SF\ param)}{SIGMCQ(old\ SF\ param)}\right)_{at\ the\ event(x,y,Q^2)}.$$

The flux measurements are made in energy bins so the flux part of the re-weight only depends on E_ν. The SF parameterization reweight values are determined by a call to NUMONTE's differential cross section routine SIGMCQ. This routine determines the differential cross section at a particular x, y and Q^2 given a SF parameterization. It is based on the following differential cross section:

$$\frac{d^2\sigma^{\nu(\bar{\nu})}}{dx\,dy} = \frac{G_F^2 ME}{\pi}\left[\begin{array}{l}\left(1-y-\dfrac{Mxy}{2E}+\dfrac{y^2}{2}\dfrac{1+4M^2x^2/Q^2}{1+R(x,Q^2)}\right)F_2^{\nu(\bar{\nu})} \\ \pm y\left(1-\dfrac{y^2}{2}\right)\nu F_3^{\nu(\bar{\nu})}\end{array}\right].$$

Various corrections to this cross section are discussed in section 4.5.

5.2 The Flux Measurement

A subset of the full CCFR charged current event data set is used for the flux measurement. The events in this set have low hadron energy, or low ν where ν is defined as

$$\nu = E_\nu - E_\mu = E_{HAD}.$$

As will be shown, this method cannot determine the absolute flux, but it can determine the relative flux between two energy bins $\Phi(E_i)/\Phi(E_j)$, and the relative flux between neutrinos and anti-neutrinos $\Phi^\nu/\Phi^{\bar{\nu}}$.

The method is derived from the most general form of the charged-current neutrino-nucleon cross-section:

$$\frac{d^2\sigma^{\nu,\bar{\nu}}}{dx\,dy}=\frac{G^2 s}{2\pi}\left[\left(1-y-\frac{Mxy}{2E}\right)F_2(x,Q^2)+\frac{y^2}{2}2xF_1(x,Q^2)\pm y\left(1-\frac{y}{2}\right)xF_3(x,Q^2)\right], \tag{5.2}$$

where the +(–) sign in the last term distinguishes the neutrino(antineutrino) versions. This equation can be transformed using $2xF_1=\left[\left(1+4M^2x^2/Q^2\right)\Big/\left(1+R(x,Q^2)\right)\right]F_2$, $s=2ME$, and $y=\nu/E$ to get

$$\frac{d^2\sigma^{\nu,\bar{\nu}}}{dx\,d\nu}=\frac{G^2 M}{\pi}\left[\left(1-\frac{\nu}{E}-\frac{Mx\nu}{2E^2}\right)F_2+\left(\frac{\nu^2}{2E^2}\frac{1+2Mx/\nu}{1+R}\right)F_2\pm\frac{\nu}{E}\left(1-\frac{\nu}{2E}\right)xF_3\right] \tag{5.3}$$

Organizing Equation 5.3 in terms of ν/E gives:

$$\frac{d^2\sigma^{\nu,\bar{\nu}}}{dx\,d\nu}=\frac{G^2 M}{\pi}\left[F_2-\frac{\nu}{E}\left(F_2\mp xF_3\right)+\frac{\nu^2}{2E^2}\left(\left(\frac{1+2Mx/\nu}{1+R}-\frac{Mx}{\nu^*}\right)F_2\mp xF_3\right)\right]. \tag{5.4}$$

Define $\tilde{R}(x,Q^2)$ such that

$$1+\tilde{R}=\frac{1+2Mx/\nu}{1+R_{long}}-\frac{Mx}{\nu}. \tag{5.5}$$

Equation 5.4 becomes a simple function of ν:

$$\frac{d^2\sigma^{\nu,\bar{\nu}}}{dx\,d\nu}=\frac{G^2 M}{\pi}\left[F_2-\frac{\nu}{E}\left(F_2\mp xF_3\right)+\frac{\nu^2}{2E^2}\left(F_2\mp xF_3+\tilde{R}F_2\right)\right]. \tag{5.6}$$

Integrating this over all x with ν and E fixed gives

$$\frac{d\sigma^{\nu,\bar{\nu}}}{d\nu} = \frac{G^2 M}{\pi}\left[\int F_2 - \frac{\nu}{E}\left(\int F_2 \mp \int xF_3\right) + \frac{\nu^2}{2E^2}\left(\int F_2 \mp \int xF_3 + \int \tilde{R}F_2\right)\right], \quad (5.7)$$

where $\int F = \int_0^1 F(x,Q^2)dx$ for F_2 and xF_3.

Multiplying both sides of Equation 5.7 by $\Phi(E)$:

$$\frac{dN}{d\nu} = \Phi(E)\left(A + \frac{\nu}{E}B - \frac{\nu^2}{2E^2}C\right) \quad (5.8)$$

where

$$A = \frac{G^2 M}{\pi}\int F_2\,, \quad (5.9)$$

$$B = -\frac{G^2 M}{\pi}\int\left(F_2 \mp xF_3\right), \quad (5.10)$$

and

$$C = B - \frac{G^2 M}{\pi}\int F_2\tilde{R}. \quad (5.11)$$

Therefore, the derivative of the number of events with respect to ν is proportional to the flux times a function with a known energy dependence. The energy dependence comes in terms that are quadratic in ν/E, so if Equation 5.8 is integrated up to a small value of $\nu \equiv \nu_o$, the energy dependence of the resulting term will be small (see Figure 5.6). With the definition

$$\frac{B}{A} = -\left(1 \mp \frac{\int xF_3}{\int F_2}\right), \quad (5.12)$$

we can integrate with respect to ν and Equation 5.8 becomes

$$N(\nu<\nu_o)=\Phi(E)\int_0^{\nu_o} d\nu A\left(1+\frac{\nu}{E}\left(\frac{B}{A}\right)-\frac{\nu^2}{2E^2}\left(\frac{B}{A}-\frac{\int F_2\tilde{R}}{\int F_2}\right)\right). \tag{5.13}$$

$dN/d\nu$ can be determined empirically by binning events in $(E_\nu, E_{HAD}<\nu_o)$. This procedure is fully described in the next section.

5.2.1 Flux Extraction

For the flux analysis, all events are accepted that pass the standard fiducial and geometric cuts (Section 3.3) and pass the following kinematic cuts:

- $\theta_\mu < 150 mr$ — This cut assures good acceptance of the muon track as it passes through the muon spectrometer which assures a good muon Energy measurement.

- $E_\mu > 15 GeV$ — $15\ GeV$ is the lower limit of acceptance of the muon spectrometer.

- $30 GeV < E_\nu < 360 GeV$ — The lower limit of 30 GeV was chosen because below that energy a large acceptance correction is required and the ν/E corrections become important. The upper limit of 360 GeV was chosen because above that energy the error on the Monte-Carlo smearing corrections becomes greater than 10%; also, the number of anti-neutrino events above 360 GeV is small and hence would not make a significant impact on the analysis.

- $E_{HAD} < \nu_0 = 20 GeV$ — The choice of 20 GeV was made so that there would be sufficient statistics in the higher energy bins, while minimizing the systematic

correlations with the structure function data sample ($E_{HAD} > 10 GeV$); Table 5.1 lists the number of events as function of E_{HAD}. Also, the hadron energy resolution has been shown to be well understood down to $20\,GeV$ [Sak90] so that mis-measuring the hadron energy near the region of the cut is not a concern.

The events are sub-divided into 19 energy bins with widths which vary to accommodate the change in the number of events as a function of energy and the energy resolution. Table 5.1 shows the number of flux events in each energy bin.

Within each E_ν bin the events are further divided into E_{HAD} bins; these E_{HAD} bins are limited by smearing and statistics to be 2 GeV wide, for a total of 10 bins with ν_o = 20 GeV. The events in $\left(E_\nu, E_{HAD}\right)$ bins form a $dN/d\nu$ distribution which can be converted into the flux $\Phi(E)$ by inverting equation 5.13:

$$\Phi(E) \propto \int_0^{\nu_o} \frac{dN/d\nu}{\left[1+\frac{\nu}{E}\left(\langle B/A\rangle\right)-\frac{\nu^2}{2E^2}\left(\langle B/A\rangle-\int F_2\tilde{R}\Big/\int F_2\right)\right]}d\nu \qquad (5.14)$$

where <*B*/*A*> is the average of *B*/*A* as defined in Eq. 5.12.

The raw data events are corrected for detector acceptance and smearing before the flux is extracted. The quantity *B*/*A* is determined separately in each E_ν bin and then averaged to find < *B* / *A* >.

Table 5.1: Number of flux events in each energy bin.

	E744				E770			
Neutrino Type	ν	ν	$\bar{\nu}$	$\bar{\nu}$	ν	ν	$\bar{\nu}$	$\bar{\nu}$
Toroid Pol	Foc μ^-	Foc μ^+	Foc μ^-	Foc μ^+	Foc μ^-	Foc μ^+	Foc μ^-	Foc μ^+
15-30 *GeV*	4270	4681	1687	2004	5411	5430	2513	2796
30–40 *GeV*	7953	9014	2584	3150	10091	10343	4081	4584
40–50 *GeV*	12371	14025	3565	4277	15461	15945	6171	6541
50–60 *GeV*	15832	17882	4438	5119	20090	20383	7404	7929
60–70 *GeV*	17053	19365	4800	5682	22725	22753	7365	7907
70–80 *GeV*	17557	20294	4910	5715	23361	24217	7040	7330
80–90 *GeV*	16993	19809	4552	5447	22767	23573	6381	6763
90–100 *GeV*	15714	18115	3884	4549	20826	21944	5448	5971
100–120 *GeV*	25111	29240	5679	6911	32786	34977	8174	8513
120–140 *GeV*	18829	21690	3607	4299	24090	25479	5557	5932
140–160 *GeV*	15610	17879	2808	3344	20159	21594	4103	4364
160–180 *GeV*	14766	17375	2395	2947	19503	20351	3533	3706
180–200 *GeV*	15541	18190	2270	2665	20442	21738	3219	3582
200–230 *GeV*	23726	27524	3161	3785	32333	34465	4397	4591
230–260 *GeV*	20101	23384	2278	2473	27950	29577	3115	34006
260–290 *GeV*	14615	17197	1296	1559	20405	21650	1767	2015
290–320 *GeV*	10365	11871	762	889	14078	14846	1052	1126
320-360 *GeV*	9356	10306	500	641	12232	12981	711	768
360–400 *GeV*	5574	6557	230	269	7591	7930	311	380

The $dN/d\nu$ distributions are fit to the form of Equation 5.13 after the physics-model corrections are applied. However, there is an increase of events near zero hadron energy. These events are due to quasi-elastic scattering, resonance productions, and other quasi-elastic-like processes [Bel88, Bel92]. Figure 5.2 and 5.3 from Ref. [Bel88] show the kinematic region for which these processes are expected to contribute to the cross-section. Unlike the deep-inelastic interactions, whose cross-section is proportional to neutrino energy, these events have a cross-section which is constant at $0.9\times10^{-38}\ cm^2$ [Auc90].

These low-E_{HAD} processes are not included in the NUMONTE cross-section formalism of Equation 5.2. Therefore, $dN/d\nu$ is only fit from $4\ GeV < E_{HAD} < 20\ GeV$ to determine the slope parameter B/A. A typical fit is shown in Figure 5.4. The low-energy cut removes the quasi-elastic processes which can be seen as the first data point in Figure 5.4.

Since B/A is first determined separately for each E_ν bin, the $\Phi(E)$ term in the Equation 5.13 is treated as a floating normalization in the fit. This normalization vanishes when B/A is calculated from Equation 5.12. The values of B/A from all the energy bins are averaged and are displayed in Figure 5.5. The values do not show strong energy dependence. Table 5.2 shows the results.

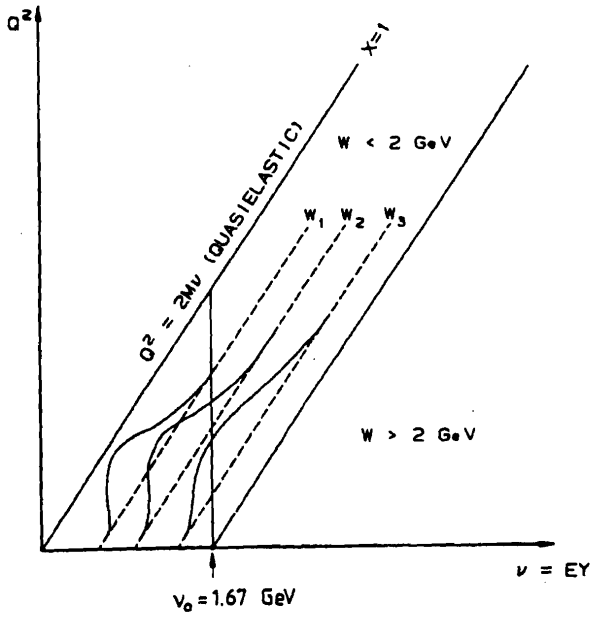

Figure 5.2: Kinematic map showing the region where quasi-elastic processes dominate the cross-section. This plot is FIG. 1 in Ref. [Bel88]. W is the invariant mass of the hadronic final state, $W^2 = 2M\nu + M^2 - Q^2$.

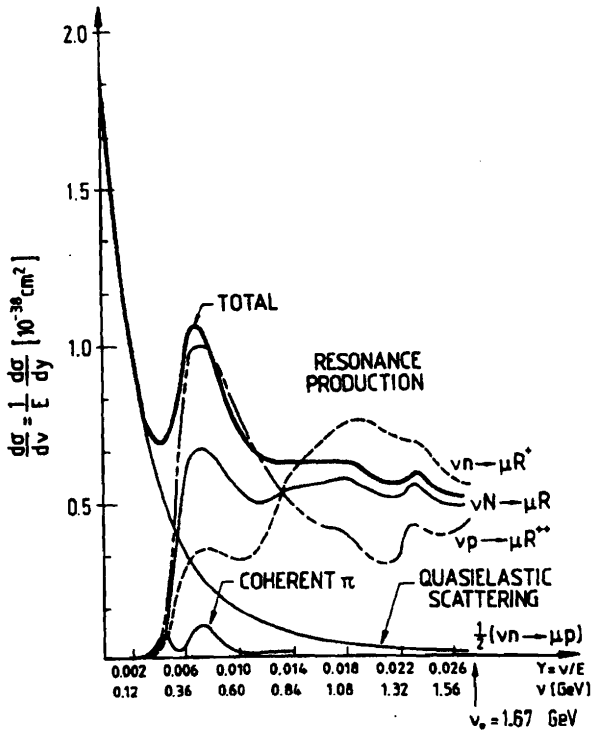

Figure 5.3: The differential cross-section $d\sigma/d\nu$ in the low-y region for E_ν = 60 GeV. This plot is FIG. 5 in Ref. [Bel88]. This plot shows that the conservative cut of $E_{HAD} = \nu > 4\ GeV$ will eliminate the quasi-elastic portion of the cross-section.

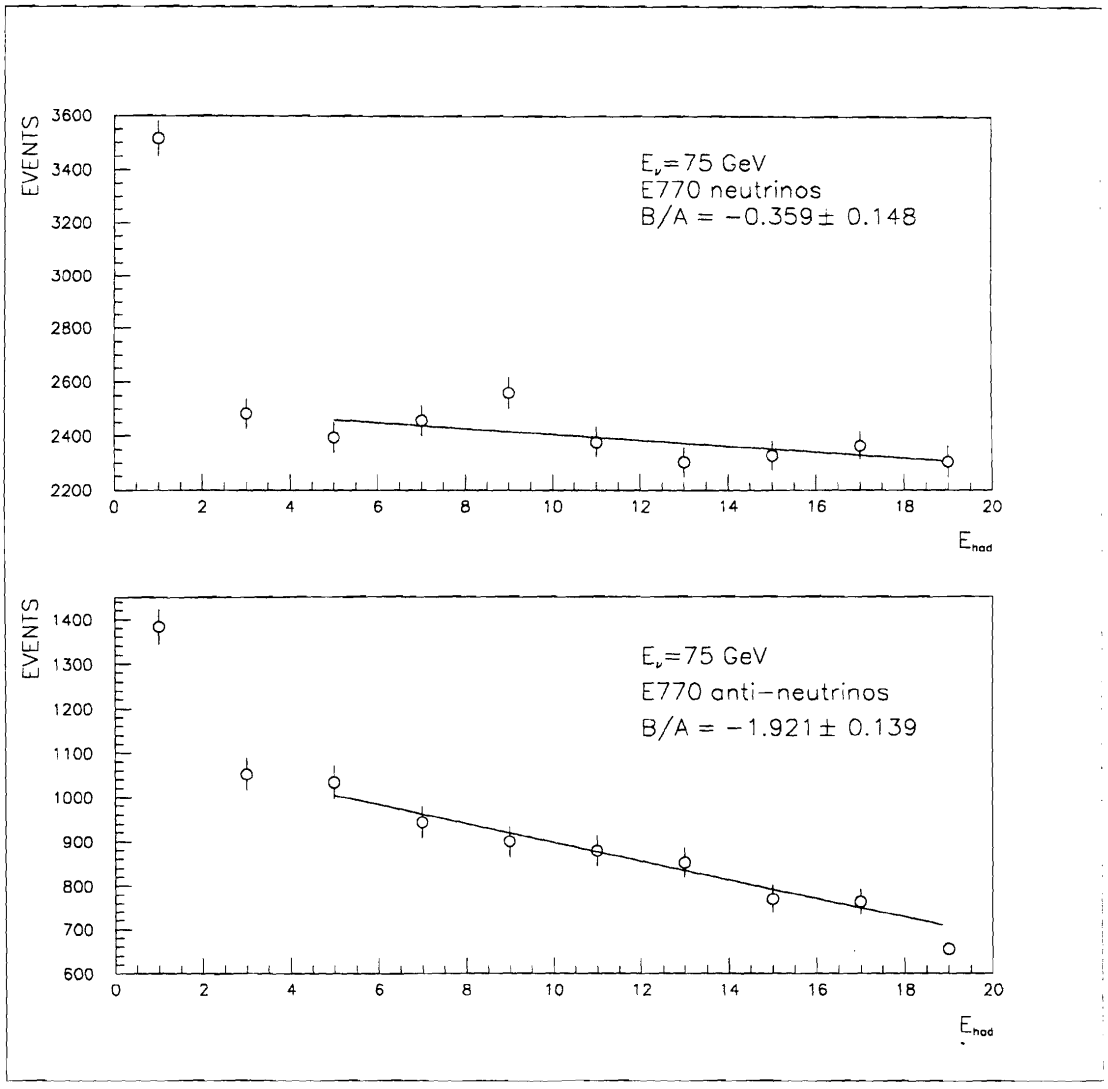

Figure 5.4: A typical fit for B/A to the $dN/d\nu$ distribution. Neutrinos (top) Anti-Neutrinos (bottom). The peak in events for $E_{HAD} < 4\ GeV$ is due to resonance production, as described in the text, and is not included in the fit for B/A.

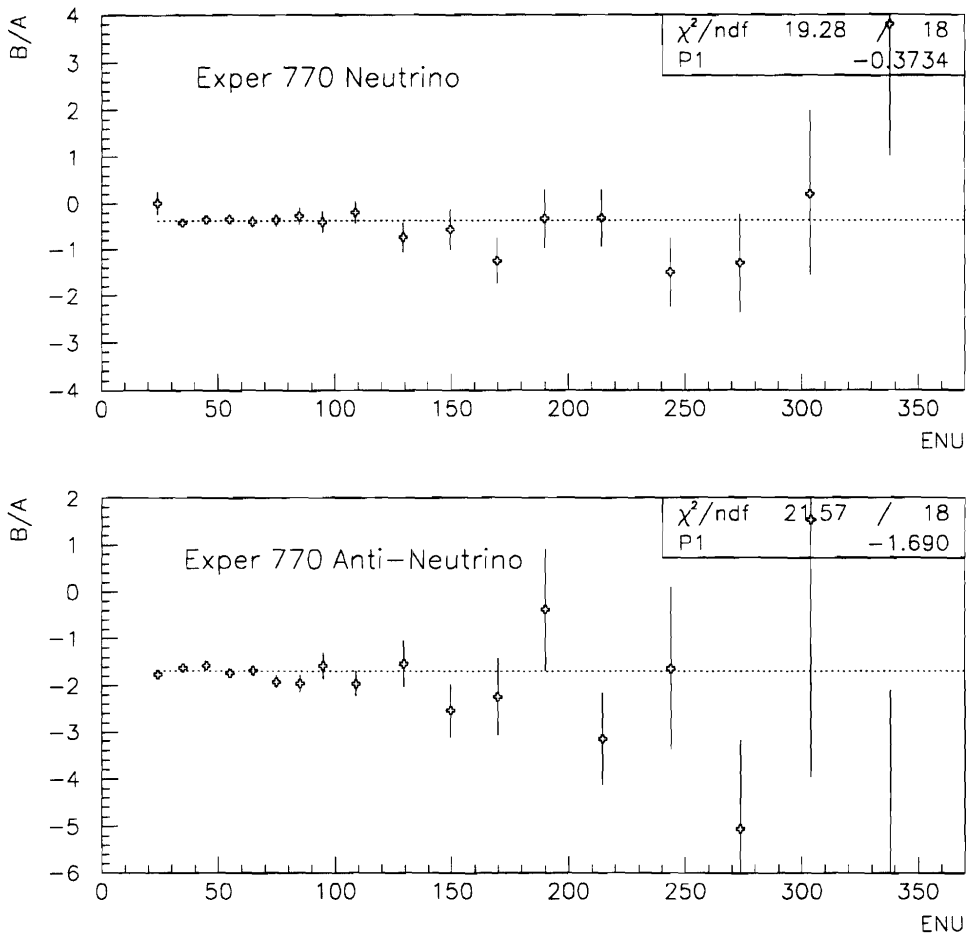

Figure 5.5: B/A as a function of energy for experiment E770. The two lines indicate the average B/A from the points in the Figure. The χ^2 of the fits to the average neutrino (anti-neutrino) values are shown in each plot.

Table 5.2: $\langle B/A \rangle$ from the flux analysis.

	ν	$\bar{\nu}$
$\langle B/A \rangle^{744}$	-0.357 ± 0.047	-1.685 ± 0.040
$\langle B/A \rangle^{770}$	-0.383 ± 0.043	-1.679 ± 0.034

Once the best values for B/A are known, the flux can be determined according to Equation 5.13. The correction implied by that equation can be substantial, especially for anti-neutrinos. The average value of the fixed-ν cut correction can be defined by

$$COR(E) = \frac{\int_0^{\nu_o} \frac{dN}{d\nu}\left[1 + \frac{\nu}{E}\left(\langle B/A\rangle\right) - \frac{\nu^2}{2E^2}\left(\langle B/A\rangle - \int F_2\tilde{R} \Big/ \int F_2\right)\right]^{-1} d\nu}{\int_0^{\nu_o} \frac{dN}{d\nu} d\nu} \qquad (5.15)$$

and is plotted in Figure 5.6.

Since σ/E is almost constant, it is conventional to plot the flux as $E\Phi$, which is approximately proportional to the number of events. Figure 5.7 shows the fully-corrected flux × energy spectra for experiments E744 and E770 as a function of energy.

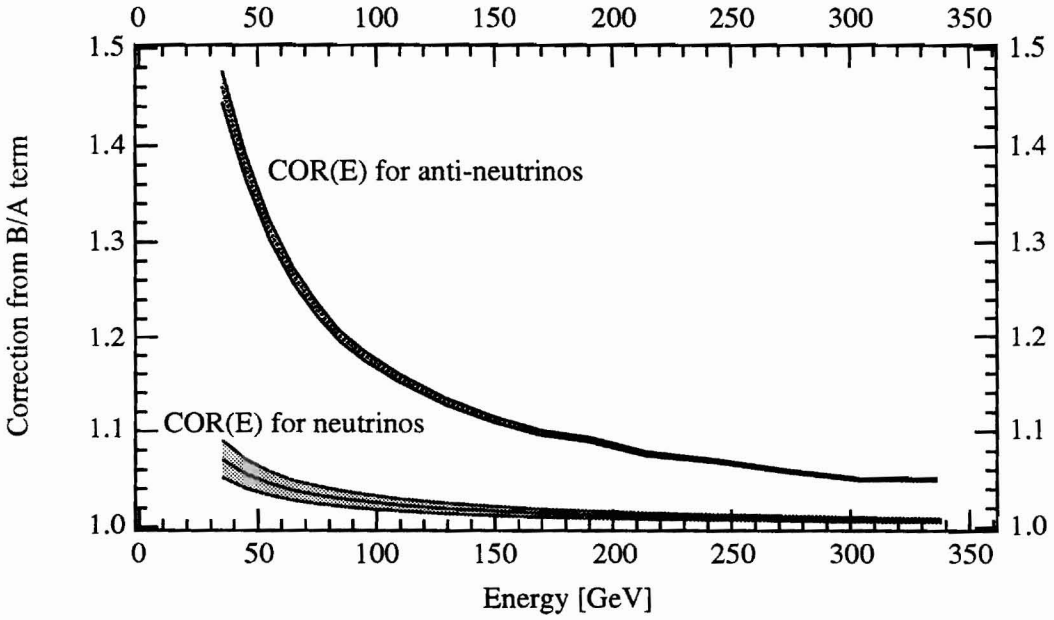

Figure 5.6: The correction due to B/A. $COR(E)$ is defined by Equation 5.15. The bands show the effect of a $\pm 1\sigma$ shift in B/A on the correction.

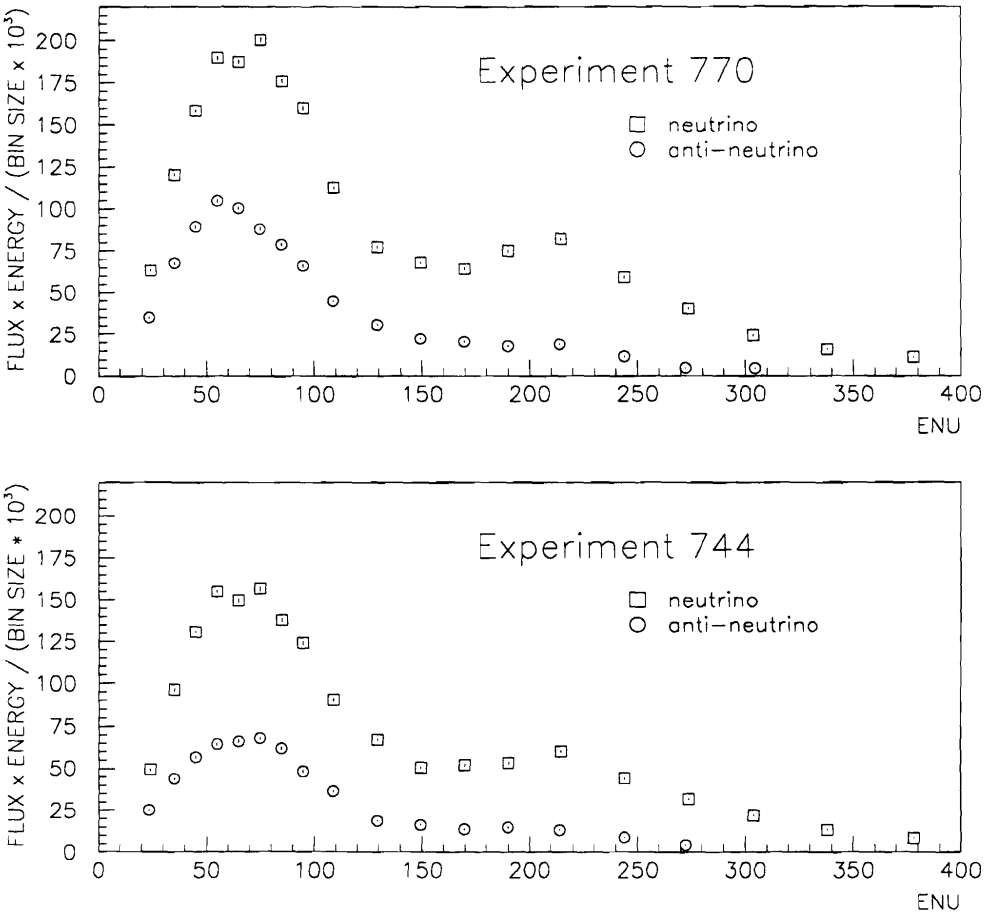

Figure 5.7: The fully-corrected flux × energy spectra for E744 and E770. The normalization along the left axes is arbitrary.

5.3 SF Parameterization

The SF measurements are parameterized using a model adapted from a leading-order calculation of the *ν-nucleon* cross-section suggested by Buras and Gaemers [Bur78]. In the Buras-Gaemers model, differential cross-sections are constructed from a set of parton momentum densities representing the valence and sea quarks inside a

nucleon. The original form of the parameterization along with the physical motivation can be found in the reference.

This SF parameterization is not used to extract physical parameters but is used to describe the SF measurements and thus represent them in the iterative cycle. In theory any form could be used for this purpose as long as it fits the SF measurements well. With this in mind alterations were made to the original Buras Gaemer model by John Kim who added new terms to the original model trying to keep the original QCD physics restrictions in place but adding greater flexibility in the fit. The alterations particularly improved the model's ability to fit our measurements in the low x region, which was important for this analysis. Figures 5.8-5.10 graphically show the final SF parameterizations.

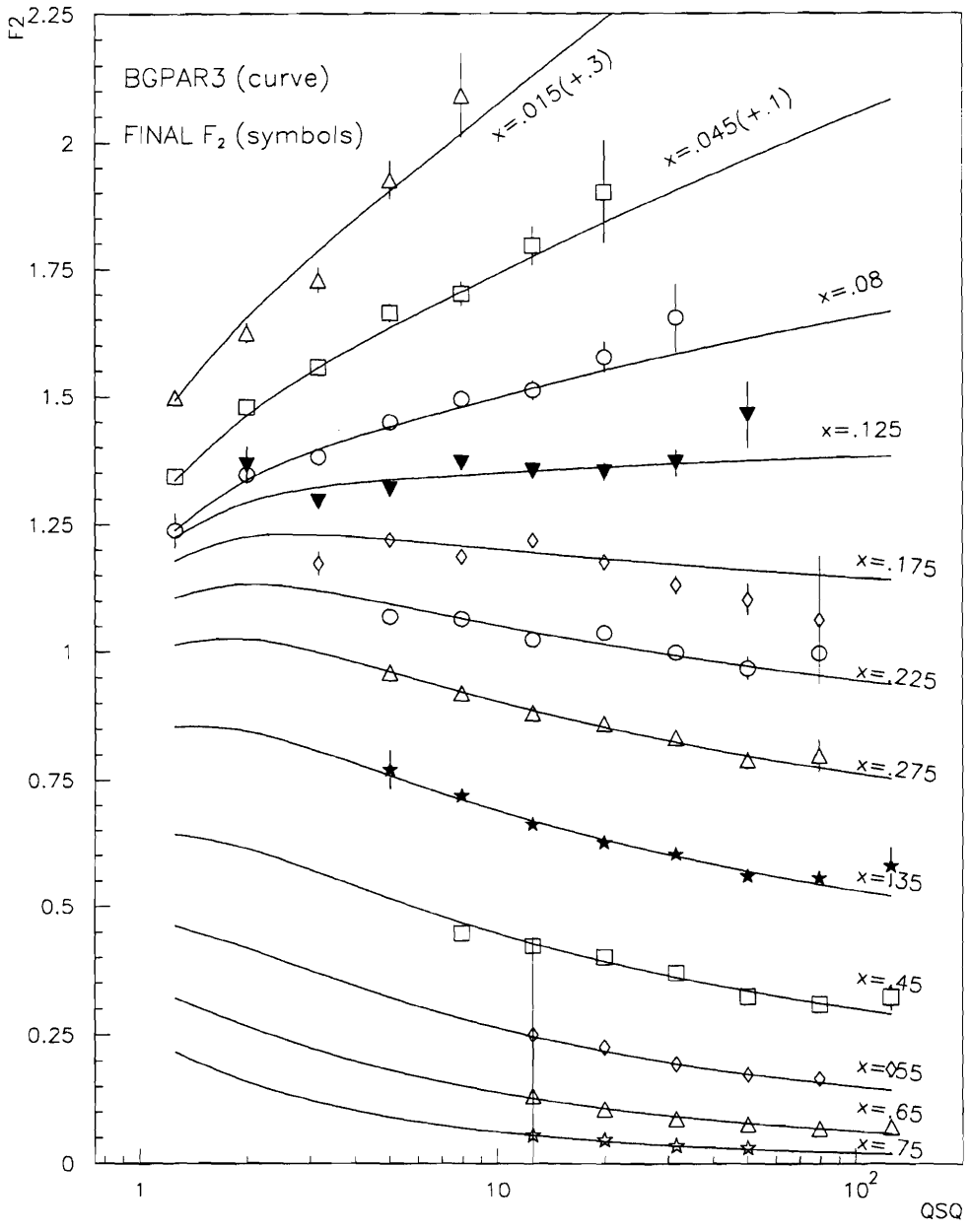

Figure 5.8: Final F_2 measurements and SF parameterization #3.

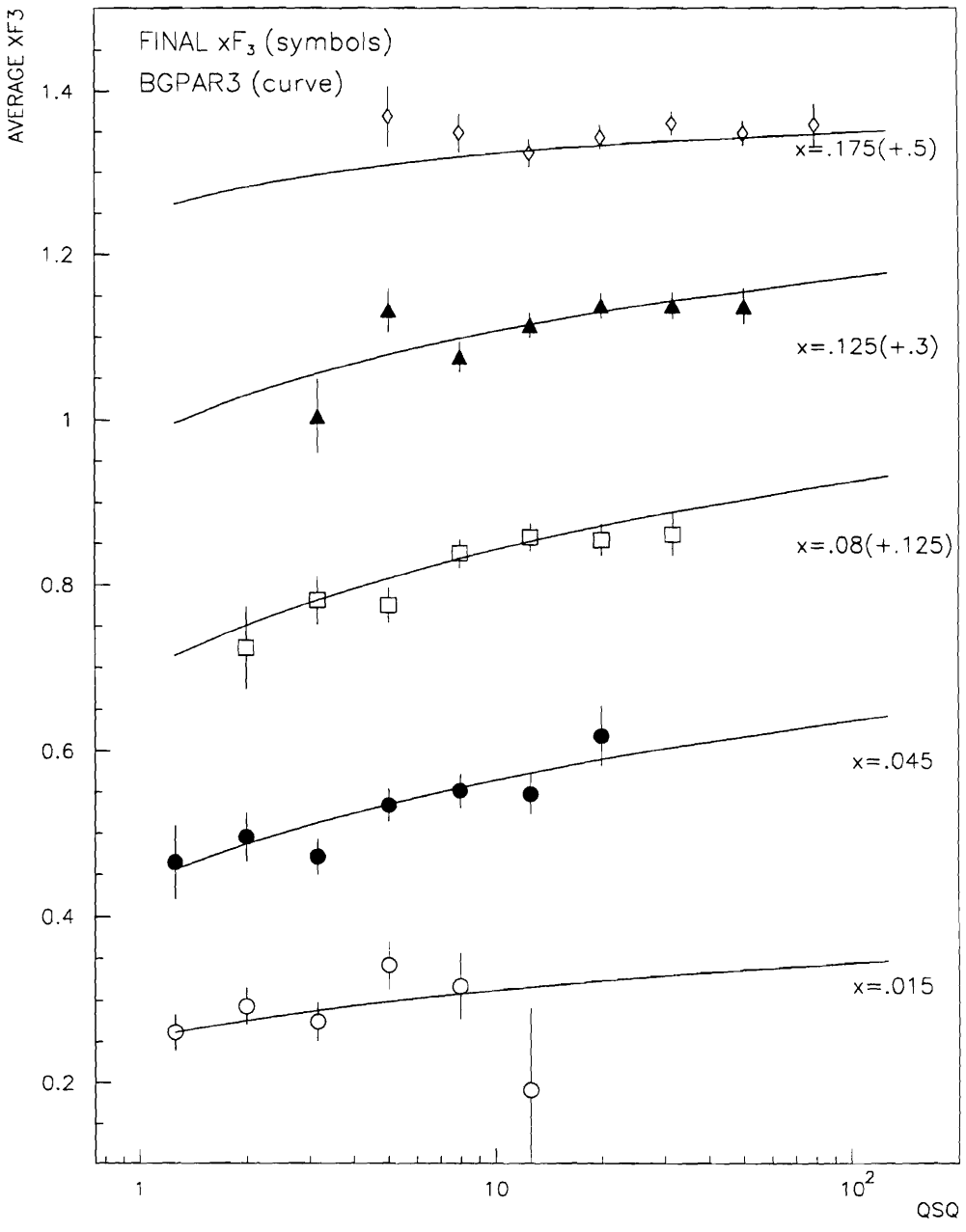

Figure 5.9: Final xF_3 measurements (*low x*) with statistical errors and the SF parameterization #3.

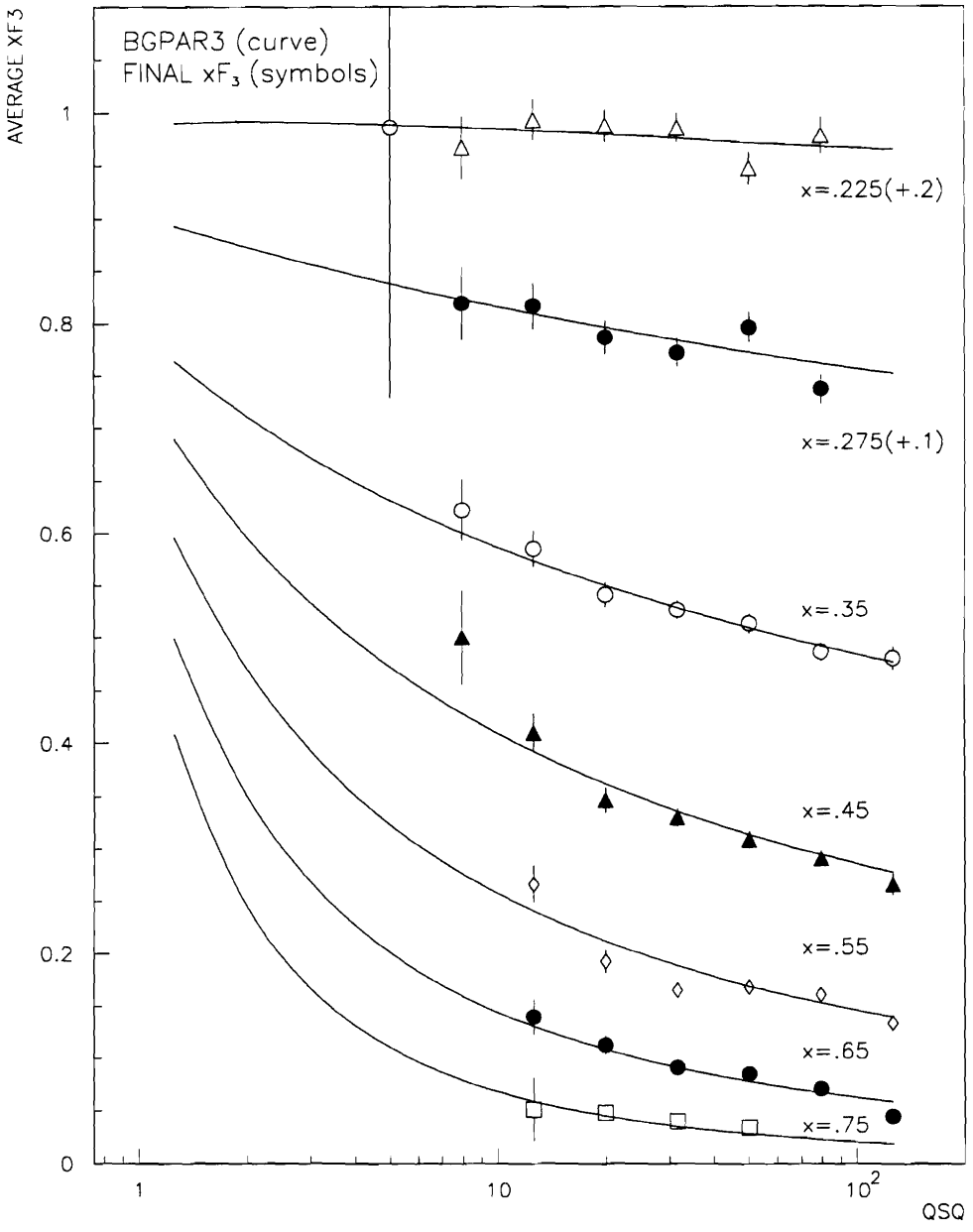

Figure 5.10: Final xF_3 measurements *(mid to high x)* with statistical errors and the SF parameterization #3.

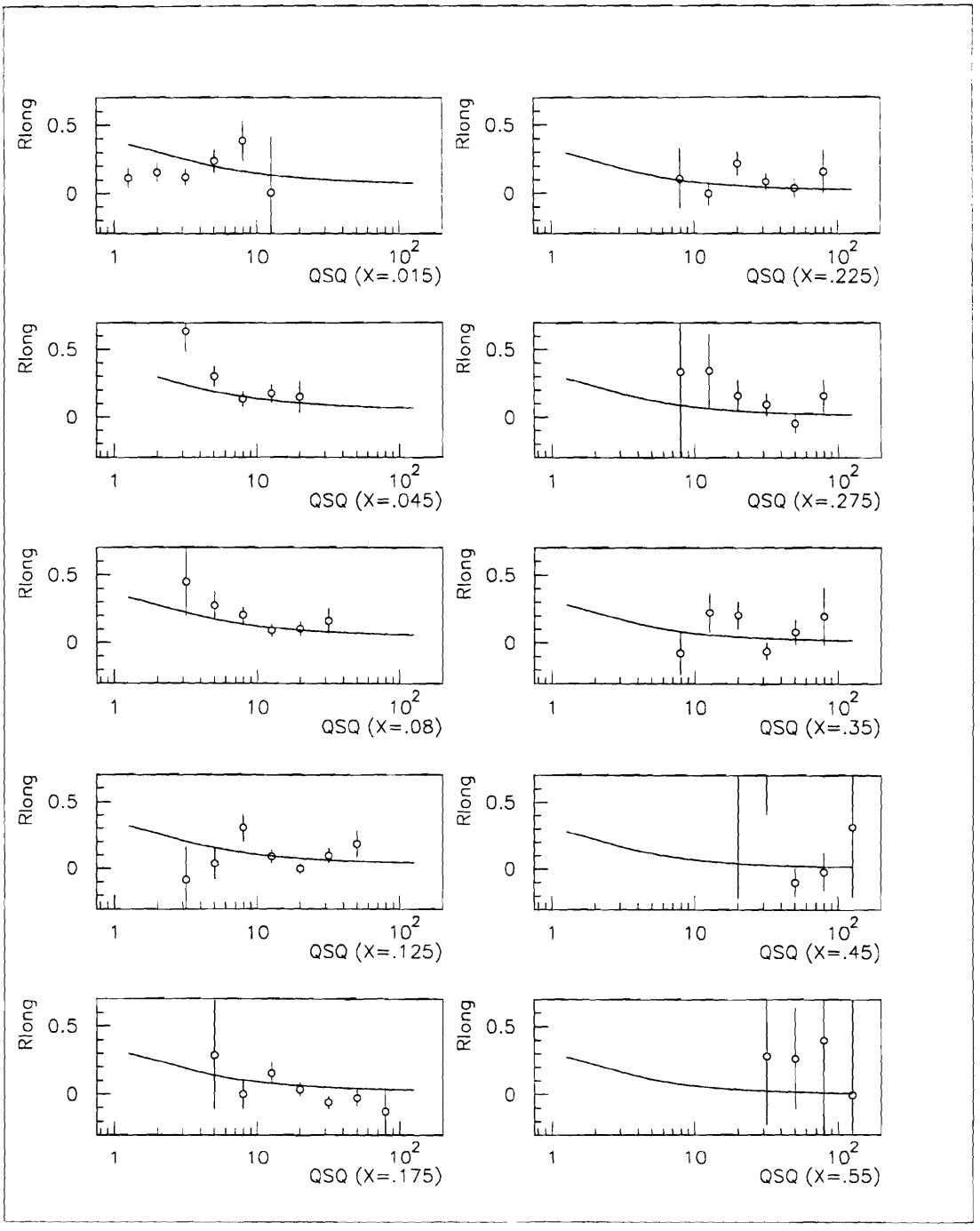

Figure 5.11: Final R_{long} measurements with statistical errors and the SF parameterization #3.

There is a potential problem with the parameterization in regions where it is not tied to our measurements. We use the SF parameterization to compute a value for our

total cross section in order to normalize the total cross section to the world average. Thus if the parameterization was wrong in the regions where we do not measure SF it could potentially cause a problem. To this end precautions were taken in the normalization of the overall cross section to the world average (see section 6.1.2) to effectively remove the influence of regions where we do not make measurements.

The final modeled form for the quark momentum densities follows:

$$U_{valence} = A_{v1}(s)x^{E_1(s)}(1-x)^{E_2(s)} + A_{v2}(s)x^{E_3(s)}(1-x)^{E_4(s)} + A_{v3}(s)x^{E_5(s)}(1-x)^{E_6(s)}, \quad (5.16)$$

$$D_{valence} = A_d(s)U_{valence}(1-x), \quad (5.17)$$

and

$$Sea = A_{s1}(s)(1-x)^{E_{s1}(s)} + A_{s2}(s)(1-x)^{E_{s2}(s)}. \quad (5.18)$$

where the Q^2 dependence is contained in

$$s = \log\left[\frac{\log(Q^2/\Lambda^2)}{\log(Q_o^2/\Lambda^2)}\right]$$

The functional dependence of the coefficients (A_i) and the exponents (E_i) on Q^2 and the fit parameters can be seen in the FORTRAN code included as Appendix J. Motivation for the parameterization can be found in reference [Bur78]. The leading order parameterization is augmented with a strange sea distribution whose parameters, A_{Rab} and η_{Rab}, were measured previously in a study of dimuon events [Rab92]:

$$Strange\ Sea = A_{Rab}(1-x)^{\eta_{Rab}}. \tag{5.19}$$

The R_{long} values are parameterized using the following form suggested by Whitlow [Whi90b]:

$$R = \frac{B_1}{\ln(Q^2/0.04)}\theta + \frac{B_2}{Q^2} + \frac{B_3}{Q^2+0.09}, \tag{5.20}$$

where

$$\theta = 1 + \frac{12Q^2}{Q^2+1} \times \frac{c^2}{c^2+x^2}, \tag{5.21}$$

with c=*0.125*. New values for the parameters *B1*, *B2* and *B3* were determined in each iterative cycle. The final values are listed in table 5.3 along with the other final SF fit parameters discussed above.

Number	Parameter	Value
1	A_0	0.3800
2	A_1	0.64439
3	A_2	-1.07296
4	A_{v2}	3.97659
5	A_{v3}	-34.2501
6	E_{10}	0.64125
7	E_{11}	0.11586
8	E_{20}	1.91858
9	E_{21}	2.49683
10	E_3	0.65179
11	E_4	3.66171
12	E_5	2.37770
13	E_6	29.4226
14	S_2	0.15934
15	S_3	0.01936
16	G_3	0.00102
17	A_{s20}	0.34649
18	A_{s21}	0.20971
19	E_{s20}	10.000
20	E_{s21}	0.04672
21	B1	0.0443
22	B2	0.5625
23	B3	-0.3134

Table 5.3: Final values for SF parameterization.

6 Structure Function Extraction

Physics measurements can be made by comparing the set of observed events to a set of events generated by a Monte Carlo that simulates a theoretical model. Typically, certain parameters of the theoretical model are varied in order to minimize the differences apparent in a given distribution. In the case of this analysis, the structure function values which parameterize the hadronic vertex are varied in order to fit the MC y-distributions to the data y-distributions.

6.1 Comparing the y-distributions

SF values are extracted by minimizing a χ^2 sum which compares the data and MC y-distributions. The Bjorken variables x, y and Q^2 are used to bin the data and MC events, the bin values are given in section 6.2.2. χ^2 is a sum (over 20 ν y-bins and 20 $\bar{\nu}$ y-bins) of the difference between the number of data events (N_{data}) and the number of MC events (N_{theory}) in a given bin. The number of MC events depends on the SF values through the cross section. These SF values are varied in order to minimize the differences in the data and MC distributions. A separate χ^2 is formed in each (x, Q^2) bin thus making the resulting SF measurements functions of x and Q^2.

$$\chi^2\Big|_{(x,Q^2)} = \sum_{20\,ybins}^{\nu} \frac{\left[N_{data} - N_{theory}(SF)\right]^2}{(error)^2} + \sum_{20\,ybins}^{\bar{\nu}} \frac{\left[N_{data} - N_{theory}(SF)\right]^2}{(error)^2} \quad (6.1)$$

where

$$N_{data} = number\ of\ data\ events\ in\ a\ (x, y, Q^2)\ bin, \quad (6.2)$$

$$N_{theory} = \left[\sum_{events in one bin} K_{type} \times MC\,event\ weight \times \frac{d\sigma_{new}}{d\sigma_{old}} \right]_{(x,y,Q^2)}, \tag{6.3}$$

$$K_{type} = \frac{\sigma^{\bar{\nu},\nu}_{CCFR}}{\sigma^{\bar{\nu},\nu}_{world}} \left(\frac{N_{data}}{N_{MC}} \right)_{type}, \tag{6.4}$$

and

$$(error)^2 = N_{data} + \sum_{(x,y,Q^2)\,bin} \left(MC\,event\ weight \times K_{type} \right)^2. \tag{6.5}$$

The four event types are ν and $\bar{\nu}$, each with toroid focusing settings μ^- and μ^+. The normalization factor K_{type} is discussed in section 6.1.2.

6.1.1 The MC Simulated Events

The CCFR Monte Carlo, NUMONTE, is used to generate a set of events by simulating the theory laid out in chapter 1. The simulation is based on a ν–N cross section which is a linear function of the SFs $2xF_1$, F_2 and xF_3:

$$\frac{d^2\sigma^{\nu(\bar{\nu})}}{dx\,dy} = \frac{G_F^2 ME}{\pi} \left[\left(1 - y - \frac{Mxy}{2E} \right) F_2^{\nu(\bar{\nu})} + \frac{y^2}{2} 2xF_1^{\nu(\bar{\nu})} \pm y \left(1 - \frac{y^2}{2} \right) \nu F_3^{\nu(\bar{\nu})} \right] \tag{6.6}$$

In order to find the values of the SFs that minimize χ^2, each theory event is re-weighted to give it an explicit SF dependence. The reweight is the ratio of a "new" form of Eqn 6.6, $d\sigma_{new}$, which keeps the SF as free variables to be used as minimization fit parameters and the "old" form, $d\sigma_{old}$, which is the cross section the event was generated with.

$$\frac{d\sigma_{new}}{d\sigma_{old}} = \frac{\dfrac{d^2\sigma^{\nu(\bar{\nu})}}{dx\,dy}\left(\text{new measured SF}\right)}{\dfrac{d^2\sigma^{\nu(\bar{\nu})}}{dx\,dy}\left(\text{event generating SF}\right)} \tag{6.7}$$

As discussed in Chapter 4, the Monte Carlo generates "true" variables (x, y and Q^2) for each event. It smears these variables to model detector effects in the data taking. It is the "true" variables that are used in calculating the cross section for each simulated event since the "true" values determine the probability for the theoretical neutrino to interact in the detector.

By contrast, the smeared variables are used to determine the binning since these are the values which would be measured if the simulated event were recorded in the CCFR detector. The smeared variables are the proper ones to use in comparisons of the theory event kinematic distributions to the measured data event distributions.

In addition to smearing there are other adjustments to consider:

(1) The Monte carlo attempts to generate a set of events which mimic what we would see in our detector. To this end corrections are put into the cross section calculation which account for charm mass suppression, the massive boson propagator, and non-isoscalar target effects. We wish to measure the actual quark distributions, not the ones we observe due to these effects. So it is necessary to fit for the SFs with these corrections removed.

(2) It is most efficient to extract values of the SF values as measured at the bin centers. Each event must be weighted to correct for shifting the values to this central position.

These corrections are accomplished through factors which multiply the event weights. These factors are obtained from NUMONTE's cross section generating subroutine SIGMCQ. This routine begins with equation 6.2 as the basis for the ν–N cross section and goes on to apply corrections and enhancements. The physics simulated in this routine is fully discussed in section 4.2.2. For convenience here, I will use the FORTRAN call itself to represent the cross section with various corrections applied. *VFAC*, m_c and *PROP* are arguments for SIGMCQ that turn on or off the isoscalar, charm mass suppression, and massive propagator corrections respectively. In terms of subroutine calls the re-weight looks like:

$$\frac{d\sigma_{new}}{d\sigma_{old}} = \frac{SIGMCQ1}{SIGMCQ2} \times \frac{SIGMCQ3}{SIGMCQ4}. \tag{6.8}$$

*SIGMCQ*1 is a mathematical reconstruction of SIGMCQ via eqn 6.6 which keeps the SF as free parameters. In this expression the SFs are determined at $x_{center}, Q^2_{center}, y_{true}, m_{charm} = 0., VFAC = 0, PROP = false$:

$$\frac{d^2\sigma^{(-)}_{\nu}}{dx\,dy} = \frac{G_F^2 ME}{\pi}\left[\left(1 - y - \frac{Mxy}{2E} + \frac{y^2}{2}\,\frac{1+\frac{4M^2x^2}{Q^2}}{1+R}\right)F_2^{(-)}_{\nu} \pm y\left(1-\frac{y^2}{2}\right)xF_3^{(-)}_{\nu}\right] \tag{6.9}$$

SIGMCQ2 is the value of the cross section which was used to generate the theoretical event (with all correction turned on):

$$SIGMCQ2 = SIGMCQ\left(x_{true}, Q^2_{true}, y_{true}, m_{charm} = 1.31, VFAC = .0567, PROP = true\right). \tag{6.10}$$

The ratio *SIGMCQ3*/*SIGMCQ4* calculates the bin center correction, and returns the charm mass suppression, massive propagator, and non-isoscalar target corrections to the theory event so that the event sums are comparable to the data sums:

$$\frac{SIGMCQ3}{SIGMCQ4} = \frac{SIGMCQ\left(x_{true}, Q^2_{true}, y_{true}, m_{charm} = 1.31, VFAC = .0567, PROP = true\right)}{SIGMCQ\left(x_c, Q^2_c, y_c, m_{charm} = 0, VFAC = 0, PROP = false\right)} \tag{6.11}$$

Notice *SIGMCQ2* equals *SIGMCQ3*, so these factors cancel each other. Putting this together, each "theory" event is constructed the following way:

$$THEORY\ EVENT = \frac{event\ weight \times K_{type}}{SIGMCQ\left(x_c, Q^2_c, y_c, m_{charm} = 0, VFAC = 0, PROP = false\right)} \times$$

$$\frac{G_F^2 ME}{\pi}\left[\left(1 - y - \frac{Mxy}{2E} + \frac{y^2}{2}\frac{1 + \frac{4M^2x^2}{Q^2}}{1 + R}\right)F_2^{(-)\nu} \pm y\left(1 - \frac{y^2}{2}\right)xF_3^{(-)\nu}\right] \tag{6.12}$$

6.1.2 Normalization

There are two normalization factors to consider.

(1) We measure the relative flux as opposed to the absolute flux. The overall normalization is determined by comparing our value of the total cross section to the world average. The values of $\sigma^{\nu N}_{world}/E = .677$ and $\left[\sigma^{\nu}/\sigma^{\bar{\nu}}\right]_{world} = .499$ were taken from the measurements of reference [Sel97] where the average was taken from the isoscalar-corrected cross sections of CCFRR '83, CDHSW '87 and CCFR '90. These values are compiled in Table 6.1.

Table 6.1: World average values of isoscalar-corrected $\sigma^{\nu N}/E$, $\sigma^{\bar{\nu}N}/E$, and $\sigma^{\bar{\nu}}/\sigma^{\nu}$ (including this experiment) for the energy range 30-200 *GeV*. Units are $10^{-38}\ cm^2\ /\ GeV$.

Experiment	$\sigma^{\bar{\nu}N}/E$	$\sigma^{\bar{\nu}N}/E$	$\sigma^{\bar{\nu}}/\sigma^{\nu}$
CCFRR [Bla83xxx]	0.669 ± 0.024	0.340 ± 0.020	0.499 ± 0.025
CDHSW [Ber87xxx]	0.686 ± 0.020	0.339 ± 0.022	0.495 ± 0.010
CCFR [Auc90xxx]	0.659 ± 0.039	0.307 ± 0.020	0.467 ± 0.028
World Avg.	**0.677 ± 0.014**	0.334 ± 0.008	0.493 ± 0.009
This expt.			0.509 ± 0.012
World Avg. + this expt			**0.499 ± 0.007**

(2) The total number of data events depends on the length of the data taking period (the number of MC events on the length of the Monte Carlo generation time). These two numbers must be normalized to each other. Because the data was taken in different modes this normalization is done by event type (neutrino/anti-neutrino, toroid focus/defocus).

The world average cross section is calculated for the region: $20 < E_\nu < 200 GeV, 0 > y > 1, 0 > x > 1$. We obtain a value for our total cross section by integrating eqn 6.6 over x,y and E_ν using the parameterized form of the SF measurements. As can be seen in diagrams 5.8-5.11, the parameterization does a good job of representing our measurements. However, outside the regions where we make SF measurements the parameterization is not constrained. In theory this region could introduce uncertainties. Of particular concern is the non-perturbative region $Q^2<1$ where the cross section may not be modeled accurately. To avoid this potential problem, the normalization between data and MC is done by summing not only the events used in the SF measurements, but also events with *low* Q^2. The cuts for the normalization sums are exactly those listed in section 3.3.4 for the data selection with the following exceptions:

$$E_\nu^{\max} = 200 GeV$$

$$Q^2_{\min} = 0$$

$$E_{had}^{\min} = 0 GeV$$

Thus, each MC event is multiplied by the following factor:

$$K_{type} = \frac{\sigma^{\bar{\nu},\nu}_{CCFR}}{\sigma^{\bar{\nu},\nu}_{world}} \left(\frac{N_{data}}{N_{MC}} \right)_{type} . \qquad (6.13)$$

By including the region $0<Q^2<1$ in the term, N_{MC}, and the cross section calculation, $\sigma^{\nu,\bar{\nu}}_{CCFR}$, the potential problem from the parameterization is minimized.

6.2 Minimizing χ^2

6.2.1 The Minimization Software

The CERNLIB package MINUIT is used to minimize the χ^2 function, by varying the SF values in each (x,Q^2) bin. The SF errors are also found using the MINUIT MINOS package to determine the variation needed to change χ^2 by one unit. MINUIT computes the best-fit SF parameter values and uncertainties, including correlations between the parameters. MINOS calculates parameter errors taking into account both parameter correlations and non-linearities. Most generally MINOS produces most asymmetric errors.

Bin	Xcenter	Q^2center	Ycenter
1	0.015	1.3	0.025
2	0.045	2.05	0.075
3	0.08	3.25	0.125
4	0.125	5.14	0.175
5	0.175	8.15	0.225
6	0.225	12.9	0.275
7	0.275	20.5	0.325
8	0.35	32.5	0.375
9	0.45	51.4	0.425
10	0.55	81.5	0.475
11	0.65	129.2	0.525
12	0.75	204.8	0.575
13	0.85	324.6	0.625
14	0.9	514.5	0.675
15		815.5	0.725
16			0.775
17			0.825
18			0.875
19			0.925
20			0.975

Table 6.2 Bins

6.2.2 Bin requirements

The Bjorken variables x, y and Q^2 are used to separate the data into the bins listed in table 6.2.

.c9.'Table 6.2 Bins'; the variables x,y and Q^2.

Fits are only attempted in (x,Q^2) bins that have data in a minimum of 4 y-bins (2 ν y-bins and 2 $\bar{\nu}$ y-bins). In order to consider a y-bin for this criteria, it must have a minimum of 20 events.

6.2.3 The Fit parameters

Technically σ^{ν} and $\sigma^{\bar{\nu}}$ have six different SFs. However, we have made the following assumptions:

$$2xF_1^{\nu} = 2xF_1^{\bar{\nu}}$$

and

$$F_2^{\nu} = F_2^{\bar{\nu}}.$$

A change of variables is made between $2xF_1$ and R_{long} where

$$R_{long} = \frac{F_2}{2xF_1}(1+\frac{4m^2x^2}{Q^2})-1 \quad . \tag{6.14}$$

The parity violating information is contained in the third SF and thus $xF_3^{\nu} \neq xF_3^{\bar{\nu}}$. As derived in Chapter one:

$$xF_3^{\nu} - xF_3^{\bar{\nu}} = 4x[s(x)-c(x)] \approx 4xs(x). \tag{6.14}$$

Originally measurements were made fitting for all four of the SFs (F_2, R_{long}, xF_3^{ν} & $xF_3^{\bar{\nu}}$) simultaneously. However, correlations between R_{long} and the strange sea were prohibitively large. Alternatively, it was decided to assume a shape for the

strange sea (see below) but still fit for its magnitude *kappa* (κ). This leaves xF_3 expressed in the cross section as:

$$xF_3^{\nu,\bar{\nu}} = xF_3^{aver} \pm \Delta xF_3 \tag{6.15}$$

where a NLO value for ΔxF_3 is obtained by integrating convolutions of the quark distributions with a theoretically determined hard scattering coefficient C_3 [Her80]:

$$\Delta xF_3 = 4x\int_x^1 C_3\left[s(z,Q^2) - c(z,Q^2)\right]dz. \tag{6.16}$$

Values from the CTEQ 2M set [Lai95] are used for $c(z,Q^2)$. A shape for the strange sea comes from a NLO QCD determination of charm production in opposite-sign dimuon (2μ) events [Baz95].

$$xs(x,Q^2) = \kappa\left[\frac{xs^{2\mu}(x,Q^2)}{\kappa^{2\mu}}\right], \tag{6.17}$$

where $\kappa^{2\mu}$ and $xs^{2\mu}(x,Q^2)$ are the magnitude and shape of the strange sea from reference [Baz95]. A proportional factor κ is placed in front of the dimuon shape so that the relative size of $\left(xF_3^{\nu} - xF_3^{\bar{\nu}}\right)$ can be left as a fit parameter.

6.2.4 The Strange Sea

As discussed above, a shape for the strange sea comes from NLO measurements of charm production [Baz95]. The charm production analysis used dimuon events from the same experiment as this analysis. However, since dimuon events are cut from the data set that goes into the analysis of this thesis, the two data sets are independent.

The ν-charm production measurements determined the strange sea parameterized by α and κ where

$$xs(x,Q_0^2) = \kappa(1-x)^{\alpha}\left[\frac{\bar{u}+\bar{d}}{2}\right]. \tag{6.18}$$

Using the $\overline{MS}$ renormalization scheme, these measurements were used to generate values of $xs(x,Q^2)$ in 16 (x,Q^2) bins. For the purpose of this analysis, these 16 measurements were parameterized in each Q^2 bin in the form: $a(1-x)^b x^{-c}$. The resulting fits along with the original measurements and the parameter values can be seen in Figure 6.1. Systematic error studies (see next section) included changing this shape by one σ.

Linear interpolation (in $logQ^2$) was performed to determine values for $xs(x,Q^2)$ at values of Q^2 in between these bins.

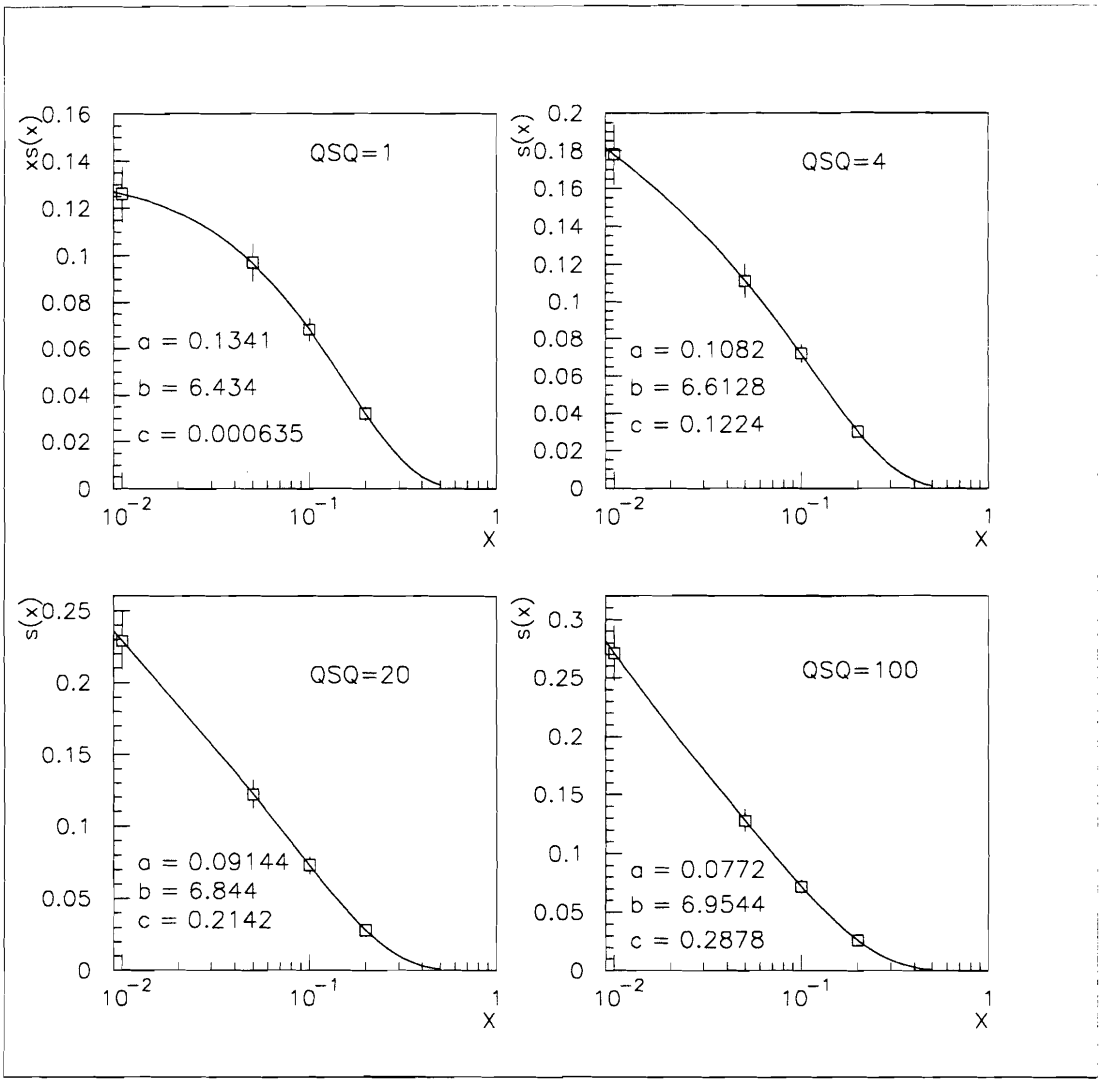

Figure 6.1: LNO Strange SeaThe points are values of $xs(x,Q^2)$ defined at NLO using the $\overline{MS}$ renormalization scheme from [Baz95]. The curve is a parameterization of the form $a(1-x)^b x^{-c}$ made separately in each Q^2 bin. The resulting fit parameters are given.

6.2.5 Three Parameter and Four Parameter fits

χ^2 is left as a function of four parameters: F_2, R_{long}, $xF_3^{average}$, and κ. Two types of fits were performed:

(1) THREE PARAMETER FITS: Values for R_{long} were determined by fixing $\kappa = \kappa_{2\mu} = 0.477$ and allowing Minuit to fit for F_2, R_{long} and $xF_3^{average}$ in each (x,Q^2) bin.

(2) FOUR PARAMETER FITS: Four parameter fits were done by allowing κ to vary between Minuit fits for F_2, R_{long} and $xF_3^{average}$. Minuit was not explicitly used to vary κ because the running time to perform 3 parameter fits in 50 (x,Q^2)-bins while varying the global parameter κ was prohibitive. Instead, separate fits were done for ten different κ values with

$$\kappa = C\kappa_{2\mu},$$

where C = 0.2, 0.4, 0.6, 0.8, 1.0, 1.2, 1.3, 1.4, 1.5, 1.6, 1.8, 2.0, 2.2 and 2.4.

In the first five x-bins, the values of χ^2 that resulted from these different κ fits were summed over Q^2:

$$\chi^2(x)\Big|_{\kappa(x)} = \sum_i \chi^2(x,Q_i^2) \quad . \tag{6.20}$$

These κ -dependent χ^2 sums were plotted in each x-bin and parameterized in the form:

$$\chi^2(\kappa(x)) = p_1 + p_2\kappa(x) + p_3\kappa^2(x). \tag{6.21}$$

An optimal value for κ was determined in each of the first five x-bins by finding the value that minimized χ^2. The error in κ was then determined by finding the κ value corresponding to $\chi^2 = \chi^2_{\min} + 1$. The resulting values and parameterizations are shown in figure 6.2. A global value for κ. is obtained by averaging the

measurements from the individual x-bins. Figure 6.3 shows the individual and averaged values.

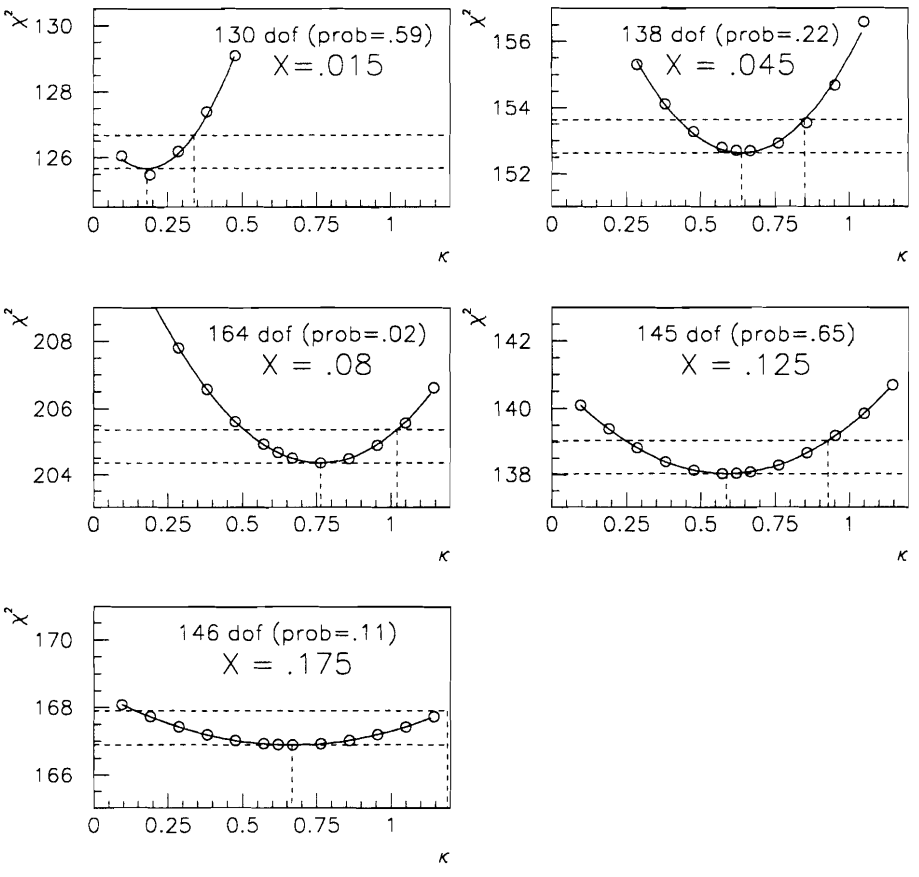

Figure 6.2: κ fit results in the first 5 x-bins. Values for $\chi^2(x,\kappa)$ are plotted and parameterized as $\chi^2(\kappa(x)) = p_1 + p_2\kappa(x) + p_3\kappa^2(x)$ in each x-bin. The optimal κ is found which minimizes the χ^2 parameterization and the error is found by increasing χ^2 by one unit. The resulting fit probability is given.

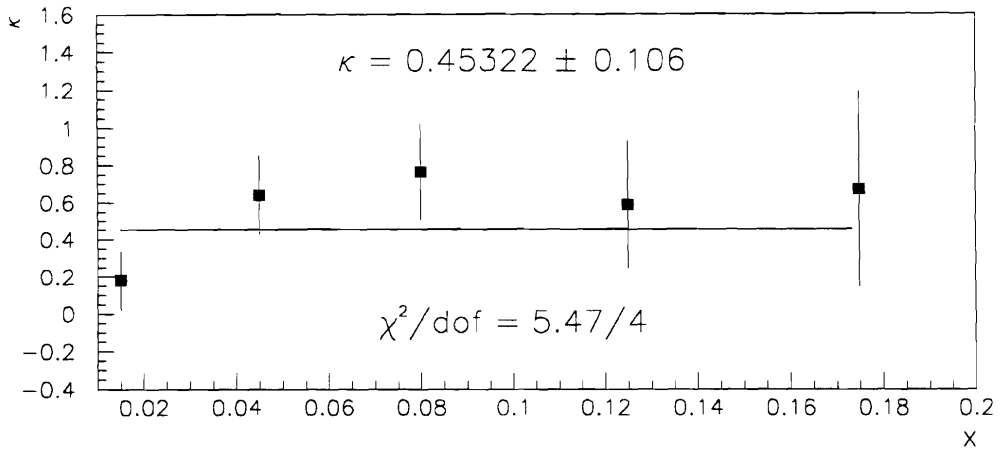

Figure 6.3: Global κ result. A global value for κ is found by averaging the results from the first 5 x-bins. The resulting χ^2 for this average and the resulting global value for κ are given.

6.3 Systematic Errors

Estimates of the systematic uncertainties are obtained by varying internal model parameters by their uncertainties and noting the corresponding shift in the SF measurements. The systematic uncertainties are itemized in the following section. The values are reported in Table 7.1 (for κ), Appendix C (for R_{long}) and Appendix E

(for F_2 and xF_3). The sources of uncertainty are assumed to be independent of one another, and the overall systematic uncertainty is found by adding the individual contributions from each source in quadrature.

MUON AND HADRON ENERGY SCALES

The hadron and muon energy calibrations for the experiment are known to within 1% [Sak90]. Alternate data sets were generated with the varied calibrations. These alternate sets result in new flux measurements. From the new data sets and the new flux measurements the SF are re-extracted and new fits are performed to determine κ.

FLUX CORRECTION

As explained in Chapter 5, the relative flux measurements are done by counting low E_{had} events with corrections that come from the slope of the line that fits these events.

$$N(\nu < \nu_0) = \Phi(E)\int_0^{\nu_0} d\nu A\left(1+\frac{\nu}{E}\left(\frac{B}{A}\right)-\frac{\nu^2}{2E^2}\left(\frac{B}{A}-\frac{\int F_2\tilde{R}}{\int F_2}\right)\right) \tag{6.22}$$

A statistical error on the slope is determined from the linear fit. This error is used as the uncertainty in $<B/A>$ in order to generate new flux measurements for the systematic study. Errors for the two experiments are determined independently. The SF are extracted with the new flux files and new fits are performed to determine κ.

CROSS SECTION NORMALIZATION

A determination of the world average cross section complete with errors was made in reference [Sel97] for use in normalizing the relative flux. For this systematic study, the central values were changed by the following amounts as determined in [Sel97]: 2.1% for $\sigma_{world}/\sigma_{ccfr}$ and 1.4% for $\sigma_{\bar{\nu}}/\sigma_{\nu}$. There is no need to re-extract the flux for these shifts since they do not change the relative values. New SF values are extracted with the altered normalization and subsequent fits for κ are performed.

CHARM QUARK MASS:

The cross section calculations used in this analysis start with a leading-order (LO) model which contains a parameter associated with the charm mass. This charmed mass parameter was measured as m_c=*1.31±0.24* in an analysis of dimuon events [Rab92]. The parameter is used in a slow rescaling correction to the bare cross section. In light of NLO measurements we know the physical charm mass to be significantly larger. However, when this analysis uses the LO model, this value (m_c=*1.31±0.24)* remains the correct one to use. It should be interpreted as a parameter of the model rather than the physically significant mass measurement. For the systematic error determination, each MC event was reweighted by a ratio of cross sections using the varied values for m_c. SIGMCQ is a FORTRAN routine in NUMONTE which calculates the LO differential cross section and is used to calculate a reweight factor for each MC event with the m_c parameter changed:

$$reweight = \frac{SIGMCQ(m_c \pm \delta m_c)}{SIGMCQ(m_c)}. \qquad (6.23)$$

Using the reweighted events, new SF were extracted and a new value for κ was determined.

CHARM SEA

For a systematic error study, an alternate charm sea distribution:

$$xc(x) = 0.10 * xs(x)$$

was used in determining $xF_3^{\nu} - xF_3^{\bar{\nu}}$. The justification for using this charm sea distribution comes from EMC F_c^2 results [Aub83].

STRANGE SEA

For use in determining $xF_3^{\nu} - xF_3^{\bar{\nu}}$, measurements of the strange sea from a NLO dimuon analysis [Baz95] were parameterized in the form $a(1-x)^b x^{-c}$. Two alternative parameterizations are made and used to determine the systematic errors. These parameterizations were created by fitting (to the same form) the strange sea central values plus or minus the errors from [Baz95]. All three resulting parameterizations are shown in diagram 6.4 along with the original measurements and errors.

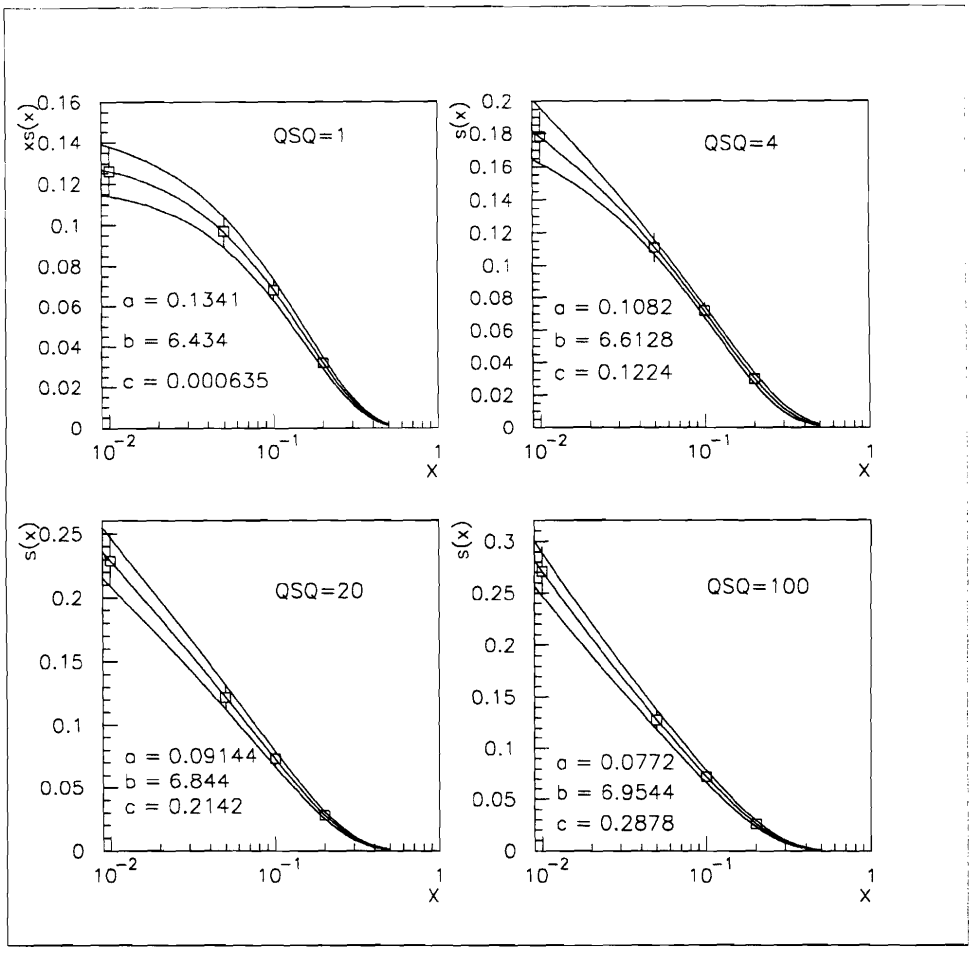

Figure 6.4: Strange sea used in systematic error study. The points are NLO strange sea measurements described in section 6.2.4. The 3 curves show the central parameterization used in determining $xF_3^{\nu} - xF_3^{\bar{\nu}}$ and the two alternate parameterizations used in the systematic studies.

6.4 Testing the method

6.4.1 Fake Data Studies

The SF extraction method used here has been tested by taking an independent Monte Carlo event sample as "fake data". The "fake data" and corresponding MC event sample contained 1 million events. Given the values of R_{long} and the strange sea

which were used by the MC to generate these event sets, it has been shown that the method returns these values within statistical errors. Figure 6.5 plots the values that result from the fake R_{long} fit, along with a curve indicating the original values used to generate the events. The resulting $\chi^2/dof = 71/65$ indicates a good result.

A second fake data study was done fitting for $\left(xF_3^{\nu} - xF_3^{\bar{\nu}} \right)$. This study also produces a good fit plotted in Figure 6.6, resulting in $\chi^2/dof = 64/66$.

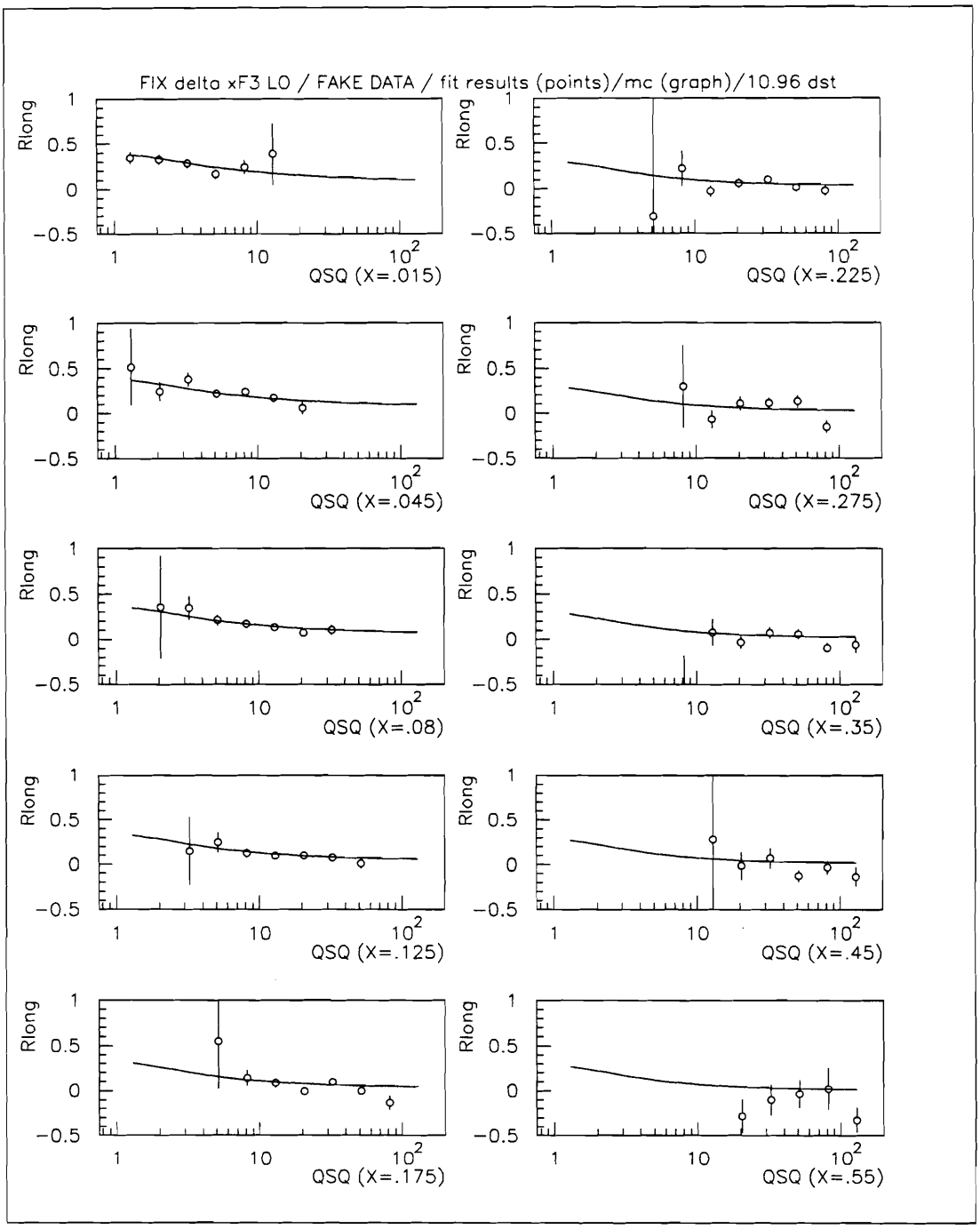

Figure 6.5: R_{long} results from fake data study. The curve shows the value of R that was used in generating fake events. The points are the resulting fit values which show good agreement with the generating function: $\chi^2 = 71/65$.

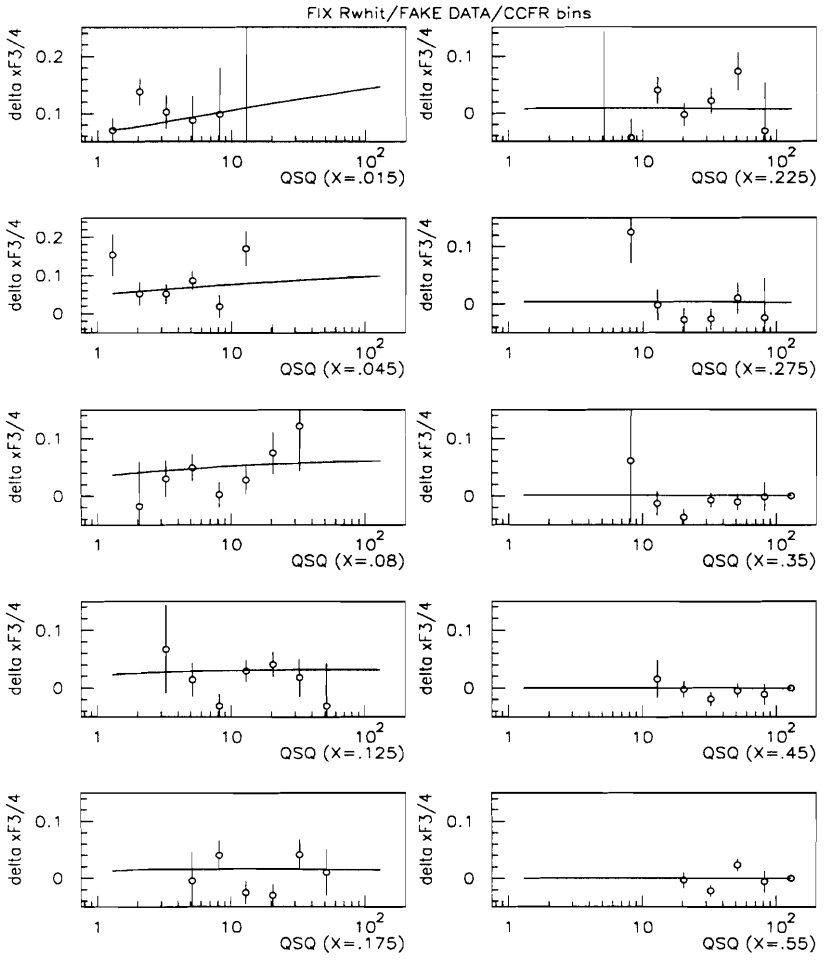

Figure 6.6: ΔxF_3 results from fake data study. The curve shows the value of ΔxF_3 that was used in generating fake events. The points are the resulting fit values which show good agreement with the generating function: $\chi^2 = 64/66$.

6.4.2 Comparing to Previous CCFR Measurements

Fixing values for R_{long}, $\left(xF_3^{\nu} - xF_3^{\bar{\nu}}\right)$, the SF parameterization, and the flux at values used by the previous CCFR SF analysis [Sel97] a two parameter fit was made. Comparisons of F_2 and xF_3 between this fit and previous results can be seen in Figures 6.7 - 6.9. The measurements agree to a few percent.

The previous analysis used the same data set. However, there are a few notable differences in the previous [Sel97] method and this two parameter fit:

1) The previous method for extracting SF, sums the events in one (x,Q^2) bin and explicitly determines the values for F_2 and xF_3 from that one number. This analysis forms a χ^2 in one (x,Q^2) bin which sums over 20 y-bins for νs, and 20 y-bins for $\bar{\nu}$s, weighting each one with its cross sectional dependence. This χ^2 is then minimized for the optimum values of the F_2 and xF_3 in that (x,Q^2) bin.

2) The previous method used an older CCFR Monte Carlo called the "fast" Monte Carlo. This analysis used a newer version called NUMONTE. The differences in these MC are not large, but are listed in section 4.1.

3) The previous method uses a cut (called TWOGAPS) which requires fitted tracks in more than one of the toroid gaps. This cut was removed for this analysis in order to widen the y-distribution. This analysis only requires a fitted track for the muon in the first toroid gap.

4) The previous method uses a slightly different version of the LO strange sea. This analysis uses the shape and magnitude of the strange sea as measured by reference [Baz95]. The previous method uses this same shape but allows the magnitude to be fit by the SF parameterization.

The primary difference in the two methods was circumvented for this 2 parameter fit. For the three parameter fits, R_{long} and κ are allowed to float and hence be measured. Whereas Seligman's R_{long} is set to the value determined by the Whitlow parameterization [Whi90b], and κ is determined by the Buras-Gaemers SF parameterization. The results of the three parameter fits are shown in Figures 7.5-7.9 both in direct comparison and in ratio form. Even for these fits the two measurements agree within a few percent.

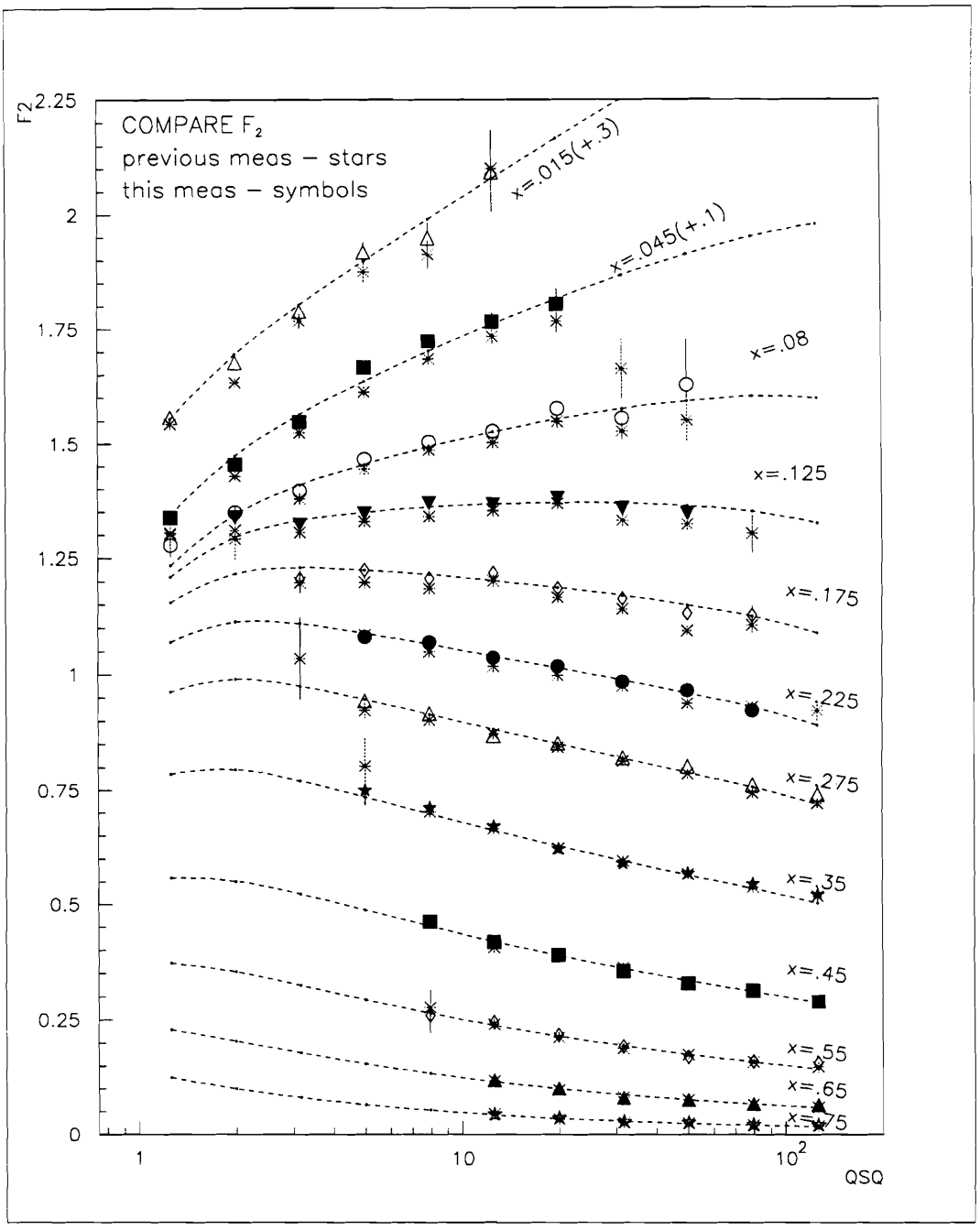

Figure 6.7: F_2 results from 2 parameter fit. Comparison of previous CCFR measurement [Sel97] of F_2 and the measurements of F_2 from this analysis which was made by fixing values for R_{long}, $\left(xF_3^{\nu} - xF_3^{\bar{\nu}} \right)$, the SF parameterization, and the flux at values used by the previous CCFR SF analysis. The dashed line shows the SF parameterization.

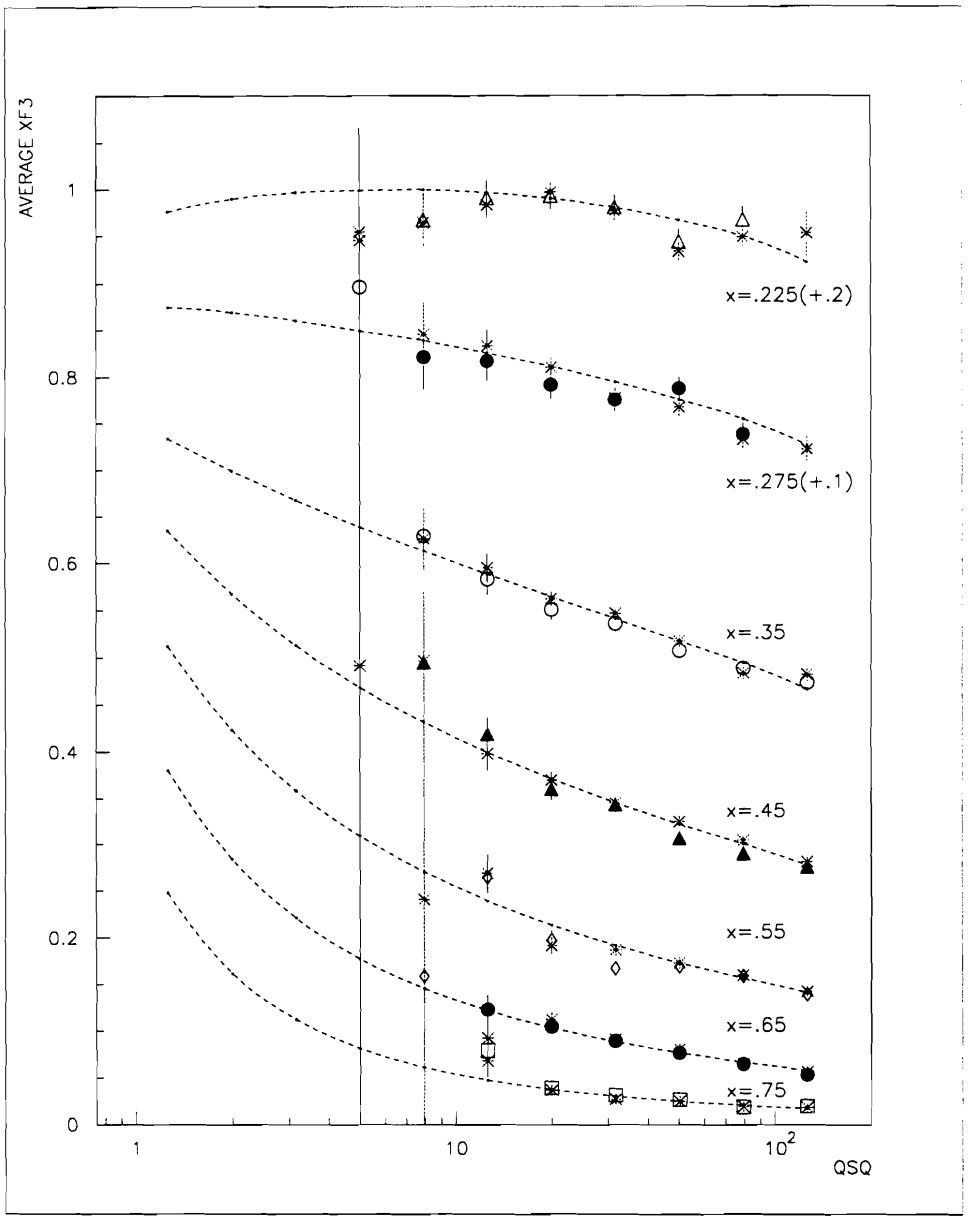

Figure 6.8: xF_3 results from 2 parameter fit. Comparison of previous CCFR measurement [Sel97] of xF_3 and the measurements of xF_3 from this analysis which was made by fixing values for R_{long}, $\left(xF_3^{\nu} - xF_3^{\bar{\nu}}\right)$, the SF parameterization, and the flux at values used by the previous CCFR SF analysis. The dashed line shows the SF parameterization. This plot shows the mid-to-higher x-bins.

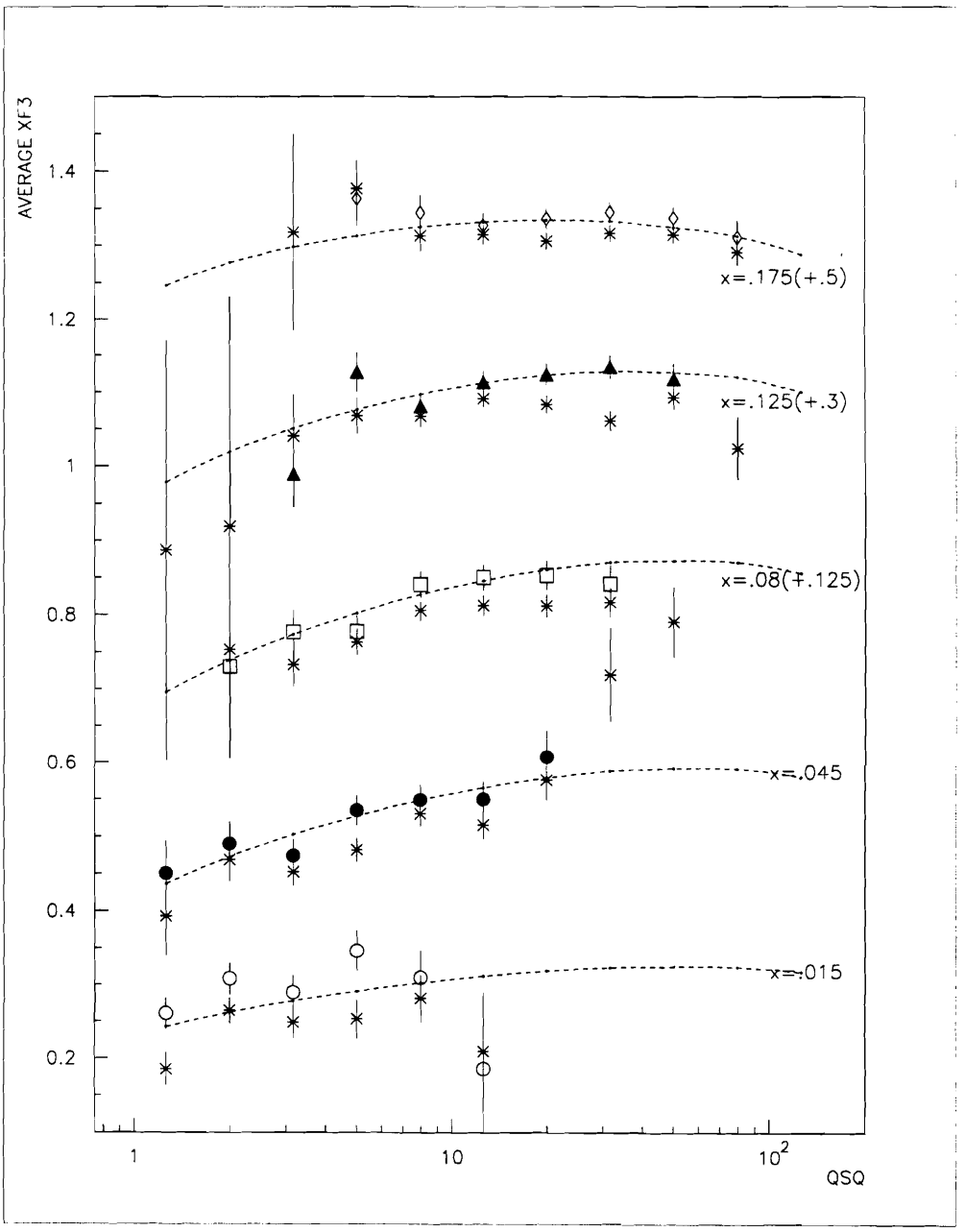

Figure 6.9: xF_3 results from 2 parameter fit. Comparison of previous CCFR measurement [Sel97] of xF_3 and the measurements of xF_3 from this analysis which was made by fixing values for R_{long}, $\left(xF_3^{\nu} - xF_3^{\bar{\nu}}\right)$, the SF parameterization, and the flux at values used by the previous CCFR SF analysis. The dashed line shows the SF parameterization. This plot shows the lower x-bins.

7 Results and Comparisons

This analysis uses the SFs, F_2, R_{long}, xF_3^{ν}, and $xF_3^{\bar{\nu}}$, as parameters to fit the MC generated y-distributions to the data y-distributions. After completing an iterative cycle, the final SF fits result in 4 sets of measurements: $R_{long}(x,Q)$, $F_2(x,Q)$, $xF_3^{av}(x,Q^2)$, and a global $\kappa = 2s/(\bar{u}+\bar{d})$ measurement. This chapter presents these measurements in both tabular and graphic formats along with statistical and systematic errors. Comparisons are made to other world measurements. The resulting y-distributions are presented in Appendix A; a typical example is shown in figure 7.1.

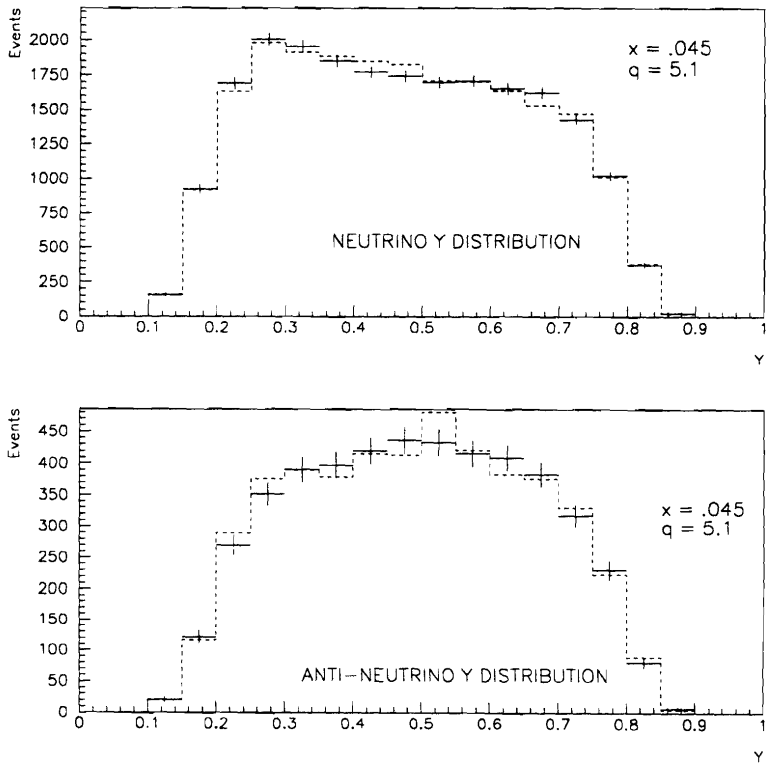

Figure 7.1: ν and $\bar{\nu}$ y-distributions for (x=.045, Q^2=5.1) Data (dashed lines) and MC (solid lines with statistical errors) y-

distributions are shown. These MC y-distributions result from the final fit with a $\chi^2/dof = 27.7/25$ (this is for the sum over ν and $\bar{\nu}$ y-bins).

7.1 R_{long} Measurements

The fit results for R_{long} are shown in Figure 7.2 along with R_{long} measurements from other experiments and the functional parameterization by Whitlow [Whi90b]. Whitlow fit all of the available measurements of R_{long} currently available in 1990 to a simple polynomial form.

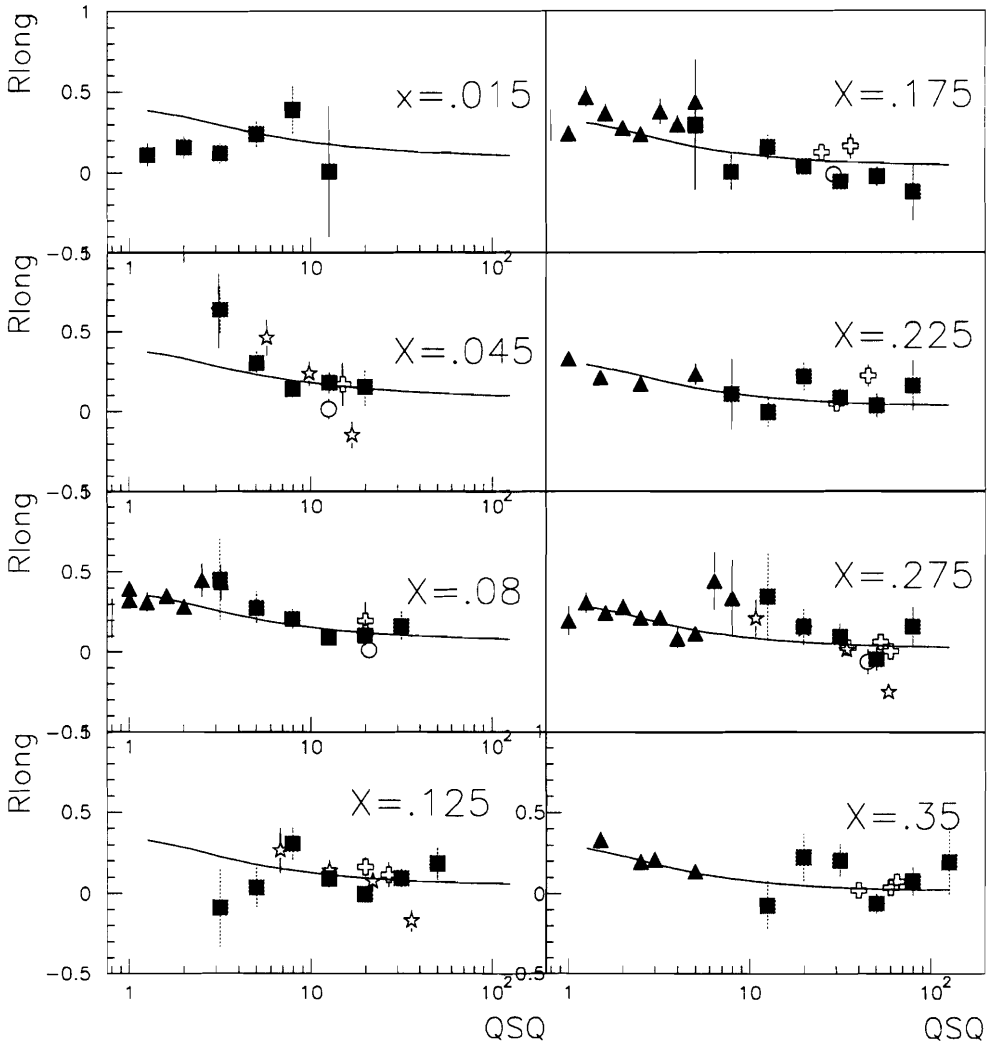

Figure 7.2: World R_{long} measurements. Measurements from this analysis *(square)*, SLAC *(triangle)* [Whi90a], EMC *(circle)* [Aub85], CDHS *(star)* [Ber91], BCDMS (cross) [Ben90]. Statistical and systematic errors are added in quadrature. The Whitlow polynomial parameterization is a fit to available measurements in 1990 *(solid line)* [Whit90b].

The R_{long} measurements of this analysis are in good agreement with the previously existing ones in regions of overlap. They bridge high and low Q^2 measurements from other experiments in many x-bins.

The region below $x=.03$ is particularly interesting. This analysis presents the first Q^2-dependent R_{long} measurements in this low-x region where Whitlow's parameterization is just an extrapolation. The new measurements do not agree with the parameterization, being as much as 50-60% lower in places. There are other measurements in this low-x region recently presented by NMC [Arn97] which were made by integrating data over Q^2. The NMC x-binning is much finer. These NMC values are plotted for comparison in figure 7.3 along with the values of x at which they were measured. The two NMC x-bins ($x=.0125$ and $x=.0175$) closest to the first x-bin of this analysis ($x=.015$) agree well with the average Q^2 behavior of our new R_{long} measurements in the first bin.

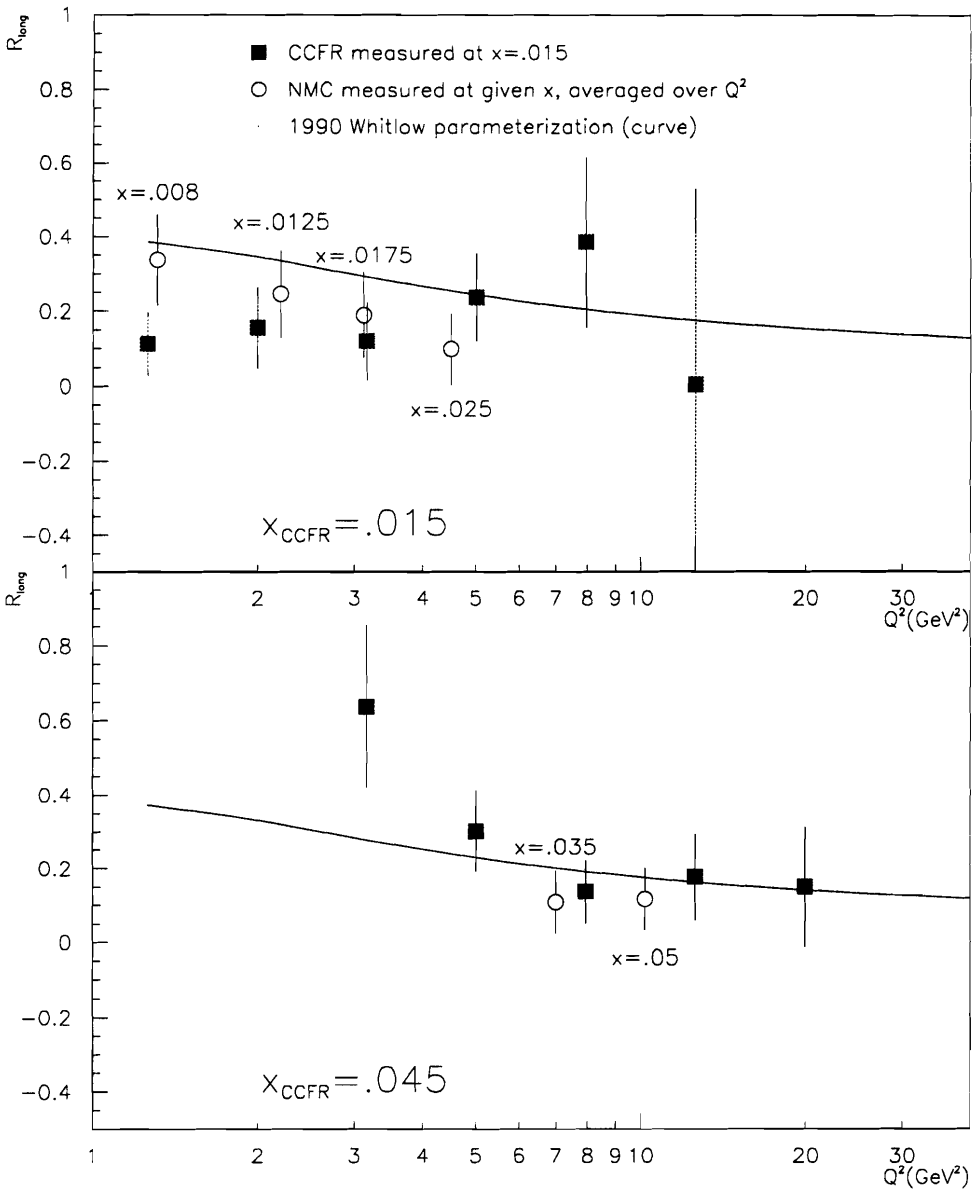

Figure 7.3: Comparison of CCFR and NMC R_{long} measurements. The first two CCFR xbins: *x=.015 (top)* and *x=.045 (bottom)* are shown with CCFR results in solid squares and NMC results [Arn97] in open circles. NMC measurements were made at various x values (shown) and averaged over all Q^2. Statistical and systematic errors are added in quadrature. The curve shows the Whitlow parameterization [Whi90b].

Theory predicts the contributions to R_{long} from the various orders of a perturbative QCD calculation, and from non-perturbative calculations to have different Q^2 dependencies. Comparisons to R_{long} data can be used to constrain models involving gluon distributions and non-perturbative contributions. In Figure 7.4 a QCD-inspired parameterization [Yan96] is plotted for R_{long} in the first x-bin using various parton distributions. This parameterization begins with the QCD calculation of R_{long} [Alt78]:

$$R_{QCD}(x,Q^2) = \frac{\alpha_s(Q^2)x^2}{2\pi 2xF_1(x,Q^2)} \int_x^1 \frac{8dz}{3z^3} \left[F_2(x,Q^2) + 4f(1-\frac{x}{z})zG(x,Q^2) \right], \qquad (7.1)$$

and incorporates the effects of massive heavy quarks, and a massive nucleon target. The calculation also includes a contribution from higher twist effects which has been phenomenologically determined from R_{long} data.

Global fitters use various data to determine predictions for the parton distributions. Although the gluons contribute to F_2, which is well measured over a large kinematic region, there is a limited amount of data which can be used solely to determine the shape of the gluon distribution. The gluon distribution is conventionally parameterized as

$$xg(x) = Ax^{-\lambda}(1+\gamma x)(1-x)^{\eta}.$$

This analysis contributes points to the important "cross over region" (x~0.01) where the $x^{-\lambda}$ shape determined by the lower-x HERA $\partial F_2 / \partial \log Q^2$ data crosses over into the $(1-x)^{\eta}$ shape determined from the higher-x prompt photon data [Mar96b]. The discrepancy between MRS predictions and the points from this analysis at

x=0.015 (Figure 7.4) suggest that including this data and the new NMC points should be quite useful.

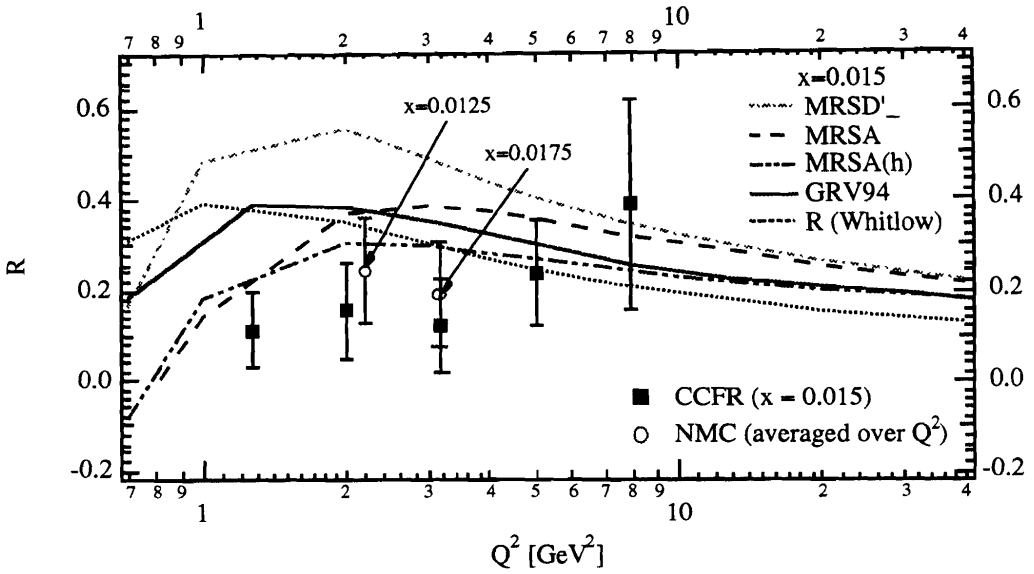

Figure 7.4: R_{long} predictions at low-x from reference [Yan96] for various parton distributions.

A table of all R_{long} measurements from this analysis (with statistical errors and correlations to F_2 and xF_3) is presented in Appendix B. R_{long} values were determined for x-bins higher than those in Figure 7.1, but these values were consistent with zero with large errors and hence not shown; their values are presented in the tables. A table which breaks down R_{long} systematic errors is presented in Appendix C.

7.2 κ Results

The difference between xF_3^{ν} and $xF_3^{\bar{\nu}}$ results in a measurement of the size of the strange sea relative to the non-strange sea:

$$\kappa = \frac{2s}{\bar{u}+\bar{d}} = 0.453 \pm 0.106 \pm \begin{matrix} 0.028 \\ 0.096 \end{matrix} \qquad (7.2)$$

This new measurement is in good agreement with the NLO dimuon result of reference [Baz95]: $\kappa^{2\mu} = 0.477 \pm 0.045 \pm 0.023 \pm 0.021$ where the first error is statistical, the second is systematic and the third is the uncertainty due to QCD scale. The agreement between these two measurements is a good indicator that the QCD phenomenology associated with the strange sea is being properly modeled. A breakdown of the systematic errors on κ from the present analysis are given in table 7.1.

Systematic Quantity being studied	Shift in systematic quantity being studied	$\frac{\Delta\kappa}{\kappa}$ result	$\Delta\kappa$ resulting from -shift in Systematic Quantity	$\Delta\kappa$ resulting from +shift in Systematic Quantity
Alternate Charm Sea	c(x) = 0.1 s(x)	14%	-0.0621	not applicable
Hadron Calibration	1%	5%	-0.0207	+0.0211
Muon Calibration	1%	3-15%	+0.0137	-0.0697
B/A flux correction E770	+21%	0.2%	+0.0010	-0.0011
B/A flux correction E744	+29%	0.6%	+0.0002	-0.0004
$\sigma^{\nu}_{CCFR} / \sigma^{\nu}_{world}$	2.1%	1%	+0.0058	-0.0053
$\sigma^{\nu} / \sigma^{\bar{\nu}}$	1.4%	0.1%	+0.0005	-0.0008
m_c	18%	2%	+0.0087	-0.0108
$xs(x,Q^2)$	10%	1%	-0.0023	+0.0051
Total Added in Quadrature			+ Sys.	+0.028
			- Sys.	-0.096
			$\pm$Stat.	$\pm$0.106

Table 7.1: Systematic and Statistical errors for κ.

This measurement of κ can be combined with two independent results to obtain a measurement of the CKM matrix element $|V_{cs}|$. From ν–*charm* production, $(\frac{\kappa}{\kappa+2}|V_{cs}|^2 B_c = (2.00 \pm 0.10 \pm 0.06 \pm 0.10) \times 10^{-2})$ is measured where the first error is statistical the second is systematic and the third is the uncertainty due to QCD μ^2 scale [Baz95]. A value for B_c ($B_c = 0.099 \pm 0.012$) is obtained by

combining charmed particle semileptonic branching ratios with ν production fractions [Baz95]. The resulting measurement of $|V_{cs}|$ is

$$|V_{cs}| = 1.05 \pm 0.10 \pm \begin{matrix} 0.07 \\ 0.11 \end{matrix}. \tag{7.3}$$

This agrees with a value of $|V_{cs}|_{De3} = 1.01 \pm .18$ [Phy96] determined from the D_{e3} decay rate. The D_{e3} result depends on theoretical assumptions about the D form factor at $Q^2=0$. By contrast, the measurement from this analysis has few theoretical assumptions and thus represents the most precise experimental determination of $|V_{cs}|$ available.

7.3 F_2 and xF_3 measurements

The F_2 and xF_3 measurements of this analysis are shown in comparison with the previous CCFR measurements [Sel97] in figures 7.5-7.7. This analysis and the previous one used different SF extraction techniques and different MCs. Also, the previous CCFR SF analysis used the Whitlow parameterization for R_{long}, and a LO dimuon value for κ [Rab92]. A more complete discussion of the differences is contained in Section 6.4.2.

Ratio plots are shown as figures 7.8 and 7.9. These ratios compare F_2 and xF_3 measurements for this new analysis and the previous analysis of Ref [Sel97]:

$$R_{new/old} = F_{new} / F_{old} \ ,$$

where $F=(F_2, xF_3)$. The relative errors on the new measurements are plotted as the errors on the ratio: $\delta R_{new/old} = \delta F_{new} / F_{new}$. However, one must keep in mind that

the new and old values are highly correlated. The ratio plots confirm that the two measurements agree within a few percent. The strong coupling constant α_s was determined from the previous measurement by considering the slopes on the SFs (particularly for $0.35>x>.65$). The ratio plots indicate that these slopes agree as well.

A table of all F_2 and xF_3 measurements from this analysis (with statistical errors and correlations) is presented in Appendix D. A table which breaks down F_2 and xF_3 systematic errors is presented in Appendix E.

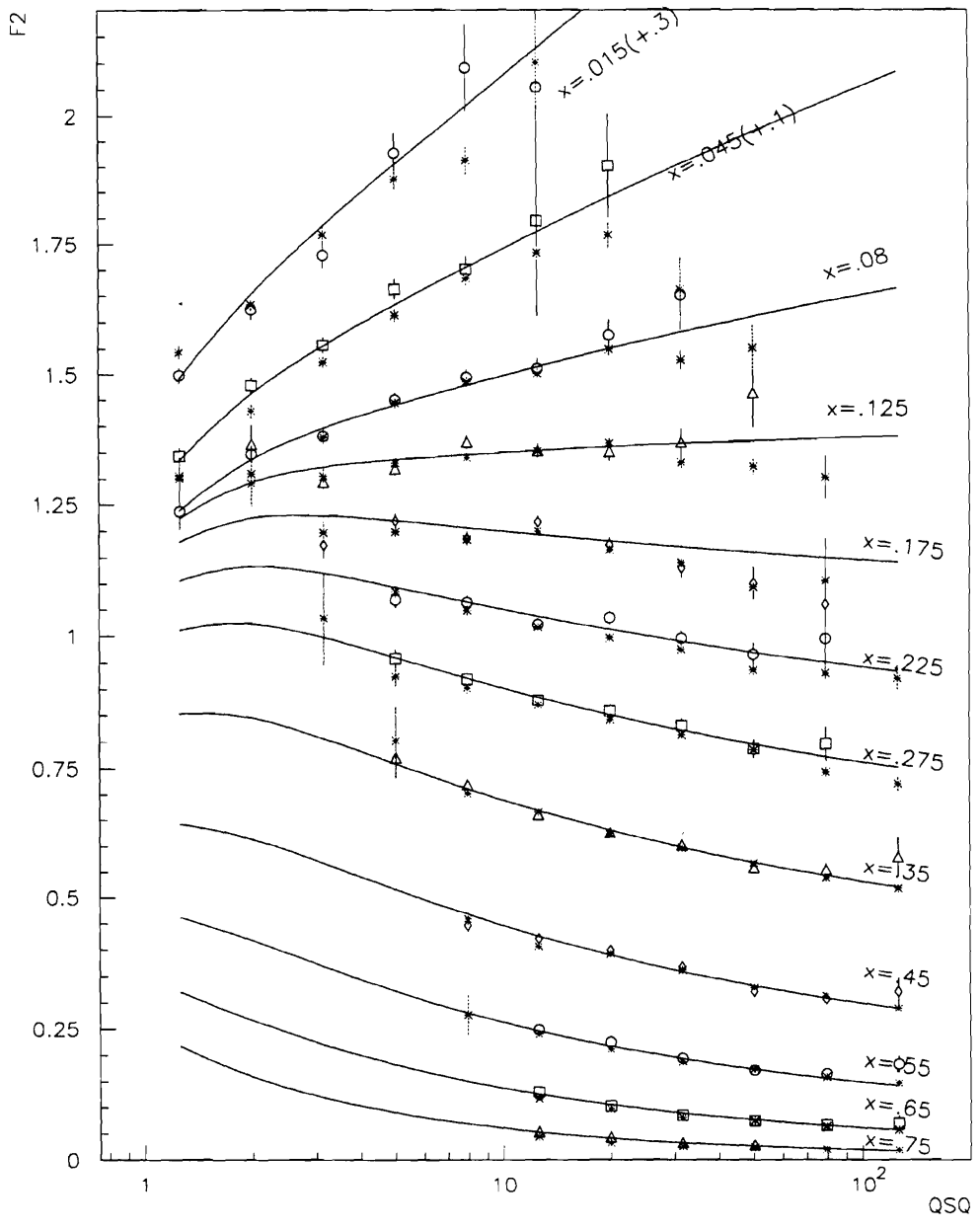

Figure 7.5: New and previous CCFR F_2 measurements. Measurements from this analysis (open symbols) compared to previous CCFR F_2 measurements (stars) [Sel97]. The curve shows the SF parameterization. All errors are statistical only.

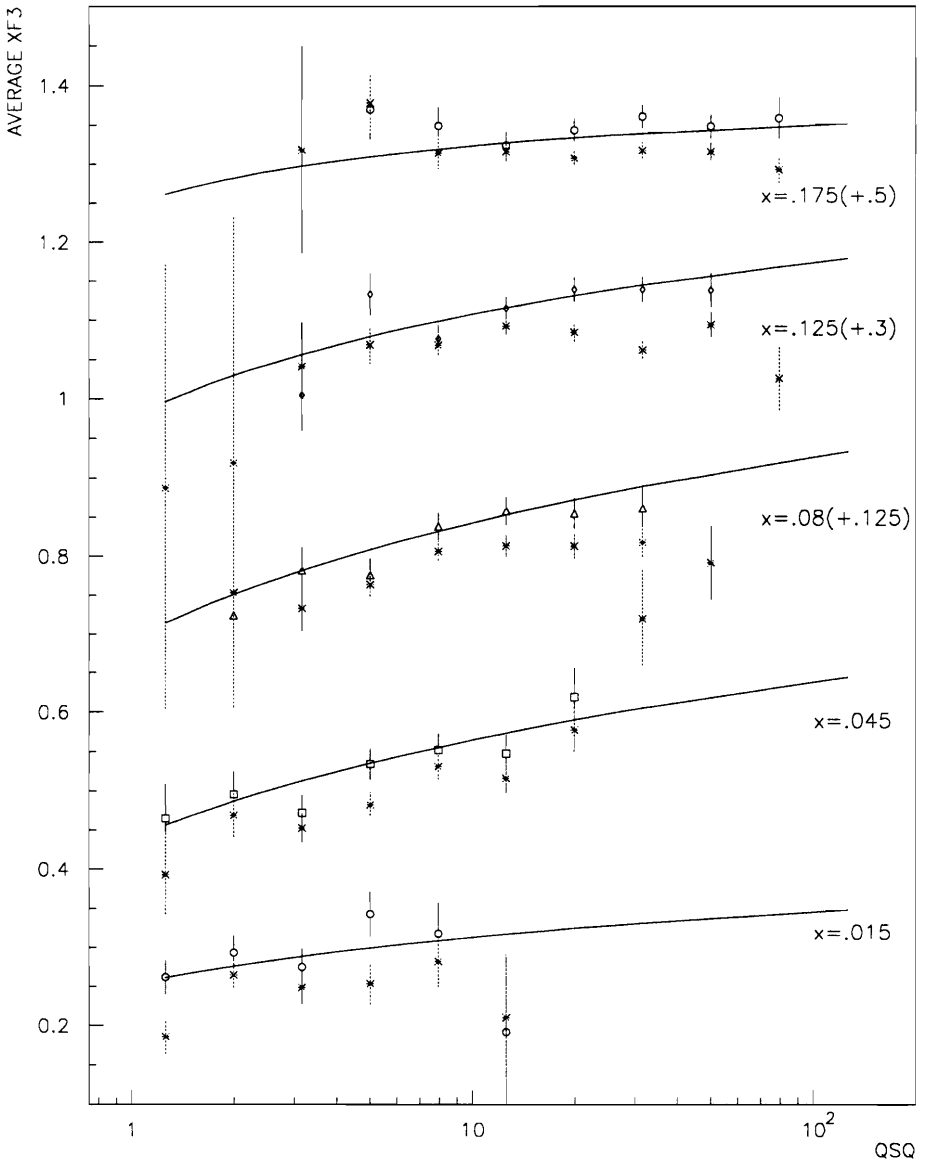

Figure 7.6: New and previous CCFR xF_3 measurements (1st 5 x-bins) . Measurements from this analysis (open symbols) compared to previous CCFR measurements (stars) [Sel97]. The curve shows the SF parameterization. All errors are statistical only.

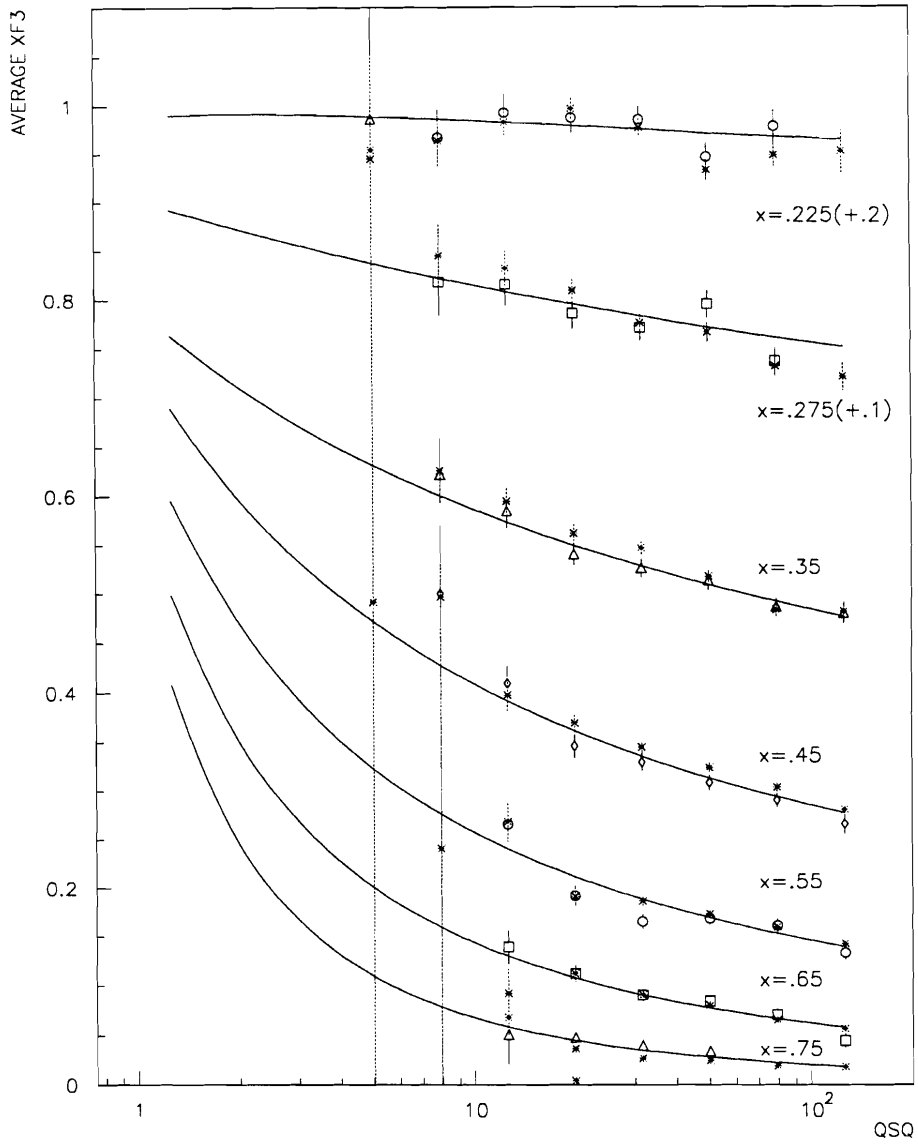

Figure 7.7: New and previous CCFR xF_3 measurements (last 7 x-bins). Measurements from this analysis (open symbols) compared to previous CCFR measurements (stars) [Sel97]. The curve shows the SF parameterization. All errors are statistical only.

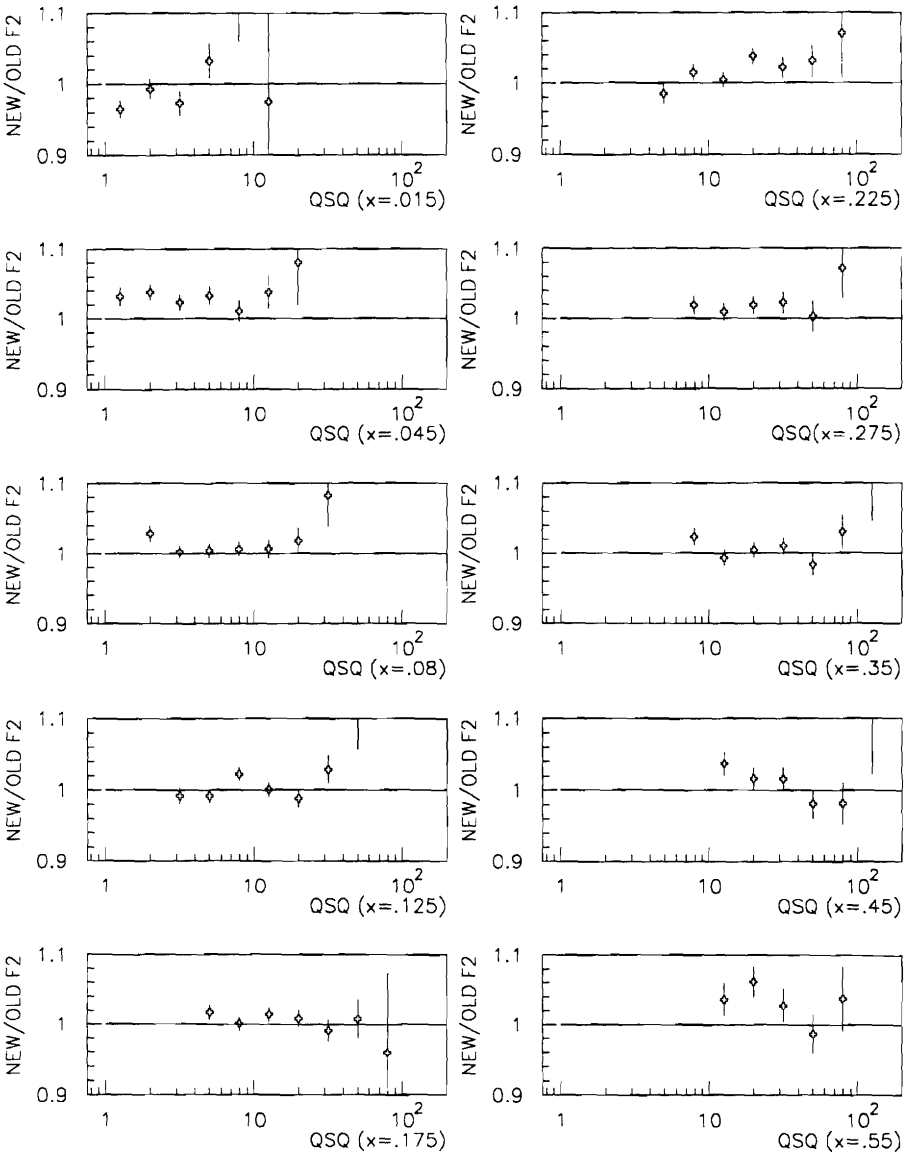

Figure 7.8: Ratio of new and old [Sel97] CCFR F_2 measurements. The error plotted is $\delta R_{new/old} = \delta F_2^{new} \Big/ F_2^{new}$.

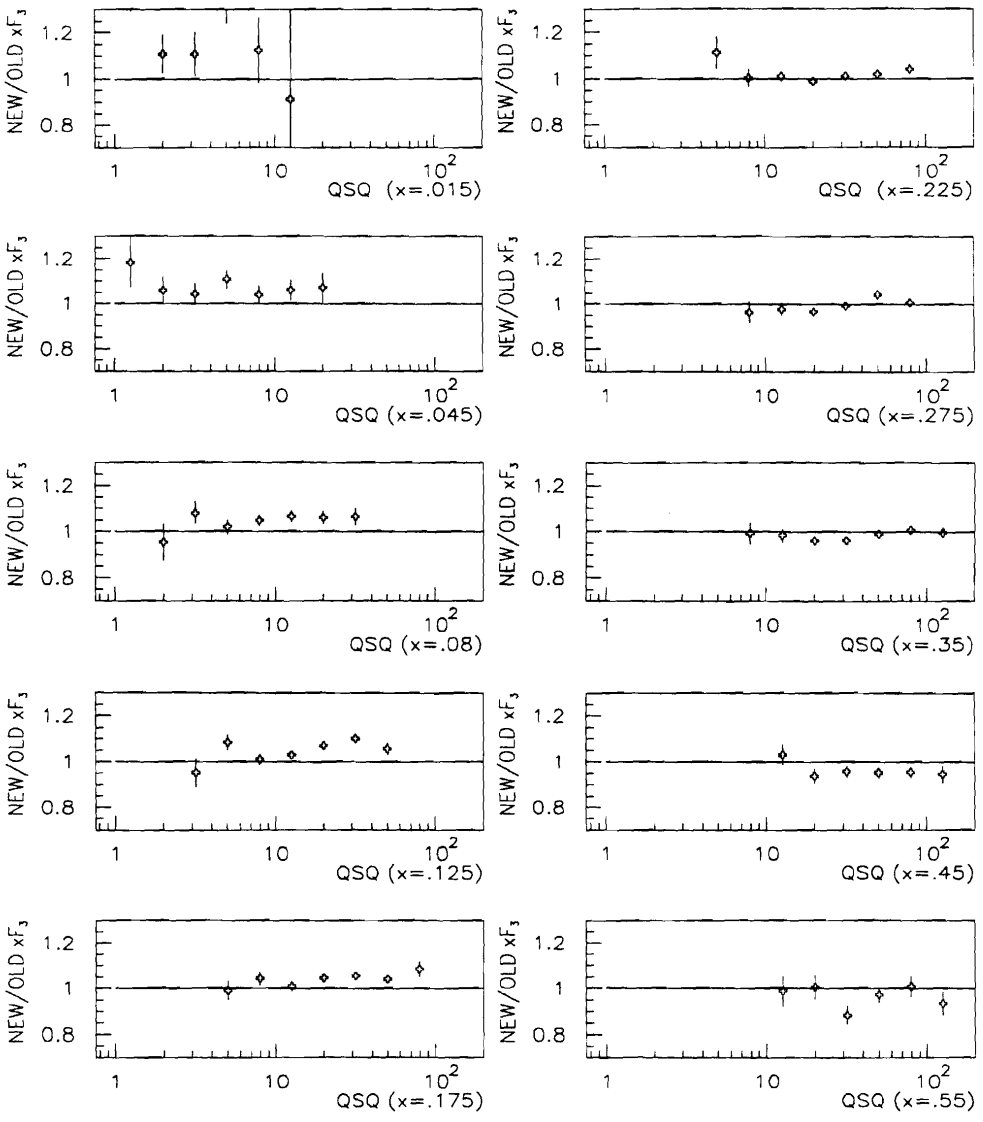

Figure 7.9: Ratio of new and old [Sel97] CCFR xF_3 measurements. The error plotted is $\delta R_{new/old} = \delta x F_3^{new} / x F_3^{new}$.

7.4 Conclusions

Deep inelastic ν scattering has long been an important source of information on nucleon structure. The momentum distributions of different quark flavors can be

uniquely measured with neutrinos due to the properties of the weak interaction. Experimentally, the cross section is relatively flat with energy and momentum transfer Q^2 which minimizes corrections due to resolution smearing and acceptance. In this analysis the large ν ($\bar{\nu}$) data sample from the CCFR experiment has been used to determine four structure functions $F_2, R_{long}, xF_3^{\nu}, and\ xF_3^{\bar{\nu}}$. These SF are crucial inputs for determining the parton distributions which are used by most high-energy particle experiments for tests of the Standard Model.

The comparison of ν and $\bar{\nu}$ scattering isolates the valence quarks and can be used to probe the strange quark components. The difference in xF_3^{ν} and $xF_3^{\bar{\nu}}$ provides a measurement of the relative magnitude of the strange sea in the important low-x region where gluon and sea effects are at a maximum.

$$\kappa = \frac{2s}{\bar{u}+\bar{d}} = 0.453 \pm 0.106 \pm \begin{matrix} 0.027 \\ 0.096 \end{matrix} \tag{7.4}$$

This κ is in good agreement with the value previously measured from ν–*charm* production $\kappa^{2\mu} = 0.477 \pm .045 \pm .023 \pm .026$ [Baz95]. A measurement of the CKM matrix element $|V_{cs}|$ is also obtained by combining this inclusive scattering result for κ with measurements from Ref [Baz95]:

$$|V_{cs}| = 1.05 \pm 0.10 \pm \begin{matrix} 0.07 \\ 0.11 \end{matrix}. \tag{7.5}$$

This $|V_{cs}|$ measurement stands as the most precise experimental determination to date, relying on few theoretical assumptions.

R_{long}, an important link to the gluon distribution, is measured in x-bins ranging from $0.015<x<0.6$ and $1<Q^2<130$. Once again, the low-x region is important and

interesting. Only one other experiment, NMC, has presented measurements of R_{long} for $x<0.03$. The NMC measurements were made by integrating over Q^2, whereas the measurements from this analysis were made (at $x=0.015$) in 6 different Q^2-bins with $Q^2<13\ GeV^2$. Both the NMC results and the ones from this analysis indicate an R_{long} significantly smaller at $x=0.015$ than the widely used parameterization of Whitlow [Whi90b] and the predictions for R_{long} using parton distributions from MRS and GRV. Currently, global fit information on the gluon shape comes from the lower-x HERA $\partial F_2 / \partial \log Q^2$ data and the higher-x prompt photon data [Mar96b]. This analysis contributes information in the important "cross over region" (x~0.01) between these two sets of data.

The structure functions F_2 and xF_3^{av} also result from the fits of this analysis. The values are within a few percent of the previous CCFR determinations presented in reference [Sel97]. The new measurements confirm the discrepancy between neutrino and charged-lepton F_2 at low-x and the measurement of the strong coupling constant, both of which are subjects of reference [Sel97].

Appendix A: Y Distributions

This Appendix contains plots of the y distributions, both for the data events (solid line) and the MC generated events (dashed line) given the final SF measurements. Each page shows the distributions for a given *xbin* (with a variety of Q^2 bins). Plots in the left-hand collumn are the neutrino distributions, plots on the right-hand side of the page are the anti-neutrino distributions.

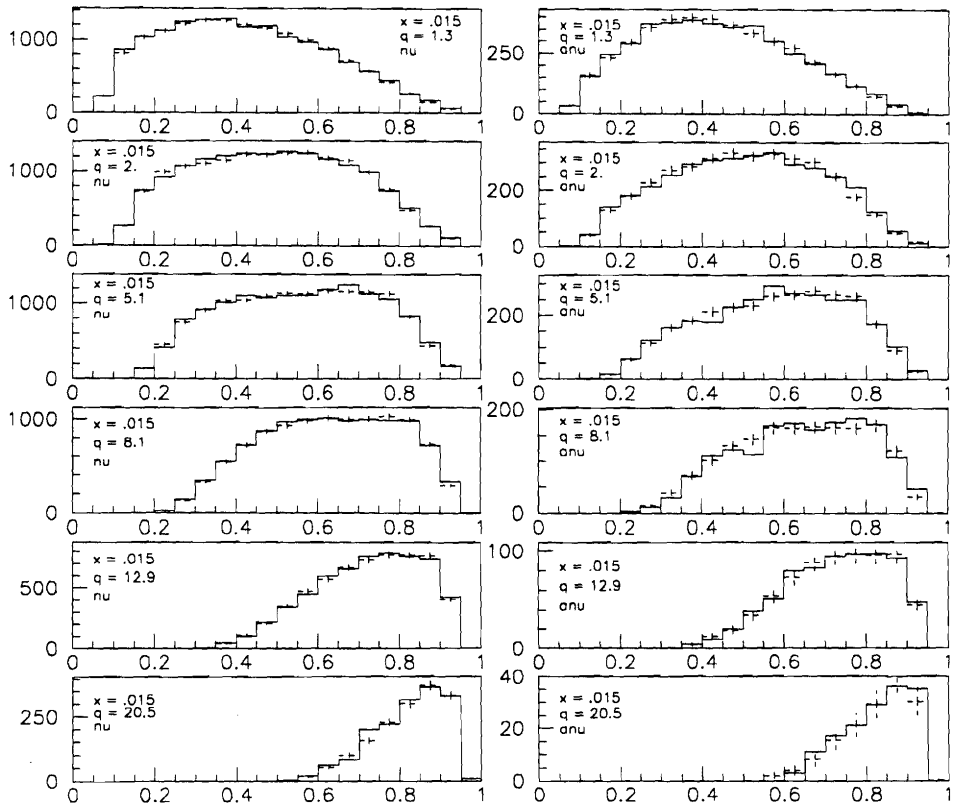

Figures A1-14: Y distributions for various Q^2 bins and *x=0.015*. Neutrino distributions are on the left, anti-neutrinos on the right. Data is plotted in the solid line, MC in the dashed line with errors.

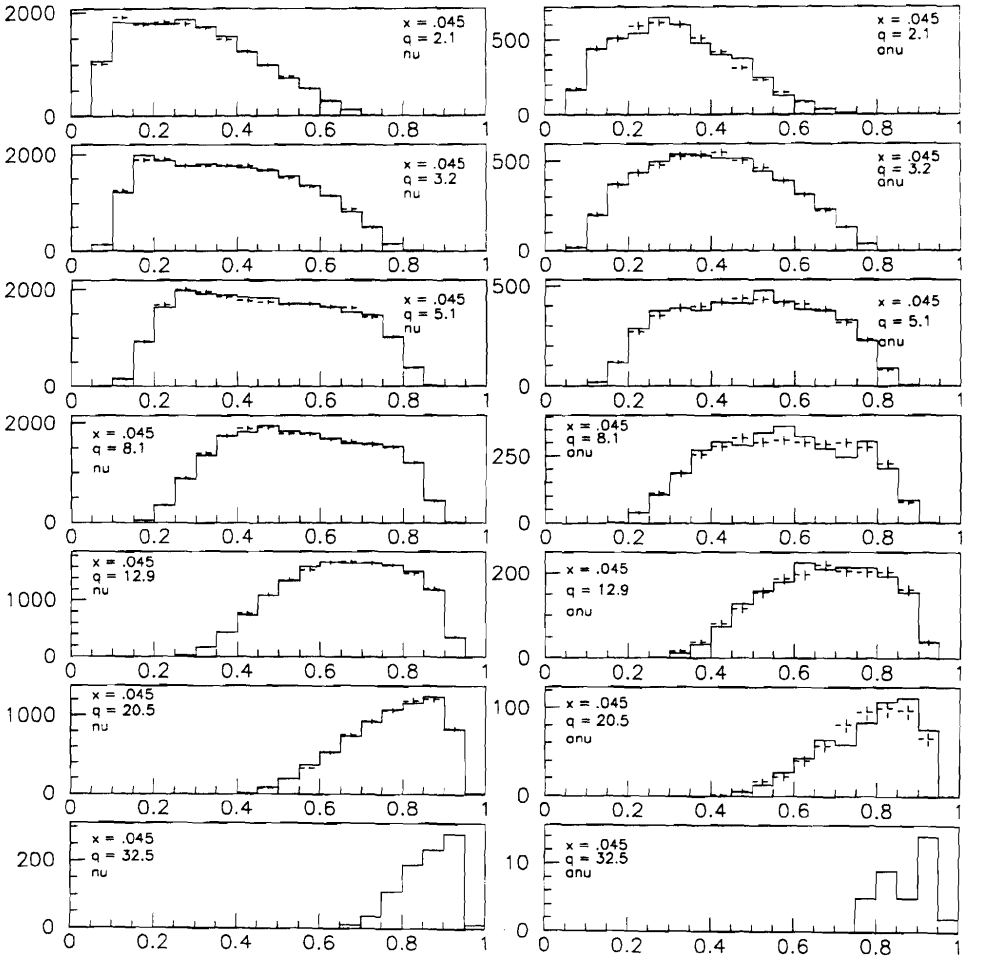

Figures A15-28: Y distributions for various Q^2 bins and *x=0.045*. Neutrino distributions are on the left, anti-neutrinos on the right. Data is plotted in the solid line, MC in the dashed line with errors.

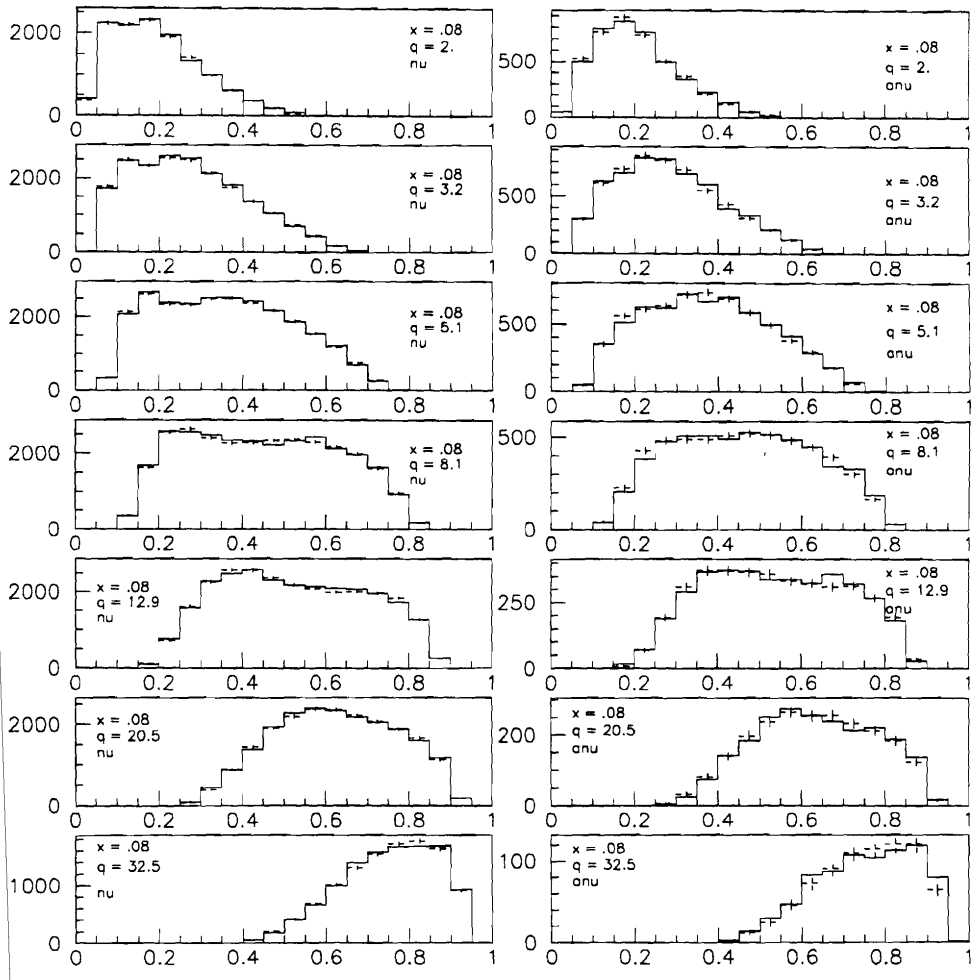

Figures A29-42: Y distributions for $x=0.08$ in various Q^2 bins. Neutrino distributions are on the left, anti-neutrinos on the right. Data is plotted in the solid line, MC in the dashed line with errors.

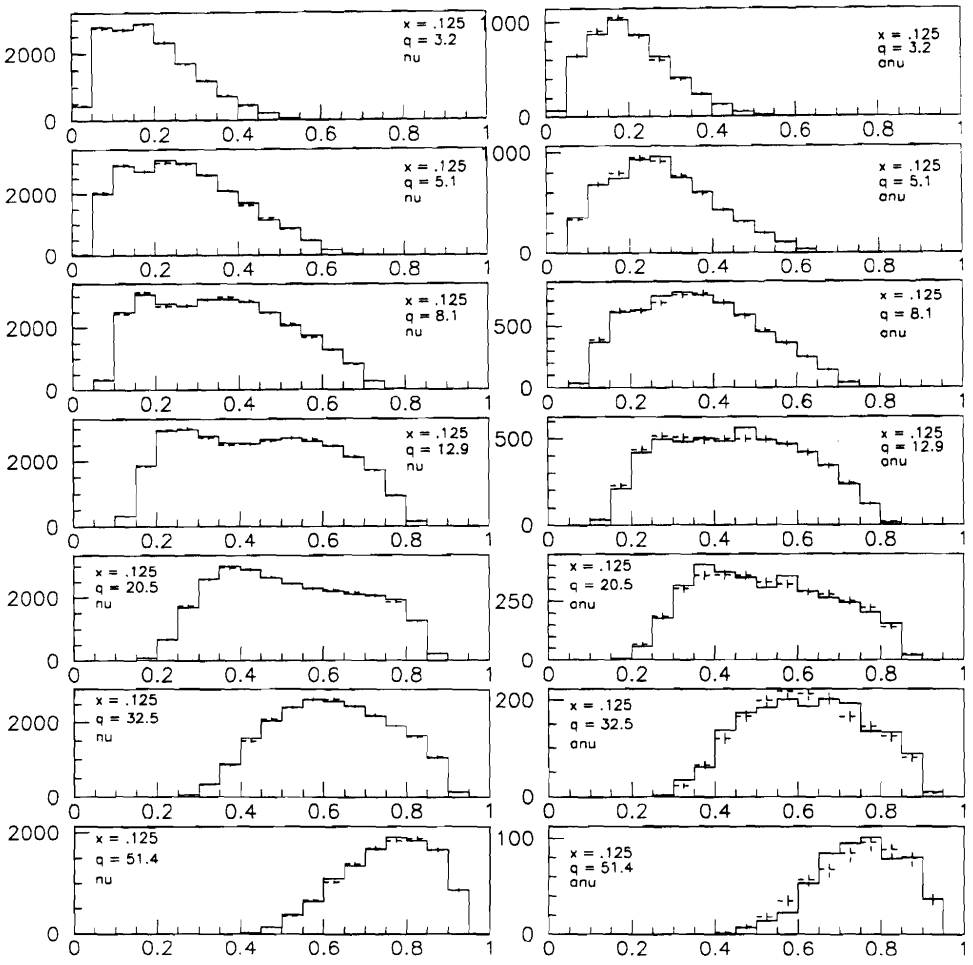

Figures A43-56: Y distributions for $x=0.125$ in various Q^2 bins. Neutrino distributions are on the left, anti-neutrinos on the right. Data is plotted in the solid line, MC in the dashed line with errors.

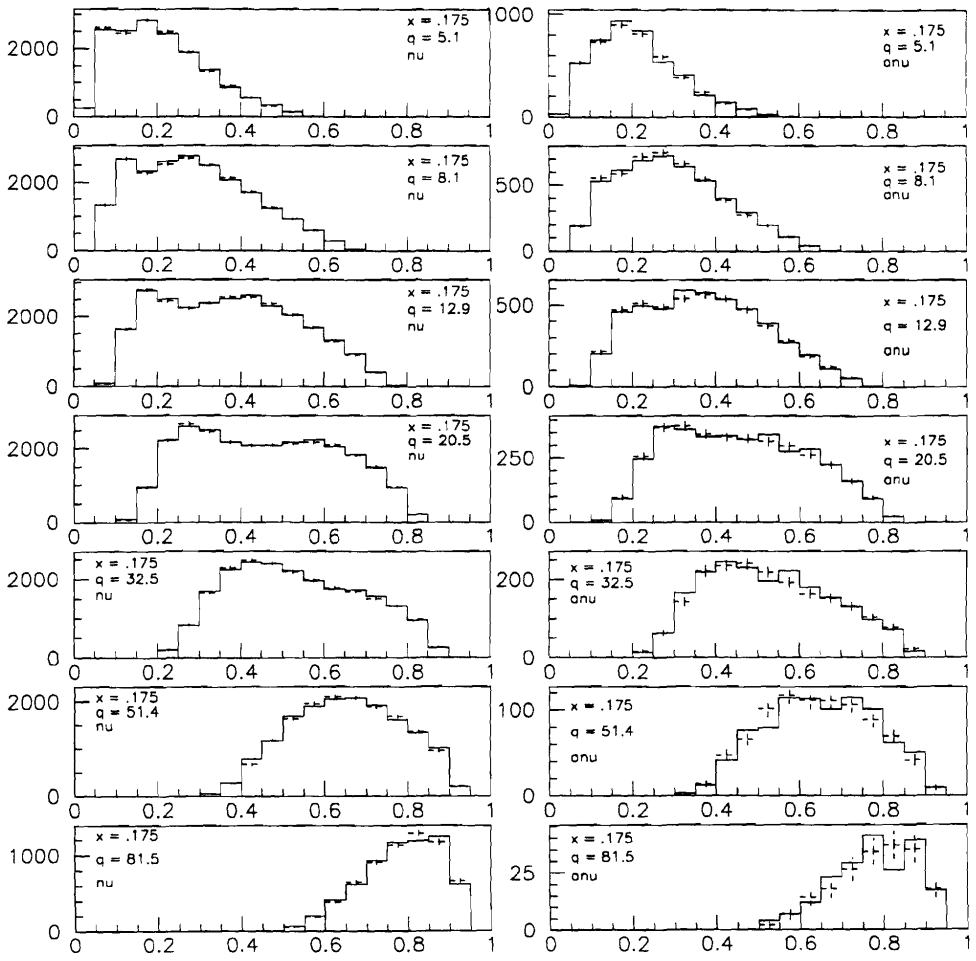

Figures A57-70: Y distributions for $x=0.175$ in various Q^2 bins. Neutrino distributions are on the left, anti-neutrinos on the right. Data is plotted in the solid line, MC in the dashed line with errors.

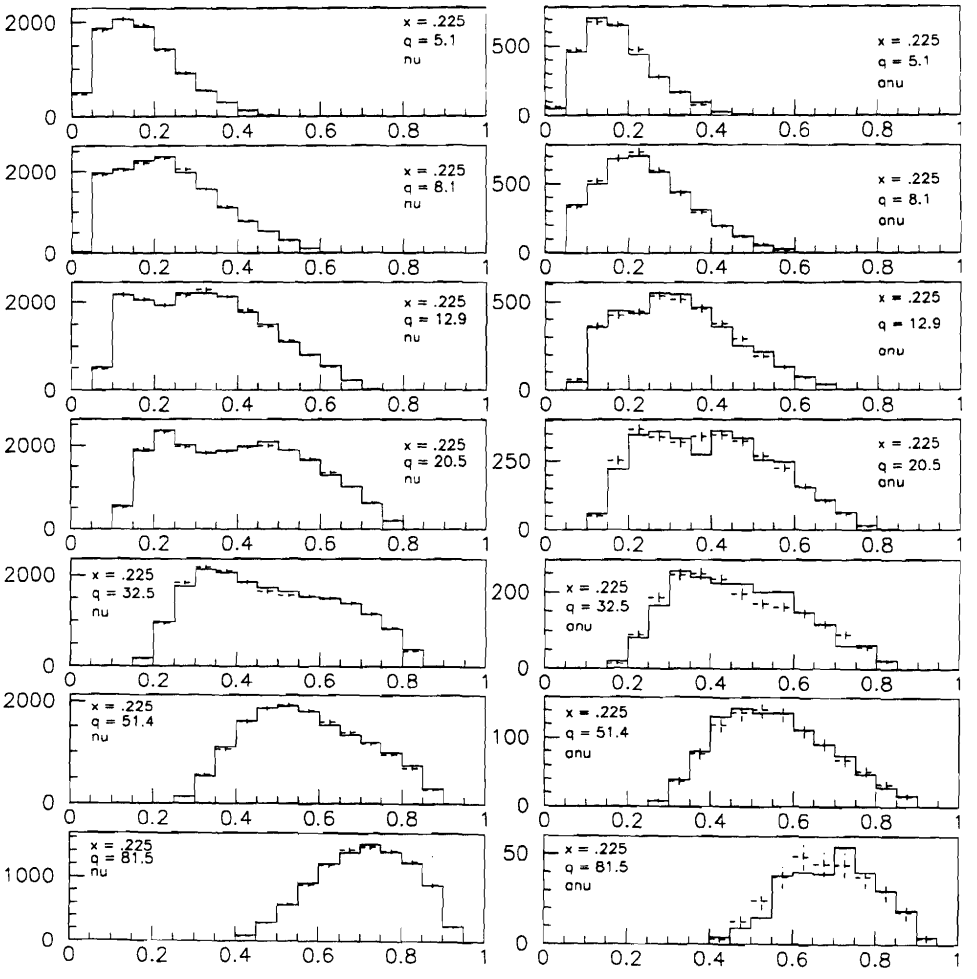

Figures A71-84: Y distributions for $x=0.225$ in various Q^2 bins. Neutrino distributions are on the left, anti-neutrinos on the right. Data is plotted in the solid line, MC in the dashed line with errors.

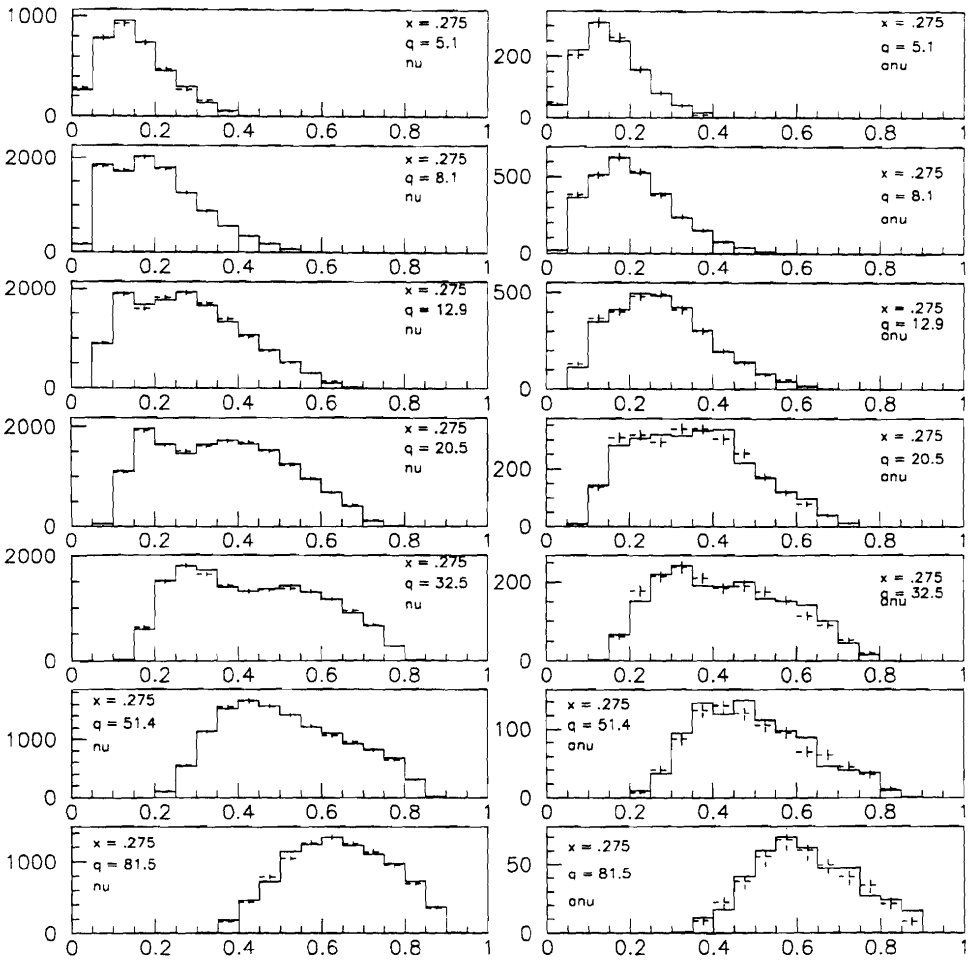

Figures A85-98: Y distributions for $x=0.275$ in various Q^2 bins. Neutrino distributions are on the left, anti-neutrinos on the right. Data is plotted in the solid line, MC in the dashed line with errors.

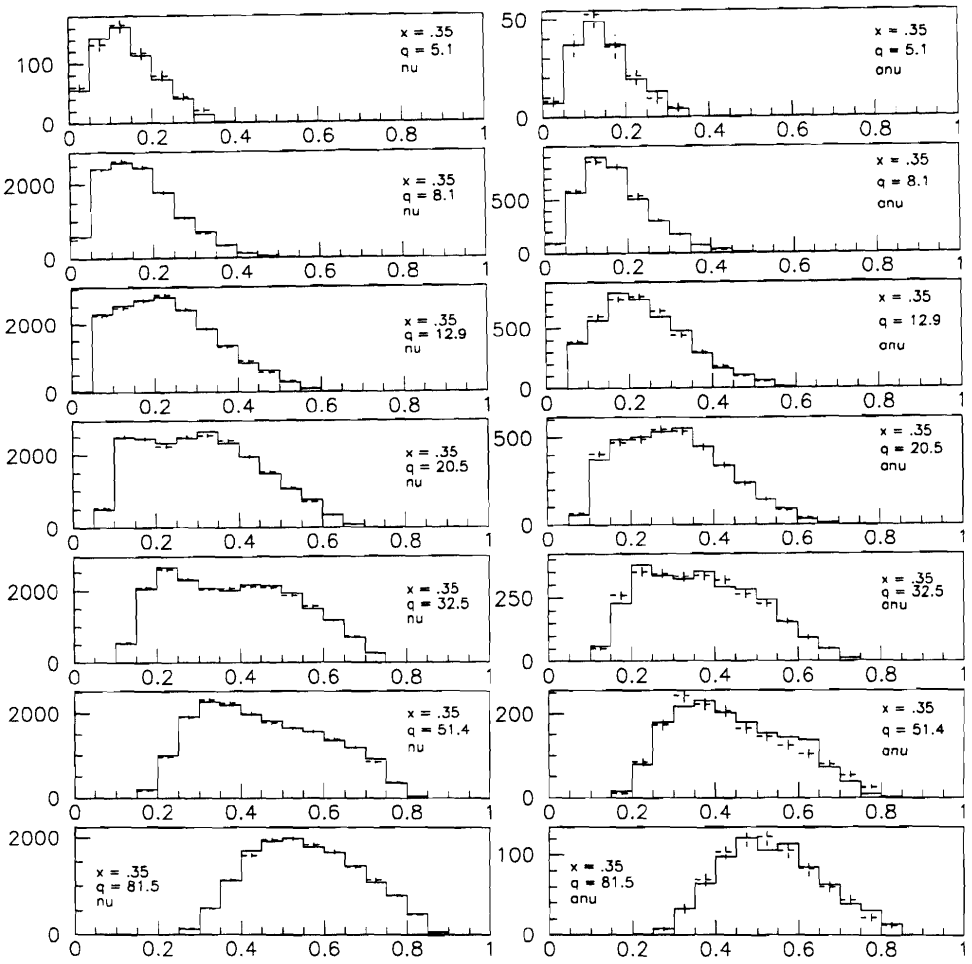

Figures A99-112: Y distributions for x=*0.35* in various Q^2 bins. Neutrino distributions are on the left, anti-neutrinos on the right. Data is plotted in the solid line, MC in the dashed line with errors.

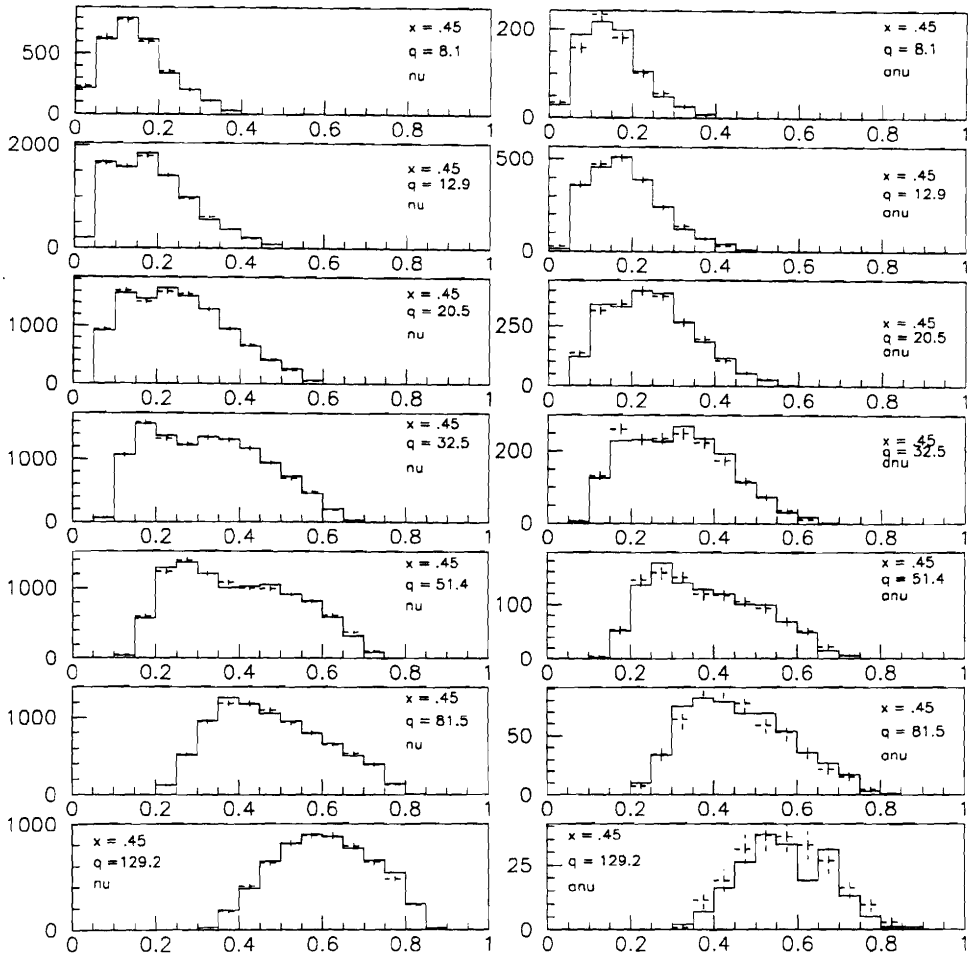

Figures A113-126: Y distributions for $x=0.45$ in various Q^2 bins. Neutrino distributions are on the left, anti-neutrinos on the right. Data is plotted in the solid line, MC in the dashed line with errors.

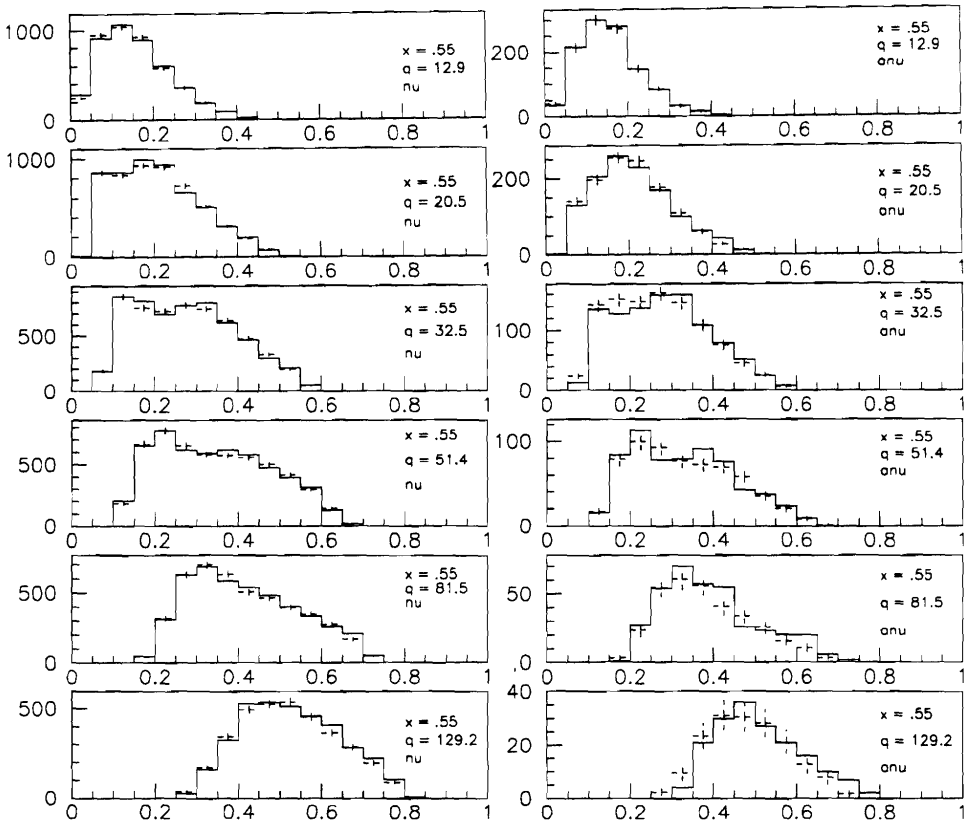

Figures A114-140: Y distributions for $x=0.55$ in various Q^2 bins. Neutrino distributions are on the left, anti-neutrinos on the right. Data is plotted in the solid line, MC in the dashed line with errors.

Appendix B: R_{long} Table

The table in this appendix contains final fit values and errors for R_{long}. The last two columns contain values for the correlated errors between R_{long} and xF_3 and F_2.

x-bin	Q^2-bin	R_{long}	δR_{long}	$\delta R_{long}F_2$	$\delta R_{long}xF_3$
1	1	0.1123	0.0690	7.275111E-04	1.232101E-04
1	2	0.1557	0.0665	9.196049E-04	1.592218E-04
1	3	0.1197	0.0599	1.146385E-03	1.405300E-04
1	4	0.2367	0.0785	2.454384E-03	2.634616E-04
1	5	0.3858	0.1382	1.003829E-02	5.687715E-04
1	6	0.0056	0.3602	1.557036E-01	1.286119E-03
2	1	2.0728	1.9247	1.989971E-02	1.824444E-03
2	2	1.9642	0.7683	7.678300E-03	4.974570E-05
2	3	0.6377	0.1448	1.659432E-03	-6.061012E-05
2	4	0.3021	0.0706	9.961260E-04	-4.356824E-05
2	5	0.1373	0.0538	1.043116E-03	-4.685600E-05
2	6	0.1776	0.0641	2.160894E-03	-3.523245E-06
2	7	0.1503	0.1137	1.079924E-02	1.132075E-04
3	2	1.3557	1.3201	1.369456E-02	7.937328E-04
3	3	0.4507	0.2151	2.032977E-03	-2.153839E-04
3	4	0.2753	0.0942	9.604751E-04	-1.038736E-04
3	5	0.2053	0.0581	6.892768E-04	-1.007147E-04
3	6	0.0902	0.0453	7.053752E-04	-8.868451E-05
3	7	0.1043	0.0541	1.409383E-03	-6.428153E-05
3	8	0.1620	0.0873	5.487917E-03	-9.227604E-05
4	3	-0.0848	0.1942	1.848976E-03	-1.743811E-04
4	4	0.0385	0.1088	9.619702E-04	-2.869766E-04
4	5	0.3041	0.0931	8.695867E-04	-2.548021E-04
4	6	0.0911	0.0488	5.256565E-04	-1.258320E-04
4	7	-0.0039	0.0409	5.914382E-04	-1.155722E-04
4	8	0.0954	0.0546	1.288728E-03	-1.256848E-04
4	9	0.1845	0.0957	5.891774E-03	-1.927685E-04
5	4	0.2896	0.3073	2.763356E-03	-1.206608E-03
5	5	0.0004	0.0993	8.858478E-04	-2.991789E-04

5	6	0.1533	0.0749	7.091486E-04	-2.574839E-04
5	7	0.0336	0.0475	5.224974E-04	-1.630566E-04
5	8	-0.0597	0.0455	7.202006E-04	-1.720861E-04
5	9	-0.0272	0.0598	1.695916E-03	-1.578868E-04
5	10	-0.1243	0.1614	2.002835E-02	-6.039187E-04
6	4	-0.1472	0.2749	2.887712E-03	-5.694398E-04
6	5	0.1055	0.1867	1.618303E-03	-6.454312E-04
6	6	-0.0049	0.0855	7.519053E-04	-3.432191E-04
6	7	0.2167	0.0831	8.032043E-04	-3.163540E-04
6	8	0.0843	0.0579	6.816080E-04	-2.568353E-04
6	9	0.0359	0.0682	1.323786E-03	-2.594120E-04
6	10	0.1580	0.1482	8.306069E-03	-3.940872E-04
7	5	0.3353	0.4343	3.766972E-03	-1.626769E-03
7	6	0.3443	0.2270	1.874028E-03	-1.076548E-03
7	7	0.1596	0.1083	9.505078E-04	-3.673645E-04
7	8	0.0950	0.0787	8.142566E-04	-3.186411E-04
7	9	-0.0466	0.0683	1.026103E-03	-3.243257E-04
7	10	0.1593	0.1144	3.380763E-03	-4.910685E-04
8	6	-0.0731	0.1338	7.311442E-04	-3.464988E-04
8	7	0.2226	0.1300	6.824127E-04	-3.867886E-04
8	8	0.2034	0.0942	5.554904E-04	-2.712950E-04
8	9	-0.0608	0.0593	4.546530E-04	-1.933686E-04
8	10	0.0798	0.0857	1.048503E-03	-1.975562E-04
8	11	0.1946	0.1919	6.993119E-03	-5.145988E-04
9	6	0.0000	0.0000	1.014588E-02	-5.727907E-03
9	7	1.5618	1.0607	4.625710E-03	-2.696357E-03
9	8	0.9569	0.4340	1.994191E-03	-1.155489E-03
9	9	-0.0997	0.0981	5.530574E-04	-2.324240E-04
9	10	-0.0235	0.1272	1.058599E-03	-2.371378E-04
9	11	0.3121	0.4009	9.620568E-03	-7.028439E-04
10	8	0.2871	0.3694	1.303082E-03	-4.319994E-04
10	9	0.2695	0.2947	1.165214E-03	-5.336610E-04
10	10	0.4027	0.5838	3.841107E-03	-1.104434E-03

x-bin	Q^2-bin	R_{long}	δR_{long}	$\delta R_{long}F_2$	$\delta R_{long}xF_3$
11	7	0.1026	0.8974	2.377611E-03	-8.895516E-04
11	9	-0.2071	0.2460	6.240068E-04	-2.450626E-04
11	10	-0.2250	0.4186	1.829415E-03	-3.214693E-04
12	8	-0.2832	0.5225	7.588494E-04	-3.374015E-04
12	9	-0.3006	0.4286	6.900917E-04	-2.363344E-04
13	7	-0.5611	0.3986	1.002944E-04	-3.485543E-05
13	9	-0.6425	0.2687	5.496968E-05	-2.331760E-05

Appendix C: Systematic Error Tables for R_{long}

This appendix contains tables of systematic errors for R_{long}. The headings on the tables refer to the following numbering scheme:

Number	Systematic Change	% Variation	direction
1	Hadron Energy Calibration	1%	+
2	"		-
3	Muon Energy Calibration	1%	+
4	"		-
5	770 <B/A> Correction	29%	-
6	"	2.4%	+
7	744 <B/A> Correction	21%	-
8	"	2.3%	+
9	$\sigma^{CCFR}/\sigma^{world}$	2.1%	+
10	"		-
11	$\sigma^{\nu}/\sigma^{\bar{\nu}}$	1.4%	+
12	"		-
13	Charm Mass Parameter	18%	+
14	"		-
15	Strange Sea Shape	10%	+
16	"		-
17	Charm Sea Distribution	Alternate xc(x)=.1xs(x)	not applicable

x	Q^2	$dR1$	$dR2$	$dR3$	$dR4$	$dR5$
0.015	1.26	0.0104	-0.0363	-0.0010	-0.0220	0.0004
0.015	2.00	0.0074	-0.0194	-0.0311	0.0279	0.0005
0.015	3.16	-0.0086	-0.0377	-0.0386	-0.0111	0.0003
0.015	5.01	0.0250	-0.0037	0.0095	-0.0031	0.0004
0.015	7.94	-0.1144	-0.0824	-0.0951	-0.0745	0.0004
0.015	12.59	0.1987	-0.3477	-0.2986	0.1589	0.0000
0.045	1.26	0.0003	0.4961	-0.4544	0.6615	0.0107
0.045	2.00	-0.1648	0.1032	-0.0040	-0.1593	0.0044
0.045	3.16	-0.0410	-0.0338	-0.0182	0.0140	0.0009
0.045	5.01	0.0018	-0.0261	-0.0045	-0.0114	0.0003
0.045	7.94	-0.0127	0.0100	-0.0374	0.0321	0.0003
0.045	12.59	0.0018	-0.0075	0.0047	-0.0195	0.0003
0.045	19.95	-0.0297	0.0138	-0.0311	0.0289	0.0002
0.080	1.26	-0.0179	-0.3910	-0.0253	-0.2392	0.0002
0.080	2.00	-0.6310	0.3387	-0.2437	0.1921	0.0056
0.080	3.16	-0.0860	0.0460	0.0891	-0.1113	0.0010
0.080	5.01	-0.0277	0.0001	0.0162	-0.0539	0.0004
0.080	7.94	-0.0082	-0.0080	-0.0205	0.0004	0.0002
0.080	12.59	0.0117	-0.0070	-0.0131	0.0127	0.0002
0.080	19.95	-0.0166	0.0129	0.0191	-0.0168	0.0002
0.080	31.62	-0.0215	-0.0033	-0.0219	0.0075	0.0002
0.125	3.16	-0.0946	-0.0257	-0.1537	-0.0309	0.0008
0.125	5.01	-0.0132	0.0239	0.0380	-0.0066	0.0002
0.125	7.94	0.0222	0.0078	0.0219	-0.0197	0.0002
0.125	12.59	-0.0042	-0.0126	-0.0236	-0.0258	0.0001
0.125	19.95	0.0243	-0.0013	0.0094	0.0046	0.0001
0.125	31.62	-0.0324	0.0073	0.0058	-0.0215	0.0001
0.125	50.12	-0.0514	-0.0062	-0.0182	-0.0339	0.0001
0.175	3.16	0.0054	0.0144	-0.0156	-0.1005	0.0002
0.175	5.01	-0.0870	0.0281	-0.2071	0.0760	0.0008
0.175	7.94	0.0001	0.0028	0.0236	-0.0286	0.0001
0.175	12.59	-0.0329	0.0272	-0.0064	0.0457	0.0000
0.175	19.95	0.0222	-0.0119	-0.0258	0.0200	0.0000
0.175	31.62	0.0229	-0.0145	0.0044	0.0078	0.0000
0.175	50.12	0.0062	0.0277	0.0434	-0.0284	0.0000
0.175	79.43	-0.1434	0.0604	-0.0682	-0.0257	0.0000
0.225	5.01	-0.0141	0.0469	0.0886	-0.0822	0.0005
0.225	7.94	0.0306	-0.0457	-0.0100	0.0115	0.0001
0.225	12.59	0.0117	-0.0034	-0.0629	-0.0063	0.0000
0.225	19.95	0.0291	-0.0082	0.0531	0.0194	-0.0001
0.225	31.62	0.0374	-0.0256	-0.0121	0.0401	-0.0001
0.225	50.12	-0.0203	0.0189	0.0179	0.0343	0.0000
0.225	79.43	-0.0598	-0.0385	-0.0204	-0.0221	0.0000
0.275	7.94	0.0766	0.1063	0.2446	0.1534	-0.0003
0.275	12.59	-0.0058	0.0184	0.0299	0.0618	-0.0001
0.275	19.95	0.0262	0.0081	-0.0262	0.0003	0.0000
0.275	31.62	0.0187	-0.0049	-0.0144	0.0384	-0.0001
0.275	50.12	0.0144	-0.0180	0.0139	0.0086	-0.0001
0.275	79.43	-0.0487	0.0244	-0.0992	0.0187	0.0000
0.350	7.94	-2.1598	-0.8845	-2.4805	-1.0303	-1.6021

x	Q^2	*dR*6	*dR*7	*dR*8	*dR*9	*dR*10
0.015	1.26	-0.0006	0.0002	-0.0005	-0.0038	0.0035
0.015	2.00	-0.0004	0.0004	-0.0004	-0.0034	0.0035
0.015	3.16	-0.0003	0.0004	-0.0003	-0.0022	0.0021
0.015	5.01	-0.0003	0.0002	-0.0002	-0.0027	0.0027
0.015	7.94	-0.0004	0.0001	-0.0001	-0.0034	0.0033
0.015	12.59	0.0001	-0.0001	0.0001	-0.0011	0.0009
0.045	1.26	-0.0087	0.0032	-0.0022	-0.0693	0.0665
0.045	2.00	-0.0042	0.0021	-0.0020	-0.0363	0.0359
0.045	3.16	-0.0009	0.0006	-0.0006	-0.0073	0.0073
0.045	5.01	-0.0005	0.0003	-0.0004	-0.0031	0.0029
0.045	7.94	-0.0002	0.0002	-0.0002	-0.0020	0.0020
0.045	12.59	-0.0002	0.0001	-0.0001	-0.0020	0.0019
0.045	19.95	-0.0002	0.0000	0.0000	-0.0020	0.0019
0.080	1.26	0.0000	0.0001	0.0002	-0.0013	0.0013
0.080	2.00	-0.0054	0.0007	-0.0007	-0.0373	0.0378
0.080	3.16	-0.0010	0.0004	-0.0004	-0.0079	0.0078
0.080	5.01	-0.0004	0.0002	-0.0002	-0.0038	0.0038
0.080	7.94	-0.0002	0.0002	-0.0002	-0.0019	0.0019
0.080	12.59	-0.0001	0.0001	-0.0001	-0.0014	0.0014
0.080	19.95	-0.0002	0.0000	0.0000	-0.0018	0.0018
0.080	31.62	-0.0002	-0.0001	0.0000	-0.0018	0.0019
0.125	3.16	-0.0006	0.0002	-0.0001	-0.0041	0.0040
0.125	5.01	-0.0001	0.0002	-0.0001	-0.0020	0.0021
0.125	7.94	-0.0003	0.0001	-0.0002	-0.0027	0.0024
0.125	12.59	-0.0001	0.0001	-0.0001	-0.0011	0.0011
0.125	19.95	-0.0001	0.0001	-0.0001	-0.0008	0.0009
0.125	31.62	-0.0001	0.0000	0.0000	-0.0011	0.0012
0.125	50.12	-0.0001	-0.0001	0.0001	-0.0019	0.0019
0.175	3.16	-0.0003	0.0001	0.0000	-0.0012	0.0012
0.175	5.01	-0.0010	-0.0001	-0.0002	-0.0066	0.0063
0.175	7.94	-0.0001	0.0001	-0.0001	-0.0013	0.0014
0.175	12.59	0.0000	0.0001	-0.0001	-0.0009	0.0009
0.175	19.95	0.0001	0.0000	0.0000	-0.0007	0.0006
0.175	31.62	0.0000	0.0001	0.0000	-0.0003	0.0003
0.175	50.12	0.0000	-0.0001	0.0001	-0.0010	0.0010
0.175	79.43	-0.0003	-0.0001	0.0001	-0.0010	0.0003
0.225	5.01	-0.0005	-0.0001	0.0002	-0.0041	0.0042
0.225	7.94	-0.0001	0.0001	-0.0001	-0.0020	0.0019
0.225	12.59	0.0001	0.0000	0.0001	-0.0009	0.0011
0.225	19.95	0.0001	0.0000	0.0000	-0.0007	0.0007
0.225	31.62	0.0001	0.0000	0.0000	-0.0004	0.0003
0.225	50.12	0.0000	0.0000	0.0000	-0.0002	0.0002
0.225	79.43	0.0000	0.0000	0.0000	-0.0008	0.0008
0.275	7.94	-0.0007	-0.0008	-0.0001	-0.0051	0.0036
0.275	12.59	0.0001	0.0000	0.0000	-0.0014	0.0015
0.275	19.95	0.0000	0.0000	0.0000	-0.0008	0.0008
0.275	31.62	0.0001	0.0001	0.0000	0.0002	-0.0002
0.275	50.12	0.0000	0.0000	0.0000	-0.0003	0.0003
0.275	79.43	0.0000	-0.0001	0.0001	-0.0009	0.0010
0.350	7.94	-1.6060	-1.6052	-1.6030	-1.6202	1.2911

x	Q^2	$dR11$	dR12	dR13	$dR14$	$dR15$	$dR16$	$dR17$
0.015	1.26	-0.0019	0.0016	0.0465	0.0054	-0.0280	0.0260	0.0131
0.015	2.00	-0.0020	0.0020	0.0974	0.0616	-0.0278	0.0249	0.0137
0.015	3.16	-0.0019	0.0019	0.0944	0.0549	-0.0222	0.0193	-0.0058
0.015	5.01	-0.0011	0.0011	0.1051	0.0809	-0.0225	0.0188	-0.0344
0.015	7.94	-0.0007	0.0005	0.0954	0.1543	-0.0227	0.0184	-0.0643
0.015	12.59	0.0002	-0.0001	0.0544	0.0996	-0.0055	0.0058	-0.0237
0.045	1.26	-0.0087	0.0082	0.5266	-0.6090	-0.3023	0.2549	0.1415
0.045	2.00	-0.0112	0.0114	0.5753	0.4540	-0.1642	0.1459	0.1262
0.045	3.16	-0.0033	0.0031	0.1597	0.1859	-0.0314	0.0293	0.0007
0.045	5.01	-0.0018	0.0016	0.0930	0.0889	-0.0127	0.0117	-0.0261
0.045	7.94	-0.0008	0.0008	0.0675	0.0489	-0.0062	0.0057	-0.0316
0.045	12.59	-0.0004	0.0004	0.0743	0.1376	-0.0111	0.0109	-0.0366
0.045	19.95	0.0001	-0.0002	0.0639	0.1592	-0.0083	0.0082	-0.0293
0.080	1.26	-0.0002	0.0001	0.0124	-0.0674	-0.0055	0.0056	-0.0014
0.080	2.00	-0.0013	0.0016	0.1232	-1.4829	-0.1179	0.1097	0.0354
0.080	3.16	-0.0020	0.0021	0.0868	0.0093	-0.0251	0.0248	0.0052
0.080	5.01	-0.0014	0.0014	0.0678	0.1075	-0.0111	0.0114	-0.0173
0.080	7.94	-0.0012	0.0012	0.0554	0.0902	-0.0055	0.0058	-0.0240
0.080	12.59	-0.0006	0.0006	0.0406	0.0207	-0.0100	0.0099	-0.0239
0.080	19.95	0.0000	0.0000	0.0399	0.1081	-0.0095	0.0093	-0.0250
0.080	31.62	0.0004	-0.0004	0.0391	0.1686	-0.0073	0.0071	-0.0238
0.125	3.16	-0.0003	0.0003	-0.0089	-0.2016	-0.0132	0.0133	-0.0045
0.125	5.01	-0.0011	0.0012	0.0202	-0.0081	-0.0102	0.0107	-0.0059
0.125	7.94	-0.0013	0.0008	0.0353	0.0972	-0.0105	0.0110	-0.0198
0.125	12.59	-0.0008	0.0008	0.0264	0.0676	-0.0108	0.0106	-0.0162
0.125	19.95	-0.0004	0.0004	0.0214	0.0128	-0.0080	0.0078	-0.0147
0.125	31.62	0.0000	0.0001	0.0224	0.1084	-0.0076	0.0074	-0.0161
0.125	50.12	0.0004	-0.0007	0.0209	0.1701	-0.0061	0.0057	-0.0152
0.175	3.16	0.0001	-0.0002	0.0009	-0.1057	-0.0052	0.0052	-0.0049
0.175	5.01	0.0006	-0.0010	0.0150	-0.2178	-0.0242	0.0240	-0.0084
0.175	7.94	-0.0006	0.0007	0.0195	0.0359	-0.0108	0.0112	-0.0057
0.175	12.59	-0.0008	0.0009	0.0250	0.0930	-0.0123	0.0121	-0.0101
0.175	19.95	-0.0005	0.0004	0.0193	0.0470	-0.0082	0.0080	-0.0086
0.175	31.62	-0.0004	0.0004	0.0148	0.0083	-0.0055	0.0054	-0.0073
0.175	50.12	0.0002	-0.0001	0.0136	0.1293	-0.0043	0.0043	-0.0060
0.175	79.43	0.0000	-0.0004	0.0127	0.1441	-0.0022	0.0014	-0.0052
0.225	5.01	0.0012	-0.0013	0.0091	-0.1774	-0.0148	0.0144	-0.0079
0.225	7.94	-0.0006	0.0005	0.0271	-0.0193	-0.0189	0.0180	-0.0046
0.225	12.59	-0.0002	0.0004	0.0237	0.0748	-0.0097	0.0096	-0.0035
0.225	19.95	-0.0006	0.0006	0.0213	0.1021	-0.0110	0.0108	-0.0046
0.225	31.62	-0.0003	0.0002	0.0170	0.0189	-0.0069	0.0069	-0.0042
0.225	50.12	-0.0003	0.0003	0.0188	0.0800	-0.0052	0.0052	-0.0054
0.225	79.43	0.0000	0.0000	0.0129	0.2086	-0.0047	0.0047	-0.0032
0.275	7.94	-0.0001	-0.0012	0.0276	-0.1231	-0.0379	0.0320	-0.0085
0.275	12.59	-0.0005	0.0005	0.0311	0.1028	-0.0189	0.0181	0.0041
0.275	19.95	-0.0003	0.0003	0.0201	0.1086	-0.0094	0.0094	-0.0015
0.275	31.62	-0.0006	0.0006	0.0172	0.0509	-0.0069	0.0070	-0.0011
0.275	50.12	-0.0001	0.0001	0.0131	0.0220	-0.0043	0.0043	-0.0012
0.275	79.43	0.0001	-0.0002	0.0158	0.1806	-0.0046	0.0048	-0.0018
0.350	7.94	-1.5979	-1.6105	1.2900	-3.2722	-1.7779	-1.4726	-1.6355

Appendix D: SF Table

The table in this appendix contains final fit values and errors for F_2 and xF_3. The last column contain values for the correllated error between xF_3 and F_2.

x-bin	Q^2-bin	F_2	δF_2	xF_3	δxF_3	$\delta F_2 xF_3$
1	1	1.1981	0.0154	0.2616	0.0216	-5.641292e-05
1	2	1.3241	0.0190	0.2931	0.0217	-7.057872e-05
1	3	1.4285	0.0249	0.2748	0.0235	-1.235658e-04
1	4	1.6261	0.0387	0.3422	0.0288	-2.340551e-04
1	5	1.7905	0.0824	0.3169	0.0399	-6.470725e-04
1	6	1.7549	0.4423	0.1916	0.0993	-5.395122e-03
2	1	1.2431	0.0161	0.4649	0.0440	-1.100360e-04
2	2	1.3790	0.0154	0.4955	0.0288	-6.986577e-05
2	3	1.4568	0.0162	0.4718	0.0220	-6.285601e-05
2	4	1.5633	0.0188	0.5342	0.0201	-7.434153e-05
2	5	1.6017	0.0242	0.5519	0.0210	-1.242793e-04
2	6	1.6955	0.0390	0.5476	0.0238	-2.186262e-04
2	7	1.8021	0.1012	0.6184	0.0365	-5.983104e-04
3	2	1.3468	0.0159	0.5991	0.0490	-1.242069e-04
3	3	1.3814	0.0140	0.6567	0.0294	-6.556166e-05
3	4	1.4500	0.0142	0.6508	0.0211	-4.822653e-05
3	5	1.4948	0.0156	0.7129	0.0174	-5.083048e-05
3	6	1.5116	0.0193	0.7324	0.0175	-7.878879e-05
3	7	1.5757	0.0299	0.7291	0.0193	-1.291334e-04
3	8	1.6531	0.0672	0.7359	0.0254	-3.343031e-04
4	3	1.2945	0.0142	0.7043	0.0446	-1.079901e-04
4	4	1.3183	0.0127	0.8327	0.0266	-5.706172e-05
4	5	1.3697	0.0128	0.7756	0.0186	-4.465632e-05
4	6	1.3534	0.0138	0.8145	0.0154	-4.159773e-05
4	7	1.3515	0.0174	0.8385	0.0155	-6.416773e-05
4	8	1.3691	0.0266	0.8386	0.0161	-9.932363e-05
4	9	1.4634	0.0649	0.8374	0.0211	-2.512206e-04

x-bin	Q^2-bin	F_2	δF_2	xF_3	δxF_3	$\delta F_2 xF_3$
5	4	1.2193	0.0134	0.8686	0.0372	-9.136189e-05
5	5	1.1862	0.0124	0.8482	0.0238	-4.808985e-05
5	6	1.2176	0.0126	0.8232	0.0172	-4.172411e-05
5	7	1.1752	0.0138	0.8427	0.0146	-4.176657e-05
5	8	1.1304	0.0185	0.8595	0.0151	-7.111403e-05
5	9	1.1021	0.0306	0.8471	0.0152	-9.231649e-05
5	10	1.0615	0.1260	0.8576	0.0260	-5.741315e-04
6	4	1.0687	0.0152	0.8387	0.0519	-1.234716e-04
6	5	1.0644	0.0125	0.7668	0.0293	-6.329233e-05
6	6	1.0232	0.0118	0.7927	0.0194	-4.307317e-05
6	7	1.0357	0.0125	0.7870	0.0150	-3.596353e-05
6	8	0.9970	0.0144	0.7851	0.0139	-5.036090e-05
6	9	0.9665	0.0218	0.7467	0.0147	-8.578492e-05
6	10	0.9958	0.0581	0.7780	0.0173	-1.585177e-04
7	5	0.9190	0.0125	0.7187	0.0346	-7.549347e-05
7	6	0.8794	0.0114	0.7161	0.0218	-4.877093e-05
7	7	0.8592	0.0115	0.6863	0.0159	-3.223169e-05
7	8	0.8328	0.0128	0.6717	0.0139	-3.979334e-05
7	9	0.7884	0.0172	0.6958	0.0140	-7.010171e-05
7	10	0.7975	0.0315	0.6372	0.0136	-1.176388e-04
8	5	0.7193	0.0091	0.6221	0.0292	-4.226384e-05
8	6	0.6621	0.0075	0.5849	0.0172	-2.155441e-05
8	7	0.6265	0.0070	0.5408	0.0115	-1.634767e-05
8	8	0.6027	0.0075	0.5264	0.0092	-1.507379e-05
8	9	0.5592	0.0091	0.5131	0.0089	-2.302011e-05
8	10	0.5550	0.0135	0.4868	0.0084	-2.682187e-05
8	11	0.5797	0.0376	0.4804	0.0110	-9.446738e-05
9	6	0.4222	0.0067	0.4098	0.0179	-1.999260e-05
9	7	0.3997	0.0060	0.3465	0.0116	-1.354884e-05
9	8	0.3685	0.0059	0.3303	0.0086	-1.125268e-05
9	9	0.3229	0.0067	0.3091	0.0078	-1.334250e-05
9	10	0.3081	0.0093	0.2910	0.0075	-1.672954e-05
9	11	0.3224	0.0251	0.2660	0.0101	-4.925880e-05

x-bin	Q^2-bin	F_2	δF_2	xF_3	δxF_3	$\delta F_2 xF_3$
10	6	0.2495	0.0057	0.2662	0.0179	-1.765148e-05
10	7	0.2253	0.0048	0.1926	0.0108	-8.385442e-06
10	8	0.1940	0.0045	0.1655	0.0075	-5.938795e-06
10	9	0.1728	0.0048	0.1684	0.0060	-6.680654e-06
10	10	0.1654	0.0074	0.1614	0.0070	-1.525501e-05
10	11	0.1842	0.0149	0.1335	0.0073	-2.413147e-05
11	7	0.1044	0.0034	0.1122	0.0088	-4.561822e-06
11	8	0.0863	0.0031	0.0913	0.0061	-3.477495e-06
11	9	0.0766	0.0031	0.0849	0.0046	-2.917172e-06
11	10	0.0678	0.0049	0.0710	0.0056	-6.239218e-06
11	11	0.0713	0.0146	0.0448	0.0071	-6.213624e-06
12	7	0.0454	0.0013	0.0482	0.0056	-8.983853e-07
12	8	0.0341	0.0018	0.0401	0.0039	-1.334254e-06
12	9	0.0302	0.0019	0.0345	0.0031	-1.190416e-06
13	7	0.0049	0.0003	0.0056	0.0009	-4.464691e-08
13	8	0.0035	0.0002	0.0040	0.0005	-1.945894e-08
13	9	0.0024	0.0002	0.0025	0.0004	-2.796024e-08

Appendix E: F_2 Systematic Error Tables

This appendix contains tables of systematic errors for F_2. The headings on the tables refer to the following numbering scheme:

#	Systematic Change	
1	Hadron Energy Calibration	+
2	"	-
3	Muon Energy Calibration	+
4	"	-
5	770 <B/A> Correction	-
6	"	+
7	744 <B/A> Correction	-
8	"	+
9	$\sigma^{CCFR}/\sigma^{world}$	+
10	"	-
11	$\sigma^{\nu}/\sigma^{\bar{\nu}}$	+
12	"	-
13	Charm Mass Parameter	+
14	"	-
15	Strange Sea	+
16	"	-

Bin	Xcenter	Q^2center
1	0.015	1.3
2	0.045	2.05
3	0.08	3.25
4	0.125	5.14
5	0.175	8.15
6	0.225	12.9
7	0.275	20.5
8	0.35	32.5
9	0.45	51.4
10	0.55	81.5

11	0.65	129.2
12	0.75	204.8
13	0.85	324.6
14	0.9	514.5
15		815.5

xbin	Q^2	δF_2 1	δF_2 2	δF_2 3	δF_2 4	δF_2 5
1	1	0.0413	0.0409	0.0569	0.0256	-0.0015
1	2	0.0435	0.0492	0.0669	0.0300	-0.0017
1	3	0.0395	0.0514	0.0668	0.0204	-0.0018
1	4	0.0543	0.0779	0.1053	0.0194	-0.0020
1	5	-0.0211	0.0622	0.0749	-0.0180	-0.0022
1	6	0.2440	-0.2211	-0.2342	0.2227	-0.0023
2	1	0.0419	0.0412	0.0477	0.0288	-0.0015
2	2	0.0429	0.0460	0.0585	0.0349	-0.0017
2	3	0.0455	0.0483	0.0679	0.0297	-0.0018
2	4	0.0444	0.0557	0.0809	0.0282	-0.0019
2	5	0.0362	0.0723	0.0690	0.0343	-0.0020
2	6	0.0378	0.0740	0.0896	0.0145	-0.0021
2	7	0.0009	0.1176	0.0981	0.0325	-0.0021
3	2	0.0371	0.0446	0.0572	0.0295	-0.0016
3	3	0.0429	0.0444	0.0546	0.0308	-0.0017
3	4	0.0442	0.0460	0.0606	0.0266	-0.0018
3	5	0.0459	0.0509	0.0649	0.0334	-0.0018
3	6	0.0423	0.0611	0.0640	0.0303	-0.0018
3	7	0.0291	0.0739	0.0903	0.0184	-0.0019
3	8	0.0093	0.0872	0.0850	0.0203	-0.0019
4	3	0.0417	0.0376	0.0429	0.0322	-0.0016
4	4	0.0416	0.0441	0.0508	0.0357	-0.0016
4	5	0.0446	0.0417	0.0498	0.0304	-0.0017
4	6	0.0356	0.0432	0.0538	0.0193	-0.0016
4	7	0.0420	0.0519	0.0595	0.0320	-0.0016
4	8	0.0186	0.0640	0.0615	0.0177	-0.0016
4	9	-0.0165	0.0685	0.0760	-0.0094	-0.0017
5	4	0.0459	0.0345	0.0385	0.0402	-0.0015
5	5	0.0417	0.0369	0.0428	0.0353	-0.0014
5	6	0.0379	0.0398	0.0436	0.0432	-0.0015
5	7	0.0365	0.0366	0.0358	0.0345	-0.0014
5	8	0.0327	0.0346	0.0429	0.0267	-0.0014
5	9	0.0279	0.0602	0.0647	0.0092	-0.0013
5	10	-0.1020	0.1050	0.0084	-0.0251	-0.0012
6	4	0.0360	0.0279	0.0359	0.0363	-0.0013
6	5	0.0393	0.0256	0.0310	0.0352	-0.0013
6	6	0.0404	0.0239	0.0193	0.0367	-0.0012
6	7	0.0339	0.0281	0.0380	0.0311	-0.0012
6	8	0.0370	0.0303	0.0367	0.0387	-0.0012
6	9	0.0167	0.0380	0.0355	0.0341	-0.0012
6	10	-0.0110	0.0237	0.0368	0.0022	-0.0012
7	5	0.0382	0.0241	0.0258	0.0385	-0.0011
7	6	0.0310	0.0202	0.0247	0.0342	-0.0011
7	7	0.0278	0.0276	0.0224	0.0283	-0.0010
7	8	0.0260	0.0197	0.0182	0.0271	-0.0010
7	9	0.0238	0.0238	0.0224	0.0263	-0.0009
7	10	0.0077	0.0333	0.0090	0.0233	-0.0009
8	5	0.0330	0.0164	0.0125	0.0369	-0.0009
8	6	0.0287	0.0134	0.0115	0.0322	-0.0008
8	7	0.0292	0.0121	0.0099	0.0315	-0.0007
8	8	0.0251	0.0139	0.0068	0.0248	-0.0007

8	9	0.0191	0.0110	0.0061	0.0215	-0.0007
8	10	0.0169	0.0237	0.0209	0.0155	-0.0006
8	11	0.0032	0.0362	0.0068	0.0261	-0.0007
9	6	0.0219	0.0077	0.0074	0.0240	-0.0005
9	7	0.0192	0.0066	0.0011	0.0219	-0.0005
9	8	0.0182	0.0074	0.0027	0.0268	-0.0004
9	9	0.0157	0.0035	-0.0026	0.0223	-0.0004
9	10	0.0127	0.0041	0.0006	0.0200	-0.0004
9	11	0.0098	0.0055	0.0079	0.0080	-0.0004
10	6	0.0113	0.0004	-0.0042	0.0160	-0.0003
10	7	0.0130	0.0027	0.0023	0.0189	-0.0003
10	8	0.0121	0.0016	-0.0024	0.0176	-0.0002
10	9	0.0102	-0.0036	-0.0057	0.0101	-0.0002
10	10	0.0081	0.0047	-0.0002	0.0122	-0.0002
10	11	-0.0072	-0.0086	-0.0024	0.0163	-0.0002
11	7	0.1044	0.1044	0.1044	0.1044	0.1044
11	8	0.0863	0.0863	0.0863	0.0863	0.0863
11	9	0.0766	0.0766	0.0766	0.0766	0.0766
11	10	0.0678	0.0678	0.0678	0.0678	0.0678
11	11	0.0713	0.0713	0.0713	0.0713	0.0713
12	7	0.0454	0.0454	0.0454	0.0454	0.0454
12	8	0.0341	0.0341	0.0341	0.0341	0.0341
12	9	0.0302	0.0302	0.0302	0.0302	0.0302
13	7	0.0049	0.0049	0.0049	0.0049	0.0049
13	8	0.0035	0.0035	0.0035	0.0035	0.0035
13	9	0.0024	0.0024	0.0024	0.0024	0.0024

xbin	Q^2	δF_2 6	δF_2 7	δF_2 8	δF_2 9	δF_2 10
1	1	0.0014	-0.0013	0.0012	1.1981	-0.0150
1	2	0.0016	-0.0014	0.0014	1.3241	-0.0166
1	3	0.0017	-0.0015	0.0015	1.4285	-0.0183
1	4	0.0020	-0.0018	0.0017	1.6261	-0.0205
1	5	0.0021	-0.0020	0.0019	1.7905	-0.0225
1	6	0.0024	-0.0023	0.0022	1.7549	-0.0216
2	1	0.0014	-0.0013	0.0012	1.2431	-0.0151
2	2	0.0016	-0.0014	0.0014	1.3790	-0.0168
2	3	0.0017	-0.0015	0.0015	1.4568	-0.0179
2	4	0.0018	-0.0016	0.0016	1.5633	-0.0193
2	5	0.0019	-0.0017	0.0016	1.6017	-0.0199
2	6	0.0020	-0.0018	0.0017	1.6955	-0.0210
2	7	0.0020	-0.0021	0.0020	1.8021	-0.0213
3	2	0.0015	-0.0014	0.0013	1.3468	-0.0162
3	3	0.0016	-0.0014	0.0014	1.3814	-0.0168
3	4	0.0017	-0.0015	0.0015	1.4500	-0.0176
3	5	0.0017	-0.0015	0.0015	1.4948	-0.0184
3	6	0.0018	-0.0016	0.0015	1.5116	-0.0186
3	7	0.0018	-0.0017	0.0016	1.5757	-0.0191
3	8	0.0018	-0.0019	0.0018	1.6531	-0.0192
4	3	0.0015	-0.0013	0.0013	1.2945	-0.0156
4	4	0.0015	-0.0014	0.0013	1.3183	-0.0160
4	5	0.0016	-0.0014	0.0013	1.3697	-0.0167
4	6	0.0016	-0.0014	0.0013	1.3534	-0.0165
4	7	0.0015	-0.0014	0.0013	1.3515	-0.0164
4	8	0.0016	-0.0014	0.0014	1.3691	-0.0166
4	9	0.0016	-0.0016	0.0016	1.4634	-0.0169
5	4	0.0014	-0.0013	0.0012	1.2193	-0.0146
5	5	0.0014	-0.0012	0.0012	1.1862	-0.0143
5	6	0.0014	-0.0013	0.0012	1.2176	-0.0148
5	7	0.0014	-0.0012	0.0012	1.1752	-0.0143
5	8	0.0013	-0.0011	0.0011	1.1304	-0.0138
5	9	0.0012	-0.0012	0.0011	1.1021	-0.0130
5	10	0.0009	-0.0012	0.0011	1.0615	-0.0126
6	4	0.0012	-0.0011	0.0010	1.0687	-0.0128
6	5	0.0012	-0.0011	0.0010	1.0644	-0.0128
6	6	0.0012	-0.0010	0.0010	1.0232	-0.0123
6	7	0.0012	-0.0011	0.0010	1.0357	-0.0125
6	8	0.0011	-0.0010	0.0010	0.9970	-0.0121
6	9	0.0011	-0.0010	0.0009	0.9665	-0.0117
6	10	0.0011	-0.0010	0.0010	0.9958	-0.0119
7	5	0.0010	-0.0010	0.0009	0.9190	-0.0110
7	6	0.0010	-0.0009	0.0009	0.8794	-0.0106
7	7	0.0010	-0.0009	0.0008	0.8592	-0.0103
7	8	0.0010	-0.0008	0.0008	0.8328	-0.0101
7	9	0.0009	-0.0008	0.0008	0.7884	-0.0095
7	10	0.0009	-0.0008	0.0008	0.7975	-0.0095
8	5	0.0008	-0.0007	0.0007	0.7193	-0.0087
8	6	0.0008	-0.0007	0.0006	0.6621	-0.0080
8	7	0.0007	-0.0006	0.0006	0.6265	-0.0075
8	8	0.0007	-0.0006	0.0006	0.6027	-0.0072

8	9	0.0006	-0.0006	0.0005	0.5592	-0.0067
8	10	0.0006	-0.0006	0.0006	0.5550	-0.0066
8	11	0.0006	-0.0007	0.0005	0.5797	-0.0066
9	6	0.0005	-0.0004	0.0004	0.4222	-0.0051
9	7	0.0005	-0.0004	0.0004	0.3997	-0.0048
9	8	0.0004	-0.0004	0.0004	0.3685	-0.0044
9	9	0.0004	-0.0003	0.0003	0.3229	-0.0039
9	10	0.0003	-0.0003	0.0003	0.3081	-0.0037
9	11	0.0004	-0.0003	0.0003	0.3224	-0.0040
10	6	0.0003	-0.0003	0.0002	0.2495	-0.0030
10	7	0.0003	-0.0002	0.0002	0.2253	-0.0027
10	8	0.0002	-0.0002	0.0002	0.1940	-0.0023
10	9	0.0002	-0.0002	0.0002	0.1728	-0.0021
10	10	0.0002	-0.0002	0.0002	0.1654	-0.0019
10	11	0.0002	-0.0002	0.0002	0.1842	-0.0021
11	7	0.1044	0.1044	0.1044	0.1044	0.1044
11	8	0.0863	0.0863	0.0863	0.0863	0.0863
11	9	0.0766	0.0766	0.0766	0.0766	0.0766
11	10	0.0678	0.0678	0.0678	0.0678	0.0678
11	11	0.0713	0.0713	0.0713	0.0713	0.0713
12	7	0.0454	0.0454	0.0454	0.0454	0.0454
12	8	0.0341	0.0341	0.0341	0.0341	0.0341
12	9	0.0302	0.0302	0.0302	0.0302	0.0302
13	7	0.0049	0.0049	0.0049	0.0049	0.0049
13	8	0.0035	0.0035	0.0035	0.0035	0.0035
13	9	0.0024	0.0024	0.0024	0.0024	0.0024

xbin	Q_2	δF_2 11	δF_2 12	$\delta F_2$13	δF_2 14	δF_2 15	δF_2 16
1	1	0.0076	-0.0077	0.0746	0.0897	0.0046	-0.0046
1	2	0.0085	-0.0086	0.0191	0.0357	0.0060	-0.0057
1	3	0.0091	-0.0092	-0.0158	0.0019	0.0082	-0.0074
1	4	0.0106	-0.0107	-0.0340	-0.0072	0.0108	-0.0095
1	5	0.0119	-0.0121	-0.0474	0.0367	0.0151	-0.0127
1	6	0.0128	-0.0128	-0.0378	0.1262	0.0200	-0.0202
2	1	0.0077	-0.0078	0.0472	0.0616	0.0015	-0.0015
2	2	0.0086	-0.0087	0.0311	0.0441	0.0019	-0.0019
2	3	0.0091	-0.0093	0.0205	0.0352	0.0023	-0.0022
2	4	0.0098	-0.0100	0.0155	0.0321	0.0024	-0.0023
2	5	0.0101	-0.0102	0.0123	0.0270	0.0025	-0.0023
2	6	0.0109	-0.0110	0.0178	0.0773	0.0073	-0.0074
2	7	0.0122	-0.0125	0.0269	0.1716	0.0112	-0.0114
3	2	0.0084	-0.0085	0.0212	0.0265	0.0009	-0.0009
3	3	0.0085	-0.0086	0.0303	0.0355	0.0011	-0.0011
3	4	0.0091	-0.0092	0.0359	0.0462	0.0011	-0.0012
3	5	0.0093	-0.0094	0.0372	0.0525	0.0011	-0.0012
3	6	0.0094	-0.0095	0.0360	0.0409	0.0039	-0.0039
3	7	0.0102	-0.0103	0.0371	0.0815	0.0059	-0.0058
3	8	0.0113	-0.0114	0.0392	0.1768	0.0078	-0.0077
4	3	0.0079	-0.0080	0.0132	0.0112	0.0006	-0.0007
4	4	0.0081	-0.0082	0.0229	0.0221	0.0008	-0.0009
4	5	0.0084	-0.0086	0.0272	0.0322	0.0009	-0.0011
4	6	0.0083	-0.0084	0.0270	0.0377	0.0023	-0.0023
4	7	0.0084	-0.0085	0.0251	0.0285	0.0033	-0.0032
4	8	0.0087	-0.0087	0.0220	0.0643	0.0043	-0.0043
4	9	0.0097	-0.0100	0.0182	0.1541	0.0058	-0.0058
5	4	0.0075	-0.0076	0.0052	-0.0018	0.0007	-0.0007
5	5	0.0073	-0.0074	0.0099	0.0066	0.0010	-0.0010
5	6	0.0075	-0.0075	0.0112	0.0147	0.0015	-0.0015
5	7	0.0072	-0.0073	0.0096	0.0151	0.0020	-0.0020
5	8	0.0069	-0.0070	0.0064	0.0048	0.0025	-0.0025
5	9	0.0071	-0.0071	0.0028	0.0625	0.0034	-0.0033
5	10	0.0068	-0.0072	-0.0003	0.1452	0.0042	-0.0048
6	4	0.0065	-0.0066	-0.0053	-0.0147	0.0006	-0.0006
6	5	0.0065	-0.0066	0.0002	-0.0080	0.0009	-0.0009
6	6	0.0063	-0.0063	0.0027	0.0010	0.0010	-0.0010
6	7	0.0064	-0.0064	0.0019	0.0067	0.0012	-0.0012
6	8	0.0061	-0.0062	0.0004	0.0005	0.0015	-0.0016
6	9	0.0059	-0.0060	-0.0014	0.0149	0.0020	-0.0020
6	10	0.0063	-0.0063	-0.0065	0.0881	0.0027	-0.0027
7	5	0.0056	-0.0057	-0.0044	-0.0129	0.0007	-0.0007
7	6	0.0054	-0.0054	0.0000	-0.0047	0.0006	-0.0006
7	7	0.0052	-0.0053	0.0010	0.0017	0.0008	-0.0008
7	8	0.0050	-0.0051	0.0008	0.0033	0.0009	-0.0009
7	9	0.0048	-0.0049	0.0003	0.0009	0.0012	-0.0012
7	10	0.0049	-0.0050	-0.0020	0.0437	0.0016	-0.0017
8	5	0.0044	-0.0044	-0.0072	-0.0151	0.0005	-0.0004
8	6	0.0040	-0.0040	-0.0014	-0.0073	0.0004	-0.0003
8	7	0.0038	-0.0039	0.0026	0.0013	0.0004	-0.0004
8	8	0.0037	-0.0037	0.0044	0.0062	0.0004	-0.0005

8	9	0.0034	-0.0034	0.0059	0.0030	0.0006	-0.0006
8	10	0.0035	-0.0035	0.0050	0.0220	0.0007	-0.0007
8	11	0.0037	-0.0039	0.0071	0.0641	0.0009	-0.0010
9	6	0.0025	-0.0026	-0.0037	-0.0086	0.0001	-0.0001
9	7	0.0025	-0.0025	0.0011	-0.0006	0.0001	-0.0001
9	8	0.0022	-0.0023	0.0042	0.0044	0.0001	-0.0002
9	9	0.0020	-0.0020	0.0059	0.0052	0.0002	-0.0002
9	10	0.0019	-0.0019	0.0065	0.0078	0.0002	-0.0003
9	11	0.0019	-0.0019	0.0069	0.0318	0.0003	-0.0003
10	6	0.0015	-0.0015	-0.0054	-0.0079	0.0000	0.0000
10	7	0.0014	-0.0014	-0.0020	-0.0032	0.0000	0.0000
10	8	0.0012	-0.0012	0.0008	0.0005	0.0000	0.0000
10	9	0.0011	-0.0011	0.0026	0.0017	0.0001	-0.0001
10	10	0.0010	-0.0010	0.0039	0.0050	0.0001	-0.0001
10	11	0.0012	-0.0012	0.0052	0.0182	0.0001	-0.0001
11	7	0.1044	0.1044	0.1044	0.1044	0.1044	0.1044
11	8	0.0863	0.0863	0.0863	0.0863	0.0863	0.0863
11	9	0.0766	0.0766	0.0766	0.0766	0.0766	0.0766
11	10	0.0678	0.0678	0.0678	0.0678	0.0678	0.0678
11	11	0.0713	0.0713	0.0713	0.0713	0.0713	0.0713
12	7	0.0454	0.0454	0.0454	0.0454	0.0454	0.0454
12	8	0.0341	0.0341	0.0341	0.0341	0.0341	0.0341
12	9	0.0302	0.0302	0.0302	0.0302	0.0302	0.0302
13	7	0.0049	0.0049	0.0049	0.0049	0.0049	0.0049
13	8	0.0035	0.0035	0.0035	0.0035	0.0035	0.0035
13	9	0.0024	0.0024	0.0024	0.0024	0.0024	0.0024

Appendix F: xF_3 Systematic Error Tables

This appendix contains tables of systematic errors for xF_3. The headings on the tables refer to the following numbering scheme:

#	Systematic Change	
1	Hadron Energy Calibration	+
2	"	-
3	Muon Energy Calibration	+
4	"	-
5	770 <B/A> Correction	-
6	"	+
7	744 <B/A> Correction	-
8	"	+
9	$\sigma^{CCFR}/\sigma^{world}$	+
10	"	-
11	$\sigma^{\nu}/\sigma^{\bar{\nu}}$	+
12	"	-
13	Charm Mass Parameter	+
14	"	-
15	Strange Sea	+
16	"	-

Bin	Xcenter	Q^2center
1	0.015	1.3
2	0.045	2.05
3	0.08	3.25
4	0.125	5.14
5	0.175	8.15
6	0.225	12.9
7	0.275	20.5
8	0.35	32.5
9	0.45	51.4

10	0.55	81.5
11	0.65	129.2
12	0.75	204.8
13	0.85	324.6
14	0.9	514.5
15		815.5

xbin	Q^2	δxF_3 1	δxF_3 2	δxF_3 3	δxF_3 4	δxF_3 5
1	1	-0.0129	-0.0110	-0.0051	-0.0125	0.0000
1	2	-0.0142	-0.0059	-0.0158	-0.0095	0.0000
1	3	-0.0087	-0.0049	-0.0035	-0.0098	0.0000
1	4	-0.0100	-0.0061	-0.0067	-0.0037	-0.0001
1	5	-0.0194	-0.0123	-0.0214	-0.0155	-0.0001
1	6	-0.0018	-0.0398	-0.0005	-0.0403	0.0000
2	1	-0.0210	-0.0106	-0.0165	-0.0069	0.0001
2	2	-0.0136	-0.0080	-0.0107	-0.0036	-0.0001
2	3	-0.0091	-0.0013	-0.0111	-0.0124	-0.0002
2	4	-0.0021	-0.0011	-0.0030	-0.0021	-0.0003
2	5	-0.0067	-0.0015	-0.0047	-0.0034	-0.0004
2	6	0.0067	0.0002	0.0103	-0.0018	-0.0004
2	7	-0.0140	0.0065	0.0027	-0.0150	-0.0005
3	2	-0.0220	-0.0327	-0.0479	-0.0184	0.0001
3	3	-0.0114	-0.0096	-0.0026	-0.0091	-0.0002
3	4	-0.0068	0.0032	-0.0030	0.0007	-0.0004
3	5	-0.0042	0.0029	0.0091	-0.0087	-0.0005
3	6	0.0023	0.0112	0.0208	0.0000	-0.0006
3	7	0.0002	0.0098	-0.0002	0.0031	-0.0006
3	8	0.0031	0.0094	0.0184	-0.0161	-0.0007
4	3	-0.0211	-0.0304	-0.0321	-0.0313	0.0000
4	4	0.0108	-0.0069	-0.0038	0.0197	-0.0005
4	5	0.0004	0.0031	-0.0085	0.0021	-0.0006
4	6	0.0068	0.0129	0.0166	0.0056	-0.0007
4	7	0.0036	0.0135	0.0164	0.0028	-0.0008
4	8	0.0203	0.0219	0.0333	0.0124	-0.0008
4	9	-0.0002	0.0190	0.0237	-0.0046	-0.0008
5	4	-0.0246	-0.0026	-0.0095	-0.0226	-0.0004
5	5	0.0097	-0.0003	0.0076	0.0192	-0.0006
5	6	0.0130	0.0049	0.0049	0.0058	-0.0007
5	7	0.0053	0.0141	0.0153	0.0089	-0.0008
5	8	0.0096	0.0196	0.0134	0.0045	-0.0008
5	9	0.0098	0.0139	0.0205	0.0069	-0.0009
5	10	0.0071	0.0266	0.0444	-0.0054	-0.0009
6	4	-0.0007	0.0026	-0.0411	0.0288	-0.0003
6	5	-0.0090	-0.0146	-0.0179	-0.0010	-0.0004
6	6	0.0123	-0.0019	0.0101	0.0111	-0.0006
6	7	0.0144	0.0233	0.0106	0.0208	-0.0007
6	8	0.0106	0.0135	0.0150	0.0188	-0.0008
6	9	0.0130	0.0114	0.0110	0.0065	-0.0007
6	10	0.0087	0.0288	0.0303	0.0078	-0.0008
7	5	0.0078	-0.0007	-0.0018	0.0118	-0.0003
7	6	0.0143	-0.0028	-0.0062	0.0123	-0.0006
7	7	0.0114	0.0040	0.0004	0.0133	-0.0006
7	8	0.0164	0.0127	0.0019	0.0124	-0.0006
7	9	0.0144	0.0130	0.0051	0.0201	-0.0007
7	10	0.0150	0.0174	0.0188	0.0052	-0.0007
8	5	0.0129	-0.0075	-0.0058	0.0235	-0.0003
8	6	0.0037	-0.0021	-0.0120	0.0097	-0.0004
8	7	0.0116	0.0000	-0.0051	0.0146	-0.0005
8	8	0.0084	0.0045	0.0059	0.0126	-0.0005
8	9	0.0104	0.0102	0.0026	0.0183	-0.0005

8	10	0.0128	0.0079	0.0093	0.0161	-0.0005
8	11	0.0081	0.0161	0.0124	0.0165	-0.0005
9	6	0.0048	-0.0068	-0.0055	0.0081	-0.0003
9	7	0.0041	0.0003	-0.0125	0.0153	-0.0003
9	8	0.0086	-0.0035	-0.0045	0.0152	-0.0003
9	9	0.0044	0.0050	-0.0028	0.0137	-0.0003
9	10	0.0074	0.0000	-0.0042	0.0087	-0.0003
9	11	0.0087	0.0049	-0.0035	0.0111	-0.0003
10	6	0.0056	0.0038	0.0049	0.0137	-0.0002
10	7	0.0010	-0.0043	-0.0109	0.0045	-0.0001
10	8	0.0039	-0.0011	-0.0037	0.0065	-0.0001
10	9	0.0079	0.0011	-0.0033	0.0106	-0.0002
10	10	0.0078	0.0051	0.0060	0.0146	-0.0002
10	11	0.0050	0.0014	-0.0066	0.0157	-0.0001
11	7	0.1122	0.1122	0.1122	0.1122	0.1122
11	8	0.0913	0.0913	0.0913	0.0913	0.0913
11	9	0.0849	0.0849	0.0849	0.0849	0.0849
11	10	0.0710	0.0710	0.0710	0.0710	0.0710
11	11	0.0448	0.0448	0.0448	0.0448	0.0448
12	7	0.0482	0.0482	0.0482	0.0482	0.0482
12	8	0.0401	0.0401	0.0401	0.0401	0.0401
12	9	0.0345	0.0345	0.0345	0.0345	0.0345
13	7	0.0056	0.0056	0.0056	0.0056	0.0056
13	8	0.0040	0.0040	0.0040	0.0040	0.0040
13	9	0.0025	0.0025	0.0025	0.0025	0.0025

xbin	Q_2	δxF_3 6	δxF_3 7	δxF_3 8	δxF_3 9	δxF_3 10
1	1	-0.0001	-0.0003	0.0002	0.2616	-0.0025
1	2	0.0000	-0.0003	0.0002	0.2931	-0.0029
1	3	0.0000	-0.0002	0.0002	0.2748	-0.0029
1	4	0.0001	-0.0003	0.0003	0.3422	-0.0038
1	5	0.0001	-0.0003	0.0003	0.3169	-0.0033
1	6	0.0001	-0.0001	0.0002	0.1916	-0.0023
2	1	-0.0001	-0.0004	0.0004	0.4649	-0.0040
2	2	0.0001	-0.0005	0.0005	0.4955	-0.0045
2	3	0.0002	-0.0004	0.0004	0.4718	-0.0050
2	4	0.0003	-0.0005	0.0004	0.5342	-0.0060
2	5	0.0003	-0.0005	0.0005	0.5519	-0.0063
2	6	0.0004	-0.0005	0.0005	0.5476	-0.0063
2	7	0.0005	-0.0006	0.0005	0.6184	-0.0072
3	2	-0.0001	-0.0006	0.0006	0.5991	-0.0049
3	3	0.0002	-0.0007	0.0006	0.6567	-0.0063
3	4	0.0004	-0.0006	0.0006	0.6508	-0.0071
3	5	0.0005	-0.0007	0.0006	0.7129	-0.0080
3	6	0.0006	-0.0007	0.0007	0.7324	-0.0084
3	7	0.0006	-0.0007	0.0006	0.7291	-0.0087
3	8	0.0007	-0.0007	0.0006	0.7359	-0.0088
4	3	0.0001	-0.0007	0.0007	0.7043	-0.0064
4	4	0.0005	-0.0008	0.0008	0.8327	-0.0087
4	5	0.0005	-0.0007	0.0007	0.7756	-0.0086
4	6	0.0007	-0.0008	0.0007	0.8145	-0.0094
4	7	0.0007	-0.0008	0.0008	0.8385	-0.0098
4	8	0.0008	-0.0008	0.0008	0.8386	-0.0099
4	9	0.0008	-0.0008	0.0008	0.8374	-0.0097
5	4	0.0004	-0.0009	0.0008	0.8686	-0.0088
5	5	0.0006	-0.0008	0.0008	0.8482	-0.0092
5	6	0.0006	-0.0008	0.0008	0.8232	-0.0093
5	7	0.0007	-0.0008	0.0008	0.8427	-0.0097
5	8	0.0008	-0.0008	0.0008	0.8595	-0.0100
5	9	0.0008	-0.0008	0.0008	0.8471	-0.0101
5	10	0.0008	-0.0009	0.0008	0.8576	-0.0099
6	4	0.0003	-0.0009	0.0008	0.8387	-0.0081
6	5	0.0004	-0.0007	0.0007	0.7668	-0.0081
6	6	0.0006	-0.0008	0.0007	0.7927	-0.0089
6	7	0.0007	-0.0008	0.0007	0.7870	-0.0090
6	8	0.0007	-0.0008	0.0007	0.7851	-0.0092
6	9	0.0007	-0.0007	0.0007	0.7467	-0.0087
6	10	0.0008	-0.0008	0.0007	0.7780	-0.0091
7	5	0.0004	-0.0007	0.0007	0.7187	-0.0072
7	6	0.0005	-0.0007	0.0007	0.7161	-0.0079
7	7	0.0006	-0.0007	0.0006	0.6863	-0.0079
7	8	0.0006	-0.0007	0.0006	0.6717	-0.0078
7	9	0.0007	-0.0007	0.0006	0.6958	-0.0082
7	10	0.0006	-0.0006	0.0006	0.6372	-0.0077
8	5	0.0003	-0.0006	0.0006	0.6221	-0.0063
8	6	0.0004	-0.0006	0.0005	0.5849	-0.0063
8	7	0.0004	-0.0005	0.0005	0.5408	-0.0061
8	8	0.0005	-0.0005	0.0005	0.5264	-0.0062
8	9	0.0005	-0.0005	0.0005	0.5131	-0.0060

8	10	0.0005	-0.0005	0.0004	0.4868	-0.0058
8	11	0.0005	-0.0004	0.0005	0.4804	-0.0056
9	6	0.0003	-0.0004	0.0004	0.4098	-0.0044
9	7	0.0003	-0.0003	0.0003	0.3465	-0.0038
9	8	0.0003	-0.0003	0.0003	0.3303	-0.0039
9	9	0.0003	-0.0003	0.0003	0.3091	-0.0037
9	10	0.0003	-0.0003	0.0003	0.2910	-0.0035
9	11	0.0003	-0.0003	0.0003	0.2660	-0.0031
10	6	0.0002	-0.0003	0.0003	0.2662	-0.0027
10	7	0.0001	-0.0002	0.0002	0.1926	-0.0021
10	8	0.0001	-0.0002	0.0001	0.1655	-0.0019
10	9	0.0002	-0.0002	0.0002	0.1684	-0.0020
10	10	0.0002	-0.0002	0.0001	0.1614	-0.0019
10	11	0.0001	-0.0001	0.0001	0.1335	-0.0016
11	7	0.1122	0.1122	0.1122	0.1122	0.1122
11	8	0.0913	0.0913	0.0913	0.0913	0.0913
11	9	0.0849	0.0849	0.0849	0.0849	0.0849
11	10	0.0710	0.0710	0.0710	0.0710	0.0710
11	11	0.0448	0.0448	0.0448	0.0448	0.0448
12	7	0.0482	0.0482	0.0482	0.0482	0.0482
12	8	0.0401	0.0401	0.0401	0.0401	0.0401
12	9	0.0345	0.0345	0.0345	0.0345	0.0345
13	7	0.0056	0.0056	0.0056	0.0056	0.0056
13	8	0.0040	0.0040	0.0040	0.0040	0.0040
13	9	0.0025	0.0025	0.0025	0.0025	0.0025

xbin	Q^2	δxF_3 11	δxF_3 12	δxF_3 13	δxF_3 14	δxF_3 15	δxF_3 6
1	1	0.0020	-0.0021	-0.0822	-0.0852	0.0001	-0.0001
1	2	0.0022	-0.0022	-0.0875	-0.0907	0.0001	0.0000
1	3	0.0019	-0.0020	-0.0808	-0.0843	0.0000	0.0000
1	4	0.0023	-0.0023	-0.0732	-0.0739	0.0000	0.0000
1	5	0.0023	-0.0023	-0.0604	-0.0587	0.0000	0.0000
1	6	0.0012	-0.0011	-0.0473	-0.0450	0.0001	0.0000
2	1	0.0038	-0.0039	-0.0816	-0.0778	0.0001	-0.0001
2	2	0.0039	-0.0040	-0.0715	-0.0755	0.0001	0.0000
2	3	0.0033	-0.0033	-0.0636	-0.0732	0.0000	0.0000
2	4	0.0035	-0.0035	-0.0580	-0.0669	0.0000	0.0000
2	5	0.0036	-0.0037	-0.0529	-0.0585	0.0000	0.0000
2	6	0.0036	-0.0036	-0.0481	-0.0556	0.0000	0.0000
2	7	0.0040	-0.0040	-0.0457	-0.0360	0.0000	0.0000
3	2	0.0051	-0.0052	-0.0497	-0.0404	0.0000	0.0000
3	3	0.0050	-0.0051	-0.0374	-0.0402	0.0000	0.0000
3	4	0.0044	-0.0045	-0.0322	-0.0438	0.0000	0.0000
3	5	0.0047	-0.0048	-0.0281	-0.0415	0.0000	0.0000
3	6	0.0047	-0.0048	-0.0269	-0.0318	0.0000	0.0000
3	7	0.0045	-0.0045	-0.0285	-0.0387	0.0000	0.0000
3	8	0.0045	-0.0046	-0.0299	-0.0240	0.0000	0.0000
4	3	0.0056	-0.0057	-0.0107	-0.0003	0.0000	-0.0001
4	4	0.0059	-0.0060	-0.0033	-0.0075	0.0001	0.0000
4	5	0.0052	-0.0052	-0.0031	-0.0160	0.0000	0.0000
4	6	0.0052	-0.0052	-0.0044	-0.0183	0.0000	0.0000
4	7	0.0053	-0.0053	-0.0072	-0.0118	0.0000	0.0000
4	8	0.0052	-0.0052	-0.0117	-0.0233	0.0000	0.0000
4	9	0.0053	-0.0054	-0.0165	-0.0081	0.0000	0.0000
5	4	0.0063	-0.0065	0.0191	0.0273	0.0000	-0.0001
5	5	0.0058	-0.0059	0.0194	0.0123	0.0000	0.0000
5	6	0.0054	-0.0054	0.0162	0.0017	0.0000	0.0000
5	7	0.0054	-0.0055	0.0116	0.0007	0.0000	0.0000
5	8	0.0054	-0.0055	0.0060	0.0017	0.0000	0.0000
5	9	0.0052	-0.0053	-0.0010	-0.0132	0.0000	0.0000
5	10	0.0054	-0.0055	-0.0064	0.0188	0.0000	0.0000
6	4	0.0064	-0.0065	0.0327	0.0523	0.0000	-0.0001
6	5	0.0054	-0.0054	0.0339	0.0342	0.0000	0.0000
6	6	0.0052	-0.0053	0.0307	0.0201	0.0000	0.0000
6	7	0.0050	-0.0051	0.0253	0.0120	0.0000	0.0000
6	8	0.0049	-0.0049	0.0197	0.0162	0.0000	0.0000
6	9	0.0047	-0.0047	0.0142	0.0039	0.0000	0.0000
6	10	0.0049	-0.0050	0.0068	0.0089	0.0000	0.0000
7	5	0.0053	-0.0053	0.0394	0.0469	0.0001	0.0000
7	6	0.0048	-0.0049	0.0363	0.0298	0.0000	0.0000
7	7	0.0044	-0.0044	0.0333	0.0228	0.0000	0.0000
7	8	0.0042	-0.0043	0.0288	0.0228	0.0000	0.0000
7	9	0.0043	-0.0044	0.0233	0.0189	0.0000	0.0000
7	10	0.0039	-0.0039	0.0169	0.0074	0.0000	0.0000
8	5	0.0045	-0.0046	0.0350	0.0467	0.0000	0.0000
8	6	0.0040	-0.0041	0.0355	0.0355	0.0000	0.0000
8	7	0.0035	-0.0036	0.0315	0.0244	0.0000	0.0000
8	8	0.0033	-0.0033	0.0283	0.0219	0.0000	0.0000
8	9	0.0032	-0.0033	0.0261	0.0249	0.0000	0.0000

8	10	0.0030	-0.0030	0.0216	0.0148	0.0000	0.0000
8	11	0.0030	-0.0030	0.0193	0.0268	0.0000	0.0000
9	6	0.0028	-0.0029	0.0208	0.0240	0.0000	0.0000
9	7	0.0023	-0.0023	0.0203	0.0173	0.0000	0.0000
9	8	0.0021	-0.0021	0.0185	0.0145	0.0000	0.0000
9	9	0.0019	-0.0019	0.0182	0.0174	0.0000	0.0000
9	10	0.0018	-0.0018	0.0164	0.0142	0.0000	0.0000
9	11	0.0017	-0.0017	0.0148	0.0148	0.0000	0.0000
10	6	0.0019	-0.0019	0.0085	0.0114	0.0000	0.0000
10	7	0.0013	-0.0013	0.0082	0.0080	0.0000	0.0000
10	8	0.0011	-0.0011	0.0081	0.0066	0.0000	0.0000
10	9	0.0011	-0.0011	0.0077	0.0067	0.0000	0.0000
10	10	0.0010	-0.0010	0.0078	0.0062	0.0000	0.0000
10	11	0.0008	-0.0008	0.0072	0.0058	0.0000	0.0000
11	7	0.1122	0.1122	0.1122	0.1122	0.1122	0.1122
11	8	0.0913	0.0913	0.0913	0.0913	0.0913	0.0913
11	9	0.0849	0.0849	0.0849	0.0849	0.0849	0.0849
11	10	0.0710	0.0710	0.0710	0.0710	0.0710	0.0710
11	11	0.0448	0.0448	0.0448	0.0448	0.0448	0.0448
12	7	0.0482	0.0482	0.0482	0.0482	0.0482	0.0482
12	8	0.0401	0.0401	0.0401	0.0401	0.0401	0.0401
12	9	0.0345	0.0345	0.0345	0.0345	0.0345	0.0345
13	7	0.0056	0.0056	0.0056	0.0056	0.0056	0.0056
13	8	0.0040	0.0040	0.0040	0.0040	0.0040	0.0040
13	9	0.0025	0.0025	0.0025	0.0025	0.0025	0.0025

Appendix G: The Six Event Triggers

G.1 Trigger 1: The Charged Current Trigger

Trigger 1 is designed to identify charged-current events. It requires a muon originating in the target and penetrating into the toroid for momentum analysis.

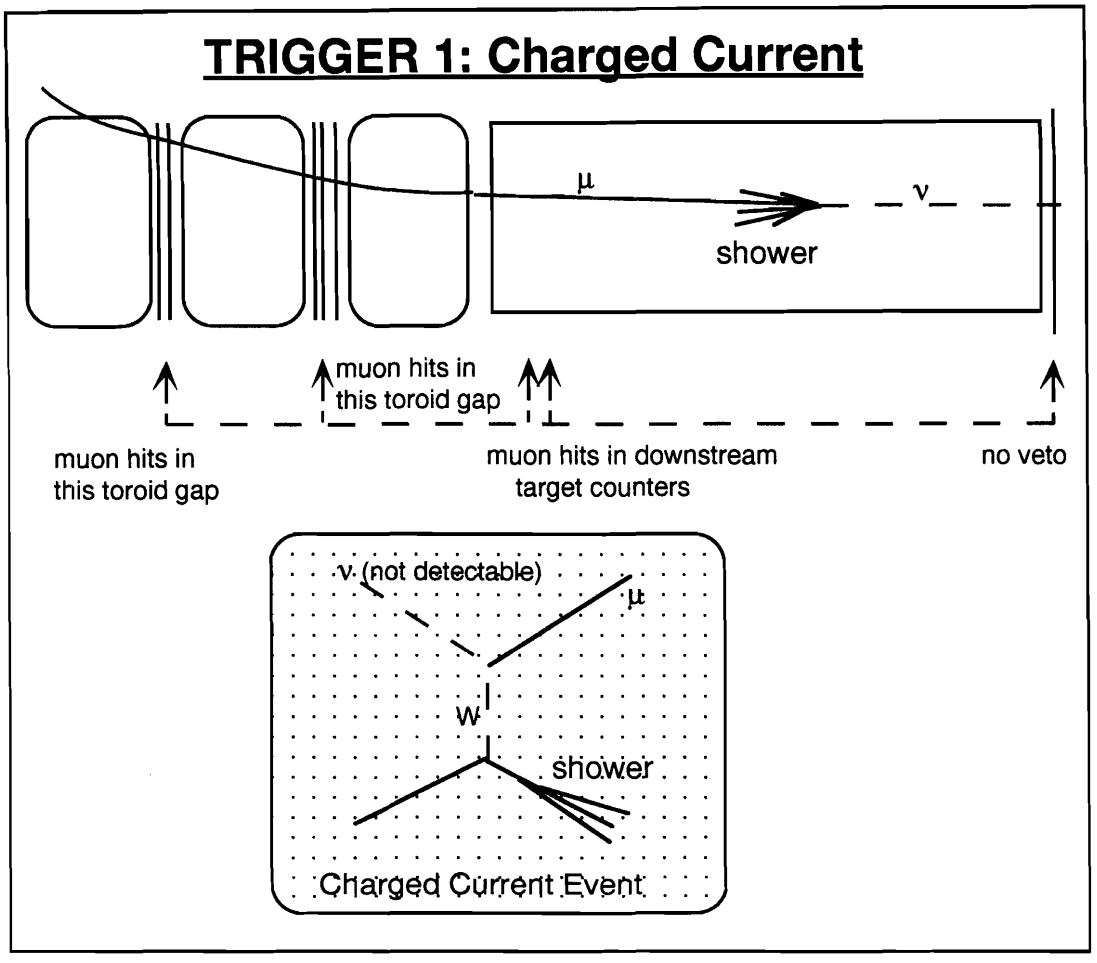

Figure G.1: Trigger 1 Schematic..The charged current trigger signature. The top diagram shows what a typical CC event looks like in the CCFR detector. The writing under the detector lists the trigger 1 criteria. The bottom figure is the feynman diagram for a CC interaction.

Trigger 1 is the primary charged-current (cc) trigger. It looks for a muon penetrating into the toroid. The typical CCFR charged current analysis requires good muon momentum identification. Asking for hits in the last target counter as well as in the toroid gaps accomplishes two tasks; the muon momentum of these events can be well established and the penetration requirement discards cosmic rays.

These events are also used for the flux determination. The flux is determined from events with low hadronic energy, so avoiding an energy requirement is beneficial to trigger 1.

Logically, either of two topologies must be satisfied: In the first, at least two of the last four counters (counters 1 through 4) must fire their s-bits, and one counter in both of the instrumented toroid gaps must also fire their sbits. The second trigger definition does not require the muon to penetrate to the last toroid gap but demands the firing of two additional target s-bits out of counters 9 through 12.

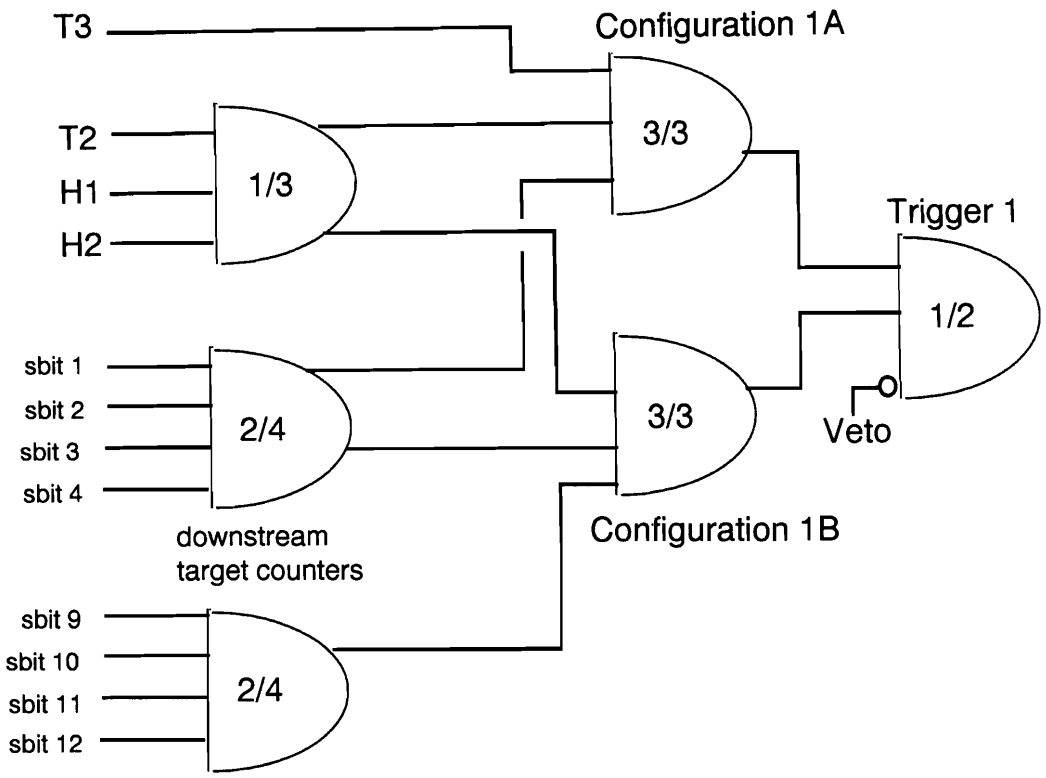

Figure G.2: Trigger 1 logic diagram..

G.2 Trigger 2: The Neutral Current Trigger

This trigger is designed to identify neutral-current events. There is no outgoing muon in a neutral current event so the trigger can only work with shower information.

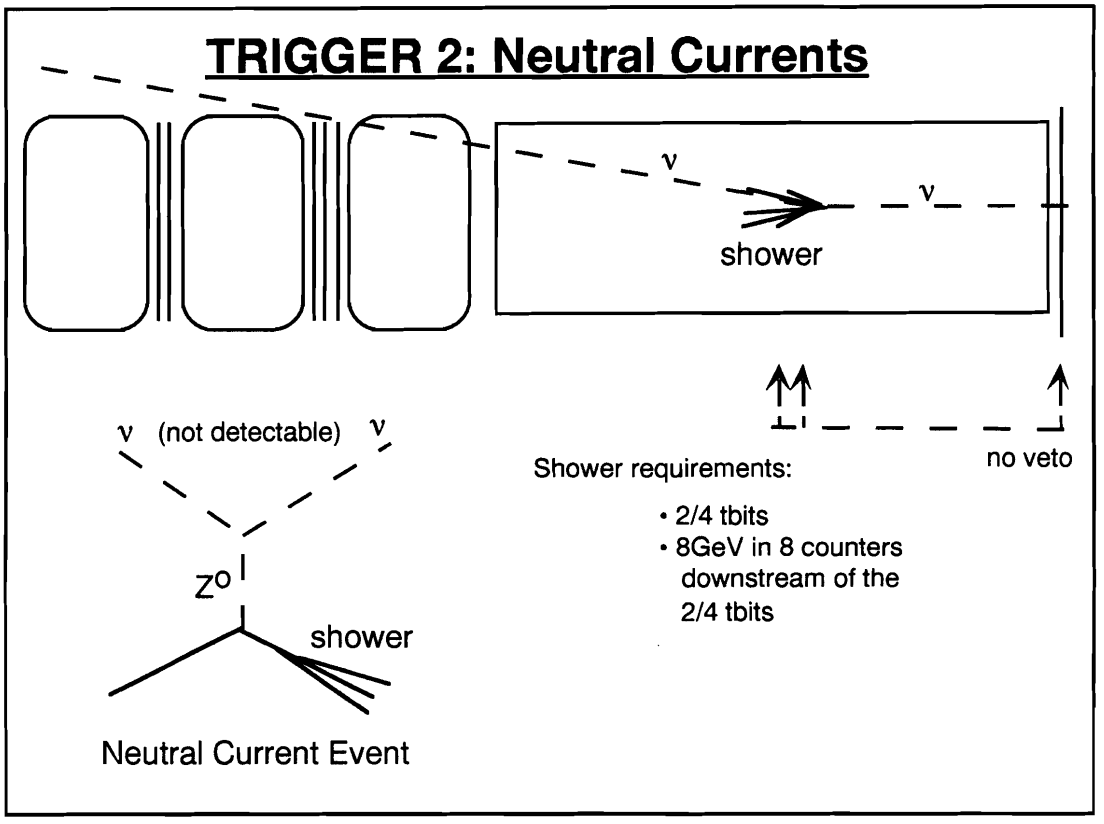

Figure G.3: Trigger 2 Schematic. The neutral current trigger signature. The top diagram shows what a typical NC event looks like in the CCFR detector. The writing under the detector lists the trigger 2 criteria. The bottom figure is the feynman diagram for a NC interaction.

Logically, trigger 2 is a large "or" of overlapping NCBITS. Recall the NCBITS have a minimal length requirement: two out of a consecutive set of four *TBITS* must fire (the *TBITS* fire for more than one minimum ionizing particle). In addition 8 GeV must be deposited in the 8 consecutive counters (the corresponding NBIT) associated with the above *TBITS*. Trigger 2 also requires there be no signal in the veto wall.

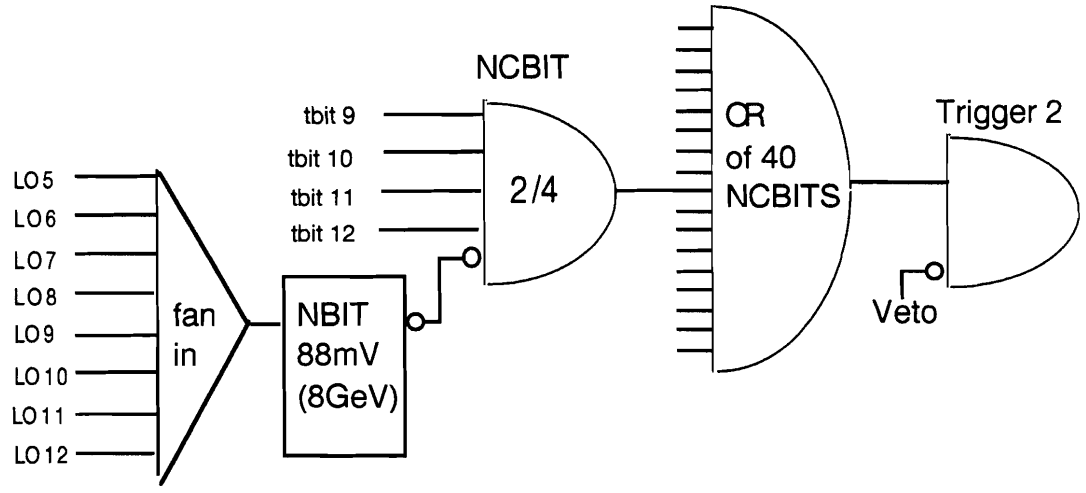

Figure G.4: Trigger 2 logic diagram..

G.3 Trigger 3: The Muon Penetration Trigger

Trigger 3 is designed to find charged current events in which the muon does not make it to the toroid gap. This includes muons which range out in the calorimeter or exit out the side before reaching the toroid. Trigger 3 looks for a reasonably long muon track in the target, and makes a small energy requirement on the shower:

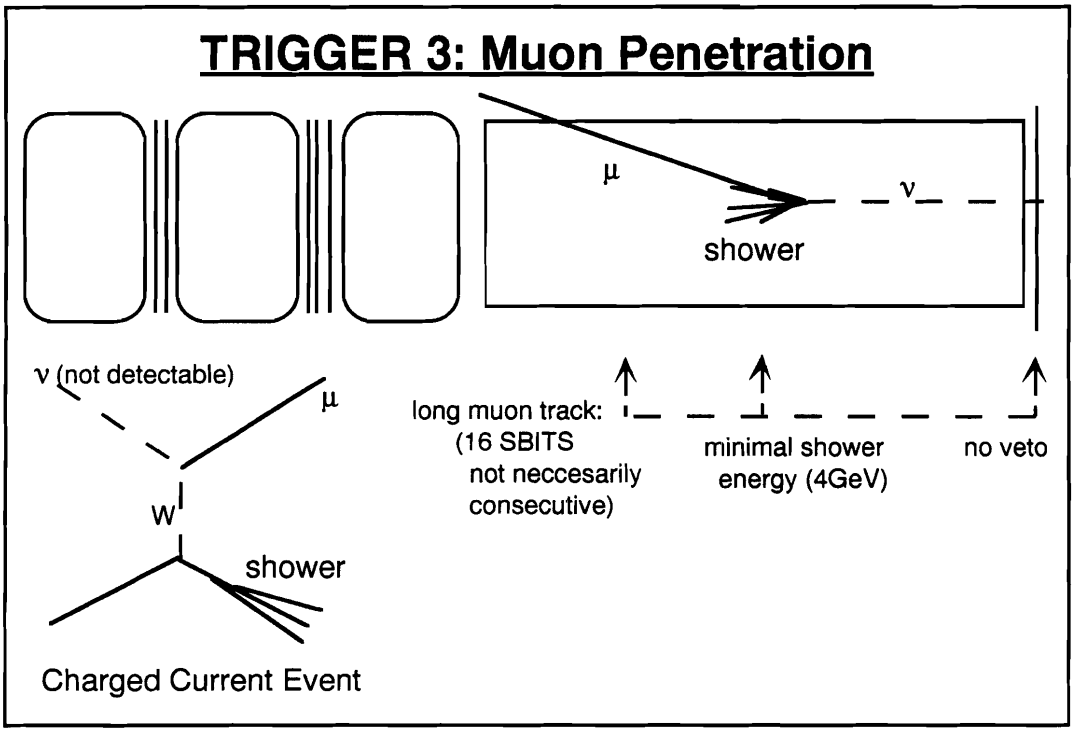

Figure G.5: (Trigger 3) The penetration trigger signature. . The top diagram shows a typical CC event that does not make it to the toroid. The writing under the detector lists the trigger 3 criteria. The bottom figure is the feynman diagram for a CC interaction.

Trigger 3 requires any 16 sbits to fire in the target (not necessarily consecutive) along with 4 *GeV* of hadronic energy deposited in any set of 8 consecutive counters (not necessarily those that fired their s-bits):

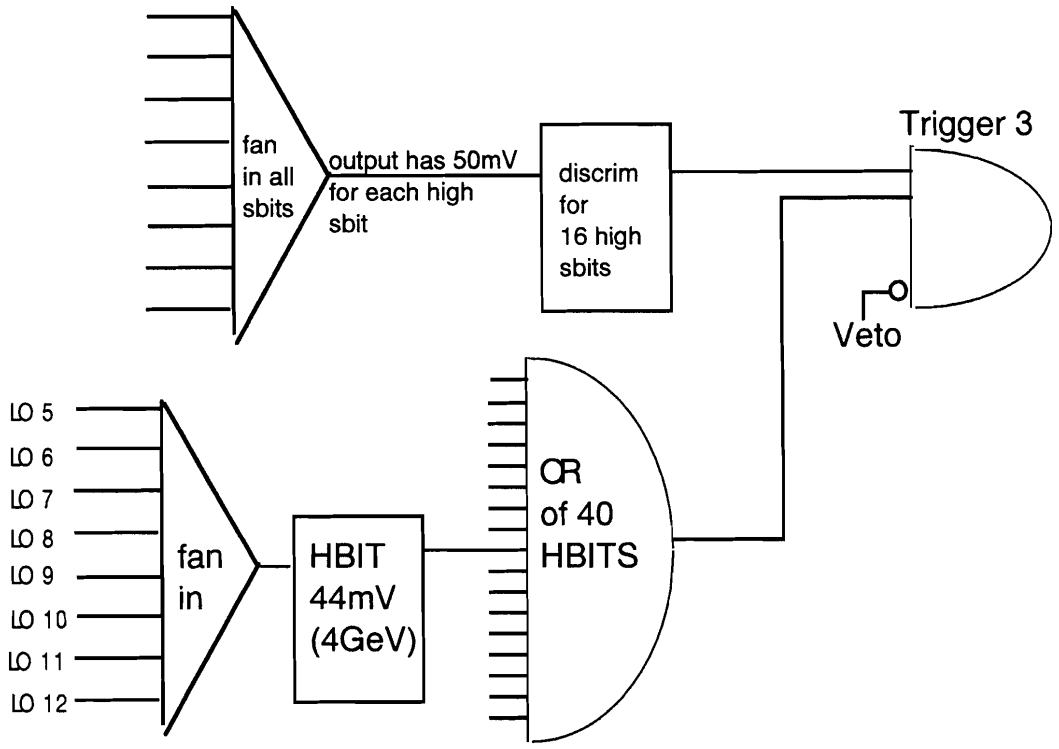

Figure G.6: Trigger 3 logic schematic.

G.4 Trigger 4: Charged Current Efficiency Trigger

Trigger 4 is used to measure the Trigger 1 inefficiency which was found it to be < 10^{-4}. It is similar to Trigger 1; instead of looking at sbits from counters 1-4 and counters 9-12, it uses counters 5-8 and 13-16. Trigger 4 uses PTOR (from trigger 6) and HBIT OR (from trigger 3) to replace the toroid gap requirements of trigger 1. Since trigger 4 makes stricter requirements than Trigger 1, all of the Trigger 4s should be included in the Trigger 1 sample.

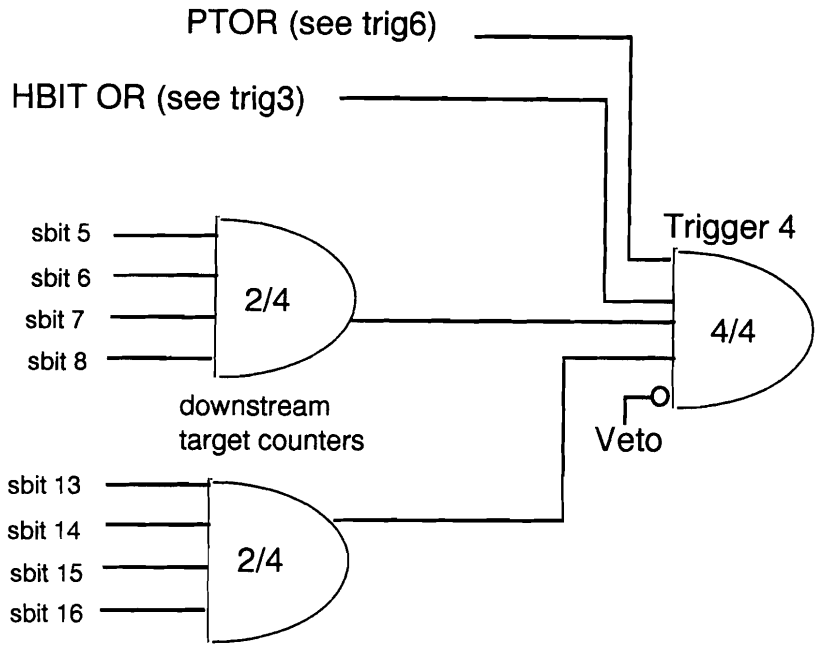

Figure G.7: Trigger 4 (the charged current efficiency trigger) logic.

G.5 Trigger 5: Test Beam Trigger

The use of this trigger is reserved for test beam running, when muon and hadron beams are directly incident on the target.

G.6 Trigger 6: Straight Through Muon Trigger

Trigger 6 is not looking for neutrino events. It is designed to select high energy muons produced upstream of Lab E that pass through the entire detector. The stiff muon tracks passing this trigger are used for calibration and drift-chamber alignment.

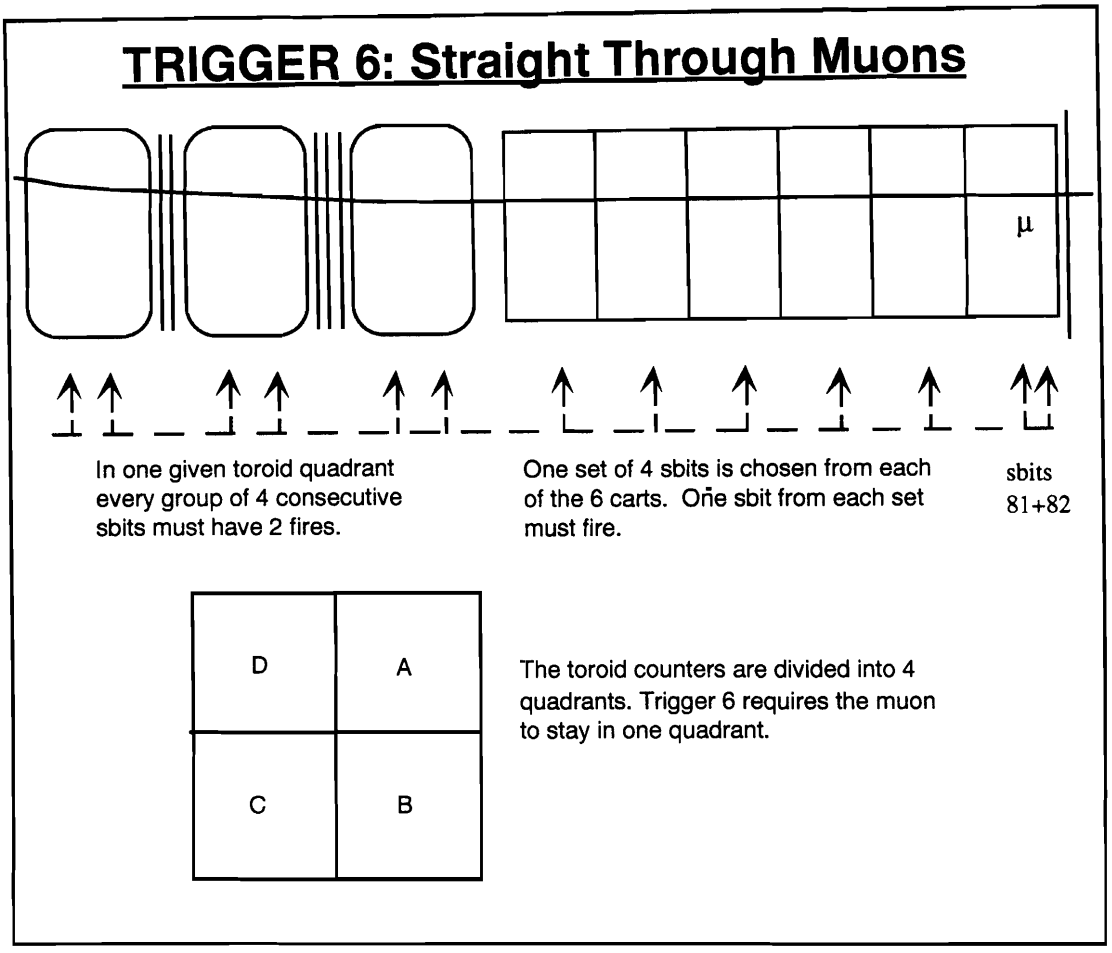

Figure H8: (Trigger 6) The straight through muon trigger. The top diagram shows a high energy muon passing through the detector typically produced by a neutrino interaction in the berm. The writing under the detector lists the trigger 6 criteria. The bottom figure shows the 4 quadrants of a toroid counter.

For trigger 6 one s-bit out of a set of four in each of the target carts must fire, sbits 81 or 82 must fire, and 2 out of each set of 4 toroid sbits must fire in one given quadrant. In E744 this trigger was prescaled down by a factor of 8. In E770 the trigger was generally not prescaled in order to accumulate additional events for counter energy calibration.

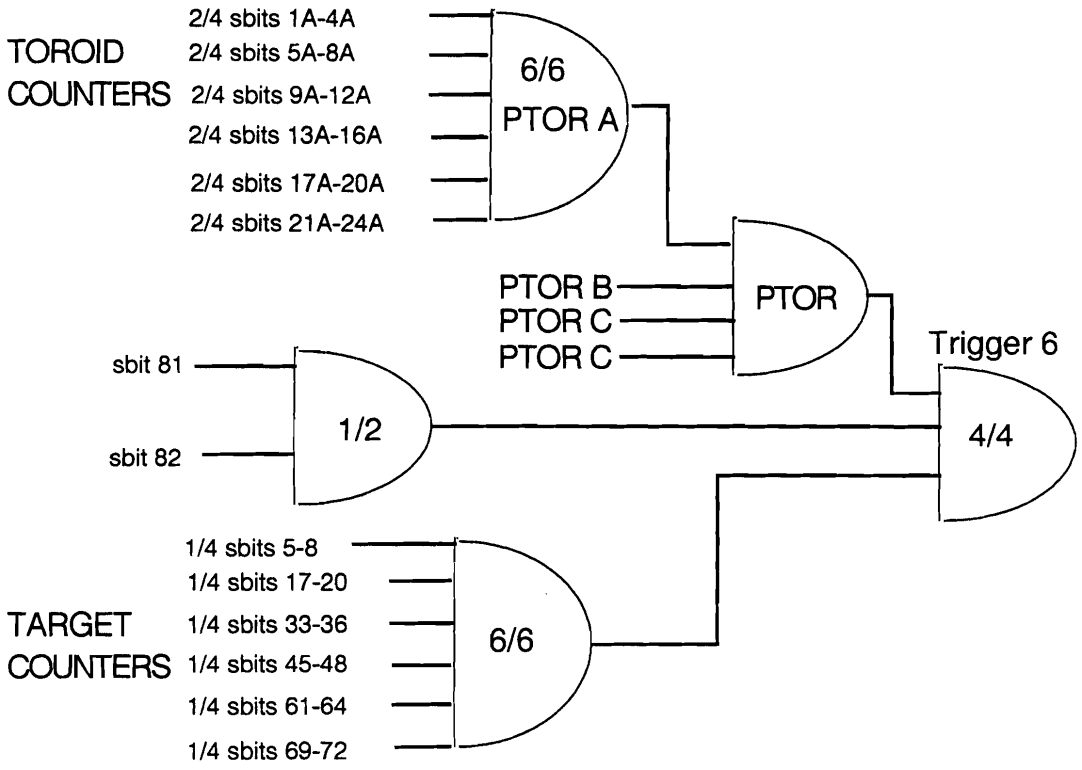

Figure G.9: Trigger 6 logic schematic.

Appendix H: Data versus MC

This appendix contains plots which compare the data and MC distributions. Plots for both E770 and E744, neutrinos and anti-neutrinos are included.

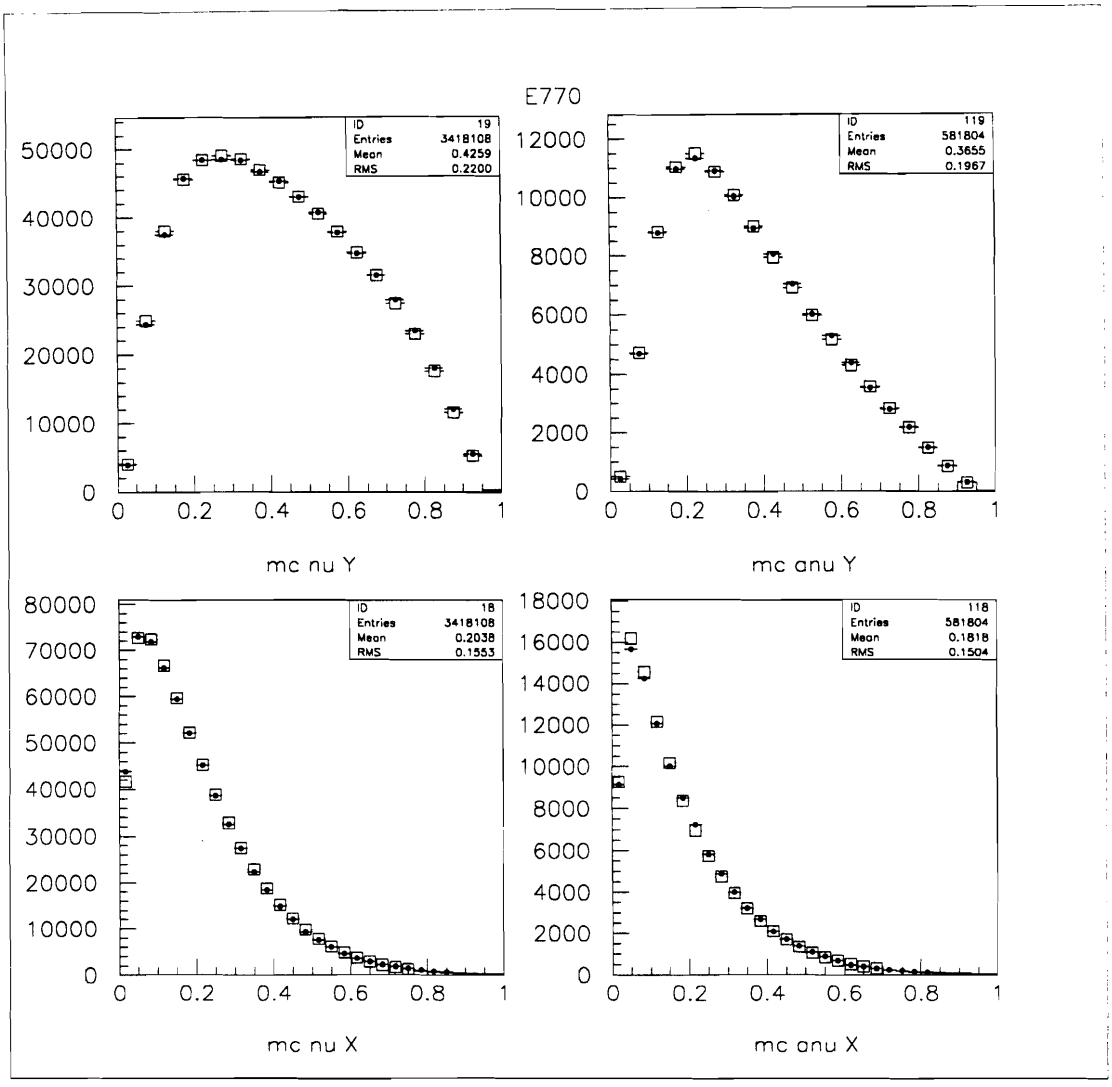

Figure H.1: Data (squares) vs MC(points) for E770 Neutrinos (right) Anti-Neutrinos (left) y-distribution(upper) x-distribution (lower)

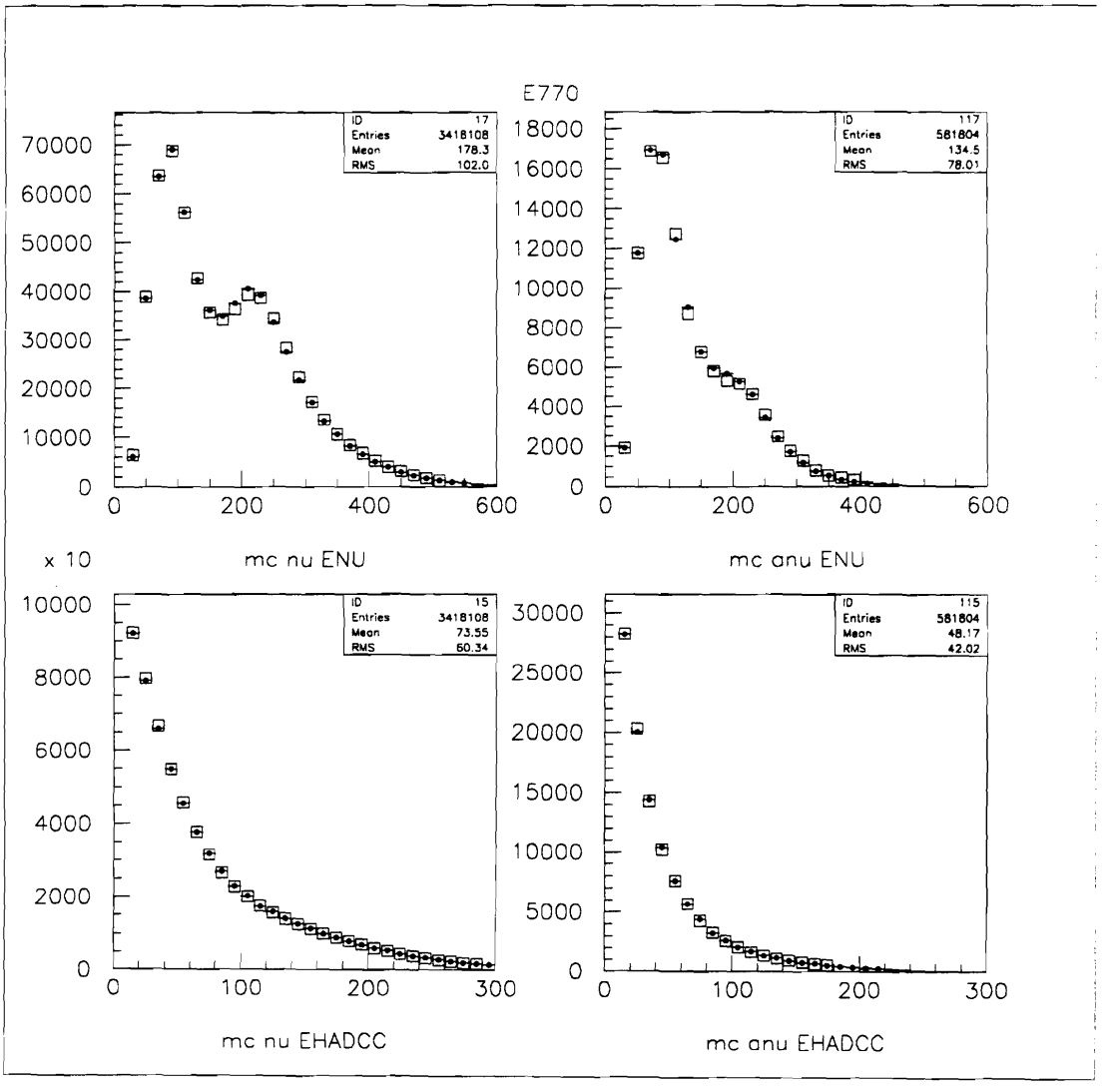

Figure H.2: Data (squares) vs MC(points) for E770 Neutrinos (right) Anti-Neutrinos (left) E_ν-distribution(upper) E_{had}-distribution (lower)

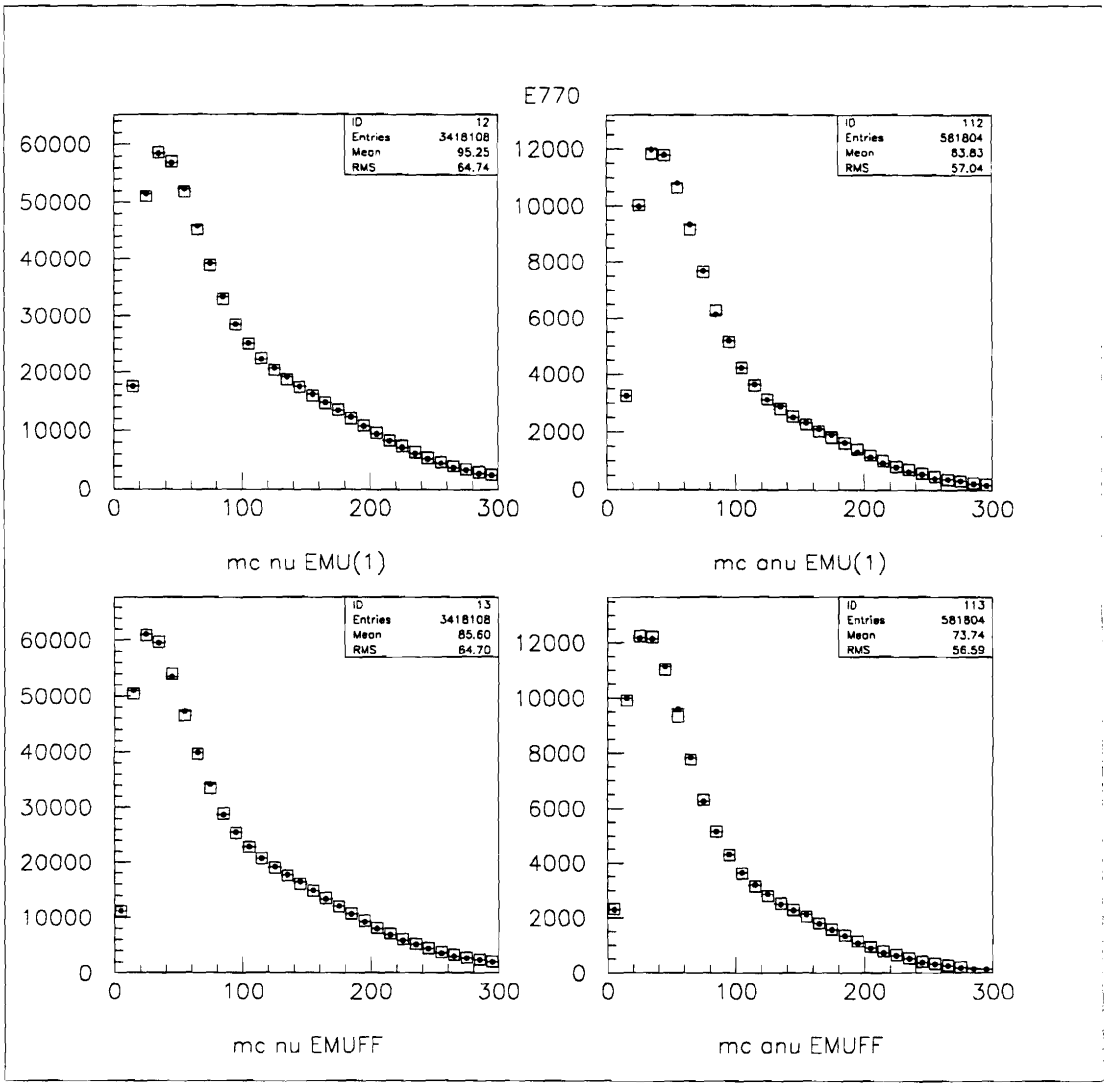

Figure H.3: Data (squares) vs MC(points) for E770 Neutrinos (right) Anti-Neutrinos (left) E_μ-distribution(upper) E_μ*(at toroid front face)*-distribution (lower)

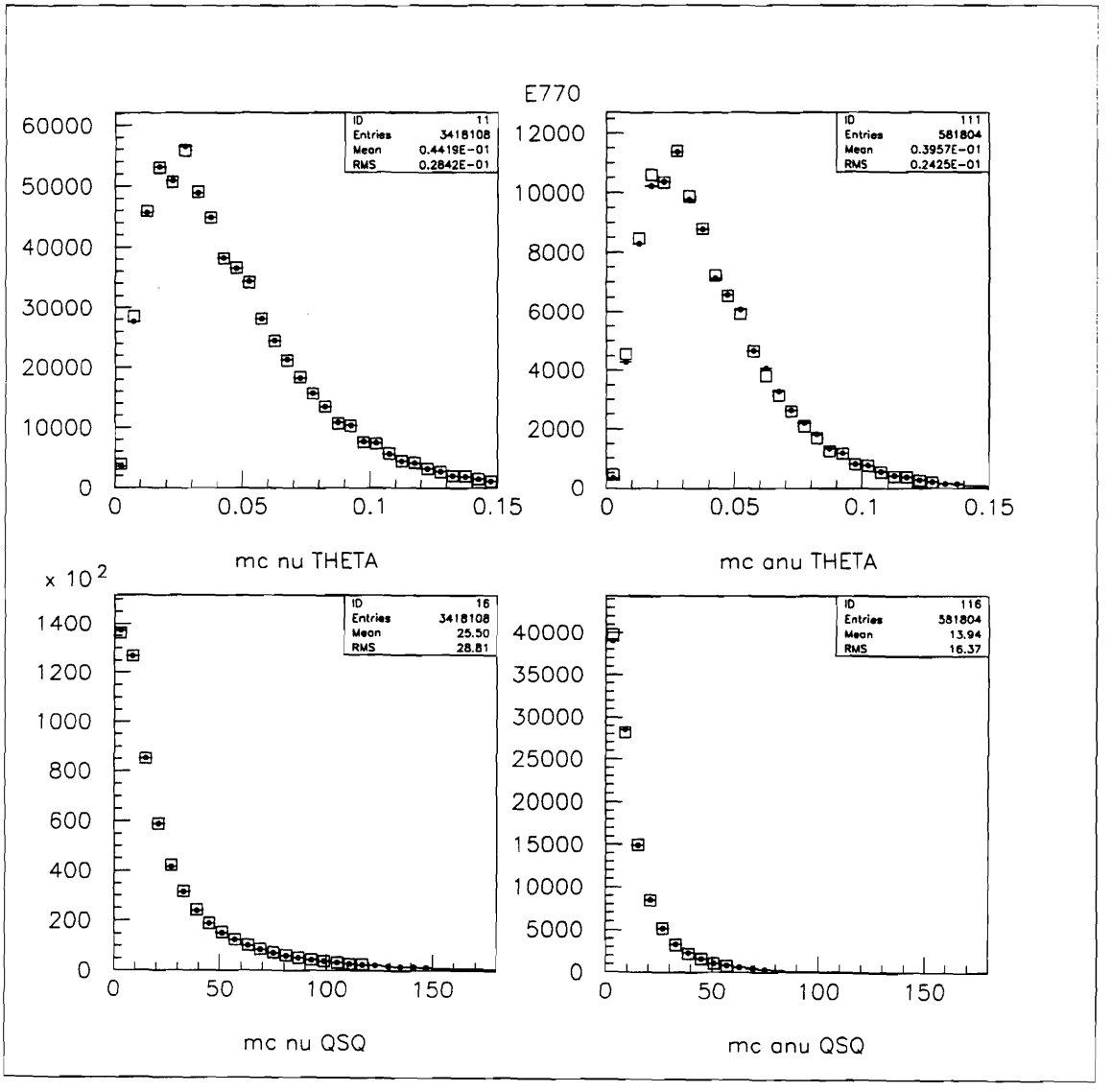

Figure H.4: Data (squares) vs MC(points) for E770 Neutrinos (right) Anti-Neutrinos (left) θ-distribution(upper) Q^2-distribution (lower)

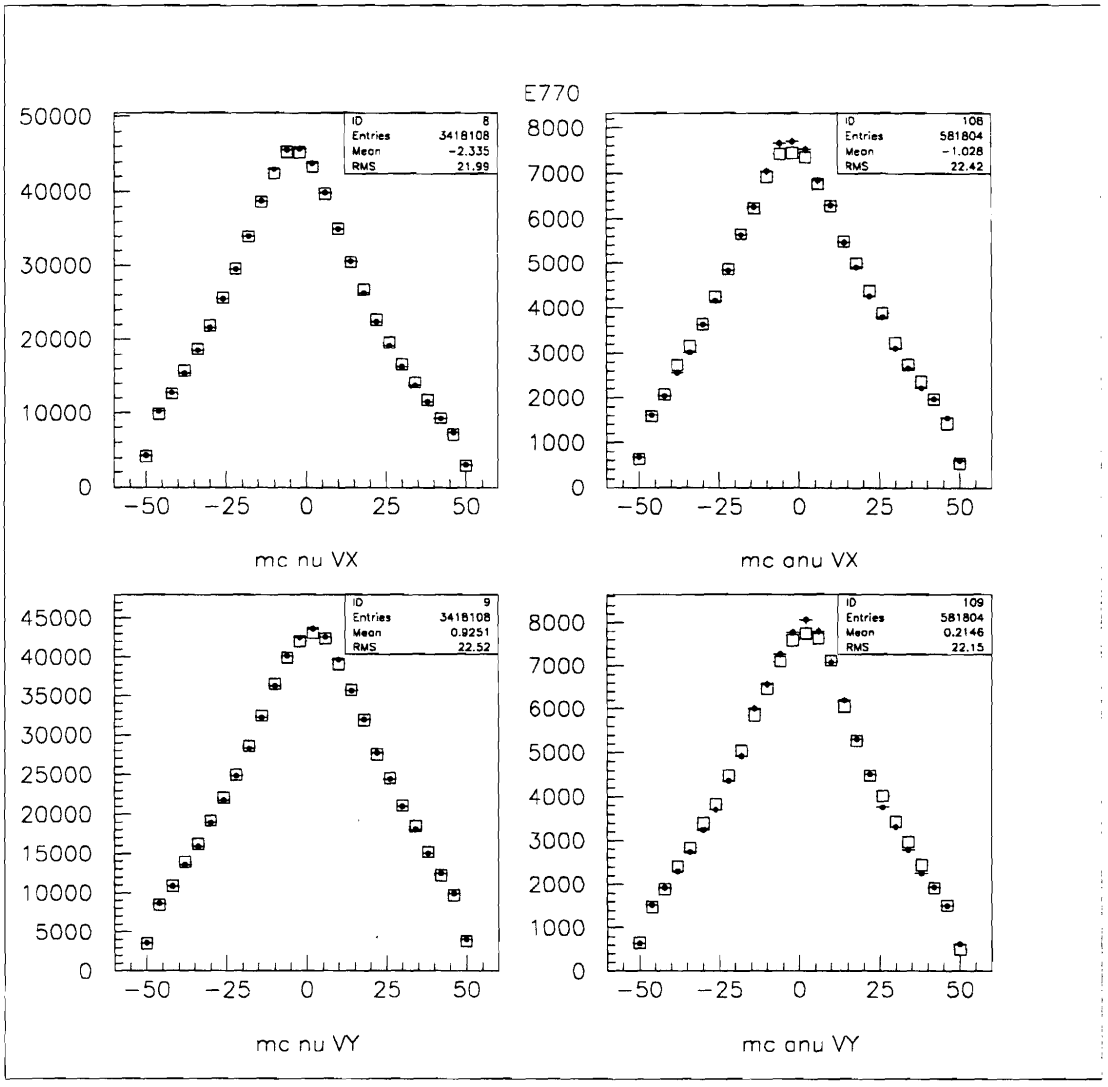

Figure H.5: Data (squares) vs MC(points) for E770 Neutrinos (right) Anti-Neutrinos (left) *x vertex*-distribution(upper) *y vertex*-distribution (lower)

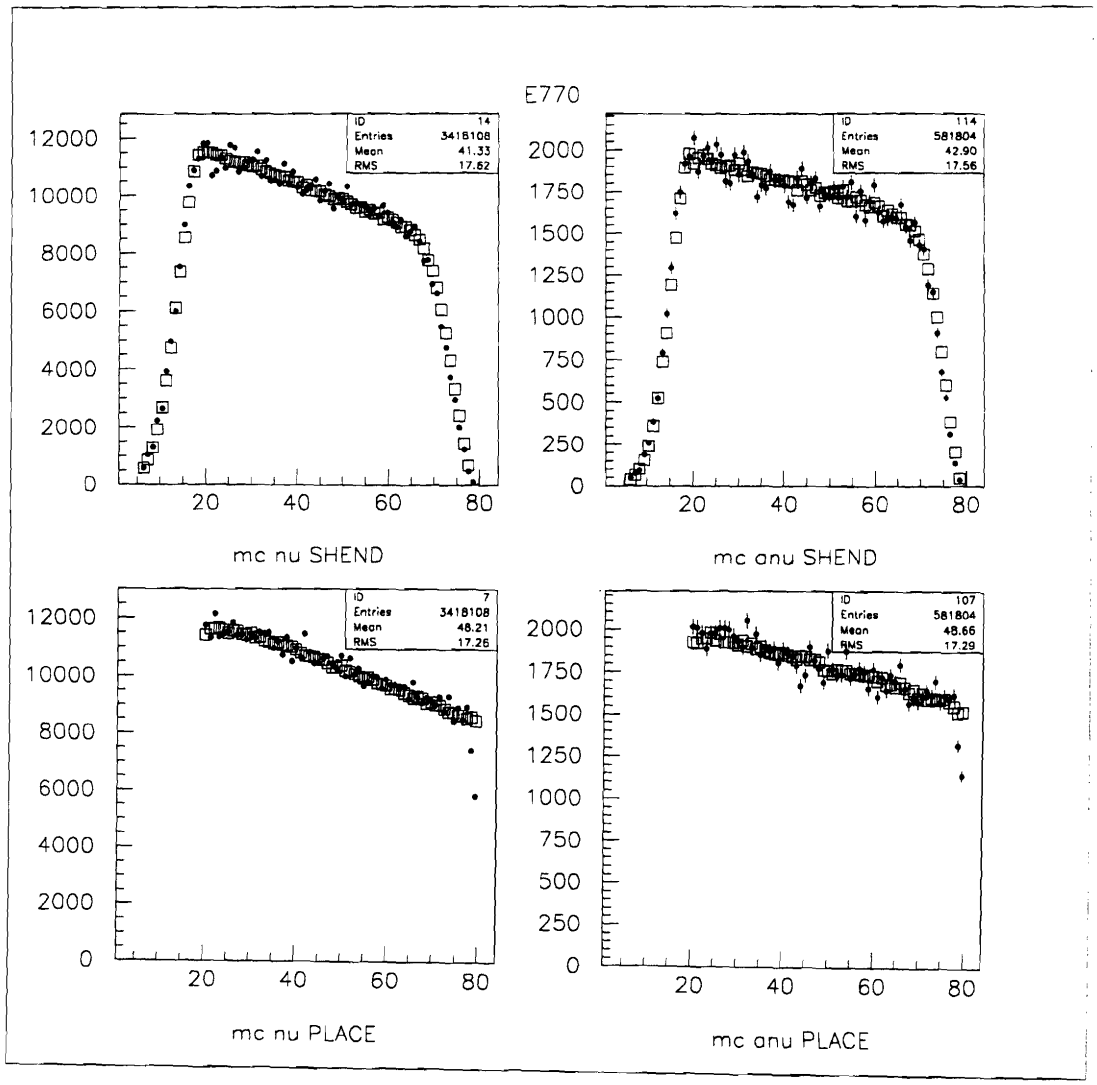

Figure H.6: Data (squares) vs MC(points) for E770 Neutrinos (right) Anti-Neutrinos (left) *shouer end*-distribution(upper) *place*-distribution (lower)

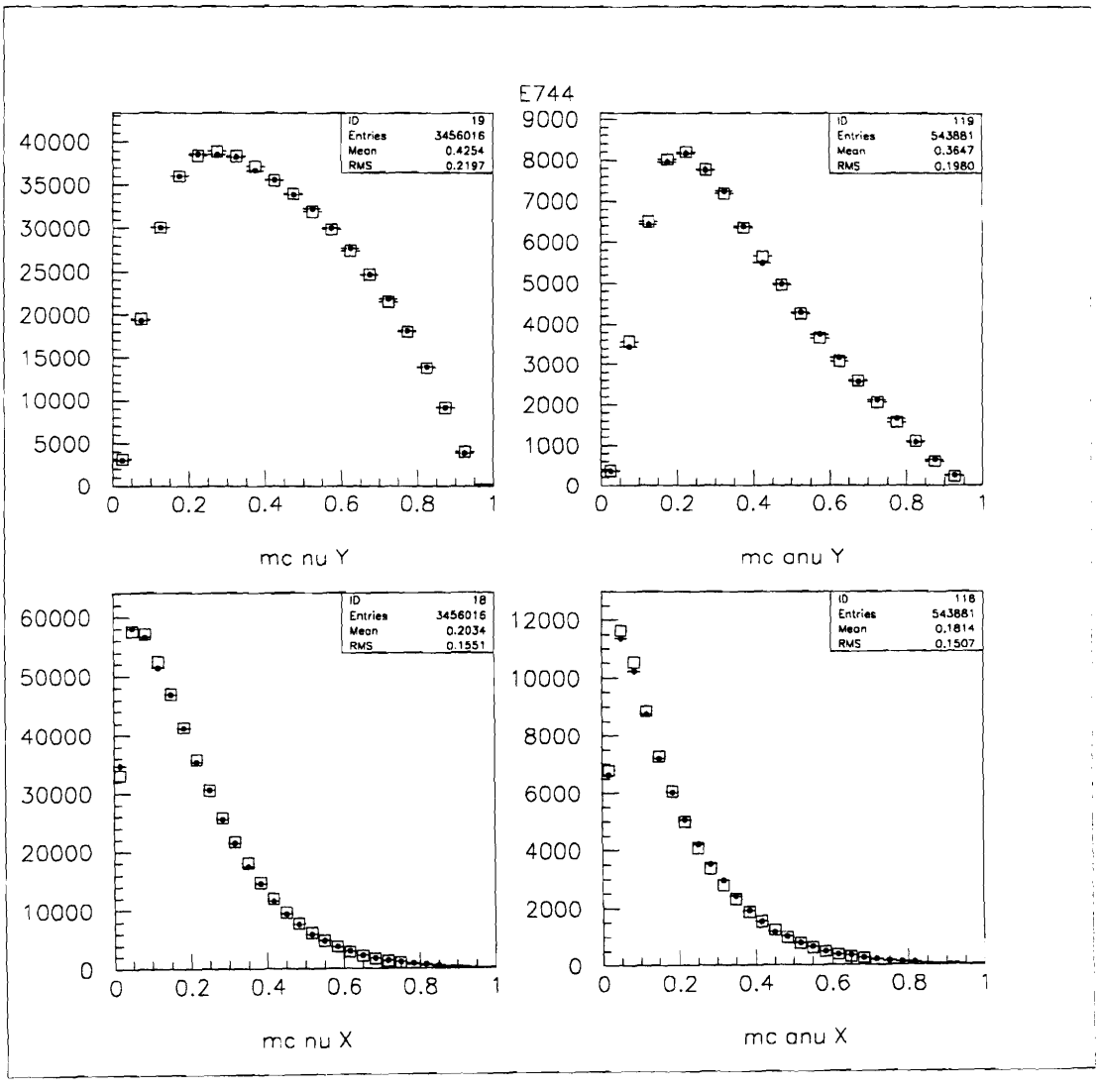

Figure H.7: Data (squares) vs MC(points) for E744 Neutrinos (right) Anti-Neutrinos (left) y-distribution(upper) x-distribution (lower)

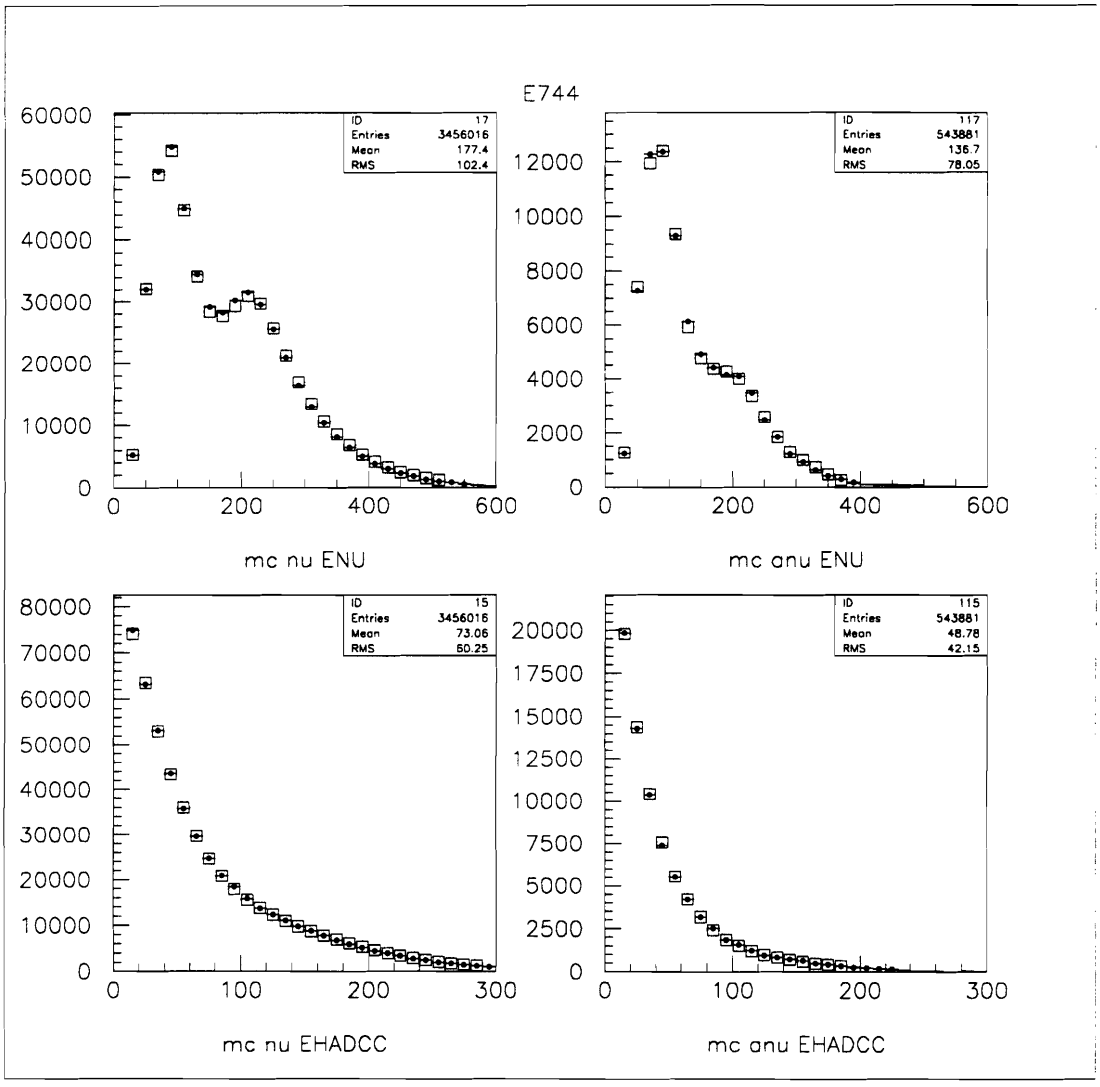

Figure H.8: Data (squares) vs MC(points) for E744 Neutrinos (right) Anti-Neutrinos (left) E_ν-distribution(upper) E_{had}-distribution (lower)

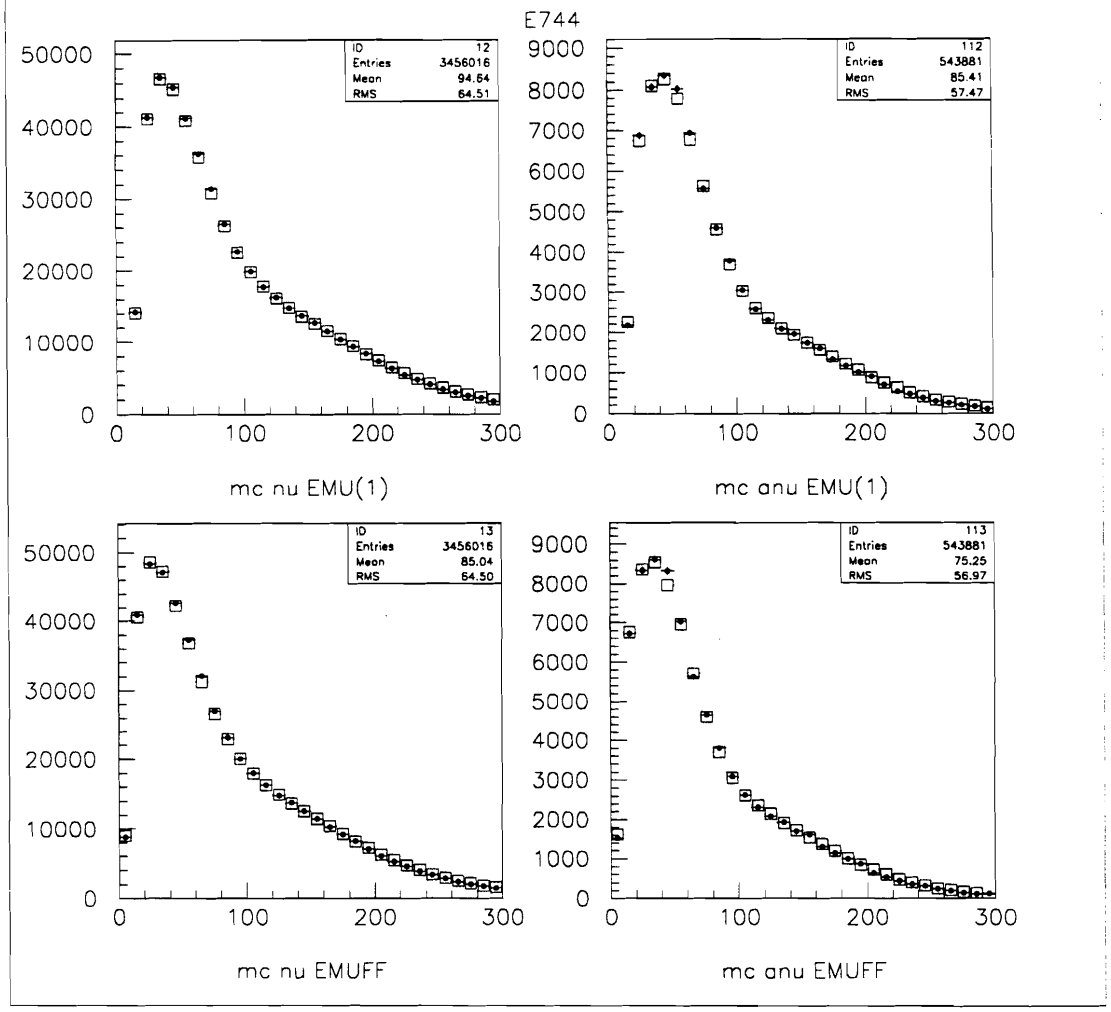

Figure H.9: Data (squares) vs MC(points) for E744 Neutrinos (right) Anti-Neutrinos (left) E_μ-distribution(upper) E_μ*(at toroid front face)*-distribution (lower)

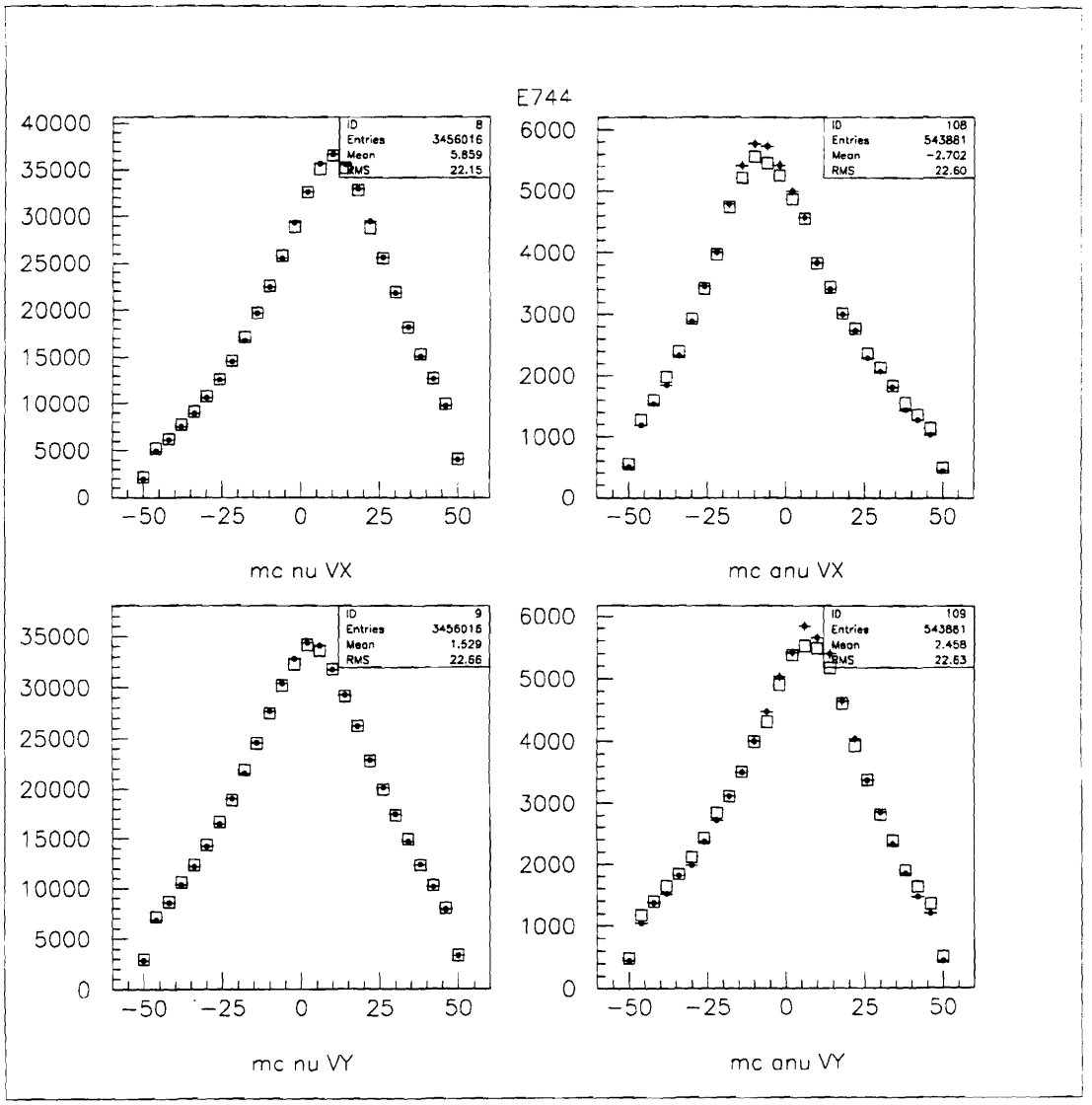

Figure H.10: Data (squares) vs MC(points) for E744 Neutrinos (right) Anti-Neutrinos (left) *x vertex*-distribution(upper) *y vertex*-distribution (lower)

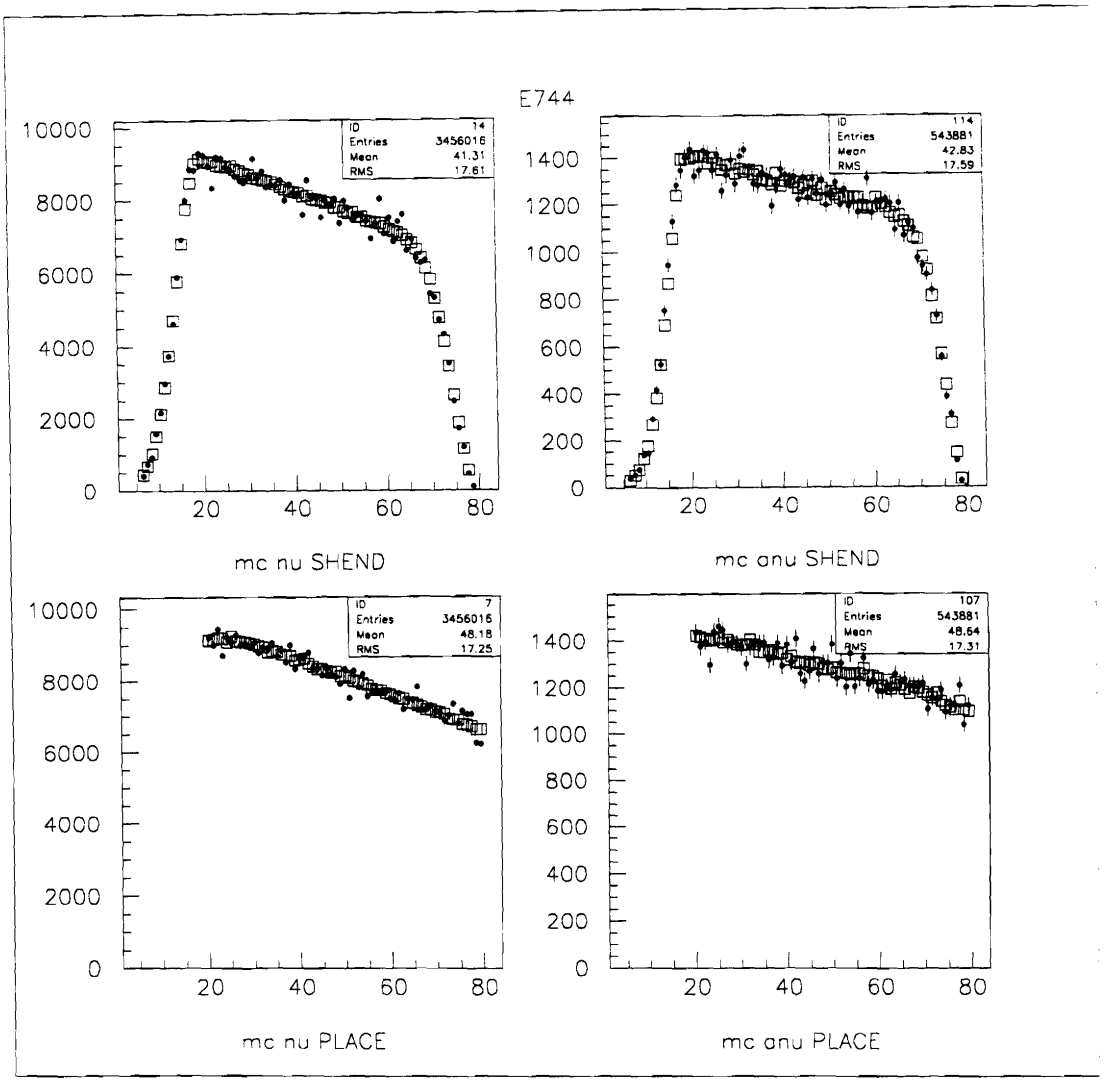

Figure H.11: Data (squares) vs MC(points) for E744 Neutrinos (right) Anti-Neutrinos (left) *shower end* distribution(upper) *place* distribution (lower)

Appendix I: Systematic Error Tables for κ

This appendix contains tables of systematic errors for $\frac{\Delta\kappa}{\kappa}$ by $x$bin. The systematic error headings on the table refers to the following numbering scheme:

Number	Systematic Change	% Variation	direction
1	Hadron Energy Calibration	1%	+
2	"		-
3	Muon Energy Calibration	1%	+
4	"		-
5	770 <B/A> Correction	29%	-
6	"	2.4%	+
7	744 <B/A> Correction	21%	-
8	"	2.3%	+
9	$\sigma^{CCFR}/\sigma^{world}$	2.1%	+
10	"		-
11	$\sigma^{\nu}/\sigma^{\bar{\nu}}$	1.4%	+
12	"		-
13	Charm Mass Parameter	18%	+
14	"		-
15	Strange Sea	10%	+
16	"		-

$\frac{\Delta\kappa}{\kappa}$(xbin)	$\frac{\Delta\kappa}{\kappa}$(1)	$\frac{\Delta\kappa}{\kappa}$(2)	$\frac{\Delta\kappa}{\kappa}$(3)	$\frac{\Delta\kappa}{\kappa}$(4)	$\frac{\Delta\kappa}{\kappa}$(5)
sys1	-.0803	0.0208	0.0246	-.0099	-.1137
sys2	0.0267	-.0597	0.0782	-.1282	-.1601
sys3	0.0651	-.1974	-.0169	-.1489	0.3143
sys4	-.0115	0.2364	-.0859	0.2871	-.0405
sys5	0.0009	0.0038	0.0046	0.0051	0.0070
sys6	-.0009	-.0037	-.0046	-.0049	-.0062
sys7	0.0002	0.0015	0.0019	0.0012	0.0017
sys8	-.0002	-.0016	-.0019	-.0011	-.0012
sys9	0.0330	-.0048	0.1164	-.0151	0.0055
sys10	0.0046	0.0233	0.0258	0.0233	0.0290
sys11	-.0003	-.0058	-.0065	-.0004	0.0012
sys12	0.0003	0.0058	0.0065	0.0004	-.0009
sys13	0.0597	0.1605	0.0273	0.1120	0.2604
sys14	0.0347	0.0111	-.0835	0.0442	0.2424
sys15	-.0671	-.0856	-.0824	-.0894	-.1188
sys16	0.0350	0.0890	0.0866	0.1039	0.1462
sys17	-.0213	-.0501	-.0908	-.1478	-.1936

Appendix J: Source Code for SF Parameterization

```
      SUBROUTINE MODEL(XIN,QSQIN,UV,DV,SEA,SSEA,R)
      Implicit None
c-----------------------------------------------------------------------
c  This returns parton distributions UV,DV,SEA,SSEA,R based on a
c  fit to the structure function data using the Buras-Gaemers
c  parametrization: cf. Nuclear Phys. B132 (1978) ppg 249-267.
c  Buras-Gaemers parametrizes with the form:
c
c  Valence = A * X**E1 * (1-X)**E2
c  Sea = AS * (1-X)**ES
c
c  There were originally nine free Buras-Gaemers parameters which were
c  fitted to the CCFR structure functions (contained in the common
c  block BGPARAM.CMN).
c
c  A0 = this is just Lambda_MSbar for calculating QSQ-dependence
c  A1 = overall normalization for valence dist (i.e. both UV and DV)
c
c  E10, E20 = exponents of the valence distribution at (QSQ=Q0-squared)
c  E11, E21 = linear behavior of exponents with S
c
c  S2,S3 = second and third moments of the SEA distribution
c  G3 = third moment of the Gluon distribution, which figures into
c  .    the QSQ-dependence of the SEA distribution
c
c-----------------------------------------------------------------------
c  Cindy has now added additional terms to this parametrization, which
c  I have altered to fit the known behavior with QSQ.  The new
c  form of the functional fits are:
c
c  Valence = A*(X**E1)*(1-X)**E2 + A2*(1-X)**E3 + A3*(1-X)**E4
c  Sea = AS*(1-X)**ES + AS2*(1-X)**ES2
c
c  This requires adding EIGHT new terms to the fit:
c  .          AV2,E30,E31,  AV3,E40,E41,  AS2,ES2
c
c  AV and AS remain the overall normalizations of the Valence and
c  Sea distributions, but
c
c  AS2 and ES2 can be fitted, but that changes how AS and ES are
c  determined.  Starting with S2 and S3, we evolve from Q0**2 to Q**2,
c  which gives us the 2nd and 3rd moments at QSQ (SQ2 and SQ3).
c  AS and ES are then chosen to force the function to give second
c  and third moments which match SQ2 and SQ3.
c
c  The additional terms in the valence distribution can rely on
c  the same approximation used by Buras-Gaemers:  linearity of the
c  exponents with S approximates the first eight moments to within
c  2%.
c-----------------------------------------------------------------------
#include <BGPARAM.CMN>
#include <TWOMU.CMN>
      real XIN,QSQIN,UV,DV,SEA,SSEA,R

      real GIMEL,RMODEL,RABIN_MODEL
      external GIMEL          !..gamma function
      external RMODEL           !..model fcn for R-Longitudinal
      external RABIN_MODEL
c
```

```
c..the following are variables which are set in initialization
      real TWOMP, Q02
      parameter( TWOMP=1.878 )
      parameter(Q02 = 12.6)

      real T0,V82,V83,QS2,QS3    !..from BG params
      save T0,V82,V83,QS2,QS3
      real X, QSQ, QSQOLD, G2
      save X, QSQ, QSQOLD, G2

      logical INIT, MESSAGE
      save INIT
c
c..the following are var's used for calculating the parton dists from BG
      real E1,E2,E3,E4,E5,E6     !..final X-dependence of Valence
      save E1,E2,E3,E4,E5,E6
      real UVTOT,DVTOT           !..normalization of Valence
      save UVTOT,DVTOT
      real AS,ES,AS2,ES2         !..final X-dependence of SEA
      save AS,ES,AS2,ES2
c
c..the following are temporary variables used in the calculation
c..of the above
      real T,S                   !..basic kinematics
      real GLS                   !.."Theoretical" GLS sum rule from A0&A1
      real TERM
      real EGN1,EGN2, D12,D13,D22,D23 !..temporary vars calculating SQ
      save EGN1,EGN2, D12,D13,D22,D23
      real SQ2,SQ3               !..1st & 2nd moments of SEA
      save SQ2,SQ3

      integer I                  !..loop variable
      integer HID                !..histogram ID# for plotting
      real*4 axis,weight
      real XT,XSTEP,F2INT        !..temp vars for calculation of G2
      parameter(XSTEP=0.002)

      real GN(2),GNP(2),GNN(2),AN(2),BN(2) !..constants from BG paper

      DATA GN,GNP,GNN,AN,BN/
     A     0.427,0.667,
     A     0.747,1.386,
     A     0.   ,0.609,
     A     0.429,0.925,
     A     0.429,0.288/
      DATA INIT /.TRUE./
      DATA MESSAGE /.TRUE./
c
c..Fortran Statement Functions: here we define all of the term's
c..dependence on X.
c
      real VTERM,VINT,SEATERM    !..Statement fcns for parton modelling
      real CPAR,F2MOD            !..Statement fcns for SF(partons)
      real BETA                  !..Statement fcns for integration
      real XV,XP,X1P,XS,XC,XF, AA,BB !..temp vars for the statement fcns

      VTERM(XV)= (XV**E1)*((1.-XV)**E2) + AV2*(XV**E3)*((1.-XV)**E4) +
     &     AV3*(XV**E5)*((1.-XV)**E6)

      VINT(XP,X1P)= BETA(E1+1.+XP, E2+1.+X1P)  +
     &     AV2*BETA(E3+1.+XP, E4+1.+X1P) +
     &     AV3*BETA(E5+1.+XP, E6+1.+X1P)

      SEATERM(XS)= AS*(1.-XS)**ES + AS2*(1.-XS)**ES2
```

```
      CPAR(XC) = (1. + RMODEL(XC,QSQ)) / (1.+(TWOMP*XC)**2./QSQ)
      F2MOD(XF) = CPAR(XF) *
     &     ( (UVTOT+DVTOT*(1-XF))*VTERM(XF) + SEATERM(XF) )

      BETA(AA,BB) = GIMEL(AA)*GIMEL(BB)/GIMEL(AA+BB)
c
c..X2F1 = UV + DV + SEA*2./(SFAC+2.) + SSEA*SFAC/(SFAC+2.)
c..F2 = X2F1 * CPAR
c..XF3 = UV+DV
c-----------------------------------------------------------------------
c..Start of Program
c..For initialization, run through the equations at Q**2=Q0**2
c..
      if (INIT .OR. (XIN .lt. 0.) ) then
        QSQ= Q02
        E1= E10
        E2= E20
        E3= E30
        E4= E40
        E5= E50
        E6= E60
        T0 = LOG( Q02/(A0**2.) )
c
c..Set the valence normalization constants according to GLS Sum Rule,
c..by calculating the integral of the modelled (UV/X) and (DV/X).
        GLS = 3.*(1. - A1/T0 - A2/(T0**2.))
        UVTOT= (2.*GLS/3.) / VINT(-1.,0.)
        DVTOT= (1.*GLS/3.) / VINT(-1.,1.)
c
c..To set the SEA normalization constants, we need the moments of
c..the valence distributions: integrals of UV+DV and X*(UV+DV)
        V82= UVTOT*VINT(0.,0.) + DVTOT*VINT(0.,1.)
        V83= UVTOT*VINT(1.,0.) + DVTOT*VINT(1.,1.)

        QS2= S2+V82
        QS3= S3+V83
c
c..Calculate the SEA term (used by F2MOD below)
        AS2= AS20 + AS21*LOG(Q02)
        ES2= ES20 + AS21*LOG(Q02)

        TERM= ABS( S3 - AS2/((ES2+1.)*(ES2+2.)) )

        if (TERM.GT.0.01) then
          ES= (S2 - AS2/(ES2+1.)) / (S3 - AS2/((ES2+1.)*(ES2+2.)))
          ES= ES - 2.
          AS= (ES+1.)*(S2 - AS2/(ES2+1.))
        else
          AS= 0.
          ES= 1.
        endif
c
c..Calculate the model's integral of F2 at (QSQ = Q02)
c..This will be used to set the parameter "G2"
        F2INT= 0.
        XT= -0.5*XSTEP
        DO I=1,500
          XT= XT + XSTEP
          F2INT= F2INT + 4.*F2MOD(XT)
        ENDDO
        XT= 0.
        DO I=1,499
          XT= XT + XSTEP
```

```
          F2INT=F2INT + 2.*F2MOD(XT)
        ENDDO
        F2INT= F2INT + F2MOD(0.)
        F2INT= F2INT*XSTEP/6.
        G2= 1. - F2INT

        INIT = .FALSE.
        QSQOLD = -999.
        if (XIN .LT. 0.) RETURN
      endif                        !..end of if (INIT .OR. (X .lt. 0.) )
c
c..Now set X and QSQ according to their input values with cutoffs
      X= XIN
      if (X .gt. 0.999) X=0.999
      QSQ= QSQIN
      if (QSQ .le. (2.*A0)) QSQ= 2.*A0

      if (QSQIN .ne. QSQOLD) THEN

        T = LOG( QSQ/(A0**2.) )
        S  = LOG(T/T0)
c
c..The QSQ-dependence of the SEA is calculated by determining the
c..first and second moments of the SEA distribution as QSQ. (SQ2 & SQ3)
        EGN1 = EXP(-GN(1)*S)
        EGN2 = EXP(-GN(2)*S)
        D12=S2*EGN1
        D13=S3*EGN2
        D22=((1.-AN(1))*QS2 - BN(1)*G2)*EXP(-GNP(1)*S)
     &       + (AN(1)*QS2+BN(1)*G2)*EXP(-GNN(1)*S)
     &       - V82*EGN1
        D23=((1-AN(2))*QS3 - BN(2)*G3)*EXP(-GNP(2)*S)
     &       + (AN(2)*QS3+BN(2)*G3)*EXP(-GNN(2)*S)
     &       - V83*EGN2
        SQ2=0.75*D22 + 0.25*D12
        SQ3=0.75*D23 + 0.25*D13
c
c..Now we choose AS and ES so that together with AS2 and ES2 they
c..give the correct values of SQ2 and SQ3.  By integrating the
c..functional form, we see that:
c
c..SQ2= Int:0-1{SEA dx}  =      AS/(ES+1)     +     AS2/(ES2+1)
c..SQ3= Int:0-1{x*SEA dx}= AS/((ES+1)*(ES+2)) + AS2/((ES2+1)*(ES2+2))
c
c..Now we fix the AS2 contributions by the parameters:
c..BS2 * AS/(ES+1) = AS2/(ES2+1)
c..BS3 * AS/((ES+1)*(ES+2)) = AS2/((ES2+1)*(ES2+2))
c  ES= (SQ2/(BS2+1.)) / (SQ3/(BS3+1.)) - 2.
c  AS= (ES+1.)*SQ2/(BS2+1.)
c  ES2= (BS2*(ES+2.)/BS3) - 2.
c  AS2= (ES2+1.)*BS2*AS/(ES+1.)
c
c..Test out not including the AS2 term in normalization (like Cindy):
c        AS = SQ2*(SQ2/SQ3-1.)
c        ES = SQ2/SQ3-2.

        AS2= AS20 + AS21*LOG(QSQ)
        ES2= ES20 + AS21*LOG(QSQ)

        TERM= ABS( SQ3 - AS2/((ES2+1.)*(ES2+2.)) )

        if (TERM.GT.0.01) then
          ES= (SQ2 - AS2/(ES2+1.)) / (SQ3 - AS2/((ES2+1.)*(ES2+2.)))
          ES= ES - 2.
```

```
          AS= (ES+1.)*(SQ2 - AS2/(ES2+1.))
        else
          AS= 0.
          ES= 1.
        endif

c
c..The QSQ-dependence for the exponents of the valence terms is handled
c..by just a linear approximation, which according to Buras & Gaemers is
c..good to within 2% for the first eight moments.
        E1 = E10 + E11*S
        if (E1.lt.0.) E1= 0.
        E2 = E20 + E21*S
        E3 = E30 + E11*S
        if (E3.lt.0.) E3= 0.
        E4 = E40 + E21*S
        E5 = E50 + E11*S
        if (E5.lt.0.) E5= 0.
        E6 = E60 + E21*S
c
c..The normalization for the valence terms is set by a version of
c..the GLS sum rule, made by fitting a first-order term which
c..works best.  We assume that (D-valence) ~= (U-valence)*(1-X)
c..and also that D-valence accounts for 1/3 of the GLS sum rule
c..in normalization.
c
        GLS = 3.*(1.- A1/T - A2/T**2.)
        UVTOT= (2.*GLS/3.) / VINT(-1.,0.)
        DVTOT= (1.*GLS/3.) / VINT(-1.,1.)

        QSQOLD = QSQ
      endif                        !..end of if (QSQ .ne. QSQOLD)
c
c..OK, these are the basic equations, which are calculated using the
      UV= UVTOT*( (X**E1)*((1.-X)**E2) + AV2*(X**E3)*((1.-X)**E4) +
     &     AV3*(X**E5)*((1.-X)**E6) )

      DV= DVTOT * VTERM(X) * (1.-X)

      SEA = SEATERM(X)

      SSEA = RABIN_MODEL(X,QSQ)
cjhk      SSEA = AS*(1./(ES+1.))*(ES+SALPHA+1.)*(1.-X)**(ES+SALPHA)

      R = RMODEL(X,QSQ)

      RETURN
      END

      DOUBLE PRECISION FUNCTION GIMEL(XX)
C     THIS IS THE GAMMA FUNCTION.  I GUESS IT'S USED INSTEAD OF THE
C     BUILT-IN FORTRAN GAMMA FUNCTION BECAUSE IT CAN HANDLE NEGATIVE
C     ARGUMENTS.
C
C     ON RETURN: IER=2 -> ARGUMENT WAS TOO LARGE
C                IER=1 -> XX NEAR NEGATIVE INTEGER OR ZERO
C                IER=0 -> NORMAL, GIMEL = GAMMA(X)
C
C     THIS USED TO BE SUBROUTINE GAMMA, BUT IT CONFLICTS WITH A
C     ROUTINE WITH THE SAME NAME IN THE FORTRAN SUBROUTINE LIBRARY.
C     08-NOV-90 WGS
C
      IMPLICIT DOUBLE PRECISION (A-H,O-Z)
C-------------------------------------------------------------
```

```
      IF(XX-34.5)6,6,4
    4 IER=2
      GIMEL=1.E38
      RETURN
    6 X=XX
      ERR=1.0E-6
      IER=0
      GIMEL=1.0
      IF(X-2.0)50,50,15
   10 IF(X-2.0)110,110,15
   15 X=X-1.0
      GIMEL=GIMEL*X
      GO TO 10
   50 IF(X-1.0)60,120,110
C        SEE IF X IS NEAR NEGATIVE INTEGER OR ZERO
   60 IF(X-ERR)62,62,80
   62 K=X
      Y=FLOAT(K)-X
      IF(ABS(Y)-ERR)130,130,64
   64 IF(1.0-Y-ERR)130,130,70
C        X NOT NEAR A NEGATIVE INTEGER OR ZERO
   70 IF(X-1.0)80,80,110
   80 GIMEL=GIMEL/X
      X=X+1.0
      GO TO 70
  110 Y=X-1.0
      GY=1.0+Y*(-0.5771017+Y*(+0.9858540+Y*(-0.8764218+Y*(+0.8328212+
     1Y*(-0.5684729+Y*(+0.2548205+Y*(-0.05149930)))))))
      GIMEL=GIMEL*GY
  120 RETURN
  130 IER=1
      RETURN
      END
```

Bibliography

[Aba96] "Measurement of the W Boson Mass" by the D0 Collaboration (S. Abachi *et al.*); *Phys. Rev. Lett.* **77***:* 3309-3314, 1996

[Abe94] "Measurement Of $\alpha_S(M_Z^2)$From Hadronic Event Observables at the Z_0 Resonance"; K. Abe, *et al.* (SLD Collaboration); *Phys. Rev.* **D51**: 962-984 (1995); hep-ex/9501003.

[Abe96] "Inclusive jet cross section in $p\bar{p}$ collisions at $\sqrt{s}$ = 1.8 *TeV*"; F. Abe, *et al.*; (CDF Collaboration); *Phys. Rev. Lett.* **77**: 438-443 (1996); hep-ex/9601008

[Ada95a] "Shadowing in Inelastic Scattering of Muons on Carbon, Calcium and Lead at Low x_{BJ}"; M. R. Adams, *et al.* (E665 Collaboration); *Z. Phys.* **C67**: 403-410 (1995); hep-ex/9505006.

[Ada95b] "Determination of the Gluon Distribution Function of the Nucleon Using Energy-Energy Angular Pattern in Deep Inelastic Muon-Deuteron Scattering"; M. R. Adams, *et al.* (E665 Collaboration); FERMILAB-PUB-95-395-E (1995).

[Ada96] "Proton and Deuteron Structure Functions in Muon Scattering at 470-GeV"; M. R. Adams, *et al.* (E665 Collaboration); *Phys.Rev.* **D54**: 3006-3056 (1996).

[Aid95] "A Direct Determination of the Gluon Density in the Proton at Low x"; S. Aid, *et al.* (H1 Collaboration); *Nucl. Phys.* **B449**: 3-24 (1995); hep-ex/9505014.

[Alt77] "Asymptotic Freedom in Parton Language"; G. Altarelli (Ecole Normale Superieure), G. Parisi (IHES, Bures); *Nucl. Phys.* **B126**: 298 (1977).

[Alt78] G. Altarelli and G. Martinelli, *Phys. Lett.B* 75 (1978) 89; M. Gluck and E. Reya, *Nucl. Phys. B* 145 (1978) 24.

[Alt82] "Partons in Quantum Chromodynamics"; G. Altarelli (Ecole Normale Superieure); *Phys. Rep.* **81**: 1-129 (1982); reprinted in *The Development of Perturbative QCD*, ed. G. Altarelli, World Scientific (1994).

[Ama95] "A Re-Evaluation of the Nuclear Structure Function Ratios for D, He, Li, C and Ca"; P. Amaudruz, *et al.* (New Muon Collaboration); *Nucl. Phys.* **B441**: 3-11 (1995); hep-ph/9503291.

[Arn84] "Measurements of the A-Dependence of Deep Inelastic Electron Scattering From Nuclei"; R. G. Arnold, *et al.*; *Phys. Rev. Lett.* **52**: 727 (1984).

[Arn93] "Quark and Gluon Distributions and α_S From Nucleon Structure Functions at Low x"; M. Arneodo et al. (New Muon Collaboration); *Phys.Lett.* **B309**: 222-230 (1993).

[Arn97] "Measurement of the Proton and the Deuteron Structure Functions, F_2^p and F_2^d, and of the Ratio σ_L/σ_T"; M. Arneodo, *et al.* (New Muon Collaboration); *Nucl. Phys.* B 483 (1997) 3.

[Aub85] J.J. Aubert *et al., Nucl. Phys.* B293 (1987) 740

[Aub83] J.J. Aubert *et al., Nucl. Phys.* B213 (1983) 31

[Auc90] "Measurement of the Inclusive Charged-Current Cross Section for Neutrino and Antineutrino Scattering on Isoscalar Nucleons"; P. S. Auchincloss, *et al.* (CCFR Collaboration); *Z. Phys.* **C48**: 411-432 (1990).

[Bac88] "A Study of Same Sign Dimuon Events in Neutrino-Nucleon Scattering"; K. T. Bachmann (Columbia University); Ph.D. Thesis, Nevis Reports 267 (1988).

[Bal95] "Determination Of α_S From F2(P) at HERA"; Richard D. Ball, Stefano Forte (CERN); *Phys. Lett.* **B358**: 365-378 (1995); hep-ph/9506233.

[Bar76] "Evidence For New Quarks and New Currents"; R. M. Barnett (Harvard University); *Phys. Rev. Lett.* **36**: 1163-1166 (1976).

[Bar86] "On the Radiative Corrections to the Neutrino Deep Inelastic Scattering"; D. Yu. Bardin and V. A. Dokuchaeva (Dubna, JINR); *JINR-E2-86-260* (1986).

[Bar96] "Review of Particle Physics"; R. M. Barnett, *et al.* (Particle Data Group); *Phys. Rev.* **D54** (1996).

[Baz91] "A Comparative Study of Structure Function Measurements from Hydrogen and Deuterium"; K. Bazizi and S. J. Wimpenny (UC, Riverside); UCR-DIS-91-02 (Jul 1991).

[Baz94] "Determination of the Strange Quark Distribution from a Next-to-Leading-Order QCD Analysis of Neutrino and Antineutrino Production of Charm"; Andrew Bazarko (Columbia University); Ph.D. Thesis, Nevis Reports 285 (1994).

[Baz95] "Determination of the Strange Quark Content of the Nucleon From a Next-To-Leading Order QCD Analysis of Neutrino Charm Production"; A.O. Bazarko, *et al.* (CCFR Collaboration); *Z. Phys.* **C65**: 189-198 (1995); hep-ex/9406007.

[Bel88] "Neutrino reactions in the low-*y* region"; R. Belusevic and D. Rein; *Phys. Rev.* **D38**: 2753-2757 (1988).

[Bel92] "Exclusive neutrino interactions on heavy nuclei"; R. Belusevic and D. Rein; *Phys. Rev.* **D46**: 3747-3750 (1992).

[Ben87] "A High Statistics Measurement of the Nucleon Structure Function $F_2(x,Q^2)$ From Deep Inelastic Muon - Carbon Scattering at High Q^2"; A. C. Benvenuti *et al.* (BCDMS Collaboration); *Phys. Lett.* **B195**: 91 (1987).

[Ben90] "A High Statistics Measurement of the Deuteron Structure Functions $F_2(x,Q^2)$ and R From Deep Inelastic Muon Scattering at High Q^2"; A. C. Benvenuti, *et al.* (BCDMS Collaboration); *Phys. Lett.* **B237**: 592 (1990).

[Ber87] "Total neutrino and antinuetrino charged current cross section measurement in 100, 160, and 200 GeV narrow band beams"; P. Berge, *et al.* (CDHS Collaboration); *Z. Phys.* **C35**: 443-452 (1987).

[Ber91] "A Measurement of Differential Cross-Sections and Nucleon Structure Functions in Charged-Current Neutrino Interactions On Iron"; P. Berge, *et al.* (CDHSW Collaboration); *Z. Phys.* **C49**: 187-223 (1991).

[Bet95] "Status of α_S Meeasurements"; S. Bethke; (Aachen, Tech. Hochsch.). PITHA-95-14, Jun 1995. Talk given at 30th Rencontres de Moriond: QCD and High Energy Hadronic Interactions, Meribel les Allues, France.

[Bjo69] "Asymptotic Sum Rules at Infinite Momentum"; J. D. Bjorken; *Phys. Rev.* **179**: 1547-1553 (1969).

[Bla83] "Measurement of the Rate of Increase of Neutrino Cross-Sections With Energy"; R. Blair, *et al.* (CCFRR Collaboration); *Phys. Rev. Lett.* **51**: 343-346 (1983).

[Blo76] "Recent Results Concerning the Electromagnetic Structure of the Nucleon"; E. D. Bloom (Cal Tech & SLAC); SLAC-PUB-1319, Oct 1973. Invited paper presented at International Symposium on Electron and Photon Interactions at High Energies (1973).

[Blu94] "Do Deep Inelastic Scattering Data Favor a Light Gluino?"; J. Blümlein and J. Botts (DESY); DESY-94-008 (Jan 1994); hep-ph/9401291.

[Bod74] "The Ratio of Deep-Inelastic eN to eP Cross-Sections in the Threshold Region"; A. Bodek, *et al.* (SLAC); *Phys. Lett.* **51B**: 417 (1974).

[Bod81] "Fermi Motion Effects in Deep Inelastic Lepton Scattering From Nuclear Targets"; A. Bodek, J. L. Ritchie (Rochester U.); *Phys. Rev.* **D23**: 1070 (1981).

[Bot93] "CTEQ Parton Distributions and Flavor Dependence of Sea Quarks"; J. Botts *et al.* (CTEQ Collaboration); *Phys. Lett.* **B304**: 159-166 (1993); hep-ph/9303255.

[Bro96] "The Quark/Antiquark Asymmetry of the Nucleon Sea"; S. Brodsky and B. Ma; *Phys. Lett.* **B381**: 317-324 (1996); hep-ph/9604393.

[Bur78] "Simple Parametrizations of Parton Distributions With Q**2 Dependence Given by Asymptotic Freedom"; A. J. Buras, K. J. F. Gaemers (CERN); *Nucl. Phys.* **B132**: 249 (1978).

[Coa95] "Measurement Of α_S From τ Decays"; T. Coan et al. (CLEO Collaboration); *Phys. Lett.* **B356**: 580-588 (1995).

[Cof87] D. Coffman, PhD thesis, Caltech, 1987.

[Dav94] "A Precise Determination of α_S From Lattice QCD"; C. T. H. Davies, *et al.*; *Phys. Lett.* **B345**: 42 (1995); hep-ph/9408328.

[Dev83] "Direct Analysis of Scaling Violations in Large Q**2 Deep Inelastic Neutrino and Muon Scattering";. A. Devoto, D. W. Duke, J. F. Owens (Florida State U.), R. G. Roberts (Rutherford); *Phys. Rev.* **D27**: 508-522 (1983).

[Das96] "Power Corrections and Renormalons in Deep Inelastic Structure Functions"; M. Dasgupta and B. R. Webber (Cambridge Univ.); *Phys. Lett.* **B382**: 273 (1996); hep-ph/9604388.

[Dok78] "Hard Semiinclusive Processes in QCD"; Yu. L. Dokshitser, D. I. Diakonov, S. I. Troyan (St. Petersburg, INP); *Phys. Lett.* **78B**: 290 (1978).

[Dok80] "Hard Processes in Quantum Chromodynamics"; Yu. L. Dokshitser, D. I. Diakonov, S. I. Troian; *Phys. Rep.* **58**: 269-395 (1980).

[Dok95] "Dispersive Approach to Power Behaved Contributions in QCD Hard Processes"; Yu. L. Dokshitser (CERN), G. Marchesini (Milan U. & INFN, Milan), B. R. Webber (Cambridge U., Cavendish Lab); CERN-TH-95-281, (Dec 1995); hep-ph/9512336.

[Don94] "Proton Structure Function at Small Q**2"; A. Donnachie (Manchester U.) and P.V. Landshoff (Cambridge U., DAMTP); *Z. Phys.* **C61**: 139-146 (1994); hep-ph/9305319.

[Flo81] "Higher-Order QCD Effects in Inclusive Annihilation and Deep-Inelastic Scattering"; E. G. Floratos, C. Kounnas (Ecole Normale Superieure), R. Lacaze (Saclay); *Nucl. Phys.* **B192**: 417 (1981).

[Fou90] "Neutrino Production of Opposite Sign Dimuons at Tevatron Energies"; C. Foudas, *et al.* (CCFR Collaboration); *Phys. Rev. Lett.* **64**: 1207 (1990).

[Geo76] "Freedom at Moderate Energies: Masses in Color Dynamics"; H. Georgi and H. D. Politzer (Harvard University); *Phys. Rev.* **D14**: 1829 (1976).

[Glu95] "Dynamical Parton Distributions of the Proton and Small x"; M. Glück, E. Reya (Dortmund U.), A. Vogt (DESY); *Z. Phys.* **C67**: 433-448 (1995).

[Gom94] "Measurement of the A-Dependence of Deep Inelastic Electron Scattering"; J. Gomez, *et al.*; *Phys. Rev.* **D49**: 4348-4372 (1994).

[Gri72] "Deep Inelastic e-P Scattering in Perturbation Theory"; V. N. Gribov, L. N. Lipatov (St. Petersburg, INP); *Sov. J. Nucl. Phys.* **15**: 438-450 (1972).

[Hai94] D. Haidt (DESY), private communication.

[Hal84] *Quarks and Leptons: An Introductory Course in Modern Particle Physics;* F. Halzen and A. D. Martin; John Wiley & Sons (1984).

[Har95] "A Measurement of Alpha-s (Q**2) From the Gross-Llewellyn-Smith Sum Rule"; D. A. Harris, *et al.* (CCFR-NUTEV Collaboration); *Moriond 1995: Hadronic:* 247-250; hep-ex/9506010.

[Her80] "Altarelli-Parisi Equation in the Next-To-Leading Order"; R. T. Herrod, S. Wada (Cambridge U., Cavendish Lab.); *Phys. Lett.* **96B**: 195 (1980).

[Hin77] "Scaling Violations and Neutrino Cross Sections"; I. Hinchcliffe and C. H. Llewellyn-Smith (Oxford Univ.); *Phys. Lett.* **70B**: 247-252 (1977).

[Jam94] *MINUIT – Function Minimization and Error Analysis;* F. James and M. Goosens (CERN); CERN Program Library entry **D506** (1994).

[Kin91] "Measuring Muon Momenta With the CCFR Neutrino Detector"; B. J. King, *et al.* (CCFR Collaboration); *Nucl. Instrum. Methods* **A302**: 254-260 (1991).

[Kin94] "A Precise Measurement of the Weak Mixing Angle in Neutrino-Nucleon Scattering"; B. J. King, Ph.D. Thesis (Columbia University); Nevis Reports 283 (1994).

[Koi78] G. Koizumi; FERMILAB-TM-0780 (1978).

[Lai95] H. L. Lai, *et al.*; *Phys. Rev. D* 51, 4763 (1995).

[Leu91] "Nucleon Structure Functions from High-Energy ν-Iron Interactions at the Fermilab Tevatron"; W. C. Leung, Ph.D. Thesis (Columbia University); Nevis Reports 276 (1991).

[Mac84a] "Nucleon Structure from Neutrino Interactions in an Iron Target with a Study of the Singlet Quark Distribution"; D. MacFarlane (California Institute of Technology); Ph.D. Thesis (1984).

[Mac84b] "Nucleon Structure Functions From High-Energy Neutrino Interactions with Iron and QCD Results"; D. MacFarlane, *et al.* (CCFRR Collaboration); *Z. Phys.* **C26**: 1 (1984).

[Mar91] "Scale Dependence of $\Lambda_{\overline{MS}}$ from Deep Inelastic Scattering"; A. D. Martin, W. J. Stirling (Durham Univ.), R. G. Roberts (Rutherford); *Phys. Lett.* **B266**: 173-177 (1991).

[Mar96] "Parton distributions: a study of the new HERA data, α_S, the gluon and $p\bar{p}$ jet production"; A. D. Martin (Durham Univ.), R. G. Roberts (Rutherford), W. J. Stirling (Durham Univ.); DTP/96/44, RAL-TR-96-037 (1996); hep-ph/9606345.

[Mar96b] "Pinning down the Glue in the Proton", A. D. Martin, W.J. Stirling (Durham U.), R. G. Roberts (Rutherford), *Phys. Lett.* **B** 354: 155-162, 1995.

[Mis89] "A Study of Wrong Sign Single Muon Production in Muon-Neutrino–Nucleon Interaction"; S. R. Mishra, *et al.* (CCFR Collaboration); *Z. Phys.* **C44**: 187 (1989).

[Mor91] "Dimuon Production In Proton-Copper Collisions at $\sqrt{s}$ = 38.8 *GeV*"; G. Moreno, *et al.*; *Phys. Rev.* **D43**: 2815-2836 (1991).

[Olt89] "Nucleon Structure Functions from High Energy Neutrino and Antineutrino Interactions in Iron"; E. Oltman (Columbia University); Ph.D. Thesis, Nevis Reports 270 (1989).

[Per82] *Introduction to High Energy Physics*; D. H. Perkins; Addison-Wesley (1982).

[Phy96] *Phys. Rev.* D 54 (1996) 94

[Pre92] *Numerical Recipes in FORTRAN – The Art of Scientific Computing, 2nd Edition;* W. H. Press, S. A. Teukolsky, W. T. Vetterling, B. P. Flannery; Cambridge University Press (1992).

[Pur84] "Nucleon Structure Functions from ν_μ-Fe Interactions and a Study of the Valence Quark Distribution"; M. Purohit (California Institute of Technology); Ph.D. Thesis (1984).

[Qui92] "Nucleon Structure Functions at the Fermilab Tevatron With a Measurement of $\Lambda_{\overline{MS}}$"; P. Z. Quintas (Columbia University); Ph.D. Thesis, Nevis Reports 277 (1992).

[Qui93] "Measurement of Λ_{QCD} from ν_μ-Fe Nonsinglet Structgure Functions at the Fermilab Tevatron"; P. Z. Quintas, *et al.* (CCFR Collaboration); *Phys. Rev. Lett.* **71**: 1307-1310 (1993).

[Rab92] "Opposite Sign Dimuon Production in Neutrino Interactions at the Fermilab Tevatron"; S. A. Rabinowitz (Columbia University); Ph. D. Thesis, Nevis Reports 279 (1992).

[Rab93] "Measurement of the Strange Sea Distribution Using Neutrino Charm Production"; S. A. Rabinowitz, *et al.* (CCFR Collaboration); *Phys. Rev. Lett.* **70**: 134-137 (1993).

[Rob90] *The Structure of the Proton;* R. G. Roberts; Cambridge University Press (1990).

[Ruj79] "Radiative Corrections to High-Energy Neutrino Scattering"; A. De Rujula, R. Petronzio (CERN), A. Savoy-Navarro (Saclay); *Nucl. Phys.* **B154**: 394 (1979).

[Sak90] "Calibration of the CCFR Target Calorimeter"; W. K. Sakumoto, *et al.* (CCFR Collaboration); *Nucl. Instrum. Meth.* **A294**: 179-192 (1990).

[Sal68] "Weak and Electromagnetic Interactions"; A. Salam (Imperial Coll., London & ICTP, Trieste); Originally printed in Svartholm: *Elementary Particle Theory, Proceedings Of The Nobel Symposium Held 1968 At Lerum, Sweden*, Stockholm 1968, 367-377; Reprinted in Lichtenberg, D. B. (ed.), Rosen, S. P. (ed.): *Developments In The Quark Theory Of Hadrons, Vol. 1*, 160-170; and in Lai, C. H. (ed.): *Gauge Theory Of Weak and Electromagnetic Interactions*, 188-198; Also in Rosner, J. L. (ed.): *New particles* 29-39.

[San93] "Neutrino Production of Same Sign Dimuons at the Fermilab Tevatron"; P. H. Sandler, *et al.* (CCFR Collaboration); *Z. Phys.* **C57**: 1-12 (1993).

[Sel97] "A Next-to-Leading-Order QCD Analysis of Neutrino-Iron Structure Functions at the Tevatron"; William Glenn Seligman (Columbia University); Ph.D. Thesis, Nevis Reports 292 (1997).

[Sid95] "Nuclear effect in the deuteron, Q^2-evolution of the $xF_3^N(x,Q^2)$ structure function and the Gross-Llewellyn Smith sum rule"; A. V. Sidorov and M. V. Tokarev {JINR); *Phys. Lett.* **B358**: 353-359 (1995).

[Sid96a] "QCD analysis of the CCFR data for xF_3 and Higher-Twist Contribution"; A. V. Sidorov (JINR); *Phys. Lett.* **B389**: 379-382 (1996); hep-ph/9607275.

[Sid96b] "Next-to-next-to-leading order QCD analysis of combined data for xF_3 structure functions and higher-twist contribution"; A. V. Sidorov (JINR); hep-ph/9609345.

[Sop89] "Factorization of Hard Processes in QCD"; D. E. Soper, J. C. Collins, and G. Sterman; *Perturbative Quantum Chromodynamics*, ed. A. H. Mueller, World Scientific (1989).

[Soz93] "Direct Photon Production in $\bar{p}p$ and pp Interactions at $\sqrt{s}$ = 24.3 *GeV*"; G. Sozzi, et al. (UA6 Collaboration); Phys. Lett. B317: 243-249 (1993).

[Sto85] "Search For Muon Neutrino and Anti-Neutrinos Oscillations in the Mass Range 15 $eV^2/c^4 < \Delta m^{**}2 < 1000\ eV^2/c^4$"; I. E. Stockdale, *et al.* (CCFR collaboration); *Z. Phys.* **C27**: 53 (1985).

[Ush88] N. Ushida *et al.* (E531 Collaboration), *Phys. Lett. B* **206**, 375 (1988).

[Vir92] "A measurement of α_S and of higher twists from a QCD analysis of high statistics F_2 data on hydrogen and deuterium targets"; M. Virchaux and A. Milsztajn (Saclay); *Phys. Lett.* **B274**: 221-229 (1992).

[Wei67] "A Model of Leptons"; S. Weinberg (MIT, LNS) *Phys. Rev. Lett.* **19**: 1264-1266 (1967); Also in: Lichtenberg, D. B. (ed.), Rosen, S. P. (ed.): *Developments In The Quark Theory Of Hadrons, Vol. 1*, 157-159; in Lai, C. H. (ed.): *Gauge Theory Of Weak and Electromagnetic Interactions*, 185-187; in Rosner, J. L. (ed.): *New Particles*, 26-28.

[Whi90a] *Deep Inelastic Structure Functions from Electron Scattering on Hydrogen, Deuterium, and Iron at* $.56 < Q^2 < 30\ GeV^2$"; L. W. Whitlow (Stanford Univ.); Ph.D. Thesis, SLAC-REPORT-357 (1990).

[Whi90b] "A Precise Extraction of R = σ_L / σ_T From a Global Analysis of the SLAC Deep Inelastic eP and eD Scattering Cross-Sections"; L. W. Whitlow, *et al.; Phys. Lett.* **B250**: 193-198 (1990).

[Yan96] "A Measurement of R = Sigma-L / Sigma-T in Deep Inelastic Neutrino-Nucleon Scattering at the Tevatron"; U. K. Yang, *et al.* (CCFR/NuTeV Collaboration); *J. Phys.* **G22**: 775-780 (1996); hep-ex/9605005.

[Ynd93] *The Theory of Quark and Gluon Interactions*; F. J. Yndurain; Berlin: Springer-Verlag (1993).

[Zhi93] J. Zhitnitsky, private communication.

[Zhu96] "The first preliminary total cross section measurement at very low x and Q^2 at HERA"; Q. Zhu (for the ZEUS collaboration); Conference proceedings of the DIS96, Rome, Italy (1996).